

https://dspace.org/

Blast wave generation and interactions

Demby, David Marc

2018

https://hdl.handle.net/10539/25892

Demby, David Marc, (2018) Blast wave generation and interaction, University of the Witwatersrand, Johannesburg, https://hdl.handle.net/10539/25892

Downloaded from a DSpace repository. https://dspace.org/

Blast Wave Generation and Interactions

David Marc Demby

A dissertation submitted to the Faculty of Faculty of Engineering and the Built Environment, University of the Witwatersrand, Johannesburg, in fulfilment of the requirements for the degree of Master of Science in Engineering.

Johannesburg, February 2018

Declaration

I declare that this dissertation is my own, unaided work, except where otherwise acknowledged. It is being submitted for the degree of Master of Science in Engineering in the University of the Witwatersrand, Johannesburg. It has not been submitted before for any degree or examination at any other university.

Signed this 27th day of February 2018



David Marc Demby

Acknowledgements

I would like to thank my esteemed supervisor Professor Beric W. Skews for his continued professional guidance, wise counsel, personal supervision and uplifting motivation throughout the two year duration of my dissertation. I am deeply appreciative of the countless hours you took to sit and meet with me to discuss my research as well as other compressible flow phenomena. I am markedly impressed and impacted by your continuous and palpable passion, enthusiasm and excitement for compressible flow phenomena. The lightening up of your face upon discussing compressible flows is indelibly imprinted on my consciousness and I can only hope to be nearly as passionate about my future work as you are of yours. Thank you for allowing me to express my own individuality and for giving me free reign to manage and channel my research in the manner and direction that I felt was the most interesting and practical for me.

To Mr. Randall T. Paton and Mr. Alessandro Filippi: Thank you for your advice and guidance on numerous numerical, experimental and social subject matters. Your continued support and insight throughout the duration of my dissertation helped to keep me focused and motivated to produce only the highest calibre of work.

To the North West Engineering workshop staff and in particular Mr. Shaun Riekert and Mr. Lionel Claasen. Thank you for all your hard work, personal assistance, technical advise throughout the design process of my blast tube as well as for the excellent manufacturing of the complex and numerous components that make up my blast tube.

To my friends and colleagues in the the Flow Research Unit and at the University of the Witwatersrand. Thank you for your continued advice, support, motivation and entertainment. Our special lunches on the bench will always hold a special place in my memories. To my special friends that make up the *Advisory Board*, thank you for never loosing faith in me and for always being there to motivate and advise me through out this long journey.

Finally, and most importantly, a very special and heartfelt thank you goes to my parents and sister who despite all the challenges endured over this long 9 year journey have unwaveringly supported me and motivated me to always try to fulfil my potential. If not for your being an indelible part and guiding force of my life, I in all likelihood would not be who I am and where I am today.

Abstract

The design, construction and validation of a non-explosively driven blast tube was undertaken in order to reduce the cost and time of blast wave experimentation as well as to enable the study of blast waves in the test laboratory environment. The design of the blast tube was performed numerically using commercially available CFD software. Numerous different driver shapes and configurations were analysed during the design process including linearly diverging drivers, straight drivers and polynomial drivers.

Based on the results and analysis performed in it was deduced that a driver section required a few key features in order to generate a blast wave with a realistic Friedlander pressure profile namely, the driver section must end in a sharp corner in order to enable expansion focusing to occur, the walls of the driver section must be divergent to cause the expansion waves to reflect downstream almost immediately after the diaphragm bursts as well to drive the expansion focusing, the walls of the driver section must transition smoothly, that is without a corner, into the expansion section walls and the walls of the driver section must be curved in order to induce smooth and continuous expansion wave reflection and focusing. After some tests were carried out on a few iterations of driver section shapes, three shapes were settled on, namely a concave driver, a linear driver and a convex driver.

Once the final design of the blast tube was settled upon, a working prototype was manufactured and assembled in the North West Engineering Laboratories and the prototype was tested. During testing of the blast tube it was found that, despite issues arising due to choice of mechanism employed to pressurise the driver being flawed, there being notches and steps at the joints along the tube length and the downstream end of the test section being closed, the blast tube did in fact generate blast waves with realistic pressure decay profiles and good visual quality. After being validated the blast tube was used to examine the diffraction of the blast wave around a 90° corner and the reflection of the blast wave induced upon impinging wedges having angles of 15°, 30° and 45°. The blast wave diffraction and reflection experimentation were carried out in the $1.2 < M_s < 1.4$ range.

Contents

Declaration i

Acknowledgements ii

Abstract iv

Contents v

List of Figures xi

List of Tables xviii

List of Symbols xix

List of Acronyms xxi

1 Introduction 1

1.1 Background 1

1.2 Research Aim 2

2 Literature Review 3

2.1 Overview of Gas Dynamics 3

2.1.1 Fundamental Equations of Flow . . . 3
2.1.1.1 Equation of State of an Ideal Gas . . . 3
2.1.1.2 Continuity Equation . . . 4
2.1.1.3 Momentum Equation . . . 4
2.1.1.4 Energy Equation . . . 5
2.1.2 Speed of Sound . . . 5
2.2 Shock Waves . . . 6
2.2.1 Stationary Normal Shock Waves . . . 6
2.2.2 Moving Normal Shock Waves . . . 9
2.2.3 Oblique Shock Waves . . . 10
2.2.4 Spherical Shock . . . 13
2.3 Explosions . . . 13
2.3.1 Nature of Explosions and Explosives . . . 13
2.3.2 Heat of Explosions . . . 15
2.3.3 Energy of Explosions . . . 16
2.3.4 Entropy of Explosions . . . 16
2.3.5 Calculating the Theoretical Explosive Yield . . . 17
2.4 Blast Waves . . . 18
2.4.1 Formation of the Blast Wave . . . 18
2.4.2 Blast Wave Configuration . . . 19
2.4.2.1 Friedlander and Modified Friedlander Pressure Profiles . . . 20
2.4.2.2 Secondary Shock Wave . . . 21

2.4.3 Peak Overpressure . . . 21
2.4.4 Blast Wave Duration . . . 22
2.4.5 Blast Wave Impulse . . . 22
2.5 Shock Tube . . . 23
2.6 Blast Tube . . . 24
2.6.1 Explosively Driven Blast Tube Configurations . . . 25
2.7 Shock Wave Reflection . . . 27
2.7.1 Normal Reflection . . . 27
2.7.2 Oblique Reflection . . . 29
2.7.2.1 Regular Reflection . . . 29
2.7.2.2 Mach Reflection . . . 31
2.7.2.3 The Transition Criteria . . . 33
2.8 Shock Wave Diffraction . . . 34
2.9 Shock and Expansion Wave Focusing . . . 39

3 Objectives **41**

4 Apparatus **42**

4.1 Design of the Blast Tube . . . 42
4.1.1 Introduction . . . 42
4.1.1.1 Design Constraints arising from the use of Existing Resources 42
4.1.2 Numerical Method . . . 43
4.1.2.1 Geometry Specification . . . 44
4.1.2.2 Mesh Specification . . . 44

4.1.2.3 Solver Settings 46
4.1.2.3.1 Solution Setup 46
4.1.2.3.2 Solution Settings 47
4.1.3 Diverging Driver Sections 48
4.1.4 Straight Driver Sections 71
4.1.5 Polynomial Driver Sections 89
4.1.6 Varying Diaphragm Location 91
4.1.7 Varying Driver Section and Transition Section Lengths 103
4.1.8 Effect of Blast Tube Length 119
4.1.9 Final Blast Tube Design and Specification 131
4.1.9.1 Driver Section 131
4.1.9.2 Transition Section 132

5 Experimental Method **134**

5.1 Experimental Facilities 134
5.1.1 Blast Tube Facility 134
5.2 Experimental Procedures and Precautions 136
5.2.1 Air Storage Vessel Pressurisation Procedure 136
5.2.2 Blast Tube Pre-Testing Procedure 137
5.2.3 Blast Tube Testing Procedure 137
5.2.4 Blast Tube Shut Down Procedure 138
5.2.5 Precautions 139
5.3 Flow Visualisation 139

6 Calibration **142**

6.1 Pneumatic Pricker 142

6.2 Blast Tube Calibration Data 142

7 Results and Discussion **145**

7.1 Data Processing 145

7.2 Validation Numerical Design and Analysis 145

7.3 Blast Wave Diffraction 151

7.4 Blast Wave Reflection 155

7.4.1 15° Reflection 155

7.4.2 30° Reflection 160

7.4.3 45° Reflection 165

7.4.4 Comparison of Blast Wave Reflection to Normal Shock Wave Reflection 169

8 Conclusions **171**

8.1 Diverging Driver Sections 171

8.2 Straight Driver Sections 172

8.3 Polynomial Section 172

8.4 Blast Tube Validation 175

8.5 Blast Wave Diffraction 175

8.6 Blast Wave Reflection 176

9 Recommendations **177**

Bibliography **179**

A Varying Diaphragm Location CFD Data **181**

A.1 Linear Driver Section CFD Data 181

A.2 Convex Driver Section CFD Data 190

B Varying Driver Section and Transition Section Lengths CFD Data **200**

B.1 Varying Linear Driver Section Length CFD Data 200

B.2 Varying Convex Driver Section Length CFD Data 212

C Digital Appendix **225**

C.1 Blast Tube Research and Design CFD Simulations 225

C.2 High Speed Experimental Images 225

C.3 Engineering Drawings of Blast Tube Driver Section 225

C.4 Engineering Drawings of Blast Tube Transition Section 225

C.5 Data Processing MATLAB Codes 225

List of Figures

2.1 Normal Shock Wave Properties adapted from (Anderson (1990)) 7

2.2 Supersonic Flow over a Concave Corner (Anderson (1990)) 11

2.3 Weak and Strong Oblique Shock Waves (adapted from Anderson 1990) 11

2.4 Transformation of an Oblique Shock to a Normal Shock (Anderson (1990)) . 13

2.5 Progression of a Pressure-Distance Plot for Typical Point Source Explosion (Kinney (1962)) 19

2.6 Ideal Blast Wave Pressure-Time Curve (Baker (1973)) 20

2.7 Initial Conditions of a Gas Driven Shock Tube (Anderson (1990)) 23

2.8 Conditions in Shock Tube after Diaphragm is Broken (Anderson (1990)) . . . 24

2.9 Normal Reflection of a Plane Shock (Kinney (1962)) 28

2.10 Normal Oblique Reflection (Kinney (1962)) 29

2.11 Steady Flow counterpart of Oblique Reflection (Skews (1966)) 30

2.12 Schematic Illustrations of wave configurations of (a) a direct-Mach Reflection - DiMR; (b) a stationary-Mach reflection - StMR; (c) an inverse-Mach reflection - InMR; (d) a transitioned regular reflection - TRR (Ben-Dor 2007) 32

2.13 Interaction of a Shock Wave with a Rectangular Block(adapted from Skews (1966), Baker (1973) and Wright (1961)) 36

2.14 The Perturbed Region Behind a Diffracting Shock Wave (Skews (1967b)) . . 37

2.15 The Focusing of Expansion Waves (Whalley (2016)) 40

4.1 The Computational Geometry Configuration 44

4.2 Refined Mesh in the Vicinity of the Shock Front 45

4.3 The Effect of Driver Divergence Angle on Pressure 51

4.4 The Effect of Driver Pressure on Pressure 54

4.5 The Effect of Expansion Section Length on Pressure 58

4.6 Effects of Driver Pressure on Rate of Change of Peak Overpressure for 60° Driver Section 59

4.7 Effects of Driver Divergence Angle on Rate of Change of Peak Overpressure . 59

4.8 Comparing the Effect of Driver Shape and Pressure on Friedlander Pressure Profile 61

4.9 X-T Diagram for Linearly Diverging Driver Sections (Pressure) 65

4.10 X-T Diagram for Linearly Diverging Driver Sections (Density) 66

4.11 X-T Diagram for Linearly Diverging Driver Sections (Temperature) 67

4.12 X-T Diagram for Linearly Diverging Driver Sections (Velocity) 68

4.13 X-T Diagram for 7.5° Linearly Diverging Driver Section at $5bar$ 69

4.14 X-T Diagram for 60° Linearly Diverging Driver Section at $5bar$ 70

4.15 X-T Diagram for 7.5° Linearly Diverging Driver Section at $15bar$ 70

4.16 X-T Diagram for 60° Linearly Diverging Driver Section at $15bar$ 70

4.17 The Effect of Driver Length on Pressure 73

4.18 The Effect of Driver Pressure on Shock Pressure Profile 76

4.19 The Effect of Expansion Section Length on Pressure for Straight Drivers . . . 79

4.20 Comparing the Effect of Driver Length and Pressure on Friedlander Pressure Profile 81

4.21 X-T Diagram for Straight Driver Sections (Pressure) 83

4.22 X-T Diagram for Straight Driver Sections (Density) 84

4.23 X-T Diagram for Straight Driver Sections (Temperature) 85

4.24 X-T Diagram for Straight Driver Sections (Velocity) 86

4.25 X-T Diagram for 580mm Straight Driver Section at 5bar 87

4.26 X-T Diagram for 65mm Straight Driver Section at 5bar 87

4.27 X-T Diagram for 580mm Straight Driver Section at 15bar 88

4.28 X-T Diagram for 65mm Straight Driver Section at 15bar 88

4.29 The 3 Driver Section Profiles Designed for Further Testing 90

4.30 The Angle of Inclination of the 3 Driver Section Profiles 90

4.31 The Development of the Blast Pressure Profile for Varying Diaphragm Locations in Concave Driver Section 94

4.32 The Effect of Varying Diaphragm Locations in the Concave Driver Section on the Pressure Profile 96

4.33 Comparing the Effect of Varying Diaphragm Location in the Concave Driver Section on Friedlander Pressure Profile 98

4.34 X-T Diagram for Varying Diaphragm Locations in the Concave Driver Section (Pressure) 100

4.35 X-T Diagram for Varying Diaphragm Locations in the Concave Driver Section (Density) 101

4.36 X-T Diagram for Varying Diaphragm Locations in the Concave Driver Section (Temperature) 102

4.37 X-T Diagram for Varying Diaphragm Locations in the Concave Driver Section (Velocity) 103

4.38 The Development of the Blast Pressure Profile for Varying Concave Driver and Transition Length . . . 106

4.39 The Effect of Varying the Concave Driver and Transition Section Length on the Pressure Profile . . . 109

4.40 Comparing the Effect of Varying the Concave Driver and Transition Section Length on the Friedlander Pressure Profile . . . 111

4.41 X-T Diagram for Varying the Concave Driver and Transition Section Length (Pressure) . . . 114

4.42 X-T Diagram for Varying the Concave Driver and Transition Section Length (Density) . . . 115

4.43 X-T Diagram for Varying the Concave Driver and Transition Section Length (Temperature) . . . 117

4.44 X-T Diagram for Varying the Concave Driver and Transition Section Length (Velocity) . . . 118

4.45 The Effect of Driver and Transition Section Shaping on Blast Pressure Profile 122

4.46 The Effect of Driver Pressure on Pressure for Concave, Linear and Convex Shaped Profiles . . . 124

4.47 The Effect of Expansion Section Length on Pressure for Concave, Linear and Convex Shaped Profiles . . . 126

4.50 Comparing the Effect of Blast Tube Length on the Friedlander Pressure Profile 128

4.51 X-T Diagram for Effect of Blast Tube Length Simulations (Pressure) . . . 129

4.52 X-T Diagram for Effect of Blast Tube Length Simulations (Density) . . . 130

4.53 X-T Diagram for Effect of Blast Tube Length Simulations (Temperature) . . . 130

4.54 X-T Diagram for Effect of Blast Tube Length Simulations (Velocity) . . . 131

4.55 Driver Section Assembly . . . 132

4.56 Driver Section Assembly . . . 133

5.1 Schematic of the Blast Tube Facility 135

5.2 Uni-Directional Schlieren Flow Visualisation Set-up 141

7.1 The Pressure Traces for the Experimental Validation of the Blast Tube having Concave, Linear and Convex Shaped Profiles 147

7.2 Transducer Pressure Profiles produced by the Experimental Validation of the Blast Tube with Concave, Linear and Convex Driver and Transition Section Inserts with Comparable Friedlander Pressure Profile 149

7.3 Verifying Visual Quality of Blast Tube with Concave, Linear and Convex Inserts 151

7.4 Development of a Diffracted Blast Wave generated by the Blast Tube having Concave Driver Section $50\mu m$ $M_0 = 1.253$ 152

7.5 Comparison of a Diffracted Blast Wave generated by the Blast Tube having Concave, Linear and Convex Driver Section 154

7.6 Development of a 15° Reflected Blast Wave generated by the Blast Tube having Concave Driver Section $50\mu m$ $M_0 = 1.240$ 158

7.7 Comparison of a 15° Wedge Blast Wave Reflection generated by the Blast Tube having Concave, Linear and Convex Driver Section 160

7.8 Development of a 30° Wedge Blast Wave Reflection generated by the Blast Tube having Concave Driver Section $50\mu m$ $M_0 = 1.265$ 162

7.9 Comparison of a 30° Wedge Blast Wave Reflection generated by the Blast Tube having Concave, Linear and Convex Driver Section 164

7.10 Development of a 45° Reflected Blast Wave generated by the Blast Tube having Concave Driver Section $50\mu m$ $M_0 = 1.242$ 167

7.11 Comparison of a 45° Wedge Blast Wave Reflection generated by the Blast Tube having Concave, Linear and Convex Driver Section 169

A.1 The Development of the Blast Pressure Profile for Varying Diaphragm Locations in the Linear Driver Section 183

A.2 The Effect of Varying Diaphragm Locations in the Linear Driver Section on the Pressure Profile . . . 185

A.3 Comparing the Effect of Varying Diaphragm Location in the Linear Driver Section on Friedlander Pressure Profile . . . 186

A.4 X-T Diagram for Varying Diaphragm Locations in Linear Driver Section (Pressure) . . . 187

A.5 X-T Diagram for Varying Diaphragm Locations in the Linear Driver Section (Density) . . . 188

A.6 X-T Diagram for Varying Diaphragm Locations in the Linear Driver Section (Temperature) . . . 189

A.7 X-T Diagram for Varying Diaphragm Locations in the Linear Driver Section (Velocity) . . . 190

A.8 The Development of the Blast Pressure Profile for Varying Diaphragm Locations in the Convex Driver Section . . . 192

A.9 The Effect of Varying Diaphragm Locations in the Convex Driver Section on the Pressure Profile . . . 194

A.10 Comparing the Effect of Varying Diaphragm Location in the Convex Driver Section on Friedlander Pressure Profile . . . 195

A.11 X-T Diagram for Varying Diaphragm Locations in the Convex Driver Section (Pressure) . . . 196

A.12 X-T Diagram for Varying Diaphragm Locations in the Convex Driver Section (Density) . . . 197

A.13 X-T Diagram for Varying Diaphragm Locations in the Convex Driver Section (Temperature) . . . 198

A.14 X-T Diagram for Varying Diaphragm Locations in the Convex Driver Section (Velocity) . . . 199

B.1 The Development of the Blast Pressure Profile for Increasing Linear Driver and Transition Length . . . 202

B.2 The Effect of Increasing the Linear Driver and Transition Section Length on the Pressure Profile 204

B.3 Comparing the Effect of Varying the Linear Driver and Transition Section Length on the Friedlander Pressure Profile 206

B.4 X-T Diagram for Varying the Linear Driver and Transition Section Length (Pressure) 207

B.5 X-T Diagram for Varying the Linear Driver and Transition Section Length (Density) 209

B.6 X-T Diagram for Varying the Linear Driver and Transition Section Length (Temperature) 210

B.7 X-T Diagram for Varying the Linear Driver and Transition Section Length (Velocity) 212

B.8 The Development of the Blast Pressure Profile for Increasing Convex Driver and Transition Length 214

B.9 The Effect of Increasing the Convex Driver and Transition Section Length on the Pressure Profile 216

B.10 Comparing the Effect of Varying the Convex Driver and Transition Section Length on the Friedlander Pressure Profile 218

B.11 X-T Diagram for Varying the Convex Driver and Transition Section Length (Pressure) 219

B.12 X-T Diagram for Varying the Convex Driver and Transition Section Length (Density) 221

B.13 X-T Diagram for Varying the Convex Driver and Transition Section Length (Temperature) 222

B.14 X-T Diagram for Varying the Convex Driver and Transition Section Length (Velocity) 224

List of Tables

4.1 Linearly Diverging Driver Pressure TNT Explosive Equivalence 49

4.2 Straight Driver Pressure TNT Explosive Equivalence 71

4.3 Varying Diaphragm Location TNT Explosive Equivalence 91

5.1 Blast Tube Facility Component List 135

5.2 Uni-Directional Schlieren Visualisation Set-up Parts List 141

6.1 Calibration of Blast Tube with Concave Shaped Driver and Transition Installed 143

6.2 Calibration of Blast Tube with Linear Shaped Driver and Transition Installed 144

6.3 Calibration of Blast Tube with Convex Shaped Driver and Transition Installed 144

List of Symbols

The units of quantities defined by a symbol are indicated in square brackets following the description of the symbol. Quantities with no indicated units may be assumed to be dimensionless.

C_p Specific Heat at constant pressure [J/K].

C_v Specific Heat at constant volume [J/K].

R_s Shock Radius [m].

p_{atm} Atmospheric Pressure [Pa].

p_o Overpressure [Pa].

t_a Arrival Time of Shock [s].

t_d Duration of Shock Overpressure [s].

u_s Velocity of Shock [m/s].

A Cross Sectional Area [m^2].

a Speed of Sound [m/s].

e Internal Energy [J/K].

F Helmholtz Free-energy [J].

f Body and Viscous Forces per mass.

β Oblique Shock Angle.

ϵ Slipstream Angle.

γ Specific Heat Ratio.

ρ Density [kg/m^3].

σ Terminator Angle.

θ Flow Deflection Angle.

h Enthalpy [J].

I Blast Wave Impulse [N/s].

M Mach Number.

n Amount of Substance [mol].

p Pressure [Pa].

q Heat Flow per mass.

R Gas Constant [J/kgK].

s Entropy [J/K].

T Temperature [K].

u x-component of Velocity [m/s].

v Volume [m^3].

z Strength of Shock.

List of Acronyms

CFD Computational Fluid Dynamics.

CHPC Centre for High Performance Computing.

DiMR Direct Mach Reflection.

InMR Inverse Mach Reflection.

StMR Stationary Mach Reflection.

TNT Symmetrical Trinitrotoluene.

TRR Transitioned Regular Reflection.

Chapter 1 Introduction

1.1 Background

Owing to current conflicts in the Middle East and Africa and the risk of terrorist attacks as well as the occurrence of industrial accidents, there is a great need for a non-explosive experimental blast wave simulator. Such a simulator would help to proliferate the design and generation of blast resistant buildings and clothing as well as enable enhanced simulation and assessment of injuries induced by blast waves.

Powerful blasts, generated by explosives, can cause extensive damage and injury and therefore it is of critical importance to gain as much knowledge about the mechanisms of such blasts, in particular the reflection and diffraction of blasts waves caused by the wave impacting buildings and objects, so as to design and plan means of mitigating the effects of such blasts. Studying the reflection and diffraction of blasts waves is also vitally important to weapon design as the location and altitude of the blast has major impacts on the effectiveness of the weapon.

At present the only way to generate a blast wave with realistic pressure-time and density-time profiles is to detonate explosives in a tube or in the open atmosphere. The diameter of explosively driven shock tubes generally ranges from 1 metre to 11 metres and such tubes can have lengths of up to 200 metres (Ben-Dor, Igra and Elperin (2001a)). This implies that cost of constructing and running such large blast tubes is quite high, making experimental testing prohibitively expensive for universities and small companies. The handling and use of high explosives also raises difficulties and concerns with regards to health and safety regulations.

The more common method for experimentally simulating blast waves is by use of shock tubes where the energy to produce the driven shock is produced either by a rapid electrical discharge, compressed gas or piston. The driver section of these shock tubes is much shorter and has less volume than the run up section so as to enable the reflected expansion wave to catch up to the generated shock wave before the shock reaches the test section. This causes

the shock to decay as it passes through the test section (Needham (2010)). However, it is important to note that so far this method has not produced pressure and density profiles that accurately match an actual explosion.

Both Needham (2010) and Ben-Dor, Igra and Elperin (2001a) postulate that blast waves with more realistic and accurate pressure-time and density-time profiles could be generated by shock tubes which have been conically shaped. It is pertinent to note that this idea was first put forward by W. S. Filler in the 1960s (Filler (1960a)). The reason a conically shaped shock tube would generate more realistic blast wave decay is due to the shock tube shaping being analogous to the spherical divergence that a free air detonation has.

Although a successful attempt has been made to simulate blast waves with a diverging area compressed-gas driven shock tube, in the form of the Advanced Blast Simulator located at DRDC Suffield Facilities, a gap in the existing knowledge still exists as the structural quality of the blast waves produced by this shock tube is unknown (Ritzel et al. (2015)). This brings into the question the feasibility of using this blast tube for visual experimentation and studying the reflection and diffraction of blast waves. For this reason, as well as the lack of literature and published work on this subject area, there is need for further research into blast tube design and blast wave interactions.

1.2 Research Aim

The two main aims of the present research were as follows. The first aim of this research was to carry out the parametric design and analysis of a blast tube, using Computational Fluid Dynamics (CFD) software, so as to enable the construction of a blast tube which was capable of generating two dimensional blast waves without the use of explosive drivers. It was required that the blast waves generated by the blast tube were to have realistic pressure profiles as well as to be of such quality so as to enable visualisation experimentation to be performed using the blast tube. The second objective of this research was aimed at examining and analysing the flow features and interactions as well as the gas dynamics that occur when blast waves impinge surfaces at varying angles to the shock front causing the wave to reflect and diffract. It is important to note that the reflection of a blast wave occurs when the wave impinges a surface which is at an angle of less than 90° to the shock front while diffraction of the blast wave occurs when the surface impinged by the wave is angled at greater than 90° to the shock front.

Chapter 2 Literature Review

2.1 Overview of Gas Dynamics

2.1.1 Fundamental Equations of Flow

The follow section is a compendium based on the work of Courant and Friedrichs (1948) where the derivations of the below mentioned equations are discussed in detail. The behaviour of a shock wave, also know as a Riemann problem due to its discontinuous nature, in one dimensional ideal gas flow is defined by the equation of state of an ideal gas as well as the conservation of continuity, momentum and energy, as shown below. An ideal gas is one where it is assumed that the gas is polytropic, that is the internal energy of the gas is solely a function of temperature.

2.1.1.1 Equation of State of an Ideal Gas

When a gas is at state of thermal equilibrium or at low density or pressure and at a temperature below that at which ionisation and dissociation of the molecules in the gas occur, which practically covers most applications of gas dynamics, the gas can be assumed with great accuracy to approximately follow the equation of state:

$$\frac{p}{\rho} = RT \text{ per unit mass} \tag{2.1}$$

If the gas obeys Equation 2.1 and is also thermally perfect, that is it is in thermodynamic equilibrium and is not undergoing chemical reactions, then the heat capacities per unit mass at constant volume C_v and at constant pressure C_p of the gas are only dependent on the temperature of the gas and not the pressure and are given by the following equations:

$$C_v = \left(\frac{de}{dT}\right)_v \qquad\qquad C_p = \left(\frac{dh}{dT}\right)_p$$

Since the internal energy of a thermally perfect gas is only a function of temperature and the enthalpy of the gas is given by

$$h = e + \frac{p}{\rho}$$

the specific heats of the gas then follow the relationship

$$C_v - C_p = R \tag{2.2}$$

where if C_v and C_p are constant the gas is said to be calorically perfect or in other words, the heat capacity of the gas is constant.

2.1.1.2 Continuity Equation

The conservation of mass of a system is characterized by the continuity equation which is written as

$$\frac{d(\rho A)}{dt} + d(\rho u A) = 0 \tag{2.3}$$

For a system which involves a constant cross-section area, such as shock tube or blast tube, the continuity equation can be reduced to

$$\frac{d\rho}{dt} + u\frac{dp}{dx} + p\frac{du}{dx} \tag{2.4}$$

2.1.1.3 Momentum Equation

For non-stationary flow that is one dimensional, the equation describing Newtons second law is

$$\frac{Du}{Dt} = \frac{du}{dt} + u\frac{du}{dx} = -\frac{1}{\rho}\frac{dp}{dx} + f \tag{2.5}$$

where f is the body and viscous forces per unit mass being applied to the gas. If the fluid is assumed to be ideal that implies that there will be no body and viscous forces in the gas , that is $f = 0$, and the momentum equation will reduce to:

$$\frac{Du}{Dt} + u\frac{du}{dx} + \frac{1}{\rho}\frac{dp}{dx} = 0 \tag{2.6}$$

2.1.1.4 Energy Equation

The conservation of energy of a system, if gravitational forces are neglected, is given by the equation:

$$q\rho Adx = \frac{d}{dt}\rho Adx(C_vT + \frac{1}{2}u^2) + \frac{d}{dx}\rho uA(C_vT + \frac{p}{\rho} + \frac{1}{2}u^2) \tag{2.7}$$

where q is the heat flow per unit mass.

2.1.2 Speed of Sound

The speed at which acoustic waves travel through a medium, assuming the medium is thermally perfect, is called the speed of sound of the medium. The speed of sound of an ideal gas which is calorically perfect can be determined using the equation:

$$a = \sqrt{\gamma RT} \tag{2.8}$$

where γ is the specific heat ratio and is equal to $\frac{C_p}{C_v}$.

2.2 Shock Waves

As mentioned in subsection 2.1.2, information or waves travel through a medium at the local speed of sound of the medium. Waves are generated by disturbances in the flow. A disturbance that is generated by the compression of the fluid, such as in the case of a piston moving in a tube, will induce a compression wave in the fluid that propagates into the fluid at the speed of sound of the undisturbed fluid upstream of the wave. The compression wave, as its name implies, causes the pressure of the fluid behind it to increase, and since the mass of the volume of fluid remains constant, this increase in pressure gives rise to an increase in temperature. Looking at Equation 2.8 it can be deduced that the increased temperature of the fluid trailing the compression wave has a higher speed of sound than the undisturbed fluid ahead of the wave which implies that any subsequent compression waves induced by further disturbances in the flow will travel faster than the preceding compression waves. This implies that later waves will always have higher velocities than the preceding waves and that the later waves will overtake the waves that proceeded them. However this is problematic as it will result in the point in the flow having more than one velocity which is an impossibility. At this point in the flow the equations describing the flow break down and a discontinuity in the flow occurs. This discontinuity propagates ahead of the disturbance at a speed faster than that of the speed of sound of the fluid upstream of the discontinuity and has a width which for almost all purposes can be considered to be infinitesimal. This compression discontinuity is called a shock wave or shock. The conservation equations detailed in subsection 2.1.1 may be used to describe a shock.

Inversely, if the fluid is expanded by a disturbance, the disturbance will generate expansion waves that will decrease the pressure in the fluid which in turn will decrease the temperature and speed of the sound of the fluid trailing the expansion wave. This means that each successive expansion wave generated by the disturbance will have a slower velocity then the wave preceding it which implies that the expansion waves do not catch up to one another but rather spread out over time. It can be understood from this that it is impossible for an expansion shock wave to form, which can be shown to conform with the second law of of thermodynamics (Courant and Friedrichs (1948)).

2.2.1 Stationary Normal Shock Waves

A normal shock wave is a shock which is perpendicular to the direction of flow. By applying the laws of one-dimensional gas dynamics, the steady flow across a stationary normal shock wave, or a normal shock wave where the frame of reference moves with the shock, may be

analysed and the change in the thermodynamics properties across the normal shock can be determined using the modified fundamental equations as given below (Anderson (1990)):

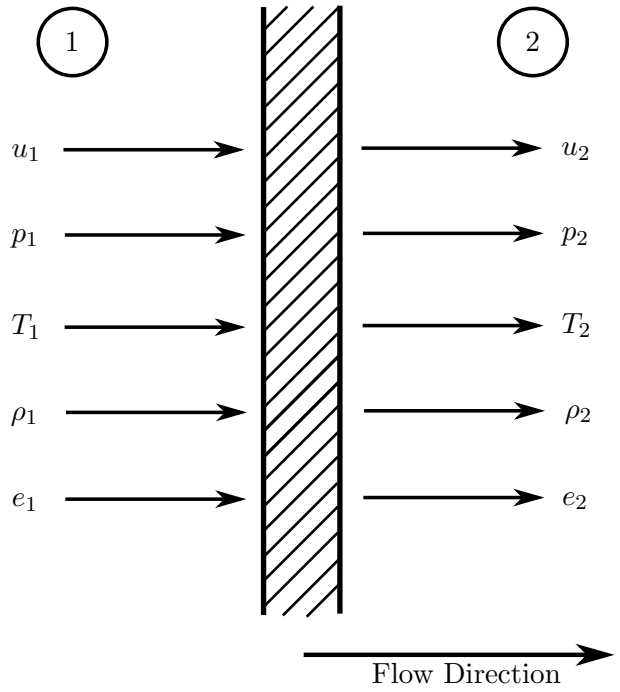


Figure 2.1: Normal Shock Wave Properties adapted from (Anderson (1990))

$$\rho_1 u_1 = \rho_2 u_2 \text{ - Continuity Equation} \tag{2.9}$$

$$p_1 + \rho_1 u_1^2 = p_2 + \rho_2 u_2^2 \text{ - Momentum Equation} \tag{2.10}$$

$$h_1 + \frac{u_1^2}{2} = h_2 + \frac{u_2^2}{2} \text{ - Energy Equation} \tag{2.11}$$

where subscript 1 denotes the properties of the fluid upstream of the shock while subscript 2 denotes downstream properties.

Using Equation 2.9 to Equation 2.11, the pressure ratio across the shock $\frac{p_2}{p_1}$ can be derived as a function of the density ratio across the shock wave $\frac{\rho_2}{\rho_1}$ and the ratio of constant heats γ of the gas (Ben-Dor, Igra and Elperin (2001b)).

$$\frac{p_2}{p_1} = \frac{u_1}{u_2} = \frac{1 + \frac{\gamma+1}{\gamma+1}\frac{\rho_2}{\rho_1}}{\frac{\gamma+1}{\gamma+1} + \frac{\rho_2}{\rho_1}} \tag{2.12}$$

This function is called the Rankine-Hugoniot relation and it shows that for an ideal diatomic gas ($\gamma = 1.4$), the pressure ratio reaches a limit of 6 and the pressure ratio tends to ∞ as the shock velocity tend to ∞. The Rankine-Hugoniot relation is a powerful tool in the study of blast waves and shock waves as it enables the downstream shock properties to be determined based solely on the upstream ambient conditions as shown below.

The normal shock, as mentioned in section 2.2, has the property of increasing the pressure, temperature and density of the fluid downstream of the shock while decreasing the velocity of the flow. By solving equations Equation 2.9 to Equation 2.11 in conjunction with Equation 2.1 algebraically, expressions for the Mach number, pressure, density and temperature of the fluid downstream of the shock with respect to the Mach number upstream of the shock can be derived. The Mach number behind a stationary normal shock can be determined by the equation (Anderson (1990)):

$$M_2 = \left[\frac{2 + (\gamma - 1)M_1^2}{2\gamma M_1^2 - (\gamma - 1)}\right]^{\frac{1}{2}} \tag{2.13}$$

where it can be seen that as the shock becomes stronger and the Mach number upstream of the shock increases, the Mach number of the fluid downstream decreases. It is important to note that the flow into a shock wave must be supersonic while the flow departing the shock is subsonic.

The ratios of the densities and velocities across the stationary shock are determined by the fraction,

$$\frac{\rho_2}{\rho_1} = \frac{u_1}{u_2} = \frac{(\gamma + 1)M_1^2}{2 + (\gamma - 1)M_1^2} \tag{2.14}$$

while the pressure and temperature ratios are given by

$$\frac{p_2}{p_1} = 1 + \frac{2\gamma}{\gamma + 1}(M_1^2 - 1) \tag{2.15}$$

where the ratio $\frac{p_2}{p_1}$ is also referred to as the strength of the shock z, and

$$\frac{T_2}{T_1} = \left[1 + \frac{2\gamma}{\gamma - 1}(M_1^2 - 1)\right]\left[\frac{2 + (\gamma - 1)M_1^2}{(\gamma + 1)M_1^2}\right] \tag{2.16}$$

respectively.

2.2.2 Moving Normal Shock Waves

The above section, 2.2.1, dealt solely with the case of a shock wave that is stationary, that is, the case where the frame of reference moves with the shock. For this research, the case of a normal shock wave which moves into air which is stationary is of particular relevance as this is analogous to a blast wave which propagates in the atmosphere. For the case of a moving shock, the relationships between the fluid properties upstream and downstream of the shock are more complex than the case of a stationary shock. The static properties of pressure, temperature and density pertain to the thermodynamic state of the gas and are thus independent of the reference frame used to analyse the shock. On the other hand the stagnation properties, namely the properties which are measured when the gas is brought to rest adiabatically, and the velocities and Mach numbers are dependent on the reference frame used as they are all dependent on the velocity of the reference frame. Since the Reynolds Transport Theorem holds for reference frames with constant velocities, the stationary normal shock relations can be used for a shock moving at constant velocity where the absolute velocities are replaced with relative velocities (Skews (1966)).

The equations detailed for the case of a stationary shock in subsection 2.2.1 may be applied to the case of a moving normal shock by superimposing a velocity u_s onto the flow field in the stationary shock case. This transforms the moving shock to a stationary shock which has gas moving into the shock at velocity u_s and leaving the shock at $u_s - u_2$.

The Mach number of the shock wave is given by:

$$M_s = \frac{u_s}{a_1} = M_1 \tag{2.17}$$

By substituting Equation 2.17 into Equation 2.14, Equation 2.15 and Equation 2.16 the density, pressure and temperature ratios can be determined based solely on the shock wave Mach number. The velocity of the flow entering the shock is given by

$$u_1 = u_s \tag{2.18}$$

while the velocity of the flow leaving the shock is determined by

$$u_2 = u_s - u_{2_{\text{move}}} \tag{2.19}$$

where $u_{2_{\text{move}}}$ is the velocity of the flow behind the moving shock.

Using Equation 2.19 in conjunction with Equation 2.13 it can be seen that Mach number of the flow behind the now stationary shock wave is calculated using the equation:

$$
\begin{aligned}
M_2 &= M_s \frac{a_1}{a_2} - M_{2_{\text{move}}} \\
M_2 &= \frac{M_1^2 - 1}{\left[\left(\gamma M_1^2 - \frac{\gamma-1}{2}\right)\left(1 + \frac{\gamma-1}{2} M_1^2\right)\right]^{\frac{1}{2}}}
\end{aligned}
\tag{2.20}
$$

2.2.3 Oblique Shock Waves

So far, only shocks that are perpendicular to the flow direction have been discussed, however shock waves in two-dimensional flow are not constrained to this position and in fact shocks may be aslope to the flow. Oblique shock waves are shocks that occur when supersonic flow is "turned in on itself". This deflection of the flow is usually caused be the flow being turned by a concave corner having an angle θ to the flow as shown in Figure 2.2 (a). In supersonic flow, the fluid upstream of an abrupt change in the direction of the flow is not informed of the direction change downstream, so the oblique shock forms in order to adjust the fluid to the changed direction of flow. The oblique shock wave has the tendency of decreasing the Mach number while increasing the pressure, density and temperature of the fluid downstream. The angle of the oblique shock with respect to the upstream flow direction β can be determined by the angle of deflection θ and the upstream Mach number M_1 through the θ-β-M relationship (Anderson (1990)):

$$
tan\theta = 2cot\beta \left[\frac{M_1^2 sin^2\beta - 1}{M_1^2\left(\gamma + cos2\beta\right) + 2}\right] \tag{2.21}
$$

It is important to note that the θ-β-M relationship is only valid when the oblique shock is attached to the corner of the ramp. At each upstream Mach number M_1, there exists a maximum deflection angle θ_{max} which determines whether or not the oblique shock is attached to the corner. If the flow is deflected by an angle θ which is larger than the maximum deflection angle θ_{max} the θ-β-M relationship is no longer applicable as the shock wave curves and detaches from the corner as illustrated in Figure 2.2 (b) below.

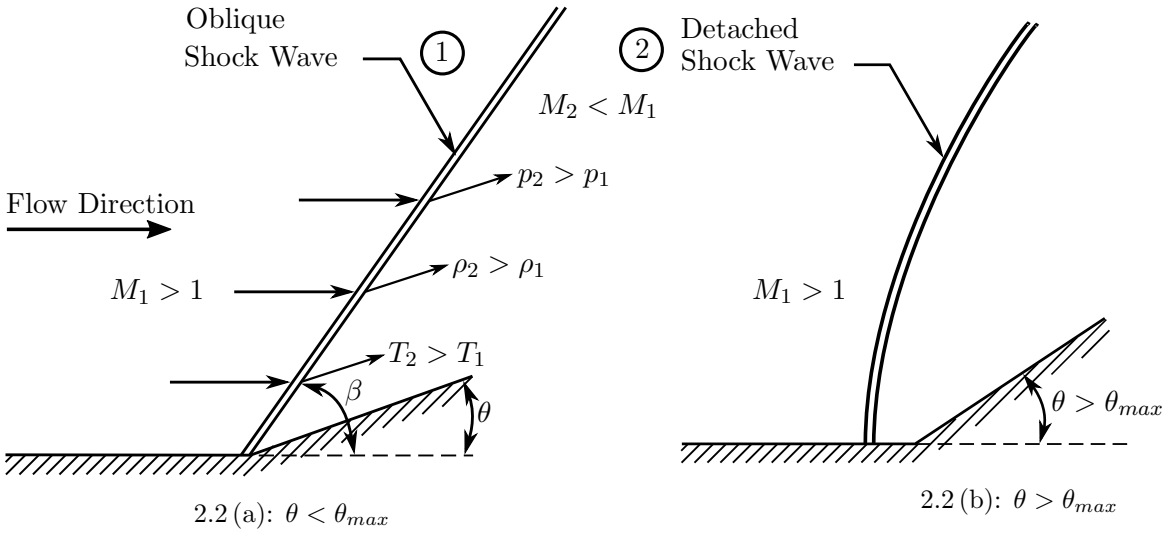


Figure 2.2: Supersonic Flow over a Concave Corner (Anderson (1990))

When θ<$\theta_{\max}$ the θ-β-M relationship produces two distinct values for β, the larger one being the strong shock solution while the lesser of the two is the weak shock solution as can be seen in Figure 2.3. The weaker shock solution is favoured as it is more representative of what naturally occurs. What determines if the oblique shock is weak or strong is the the back pressure, that is if the pressure downstream of the shock were to be increased by some independent mechanism the strong shock would occur. In the case of a weak oblique shock the Mach number of the flow downstream is supersonic while for a strong shock it is subsonic.

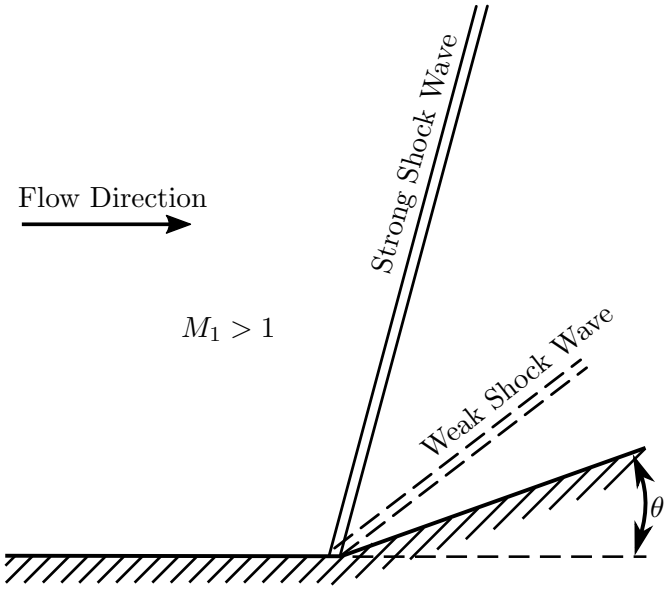


Figure 2.3: Weak and Strong Oblique Shock Waves (adapted from Anderson 1990)

As the angle of deflection of a flow tends to zero, for a flow with constant upstream Mach number, the angle of the oblique shock tends to 90° , that is a normal shock case. It is important to note that for a flow with a fixed angle of deflection, as the supersonic Mach number of the upstream flow decreases the oblique shock wave angle increases.

Since the one dimensional relations detailed in subsection 2.2.1 apply for the normal component of flow across the oblique shock, the normal shock relations, namely Equation 2.14, Equation 2.15 and Equation 2.16, can be used to analyse an oblique shock. An oblique shock can be transformed into a normal shock by resolving the upstream and downstream flows into components that are normal and parallel to the oblique shock Since the flow component which is parallel to the oblique shock never passes through the shock it remains unaffected by the shock and therefore can be neglected in the analysis. The normal component however does pass through the plane of the oblique shock and therefore is effected by the shock processes. Looking at Figure 2.4 it can be seen that the Mach number of the normal component upstream of the oblique shock is given by

$$M_{1_n} = \frac{u_1 sin\beta}{a_1} = M_1 sin\beta \tag{2.22}$$

while the Mach number of the normal component of the flow downstream is given by

$$M_{2_n} = \frac{u_2 sin\big(\beta - \theta\big)}{a_1} = M_2 sin\big(\beta - \theta\big) \tag{2.23}$$

By substituting M_{1_n} for M_1 in Equation 2.14, Equation 2.15 and Equation 2.16 the density, pressure and temperature ratios across the oblique shock can be determined. The Mach number of the flow downstream of the oblique shock related to the Mach number of the flow upstream M_1, the angle of deflection θ and the shock angle β by the equation

$$M_2 = \frac{1}{sin\big(\beta - \theta\big)} \left[\frac{2 + \big(\gamma - 1\big) M_1^2 sin^2\beta}{2\gamma M_1^2 sin^2\beta - \big(\gamma - 1\big)} \right]^{\frac{1}{2}} \tag{2.24}$$

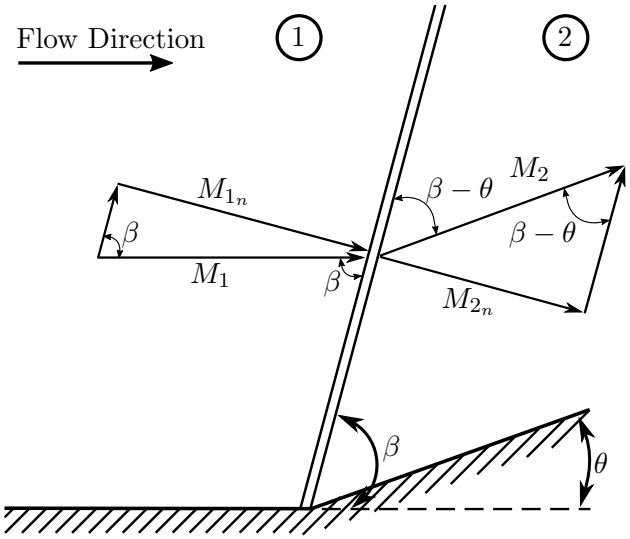


Figure 2.4: Transformation of an Oblique Shock to a Normal Shock (Anderson (1990))

2.2.4 Spherical Shock

Normal and oblique shocks, both discussed above, are plane shocks. Shocks generated by explosions on the other hand are spherical shocks which, unlike plane shocks, have curved shock fronts. Due to the shock front being extremely thin, it appears to each streamline of the flow as if the shock front is plane and therefore the normal shock relations are still valid. There are however differences in the effects that plane and spherical shocks have on the fluid following the transit of the shock. Both explosions as well as blast waves will be discussed in greater detail in subsequent sections.

2.3 Explosions

Although there are various means be which a blast wave can be generated, the method of generation most pertinent to this research is by the detonation of explosives. It is therefore of interest to get a general background on explosions and explosive shocks.

2.3.1 Nature of Explosions and Explosives

Explosions are as a result of the sudden release of large amounts of energy into the surrounding material, where the source of this energy could be from the detonation of explosives such as Symmetrical Trinitrotoluene (TNT), the ignition of wheat or coal dust, the release of pressurized steam or gas, or from a runaway nuclear fission or fusion reaction. In order to

be classified as an explosion, the release of energy must be very rapid such that the energy amasses at the source of the explosion. The amassed energy then dissipates by means of a blast wave, energised projectiles and thermal radiation (Kinney (1962)).

The quantity of energy released by an explosion determines the magnitude of the explosion, which can be expressed in units of energy, such as Joules. A more substantive and accepted method for expressing the magnitude or yield of an explosion is by using the standard relative measure which involves relating the explosive energy to the energy released by the detonation of 1 gram of TNT. A gram of TNT produces blast energy equivalent to 4.686 kilojoules. The reason TNT is used as the standard for the measure of explosive yield is because it is chemically pure, readily obtainable, quite safe to handle and produces reasonably repeatable results. Since most explosions have strengths much larger than that of a gram of TNT, particularly chemical and nuclear explosions, the standard measure of the strength of a blast wave is the defined ton of TNT, which is equivalent to the release of 4.184 million kilojoules.

There are numerous mechanisms, both direct and indirect, by which explosive energy may be transmitted to an object. The most damaging mechanism of explosive energy transmission is direct mechanical coupling as it results in the shattering of the contact object. This is particularly useful in mining and excavation as it enables the instantaneous smashing of large quantities of solid rock. Another direct method of explosive energy transmission is thermal radiation, however this mechanism is really only pertinent to nuclear blasts. Blast waves and accelerated projectiles are the two indirect mechanisms by which explosive energy is transmitted, where the pertinence of each is dependent on the yield and nature of the explosion. Blast waves are more relevant for large explosions while damage caused by flying missiles is of more import for small explosions.

An important factor of explosives is the rate at which the energy is discharged in the explosion. The intensity or shattering power of an explosion is termed the brisance. For chemical explosives the brisance is directly proportional to the speed of decomposition of the explosive. Explosives with high brisance are referred to as high explosives. High explosives tend to decompose by means of a detonation wave which travels through the explosive at speeds on the order of thousands of metres per second and at pressures many times greater than atmospheric. As mentioned previously, materials in contact with the detonating highly explosive material, such as TNT, will absorb the high intensity mechanical shock from the explosive which will cause the material to shatter. This can occur even if the the explosive material is unconfined. A explosive materials which deflagrate, such as gunpowder, do not have high brisance and therefore do not produce a shattering mechanical shock, however the explosion is enough to push back the surrounding atmosphere and produce a blast wave.

One of the main issues arising with the use of explosives is the hazards involved in handling them, particularly the inadvertent detonation of the explosive. The likelihood of an explosive being set off accidentally is dependent on the sensitivity of the explosive material. The sensitivity of an explosives is measured by the effort required to initiate the decomposition of the material, where the less effort that is required the more sensitive the explosive. The effort is quantified by the Arrhenius energy of activation required to initiate the explosive decomposition. Explosives with low activation energies are easily initiated by either thermal or mechanical means, such as by a flame or jarring. Such explosive materials are usually used as initiators for more stable but stronger explosives. This implies that the initiators, or blasting caps, are more dangerous to handle than the explosive themselves. Due to the dangers involved in handling explosives there are health and safety regulations which limit the amount of explosives that can be used as well as the conditions and facilities in which they can be handled.

Another hazard that arises with the use of explosives is storage. Some explosives have poor storage stability which means that as the explosive material ages, the sensitivity of the material increases. The only dependable means of overcoming this danger is to put large distances between the explosive store and other buildings and structures, both inhabited and otherwise. Although barricaded stores are desirable to protect the stored explosives from damage, they generally do not reduce the threat to neighbouring structures. Stored explosives also run the risk of a runaway explosion due to the accidental detonation of other explosives. The distance at which this occurs is called the sympathetic detonation distance and it dictates the distances required between explosive stores (Kinney (1962)). Both handling and storing hazards associated with explosives means that there is both a niche and demand for devising a means of generating blast waves without the use of explosives.

2.3.2 Heat of Explosions

The heat of an explosion, that is the thermal energy unleashed during an explosive decomposition, equates to an isothermal decrease in the internal energy of the system due to the explosion or mathematically as

$$\text{Heat of Explosion} = -\Delta e = -\big(e_2 - e_1\big) \tag{2.25}$$

where e_1 is internal energy of the explosives and e_2 is the internal energy of the products of the explosion (Kinney (1962)).

2.3.3 Energy of Explosions

One of the most important details when studying explosions is determining how much energy is transferred from the explosive to the blast wave. This energy transfer can be calculated using the integral

$$\int_1^2 pdv$$

which details the work of expansion carried out by the repressed gases produced by the explosion in terms of pressure p and the volume of gas v. However computing this line integral is very difficult as it requires that the initial pressure generated by the explosion as well as the pressure-volume relations of complex non-ideal gases be known. A more workable alternative is to perform a direct thermodynamic analysis of the important thermodynamic properties using the terminal values. The maximum energy release in an explosion is expressible as an isothermal reduction in the Helmholtz free-energy function. The Helmholtz free-energy is determined by the expression

$$F = e - Ts \tag{2.26}$$

which is the difference between the internal energy of the system and the temperature-entropy-product. From this expression it can be deduced that the energy of an explosion is given by

$$\text{Energy of Explosion} = \int_1^2 pdv \approx -\Delta F = -\Delta e + T\Delta s \tag{2.27}$$

where $-\Delta e$ is the decrease in internal energy which is measured as the heat of the explosion while Δs is the growth in entropy during the isothermal process (Kinney (1962)).

2.3.4 Entropy of Explosions

Entropy is a thermodynamic quantity representing the amount of energy in a system that is nolonger available for doing mechanical work. The entropy of explosions constitutes the increase in entropy that occurs when the explosive material decomposes during the explosion into the products. For solid and liquid products the entropy is not affected by pressure implying that the individual entropy per mole of such products at any pressure can be assumed

to be the standard entropy s^0. For a gaseous product that meets the ideal gas conditions, the individual entropy per mole of the product is determined by the equation:

$$s = s^0 - R \ln p \tag{2.28}$$

where s^0 is the standard molar entropy at unit pressure.

In order to be able to calculate the theoretical explosive yield, the entropy of the explosive itself is required. Unfortunately the entropy of most explosives is not easily available, however an alternative is to approximate the entropy of the explosive using the formula

$$s^0 = 15 + 5n \tag{2.29}$$

where n is the number of atoms in the material excluding hydrogen and oxygen which are accounted for by the 15 in the formula (Kinney (1962)).

2.3.5 Calculating the Theoretical Explosive Yield

The methods described above for determining the theoretical energy and yield of an explosive are quite indirect and convoluted, particularly when a complex compound explosive is used. A more straightforward means of computing the theoretical yield of an explosive is derived by acquiring values of the explosives and the products which are at partial rather than unit pressures for the Helmholtz free-energy function. For ideal gases the computation is performed with the given equation

$$F = F^0 + RT \ln p \tag{2.30}$$

where F^0 is the standard Helmholtz free-energy value and p is the partial pressure of the component gases.

By combining Equation 2.30 with Equation 2.27 the limiting amount of energy available from a tank of compressed gas to explosively expand the atmosphere can be determined. If there are n moles of an ideal gas then the energy of an isothermal expansion induced by compressed gas is calculated using

$$\text{Energy of Explosion} = \int_1^2 pdv \approx T\Delta s = nRT \ln\left(\frac{p_1}{p_2}\right) = \frac{100 p_1 v}{\gamma - 1}\left[1 - \left(\frac{p_{atm}}{p_1}\right)^{\frac{\gamma-1}{\gamma}}\right] \quad (2.31)$$

where p_1 is the absolute pressure of the compressed gas, p_2 is the final atmospheric pressure after expansion and equalisation of the gas and γ is the heat capacity ratio for gas and for air $\gamma = 1.4$ (Kinney (1962)). The above equation is of particular pertinence to the research being carried out as it enables the energy of the pressurised air in the driver section of the blast tube to be equated to an amount of TNT that would produce an equivalent blast wave.

2.4 Blast Waves

2.4.1 Formation of the Blast Wave

Blast waves are a subcategory of shock waves that form as a result of explosions occurring in the atmosphere. The sources of these explosion can be either man made such as an explosion arising from the detonation of highly explosive materials or due to runaway fission or fusion nuclear reactions, or from natural phenomena such as a volcanic eruptions or lightning bolts. In this analysis, the initial shape and size of the explosive is irrelevant to the formation of the blast wave. Rather what is important is the quantity and rapidity of the energy released in the explosion. The explosion can be assumed to initially be a small spherical volume of gas having extremely high pressure and temperature. This high pressure gas then expands rapidly, more so at the centre of the explosion than at the periphery, due to inertia of the atmosphere surrounding the explosion. This expansion of the atmosphere pushes the air surrounding the explosion away from the centre of the blast, inducing a discontinuous increase in pressure and shock front in the gas surrounding the explosion. As the explosive volume expands further, due to inertial effects, the volume over expands and a rarefaction forms at the initial point of the explosion (Kinney (1962)).

The final configuration of the blast wave, which is what differentiates it from a normal shock wave, consists of a discontinuous rise in pressure at the shock front which is followed by a logarithmic decay in the overpressure, that is the pressure above atmospheric, which usually reduces to a negative pressure phase called the expansion phase. The negative phase pressure then either asymptotically approaches pre-explosion ambient pressure or more likely ends with a second blast wave which may also be followed by a secondary negative pressure phase. As the blast wave propagates outward from the initial point of detonation the overpressure and negative pressure phase have the same duration, however the intensity of the overpressure is much greater due there being a limit on the magnitude of the negative pressure of one

atmosphere. As the blast wave propagates outward from the explosion source, the wave maintains this configuration however the magnitude of the overpressure reduces the further the wave travels until it decays into a sound wave (Needham (2010)). The formation of a generic blast wave in a uniform atmosphere is detailed in Figure 2.5.

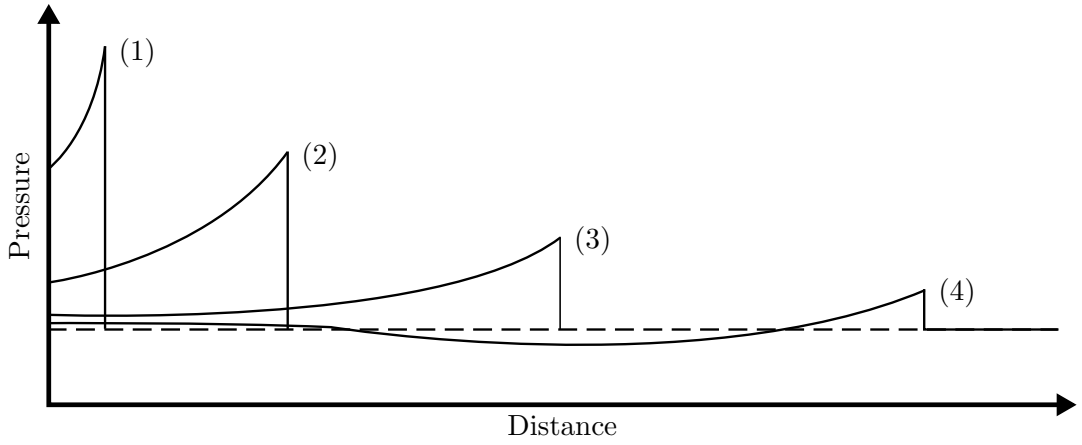


Figure 2.5: Progression of a Pressure-Distance Plot for Typical Point Source Explosion (Kinney (1962))

2.4.2 Blast Wave Configuration

A typical blast wave pressure-time profile is shown in Figure 2.6. The configuration of a blast wave is usually discussed in terms of pressure-time, density-time and temperature-time histories at different distances from the explosion centre as these properties can be measured by instrumentation placed at these different locales. The time the shock front of the blast wave takes to reach a gauge at a point away from the centre of the explosion is called the arrival time t_a. At this time the gauge, assuming it is ideal, will measure an instantaneous increase in, and peak value of, pressure, density and temperature. The peak values are then followed by a declivity in the properties measured which reach ambient values at some time t_d after the arrival of the shock front. The properties then reduce further below the ambient conditions before returning to ambient conditions after some time. The period of the time history where the pressure is above ambient conditions is called the positive phase while the duration where the pressure is below ambient is called the negative phase. The properties that are used to characterise a blast wave are the initial shock intensity which is defined by the peak overpressure as well as the Mach number of the shock, the duration of the blast wave and the impulse of the forces induced by the overpressure of the blast wave (Baker (1973)).

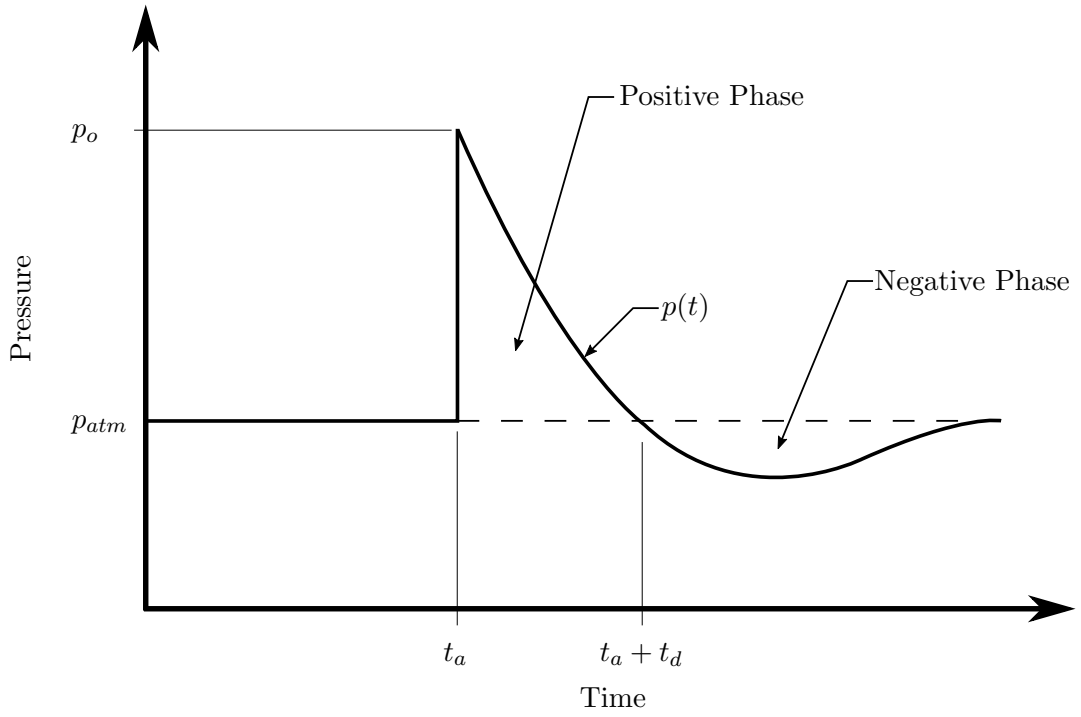


Figure 2.6: Ideal Blast Wave Pressure-Time Curve (Baker (1973))

2.4.2.1 Friedlander and Modified Friedlander Pressure Profiles

The pressure-time, density-time and temperature-time of centred blast waves, as discussed in subsection 2.4.2 have a characteristic shape that is unique to blast waves. The most poignant of these features is the approximately exponential decay that occurs in these properties, namely pressure, density and temperature, after the shock front traverses past a fixed location. This exponential decay in the flow properties is very different to the plateaued increase in flow properties and gradual decline back to ambient observed by the passing of a normal shock wave. The rate of the decay of the fluid properties trailing the blast wave shock front can be described by the equation,

$$p = p_o e^{-\frac{t}{t_d}} \left(1 - \frac{t}{t_d}\right) \tag{2.32}$$

which is known as the Friedlander equation, as it is named after its creator F. G. Friedlander (Friedlander (1946)). Equation 2.33 can be used to describe pressure-time histories for blast waves generated by a diverse assortment of explosions, both air bursts and surface burst, over a wide range of peak overpressure values.

When the peak overpressure of the blast wave exceeds $1bar$ the Friedlander equation is no longer able to accurately describe the pressure decay behind the blast wave shock front. In

these cases a a slightly modified equation, known as the Modified Friedlander Equation is used to describe the flow properties trailing the shock front. The modification to the Friedlander equation comes in the form of a coefficient, β, which is referred to as the decay parameter. The Modified Friedlander equation is given as

$$p = p_o e^{-\beta \frac{t}{t_d}} \left(1 - \frac{t}{t_d}\right) \tag{2.33}$$

2.4.2.2 Secondary Shock Wave

Although there is minimal literature on the phenomenon, the formation of a secondary blast wave after the primary blast wave is a fundamental feature of spherical explosions. Therefore the formation of a secondary shock wave after the non-explosively generated blast wave would be a good indicator of the blast tubes ability to produce realistic blast waves. The main reason for the lack of material on this blast wave feature is most pressure measurements of real world air blasts will record the reflected blast wave, that is the blast wave that impacts the ground and reflects back into the atmosphere, which invariable will effect the ability of the instrumentation to measure the secondary shock. The secondary shock forms as a result of the expansion waves, which are induced by the air being expanded as a result of the explosion, travelling towards the centre of the explosion cooling and reducing the pressure of the air as they do so. Eventually the expansion waves implode at the centre of the explosive which results in extremely low temperatures and pressures in the gas which can only be equalised by the formation of a shock wave, which then propagates outwards from the centre of the explosion and is seen after the blast wave as the secondary shock wave (Brode (1959)).

2.4.3 Peak Overpressure

The peak overpressure is the maximum increase in pressure above atmospheric that occurs due to an explosion. The overpressure reaches a peak at the blast wave shock front and decreases thereafter. The magnitude of the peak overpressure decreases as the shock front propagates outward from the explosion. The rate of decay of the peak overpressure with increasing radius, while the shock front is attached to the fireball, is approximated by the the ratio $\frac{1}{R_s{}^3}$, that is for a doubling in the radial distance the magnitude of the peak overpressure reduces by one eighth. Once the shock front has detached from the fireball the blast overpressure decays at an approximate rate of $\frac{1}{R_s{}^2}$ (Needham (2010)).

2.4.4 Blast Wave Duration

The duration of a blast wave t_d is the time it takes for the shock front and peak overpressure to decay to zero overpressure as observed by a point at some distance from the explosion. The reason why only the positive phase is considered when assessing the duration of a blast wave is due to the positive phase being much more destructive than the negative phase. Another contributing factor is the comparable ease with which the time duration of the positive phase can be accurately measured. The time duration of a blast wave is an important characteristic when studying blast waves as the ability of the wave to cause damage is dependent on the how long the forces are applied for. It is important to note that the duration of the blast wave increases as it travels further from the explosion and reaches a limit when the peak overpressure decays to zero, that is when the shock front reduces to a sound wave.

2.4.5 Blast Wave Impulse

One of the most important factors when assessing the destructive capabilities of a blast wave is the blast impulse. The blast impulse is of particular importance when analysing waves having short durations and which are generated by explosives with small yields. The impulse of a blast wave has units of force multiplied by time. The impulse per area of a blast wave is represented by the area under the positive phase section of the pressure-time graph. Although the negative impulse of the blast wave can also be calculated, due to the importance of the positive phase of the blast wave, the positive impulse per area is used to qualify the whole blast wave structure. The blast wave impulse is contingent on the peak overpressure, the duration of the positive pressure phase as well as the rate at which the overpressure decays. This last factor is important as a blast wave that has the same peak overpressure and duration as another wave but with a faster decay will have a lower blast impulse (Kinney (1962)). The impulse per unit area of a blast wave can be determined using the integral:

$$I_a = \int_0^{t_d} p dt \tag{2.34}$$

2.5 Shock Tube

Shock tubes have been in use for more than a hundred years in the study of gas dynamics and shock waves. Although there are many different shock tube configurations the one most pertinent to this research is the constant cross-sectional area shock tube. In its most basic form, the constant cross-section shock tube consists of two sections: a high-pressure section (region 4) and a low-pressure section (region 1), which are separated by a diaphragm as can be seen in Figure 2.7. The technical name for the high pressure section is the *driver* or *compression section*, while the low-pressure section is referred to as the *driven* or *expansion section*. It is important to note that gases in the driver and expansion section need not be the same. When the diaphragm is burst or removed the high pressure gas in the driver section (region 4) rushes into the low pressure gas in the expansion section (region 1), as shown in Figure 2.8. This causes a shock wave to propagate into the expansion section (region 1) while expansion waves travel into the driver section (region 4). As the shock wave propagates down the length of the expansion section (region 1) it raises the the pressure and velocity of the trailing gas. Due to the warming and compression of the gas by the shock wave in region 2 and the expansion wave cooling and expanding the gas in region 3, the gas that was originally located at the diaphragm forms an interface separating the driver and driven gases called a contact surface. It important to note that the gas on either side of the contact surface, namely in regions 2 and 3, have the same pressure and velocity but have vastly different temperatures and densities. The gas in region 3 will be much cooler than the gas in region 1 while the gas in region 2 will be at a higher temperature than region 1.

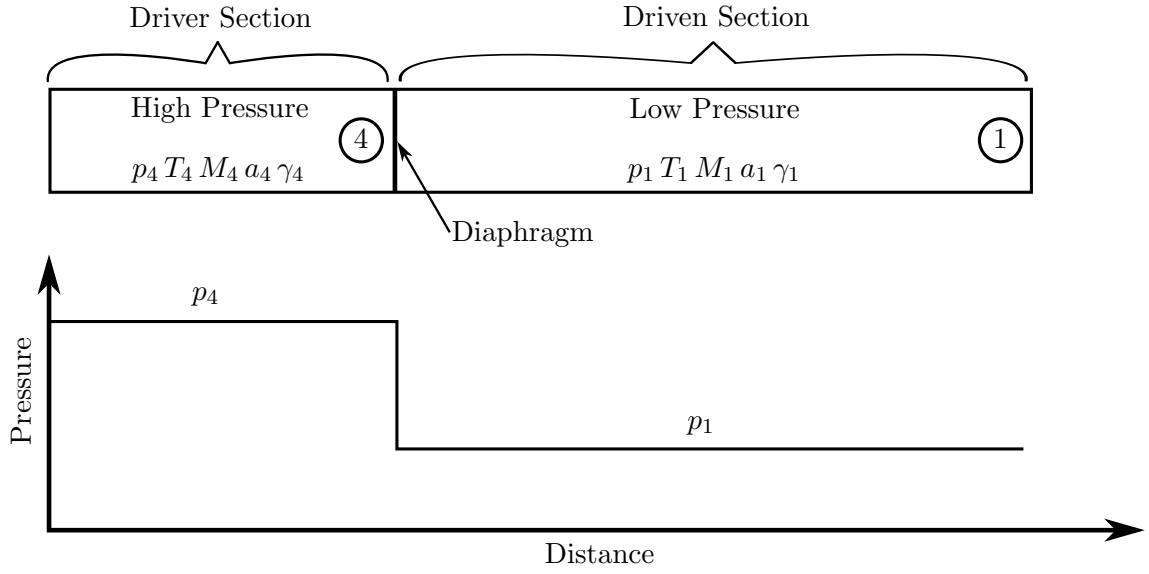


Figure 2.7: Initial Conditions of a Gas Driven Shock Tube (Anderson (1990))

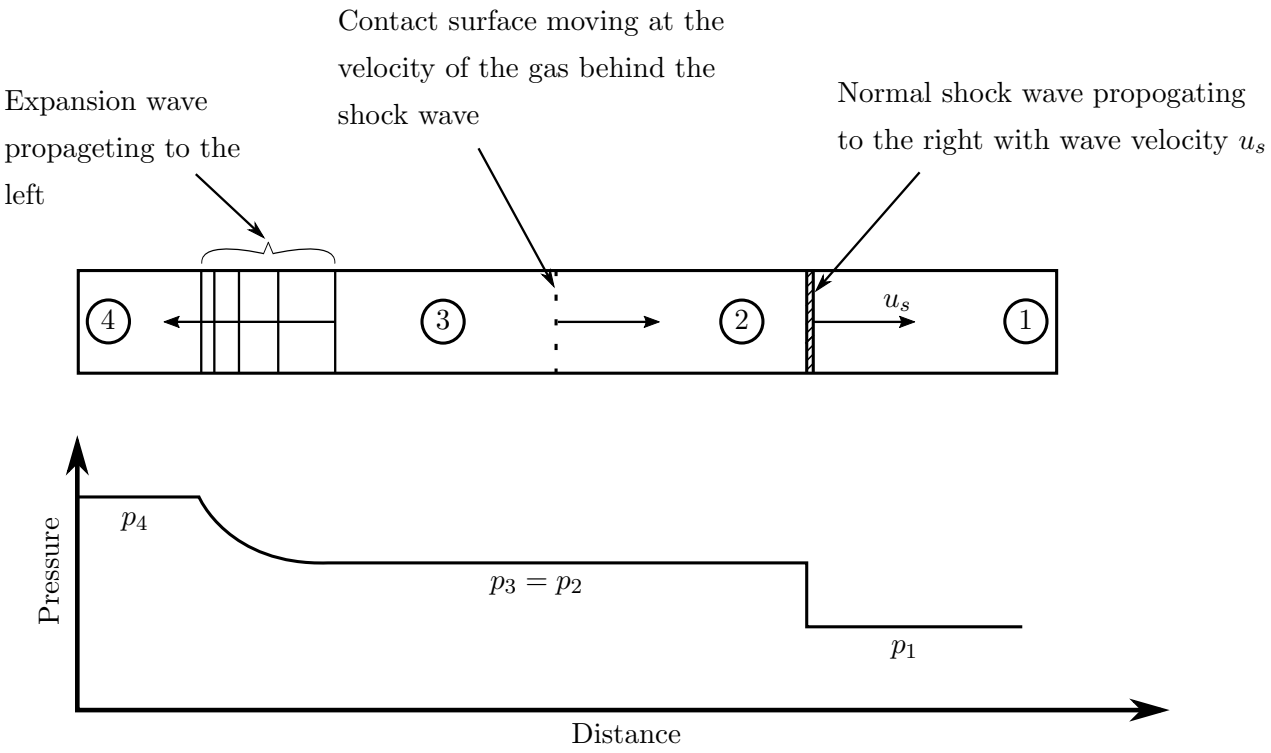


Figure 2.8: Conditions in Shock Tube after Diaphragm is Broken (Anderson (1990))

2.6 Blast Tube

At present the most effective method for generating ideal blast waves for analysis is by means of detonating explosives. Hence, blast tubes can be defined as shock tubes that are explosively driven. The general construction of current blast tubes consists of two parts namely, a long tube and an explosive energy source. The most common type of blast tube, due to its simplicity and ease of manufacture, is a round steel tube which has orifices at both ends. Explosive material can then be placed inside the tube and detonated at any position along the length of the tube. Although current blast tubes are much simpler than comparable shock tubes in that the blast tubes, unlike shock tubes, do not require complex components such as mechanical pumps, compressed gas storage or diaphragms, thereby eliminating sources of maintenance and safety issues, the operation of blast tubes is still complex and fraught with danger due to the need to handle and store explosive material. For this reason, when smaller experiments are being performed it is preferable to use modified shock tubes while for larger experiments blast tubes are used.

One of the drawbacks of a blast tube is that in order to place explosives in the tube one needs to be able to access the internals of the blast tube which results in blast tubes tending to be quite large and having diameters in the range of 1m to 22m and lengths in excess of hundreds

of metres. Another point of concern that arises with the use of explosively driven blast tubes is the need for lots of open and empty space so as to provide a buffer and distance for any stray blast waves to decay sufficiently so as to not cause any damage to civilian property or harm to civilians.

The logic behind using a blast tube to simulate blast waves for blast effect studies is based on the fact that a blast tube can be compared to placing a tube in front of an open air explosion between the explosive source and the test station or measuring equipment. The blast tube acts to prevent energy dissipating through its boundaries thus conserving the energy of the blast wave as it traverses from the source to the station. This conservation of energy allows for the use of a smaller explosive charge to simulate the blast wave induced by a much larger open air explosion. The blast tubes that are best at accurately simulating blast waves from open air explosions are blast tubes that are conically divergent. Due to the prohibitively expensive costs as well as time consuming process of fabrication, conically shaped blast tubes are rare.

In recent times there has been a push to find alternative methods for generating realistic blast waves without the need to detonate explosives. These methods have all involved modifying the standard shock tube. Modifications to the blast tube include changing the driver source from explosive material to high pressure gas, high voltage electrical discharges or high velocity pistons. An alternative modification to the shock tube has been to change the shape of the driver section of the tube such that the volume and length of the driver section is much less than that of the shock tube. This enables the expansion waves travelling away from the diaphragm towards the end of the driver section to reflect off the driver back wall and to then catch up to the shock travelling down the shock tube resulting in an exponential decay in pressure behind the shock front. The modification that generates the more realistic blast wave pressure profile is making the driver section canonical as this is resembles the spherical divergence that occurs in open-air explosions.

2.6.1 Explosively Driven Blast Tube Configurations

Although there are numerous different possible blast tube configurations, only the three most relevant to this research will be looked at. The three configurations to be looked at are all variations of a blast tube having constant cross-sectional area and having one explosive source as the driver.The three configurations are:

1. Explosive at the Centre of the Blast Tube
2. Explosive at the End of the Blast Tube

3. Explosive Outside of the Blast Tube

The centred explosive configuration correlates directly with a closed-ended shock tube. Due to the centred configuration being symmetrical about the centre of the blast tube, the blast tube can be simulated by placing a rigid wall at the centre of the blast tube and then analysing only half the blast tube. This set-up makes it analogous to a normal shock tube where the driver is high-pressure gas. Although the flow following a detonation is quite turbulent and complex, for most cases the explosive section can be considered to be of uniform temperature and pressure. These simplifications enable the centred explosive configuration to be a analysed as a 1-D problem. The development of the wave system of the centred explosive configurations is as follows. The detonation of the explosive induces high pressures in the central section of the blast tube, from which a flat-topped shock front propagates outwards towards both ends of the blast tube. As the high pressure section expands outwards, expansion waves enter the explosive section and travel inwards towards the centre of the blast tube. At the centre of the blast tube the expansion waves meet and reflect back towards the ends of the blast tube. At about two to four driver lengths the expansion waves starts to catch up to the initial shock front resulting in an exponential decay in pressure behind the shock front. As the shock front exits the end of the blast tube an expansion wave is induced which travels back down the blast tube. The products resulting from the detonation travel much slower than the shock front, however the detonation products do travel down the length of the blast tube, and depending on the strength of the explosion as well as the length of the blast tube, the products do eventually reach the end of the blast tube. If there is a large difference in the density of the detonation products and the compressed air ahead of the contact surface a large change in dynamic pressure can result.

The development of the wave system of the explosive at the end of the blast tube configuration is much the same as that of the centred explosive bar one major difference. The difference is that unlike the centred explosive configuration, the expansion wave entering the tube end after the shock wave exits combines with the expansion wave entering the explosive section. This coalescences of the expansion waves results in a steeper and more potent expansion which has a tail that travels faster than that of the centred explosive expansion tail. Consequently, the explosive at the end configuration produces a blast wave pressure profile which better matches the pressure profile of an open-air explosion.

The explosive outside the blast tube configuration is used when high-fidelity environs, that is environments having little or no distortion, are needed. The one advantage of this configuration is that, unlike the previous two configurations, the expansion wave does not need to travel through the explosive section before reaching the shock front but rather enters the tube immediately afterwards. Another advantage is that the radial pulse produced by the

explosion is not reflected inside the blast tube thereby reducing the magnitude of the pressure of the radial waves propagating down the length of the tube. The blast wave produced by the explosive outside configuration, due to the reduced radial pressure waves, has a much smoother waveform than that produced by the other two blast tube configurations.

2.7 Shock Wave Reflection

The previous sections have discussed shock wave flow where the shock wave propagated freely whether it was in a tube or the open atmosphere. However, when a shock wave encounters an obstruction or other medium it undergoes complex interactions which results in non-linear behaviour and reflection phenomena to arise. There are two main classes of shock wave reflection namely normal reflection and oblique reflection. Normal reflection results when a shock wave impacts a plane surface which is parallel to shock front while oblique reflection occurs when the shock wave impinges a surface at some angle to the shock. The oblique shock wave reflection type can be divide into two subcategories namely regular and irregular or Mach reflection. Each category of shock wave reflection will be expounded on further below. It is important to note that there are numerous other types of shock wave reflection such as von Neumann, Vasilev and Guderley reflections which are linked to weak shock wave and small wedge angles, and transitional-Mach and double-Mach reflection which are linked to strong shocks and psuedosteady flow (Ben-Dor (2007)). These other types of reflection are beyond the scope of this work and will not be discussed.

2.7.1 Normal Reflection

When an incident plane shock wave impacts a flat rigid surface at a zero angle of incidence, the motion of the fluid particles at the incident shock front is instantaneously ceased. However the particles behind the incident front, that is the particles at some distance upstream of the surface, are still travelling with a velocity similar to the original shock velocity before impact. As a result an instantaneous velocity differential arises between the stationary particles at the surface and the upstream particles, having similar magnitude and opposite direction to the incident shock front velocity. This instantaneous velocity differential induces a new, reflected shock front, which travels back into the fluid, away from the reflecting surface, in the opposite direction to the incident shock wave (Kinney (1962)). An one-dimensional normal reflection is depicted in Figure 2.9 below.

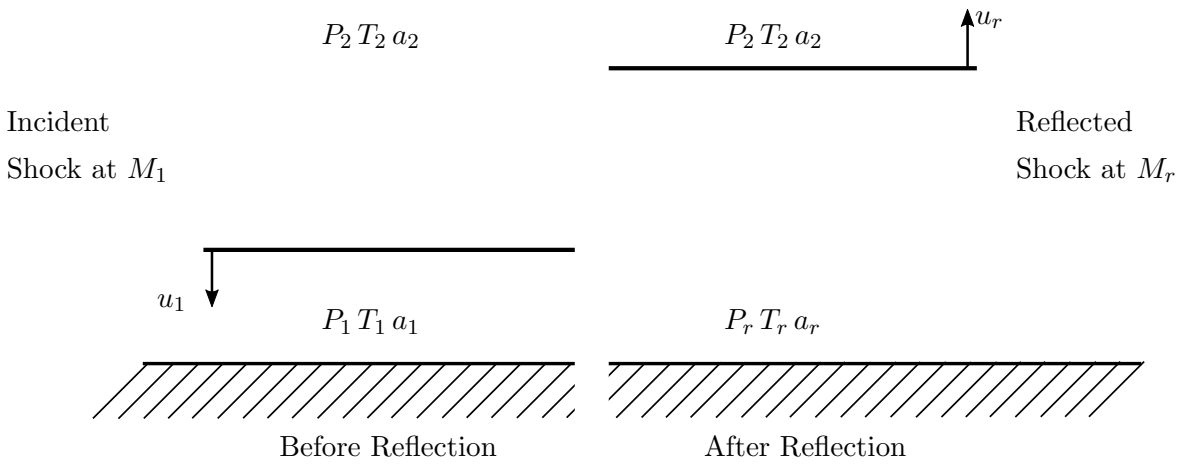


Figure 2.9: Normal Reflection of a Plane Shock (Kinney (1962))

The reflected shock wave may be analysed using the methodology used for moving shocks which is laid out in subsection 2.2.2. The relationship between the normally reflected shock wave and the incident shock wave is derived by firstly determining the velocity of the incident shock, then calculating the speed of sound in the fluid upstream of the incident shock and lastly computing the Mach number of the reflected shock using the velocity of the incident shock and the speed of sound of the fluid into which the reflected shock is travelling . This analysis yields for gasses having $\gamma = 1.4$ that the ratio of the the pressure of the fluid behind the reflected shock p_r and the ambient fluid downstream of the incident shock p_2 is given by

$$\frac{p_r}{p_2} = \frac{\left(4M_2^2 - 1\right)\left(7M_2^2 - 1\right)}{3\left(M_2^2 + 5\right)} = \frac{p_1\left(8p_1 - p_2\right)}{p_2\left(p_1 + 6p_2\right)} \tag{2.35}$$

while the relationship between the reflected shock Mach number M_r and the incident shock Mach number M_2 is

$$M_r = \left[\frac{7M_2^2 - 1}{M_2^2 + 5}\right]^{\frac{1}{2}} \tag{2.36}$$

The temperature of the fluid behind the reflected shock T_r is calculated using,

$$\frac{T_r}{T_2} = \left(\frac{a_r}{a_2}\right)^2 = \frac{\left(\frac{p_1}{p_2} + 5\right)\left(8\frac{p_1}{p_2} - 1\right)}{7\left(6\frac{p_1}{p_2} + 1\right)} \tag{2.37}$$

Due to the reflected shock moving into a fluid of higher density and pressure than the fluid into which the incident wave travelled, the density, pressure and temperature of the fluid behind the reflected shock are much higher than the properties behind the incident shock. In the above equations this can clearly be seen to be the case. For weak shocks where the shock Mach number tends to 1 in air where $\gamma = 1.4$, the overpressure ratio tends to a limiting value of 2, that is the reflected shock overpressure is twice that of the incident shock overpressure while for stronger shocks in perfect gases the ratio tends to a limiting value of 8 (Baker (1973)). It is important to note that unlike shock wave reflection, where the reflected wave travels through uniform fluid, reflected blast waves propagate into a non-uniform state fluid (Igra, Falcovitz and Heilig (2003)).

2.7.2 Oblique Reflection

2.7.2.1 Regular Reflection

A regular reflection at non-perpendicular incidence occurs when a shock wave impacts a plane rigid surface with an angle less than 90° and the phase velocity of the incident wave parallel to the plane of reflection is greater than the velocity of the reflected shock such that the reflected shock wave is unable to catch up to the incident shock wave. A regular reflection is illustrated in Figure 2.10 where OI is the incident shock wave, OR is the reflected shock and O is the point of intersection of the two waves. The incident shock wave OI travels at a speed of M_s and impinges the flat surface at an angle of incidence β_i. . The reflected wave leaves the reflecting surface at an angle of reflection of β_r and speed of M_r. Except in the case of sound waves, the angle of incidence and angle of reflection are not equal. Oblique reflection exhibits similar overpressure ratios to normal reflection, which is to be expected, since the regular oblique reflection tends to normal reflection as the angle of incidence tends to zero.

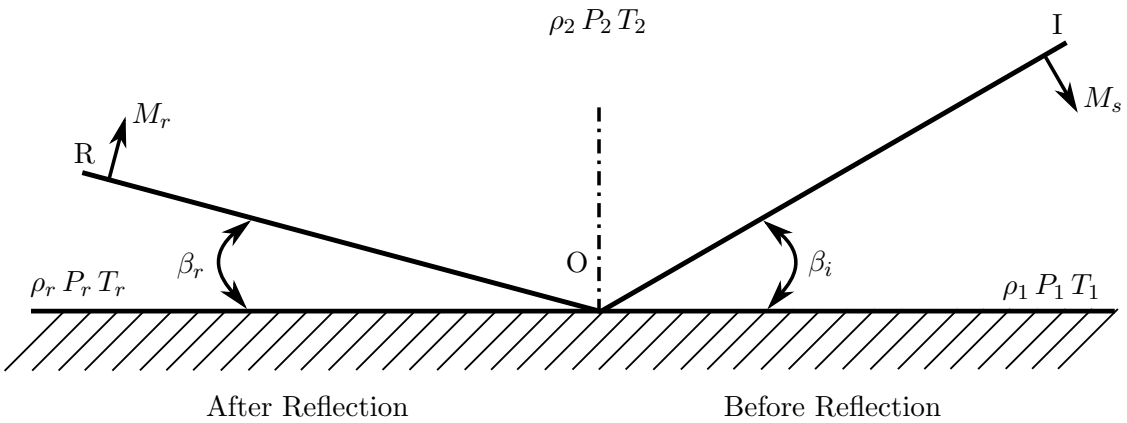


Figure 2.10: Normal Oblique Reflection (Kinney (1962))

A regular shock reflection can be analysed by transforming the moving shock case to a comparable steady flow type problem. This transformation is performed by envisaging a frame of reference located at the intersection point O which moves at the same speed as the intersection point. The speed at which the intersection point moves is u_1 which is equal to the component of the incident shock velocity which is parallel to the plane of reflection, $\frac{u_s}{\sin\beta_i}$. The velocity u_1 is then subtracted from the velocity components of the incident and reflected shock, such that it appears that there is steady flow moving into the incident shock wave. The region in front of the incident shock is assumed to be undisturbed and having a speed of sound a_1.

The steady flow regular refection as shown in Figure 2.11 can be divided into three regions. Region 1 is located in front of the incident shock wave where the streamlines entering the shock are parallel to the reflecting surface and have speed $\frac{M_1}{u_1}$. The flow then passes through the incident oblique shock wave into region 2 where the streamlines are deviated towards the reflecting surface as is the case for an oblique shock as discussed in subsection 2.2.3. Region 3 starts at the reflected shock which realigns the streamlines to be parallel to the reflecting plane. The flow adjacent to reflecting surface must be parallel to the surface as this is a physical boundary condition.

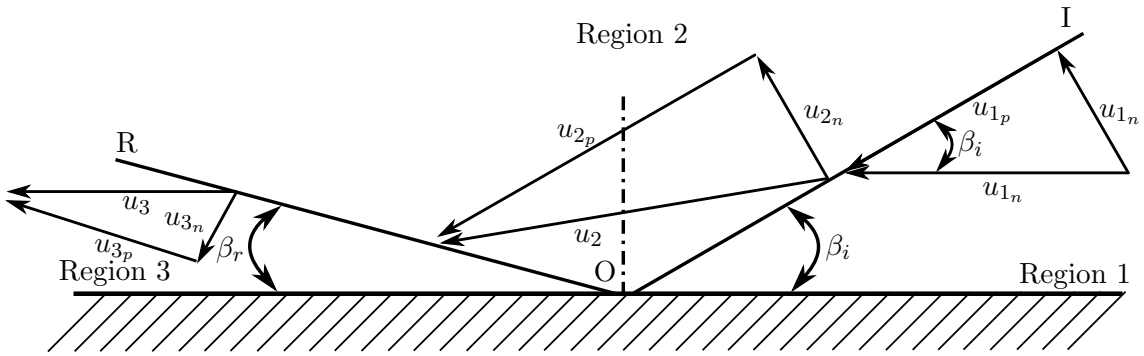


Figure 2.11: Steady Flow counterpart of Oblique Reflection (Skews (1966))

The velocities orientated parallel to the reflecting surface, u_1 which enters the incident shock and u_3 which leaves the reflected shock may be split into components normal and parallel to each shock noting that the parallel components remain unchanged as the parallel components do not enter the shocks. The normal velocity components u_1, u_{2_n}, u_{2_n}, and u_{3_n} in conjunction with the equations for stationary normal shock in subsection 2.2.1 can be used to evaluate the regular oblique shock reflection.

Computational work performed by Polachek and Seeger for gases having $\gamma = 1.4$ showed that for every shock of given strength z and angle of incidence β_i there are two possible angles of reflection where the smaller of the angles corresponds to the lower reflected pressure. In reality the lower reflection pressure occurs so the smaller angle of reflection is used. There is

a critical angle β_{crit} where the incident angle and reflection angles are equal. For an assumed perfect gas having $\gamma = 1.4$, this critical angle is 39.23°. If the angle of incidence is lower than this critical angle the overpressure ratio across the reflected shock is less than that of a comparable head on collision and the angle of reflection is smaller than the angle of incidence. The opposite holds true for an angle of incidence larger than the critical angle.

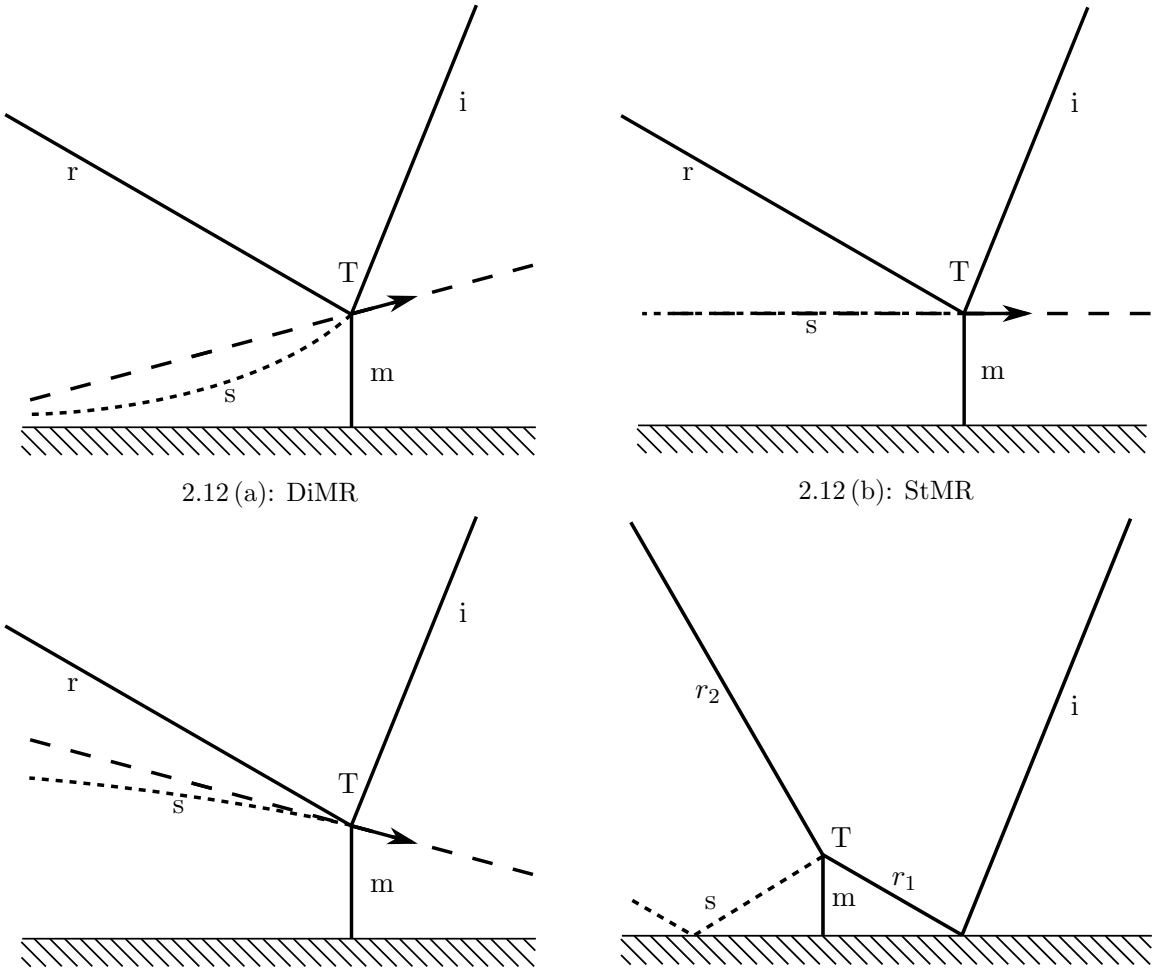
The angle of incidence for a given shock strength at which the smaller and larger angles of reflection are equal is called the extreme angle β_{ext}. When the angle of incidence is approximatively zero, that is when the incident shock impinges the surface at near head-on incidence, the flow behind the shock is supersonic. The angle of incidence at which the flow behind the incident shock is sonic is β^*. If the angle of incidence exceeds β^* the flow trailing the shock becomes subsonic which implies that the reflected shock can no longer exist. Since the sonic angle β^* is always greater than the extreme angle β_{ext}, if the angle of incidence is larger than the extreme angle Mach reflection occurs.

2.7.2.2 Mach Reflection

When the incident shock wave impinges the plane reflecting surface, such that the angle of incidence β_i is greater than the extreme angle β_{ext}, there is no two shock wave system capable of reorientating the flow to be parallel to the reflecting surface. In such cases the point of reflection, or point at which the incident wave OI and reflected wave OR intersect, moves away from the reflecting surface and a normal shock wave, called the Mach stem M in honour of the pioneering research performed by Ernst Mach on this type of reflection, forms at the reflecting surface. The normal shock allows the flow adjacent to the reflecting surface to remain parallel to the surface in compliance with the physical boundary conditions. The point at which all three shock intersect is called the triple point T and since the velocity of the flow leaving the reflected shock OR and the flow leaving the Mach stem M are not equal in magnitude a shear layer or slipstream S trails the triple point T, as shown in Figure 2.12 (d). The shear layer or slipstream S acts as a division between the regions trailing the reflected shock and Mach stem which have the same pressures and flow direction but differing velocities, densities and temperatures. It is important to note that although the base of the Mach stem is perpendicular to the reflecting surface, in steady or pseudosteady flow, near the triple point the Mach stem curves away from the direction of the flow (Ben-Dor (2007)).

According to Courant and Friedrichs (1948) there are theoretically three main types of Mach wave reflection namely Direct Mach Reflection (DiMR), Stationary Mach Reflection (StMR) and Inverse Mach Reflection (InMR) as shown in Figure 2.12 (d). The type of configuration that is assumed by the Mach reflection is dependent on the direction in which the triple point travels. The straight line path along which the triple point travels is referred to as

the shock-shock (Whitham (1958)). A DiMR occurs when a moving shock reflects into a steady flow and the triple point moves away from the reflecting surface. When the triple point tracks parallel to the reflecting surface the reflection is classified as StMR. If the flow is unsteady and the triple point moves towards the reflecting surface the reflection is classified as InMR and the Mach stem curves into the direction flow. The InMR terminates when the triple point impacts the reflecting surface and transitions into a regular reflection trailed by a Mach reflection which is induced by the slipstream interacting with reflected wave. This new wave configuration is called a transitioned regular reflection Transitioned Regular Reflection (TRR) and is imaged in Figure 2.12 (d) (Ben-Dor (2007)).



2.12 (a): DiMR

2.12 (b): StMR

2.12 (c): DiMR

2.12 (d): TRR

Figure 2.12: Schematic Illustrations of wave configurations of (a) a direct-Mach Reflection - DiMR; (b) a stationary-Mach reflection - StMR; (c) an inverse-Mach reflection - InMR; (d) a transitioned regular reflection - TRR (Ben-Dor 2007)

2.7.2.3 The Transition Criteria

The most noteworthy transition criteria which dictate whether a shock wave reflection will be regular or irregular in steady or pseudosteady flow, as put forward by and summarised by Ben-Dor (2007), are detachment, sonic and mechanical-equilibrium. The maximum-deflection condition, or detachment condition, refers to the largest incident angle at which regular reflection can occur and any angle of incidences beyond which no regular reflection can occur which is capable of turning the flow parallel to the reflecting surface. According to the sonic condition if the sound waves generate by a corner can catch up to point of reflection, which implies that the flow behind the shock is subsonic relative to the reflection point, then Mach reflection will occur. Conversely regular reflection occurs if the flow behind the shock is supersonic as the waves generated by the corner will have a relative speed slower than the shock and therefore will be unable to reach the shock.

Henderson and Lozzi (1975) found that both the maximum deflection and sonic criteria, in many cases, require discontinuous changes in pressure in the regions trailing the reflected shock wave. These discontinuous pressure changes need to be sustained by a compression or expansion wave to maintain mechanical equilibrium however during experimentation such waves were not observed. The mechanical-equilibrium condition, as proposed by Henderson and Lozzi (1975), states that the angle at which the two shock and three shock theories concur, that is, when the slipstream near the triple point is parallel to the reflecting surface and the Mach stem is straight and perpendicular to the surface, is the angle at which transition from regular to irregular reflection occurs (Ben-Dor (2007)).

A fourth transition criterion, the length-scale condition, was posited by Hornung, Oertel Jr and Sandeman (1979). The source of this criterion is the fact that a regular reflection has no length scale as both the incident and reflected waves are infinite in length, while a Mach reflection does have a length scale as the Mach stem has finite length starting at the reflection point and terminating at the triple point. The length-scale condition states that for steady flows having a speed above a critical Mach number the transition is predicted by the mechanical-equilibrium condition, while for steady and pseudosteady flows having speeds below the critical Mach number the sonic criterion predicts the transition (Ben-Dor (2007)).

2.8 Shock Wave Diffraction

The diffraction of a shock wave occurs when the shock wave undergoes an area expansion, that is the shock encounters a surface with an angle of incidence greater than 90° to the shock front. The study of the diffraction of shock waves is particularly pertinent to the analysis of blast waves as blast waves diffract when they impact man made structures, such as houses and office blocks, and changes in the physical terrain, such as hills and valleys. Such studies enable the prediction and evaluation of loadings and damage on said structures when impacted by a blast wave. What makes the study of the diffraction of blast waves particularity challenging is the changing properties behind the shock front as well as the complex wave elements and gas effects.

The shock wave diffraction that occurs when a shock impinges a rectangular body, the rectangular body be analogous of a rigid structure, is shown in Figure 2.13. Initially the shock wave travels towards the rectangular body with some velocity u as seen in Figure 2.13 (a). The shock then collides with the structure and the portion of the shock which impacts the left face reflects back upstream into the energised flow and leaves behind it stationary, high pressure air on the left face. This all occurs while the rest of the mostly undisturbed incident shock continues to traverse the top of the structure as shown in Figure 2.13 (b). Due to the corner acting as a singularity the shock diffracts outwards cylindrically as can be seen in Figure 2.13 (b). This diffracted shock acts to join the reflected and incident shocks. Due to the pressure behind the diffracted shock being less than the pressure behind the reflected shock a rarefaction or expansion wave forms at the top of the structure and it travels down the left face into the high pressure region as depicted in Figure 2.13 (b) in order to equalise the pressure. As the rarefaction wave travels downwards it induces an upward velocity in the stationary air by the left face. As the upward moving gas encounters the corner of the structure the flow induces a vortex to shed at the corner. After travelling across the left face of the structure for some time the rarefaction wave impacts the ground thereby completely relieving the pressure in front of the left face as well as weakening the reflected shock wave further as shown in Figure 2.13 (c).

In the meantime the incident shock has continued to travel over the top of the structure and when it reaches the right corner it diffracts downwards. This downward deflection of the shock wave induces strong flow at the right corner resulting in the formation of a vortex at the corner as shown in Figure 2.13 (d). The diffracted shock continues to travel down the right face until it impacts with and reflects off the ground while the incident shock continues moving off to the right as seen in Figure 2.13 (e). Once the incident shock has travelled a distance equivalent to a few body lengths of the rectangular structure, the diffracted waves reach a point of equilibrium and a steady flow is set up, the formation of which is dependent

on the speed of the flow behind the incident shock. If the flow trailing the incident wave is supersonic the reflected shock weakens and reaches a position where it cannot move any more, thereby it takes up a position corresponding to a steady flow bow shock. If on the other hand the flow behind the incident shock is subsonic both the incident and reflected shock will travel ad infinitum , weaken as they do so and a stationary shock-less flow is what remains.

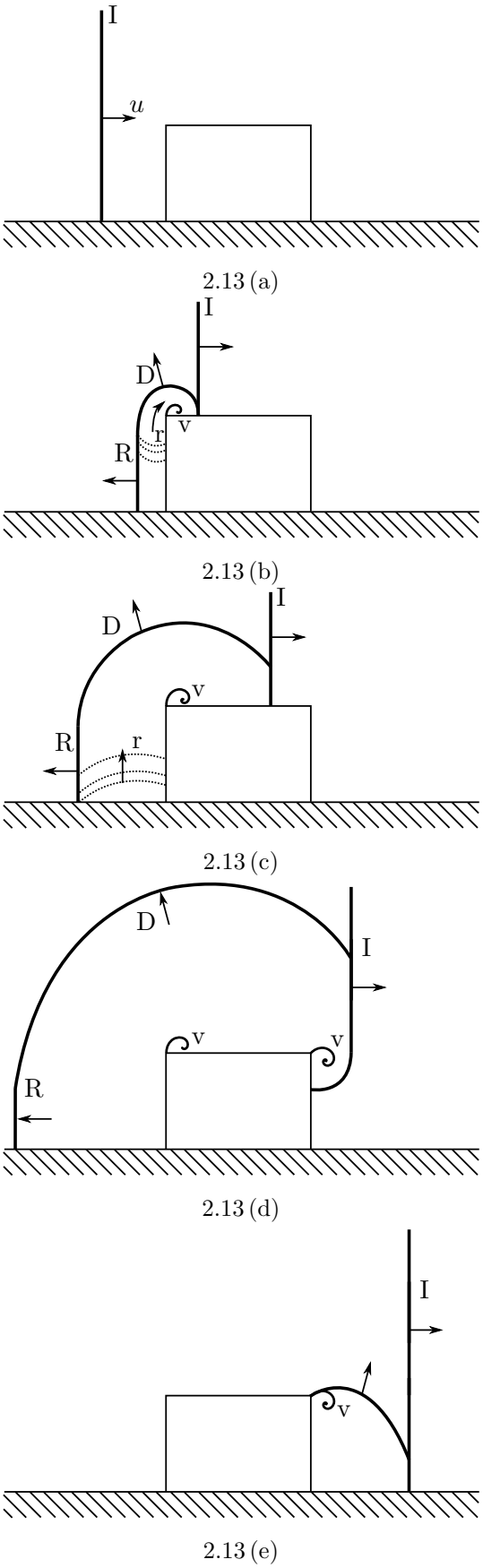


Figure 2.13: Interaction of a Shock Wave with a Rectangular Block(adapted from Skews (1966), Baker (1973) and Wright (1961))

Quite complex flow phenomena arise behind the diffracted shock. Pioneering work was performed by Skews (1966) on the diffraction of shock waves and in particular the detailing of the complex flow patterns and features that arise behind the diffracted shock. The features arising in the perturbed region trailing the diffracted shock are depicted in Figure 2.14. It can be seen in Figure 2.14 that the perturbed region is surrounded by the reflected sound wave, incident shock, the curved diffracted shock and the wall. The main features that arise are the vortex, contact surface, slipstream, terminator and second shock as can be seen Figure 2.14.

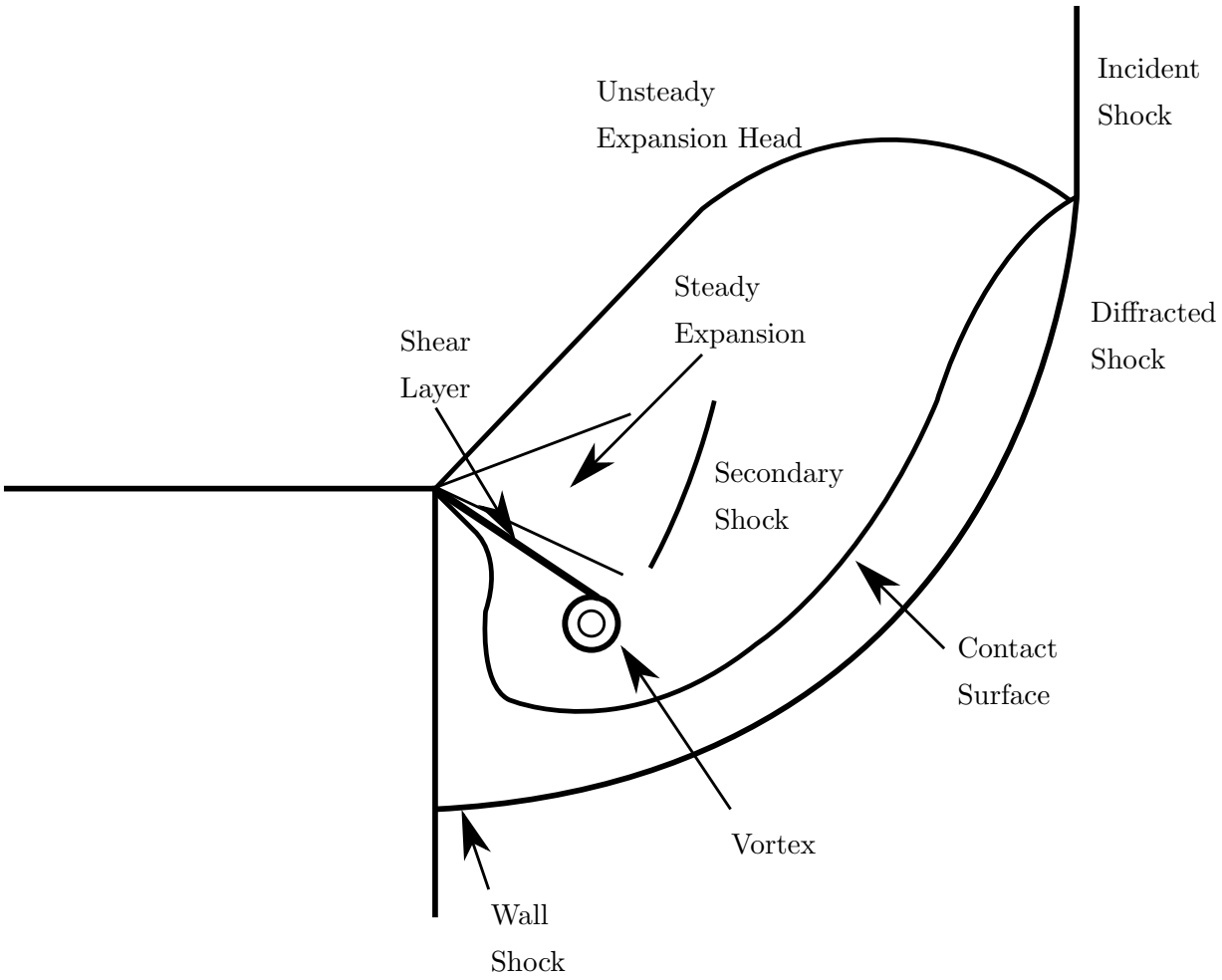


Figure 2.14: The Perturbed Region Behind a Diffracting Shock Wave (Skews (1967b))

The slipstream arises as a result of separation which forms because of the the flows inability to travel around the corner. The slipstream is not an abrupt discontinuity but rather a region in the flow which enables the high velocity flow above it to interact with the stationary flow below it. The thickness of the slipstream increases the further out from the corner it propagates. The thickness of the slipstream also tends to be effected by the corner angle whereby the smaller the corner angle is the thicker and more turbulent the slipstream. The slipstream tends to be straight, only curving at the point furthest from the corner as this point is acted upon by the vortex. The slipstream angle ϵ ,that is the angle between the

upper surface of the slipstream and the upper surface of the corner, is dependent on the pressure to which the flow expands which in turn depends on the corner angle. For large corners the slipstream angle reaches a limit and becomes independent of corner angle but is still dependent on Mach number.

The terminator is the tail of the Prandtl-Meyer fan which forms in order to expand flow past a corner. The angle between the horizontal and the terminator is called the terminator angle σ. Skews found that the terminator angle decreases with increasing incident Mach number and just as with the slipstream angle, the terminator angle reaches a limit for the larger corner angles. For corner angles between 15° and 45° the terminator angle also reaches a limit but at comparatively much lower Mach numbers. These results are indicative of there being a region of uniform flow in between the terminator and the slipstream.

The contact surface starts at the point at which the incident wave, reflected sound wave and diffracted wave meet. Close to this point the flow entropy gradients are small which causes the contact surface to be very weak in this region. The contact surface strengthens further from the point of intersection due to the gradients in entropy increasing. The reason why the contact surface is not visible at lower incident Mach numbers is due to the lower entropy changes that occur for weak shocks. Skews noted that as the incident Mach number increased the contact surface becomes more curled near the wall. For large corner angles the contact surface curls around the vortex and then straightens as it approaches the slipstream, eventually making contact with the corner. The contact surface is a good indicator of the movement of the gas in the flow as the contact surface moves at particle velocity. For corner angles larger than 90° the contact surface velocity becomes independent of the corner angle.

The two main properties that effect the formation of the features in the perturbed region are the incident shock wave Mach number and the angle of the corner wall. For corner angles larger than 45° the flow patterns basically remain the same for any given incident Mach number. For weak shock waves, that is shocks that have Mach numbers less than 2.07, the reflected sound wave propagates back upstream and the curved diffracted shock starts at the point along the incident shock at which the reflected wave and the incident wave intersect. A small vortex forms at the corner and due to the process process being polytropic no contact surface forms. As the incident Mach number is increased to 1.2 the angle at which the curvature of the diffracted shock starts increases and a contact surfaces starts to form starting from the point at which the incident wave, reflected sound wave and diffracted wave intersect. Due to the increased flow velocity trailing the incident wave a more prominent vortex forms and it travels further from the corner. As a result of the flows inability to traverse the corner a slipstream forms between the corner and the vortex. As the Mach number of the incident wave is increased further to 1.5 more flow features arise. The contact surface and slipstreams become more prominent and the ends of both curl around

the vortex. The first signs of the formation of the second shock are visible in the form of wavelets on the top of the slipstream. The second shock fully forms when the incident Mach number is increased slightly to 1.6. Upon further increases in incident Mach number the second shock and vortex interact and a further discontinuity called the terminator forms above the slipstream. When the incident Mach number reaches 2 the flow trailing the shock is nearly sonic which prevents the reflected sound wave from broadcasting upstream. As the Mach number is increased even further no new features arise.

The diffracted flow patterns described above are slightly different for corners having angles between 15° and 60°, which are considered small. For a corner angle of a 15° and incident Mach number ranging between 1.5 and 3.0, a very weak vortex forms while no slipstream is visible. Another difference is that the contact surface and second shock make contact with the wall. For a corner having an angle of 30° and incident Mach number of 2.0 a vortex is present and there is separation of the flow. When the corner angle is 45° the contact surface has a much larger curve so much so that it curls between the vortex and the wall. For a 60° corner angle the flow formation behind the diffracted shock is similar to that occurring at large corner angles.

2.9 Shock and Expansion Wave Focusing

Shock wave focusing occurs when a cylindrical shock wave implodes towards a central axis or implosion centre. The implosion of the shock wave results in very large increase in temperature, pressure and density in the gas at the central implosion region. Uniformly converging shocks can also result in shock focusing. When a finite element of the shock front converges at an individual point, perfect focusing occurs. The maximum pressures and temperatures achieved at the implosion centre are determined by the degree to which symmetry of the imploding shock front has been achieved. Shock wave focusing is used to initiate and control nuclear fusion in hydrogen bombs as well as lithotripsy which is used in the treatment of kidneys stones. The most common methods used to focus shock waves are the inverted tear-drop and logarithmic-spiral. Expansion focusing in ducts is induced by area changes in the duct cross-section which cause the ends of the expansion waves to reflect off the duct side walls towards the centreline of the duct. Extensive research into the effects of area change on expansion wave cavity flow and focusing was carried out by Whalley (2016). Although Whalley (2016) tested numerous and varying duct geometry's, it was found that although the expansion wave focusing varied for the various shapes, the basic flow patterns that arose followed a similar process. The process is as follows and shown in Figure 2.15:

1. Upon bursting of the diaphragm separating the driver and expansion sections, a shock wave propagates into the expansion section while an expansion wave spreads into the driver section.

2. As the expansion wave travels into the varying cross-section cavity, the angled duct walls cause the expansion wave to deflect which in turn gives rise to expansion wave reflection.

3. The reflected expansion waves propagate towards the centre line of the duct inducing regions of more expanded flow behind them as they do so. These trailing regions have lower temperatures and pressures than the surrounding fluid.

4. To correct for this over-expansion in the fluid, compression waves start to form at the trailing edge of the reflected expansion wave.

5. Upon the trailing edges of the reflected expansion waves and the accompanying compression waves meeting at the centreline of the duct, the waves adjoin to form an enclosed region in the flow referred to as the focus region.

6. Within the focus region the reflected expansion waves continue to reflect, resulting in the fluid being expanded by 3 or more expansion waves, inducing very low pressures and temperatures in this region.

7. While the primary reflected expansion wave and the accompanying compression waves propagate into the shaped cavity, multiple expansion wave reflections in the decreasingly smaller focus region induces intensified expansion of the fluid in this region.

8. The focus region experiences the lowest fluid properties just before the region disappears, which occurs when the compression waves reach the end of the shaped cavity.

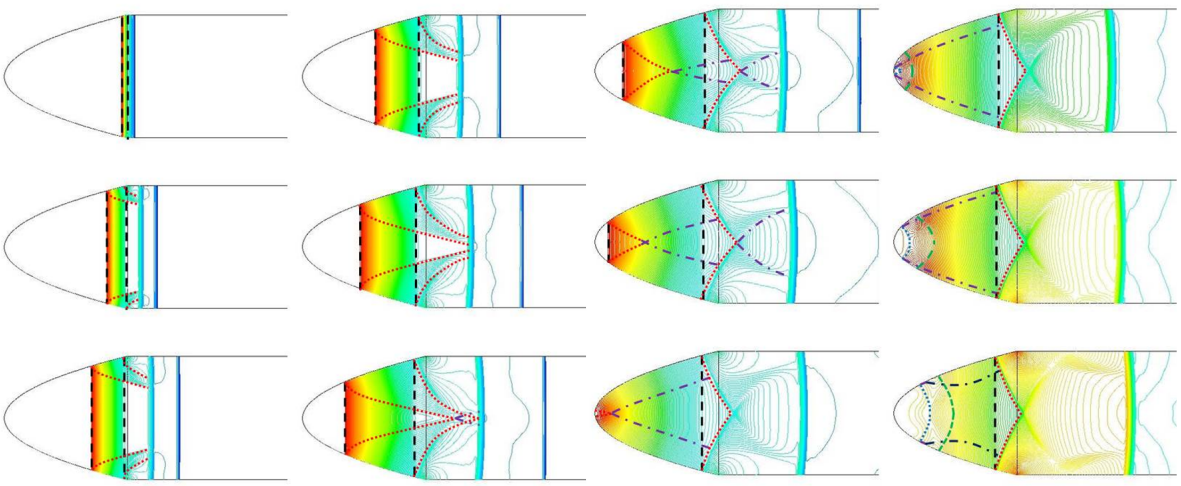


Figure 2.15: The Focusing of Expansion Waves (Whalley (2016))

Chapter 3 Objectives

The overall purpose of this research was to numerically and experimentally study a number of phenomena that arise due to the generation and behaviour of blast waves. The general objectives of the research are:

- To design and optimise a blast tube that can consistently generate blast waves having good visual quality and realistic pressure-time profiles by using CFD software to determine the required shape, divergence and length of the high-pressure driver section of the tube as well as the location of the diaphragm
- To construct the optimised blast tube and validate, using pressure measurements and visualisations, that the blast tube does in fact produce blast waves that have pressure-time profiles and formations that match the waves produced in the CFD simulations as well as that can be replicated consistently
- To study, using visual techniques such as shadowgraphy and schlieren photography, the reflection and diffraction of blast waves that occurs when the blast waves impinge different angled surfaces
- To determine, using visual techniques, the effects of different parameters, such as the driver shape and pressure, on blast wave reflection and diffraction
- To perform CFD simulations of the reflection and diffractions experiments carried out and to compare the experimental and numerical results

Chapter 4 Apparatus

4.1 Design of the Blast Tube

4.1.1 Introduction

This section details the design of the non-explosively driven blast tube. The focus of this section is on the design and construction of the driver and transition sections as these are the two key components which enable blast waves to be generated non-explosively.

4.1.1.1 Design Constraints arising from the use of Existing Resources

The cost of designing and manufacturing any new product, and in particular a new testing facilities, is large. In order to try minimise the cost of the new blast tube, existing materials and components from other pre-existing testing facilities were used. This resulted in some design constraints as elaborated upon below.

Driven Section:

As part of a Phd in Engineering, Prof Beric Skews was tasked with designing a shock tube that could produce strong plane shock waves having steady flow behind them so as to enable the study of the flow features arising from the diffraction of shocks around corners of varying angles. Since the research had been completed and the facility disassembled, it was decided that the three steel sections making up the channel of the Skews Tube, which were used for convergence in order to strengthen the shock wave, would be used as the driven section of the blast tube.

The driven section consisted of three $635mm$ long square tube sections each having internal dimensions of $76 \times 76mm$. Each of the square tubes was constructed of two $22mm$ and two $32mm$ thick steel plates which were bolted together using $M6$ hexagonal cap bolts at 28mm

spacings. The three driven sections were connected via 11.5mm thick steel spacers which had O-ring pressure seals on either side to prevent leakage at the joints. A 1000mm long fourth section that was used in blast research by fourth year engineering students was later added to the end of original three square sections so as to allow for more pressure traces to be measured and produced. The final length of the driven section of the blast tube was 3480mm.

Pressure Vessel:

So as to prevent the driver section having to be certified, and thereby increasing safety and reducing cost, it was decided that a pre-existing pressure vessel would be used to encase the driver section. The pressure vessel used was manufactured by Arlec Engineering Works and was certified to be pressurised to 40bar. The internal diameter of the pressure vessel was 150mm while the internal length was approximately 600mm. The pressure vessel had a 350mm diameter, 29mm thick flange, with 12 equidistant $M28$ bolt holes, welded to the open end which was original used to connect it to a similar flange at the end of the driven section. For the blast tube, this flange would also be used to support the driver section insert.

Test Section and Test Pieces:

Due to time and financial constraints, the test section and test pieces that were used to perform the blast wave reflection and diffraction experimentation were already machined and constructed as they were used in previous research. The test section had internal dimensions of 76mm wide, a height of 232mm and a length of 295mm. The test section had two doors containing circular high quality glass windows having diameters of 235mm so as to allow schlieren photographs of the flow experiments to me taken. The test pieces used were made of mild steel and had angles of 15°, 30°, 45° and 90°.

4.1.2 Numerical Method

In order to design and select blast tube driver geometries for fabrication and experimental testing, simulations of various geometries were run using a commercially available CFD package, ANSYS Fluent 17.2. Due to the large domain being simulated as well as the moving nature of the shocks modelled, minimal post-processing was performed but when required to, the visual quality of the simulated shock waves were determined manually using ANSYS CFD-Post. Rather than performing the standard post-processing, the simulations were programmed to monitor fluid properties at various points along the length of the tube and to export said data at various time steps. Programming scripts were then developed using MATLAB R2009b to import and process the exported data. The computational resources

that were used to run the simulations was computers in the Flow Research Unit and the Centre for High Performance Computing (CHPC) Lengua Cluster. The numerical method used is detailed below.

4.1.2.1 Geometry Specification

The geometry of the numerical domain was modelled in Autodesk Inventor 2017 to match the internal dimensions of the various driver configurations and blast tube driven section. The lengths of the blast tube driven sections in the simulations did not match the length of the actual driven section. This is as a result of the length of the actual blast tube driven section being finalised shortly before experimentation commenced and the tube lengths chosen for the simulations were done so based on the need to give the blast wave enough time to develop in the least computationally expensive way.

The geometry was set up such that there were two separate fluid domains, one for the driver section and one for the driven section. The two fluid domains were then joined by an interface boundary condition located at the membrane position. In the initial simulations, the boundary conditions of all the outer boundaries of the domain were set to walls as these would correspond to the inner surface of the walls of the blast tube. In later simulations, the boundary condition of the end of the driven section was changed to a pressure outlet so as to allow for the development and monitoring of a fully-developed blast wave pressure profile. Although the height of the blast tube domain remained at a constant $76mm$, the length of the driver and driven sections varied depending on the configuration of the blast tube being simulated. Figure 4.1 represents a typical geometry setup for a blast tube having a diverging driver section:

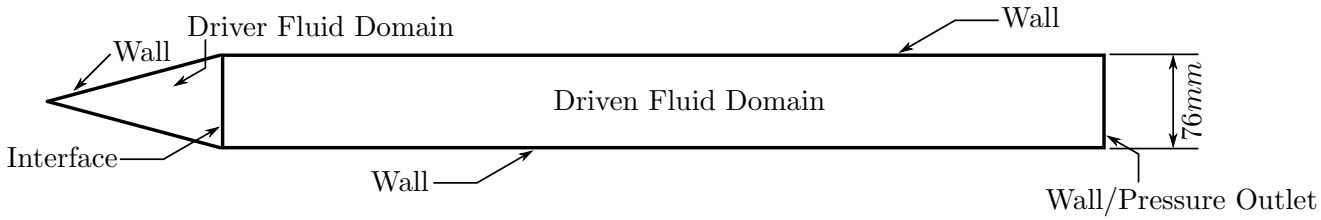


Figure 4.1: The Computational Geometry Configuration

4.1.2.2 Mesh Specification

The mesh that was used in the simulations was generated using ANSYS Workbench 17.2. An initial base mesh was applied to the blast tube fluid domain. The mesh was then configured to be adapted at every time step using adaptive mesh refinement so as to enable the mesh to

accurately model the shape and location of the shock front and contact surface. The effects of the adaptive refinement on the base mesh can be observed in Figure 4.2 where the shock front is located around $2.9m$ from the diaphragm and it can be seen that ahead of the shock front the mesh remains unrefined while behind the shock the mesh has undergone refinement.

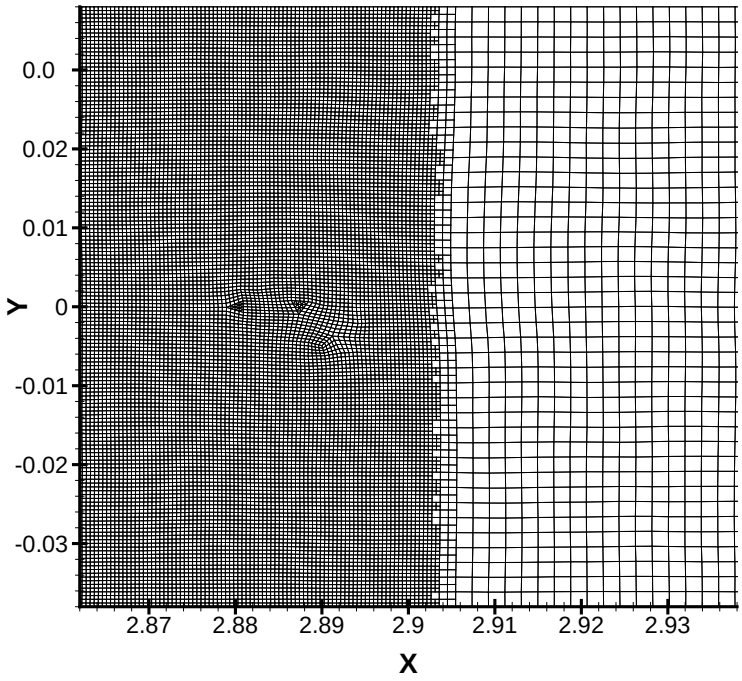


Figure 4.2: Refined Mesh in the Vicinity of the Shock Front

The flow properties that were selected for adaptive refinement were absolute-pressure, density, temperature and velocity-magnitude. The thresholds for the adaptive mesh refinement and mesh coarsening were set to 0.5 and 0.3 respectively. The method of refinement that was employed was normalised space gradient.

In order to ascertain the least computationally expensive mesh size and time step with which to run the simulations, a mesh and temporal independence study was carried out. The independence study was carried out by running a total of 9 simulations having three different quadrilateral mesh sizes namely, $3.80mm$, $1.90mm$, $0.95mm$ at 3 different time steps: $1 \times 10^{-6}s$, $5 \times 10^{-7}s$, $1 \times 10^{-7}s$. The geometry that was selected for the independence study was the blast tube having a polynomial diverging driver section and $4m$ long expansion section while the driver pressure used was $15bar$. Adaptive mesh refinement was applied, following the methodology described above, to all 9 of the simulations run for the mesh and temporal independence study. In order to determine independence, monitors measuring pressure were placed at the centre line of the blast tube at varying distances along the length of the tube.

The measurements produced by the monitors were then plotted against time for the different mesh configurations and compared. It was seen that the pressure traces at different points along the blast tube for 8 of the independence study simulations were almost identical. This is due to the adaptive mesh refinement and the decision to use an implicit solver. It is also pertinent to note that the pressure trace from the simulation having a mesh size of $3.80mm$ and time step of $1 \times 10^{-6}s$ is not plotted. This is due to the output files from this simulation being corrupted. Although not the least computationally efficient setup, it was decided that the base mesh and time step for all remaining simulations would be $1.90mm$ and $1 \times 10^{-6}s$ respectively. This was in order to obtain a more refined shock front and contact surface as well as to increase the solution stability.

4.1.2.3 Solver Settings

The solution setup and settings that were applied for the CFD simulations were as follows:

4.1.2.3.1 Solution Setup

- **General:**
  - **Solver Type:** Density Based
  - **Velocity Formulation:** Absolute
  - **Time:** Transient Unsteady
  - **2D Space:** Planar
- **Models:**
  - **Energy Model:** On
  - **Viscous Model:** Realizable k-epsilon, Standard Wall Function
- **Materials:**
  - **Fluid:** Air (Density set to ideal gas)
- **Cell Zone Conditions:**
  - **Operating Conditions:** Operating Pressure = 0Pa

- **Boundary Conditions:**
  - **Pressure Outlet:**
    - Gauge Pressure = 101325Pa
    - Backflow Turbulent Intensity (fraction) = 0.05
    - Backflow Turbulent Viscosity Ratio = 10
    - Backflow Total Temperature = 300K

4.1.2.3.2 Solution Settings

- **Solution Methods:**
  - **Formulation:** Implicit
  - **Flux Type:** Roe-FDS
  - **Spatial Discretization:**
    - **Gradient:** Least Square Cell Based
    - **Flow:** Second Order Upwind
  - **Transient Formulation:** First Order Implicit

- **Solution Controls:**
  - **Courant Number:** 0.5

- **Monitors:**
  - **Residual Convergence Monitors:**
    - Continuity Absolute Criteria = 1×10^{-4}
    - x-Velocity Absolute Criteria = 1×10^{-4}
    - y-Velocity Absolute Criteria = 1×10^{-4}
    - Energy Absolute Criteria = 1×10^{-6}
    - k Absolute Criteria = 1×10^{-5}
    - Epsilon Absolute Criteria = 1×10^{-5}

- **Solution Initialization:**
  - **Initialization Method:** Standard Initialization
  - **Reference Frame:** Absolute
  - **Initial Pressure:** 101325Pa
  - **Initial Temperature:** 300K

4.1.3 Diverging Driver Sections

As discussed previously, the most important component of any blast tube is the driver section as the size and shaping of the driver section directly effects the pressure profile of the blast wave. In this vein, it was decided that the first driver shape to be analysed in the design of the blast tube is a linearly diverging driver, that is triangular prism in shape, similar in nature to the driver sections posited and designed by Filler in his research. The reason for this choice is Filler obtained quite impressive results with his conical designs. It is important to note however that Filler's conical shock tubes where explosively driven with the main objective of amplifying the blast wave strength and that the analysis in this section is the first published extensive examination of the ability of a linearly diverging air-driven driver section to generate blast waves (Filler (1960a)).

In the design process of the linearly diverging driver section, an analysis of the CFD data was performed such that the following questions could be answered:

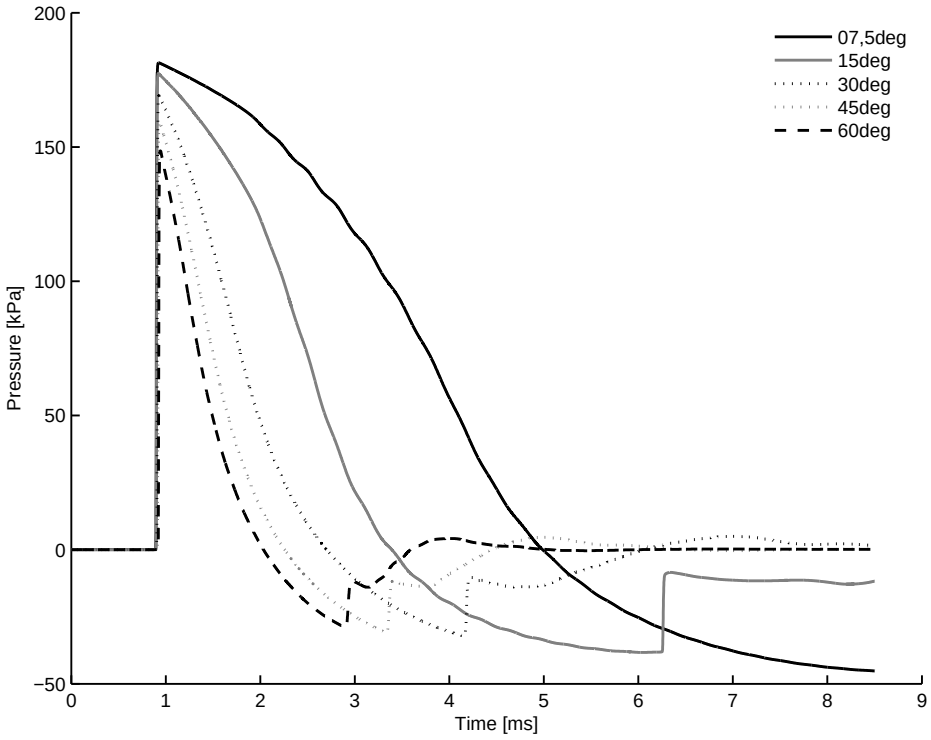
1. What effect does the driver angle have on the blast wave?
2. What effect does the driver pressure have on the blast wave?
3. How does the blast wave evolve as it propagates down the tube?
4. Do any of the linearly diverging driver sections generate a blast wave having Friedlander profile?
5. What are the flow characterisers arising from the different configurations?

The angles of divergence of the driver sections that were chosen to be examined were $7, 5°$, $15°$, $30°$, $45°$ and $60°$. Driver pressures of $5bar$, $10bar$ and $15bar$ were used for the CFD design analysis. For each of the different driver section configurations, the equivalent explosive energy was calculated using Equation 2.30 and the results of which are listed in Table 4.1 below.

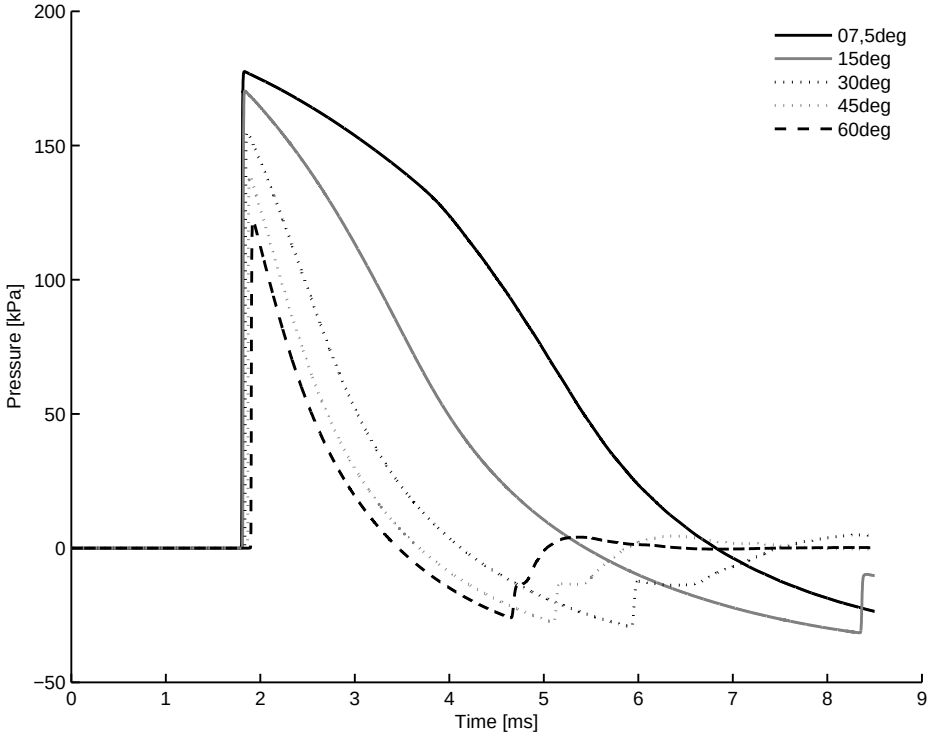
Table 4.1: Linearly Diverging Driver Pressure TNT Explosive Equivalence

Driver Section Divergence Angle	5 bar	10 bar	15 bar
7.5°	$16.68g$	$43.63g$	$73.14g$
15°	$8.31g$	$21.72g$	$36.41g$
30°	$4.08g$	$10.67g$	$17.89g$
45°	$2.64g$	$6.90g$	$11.57g$
60°	$1.89g$	$4.95g$	$8.30g$

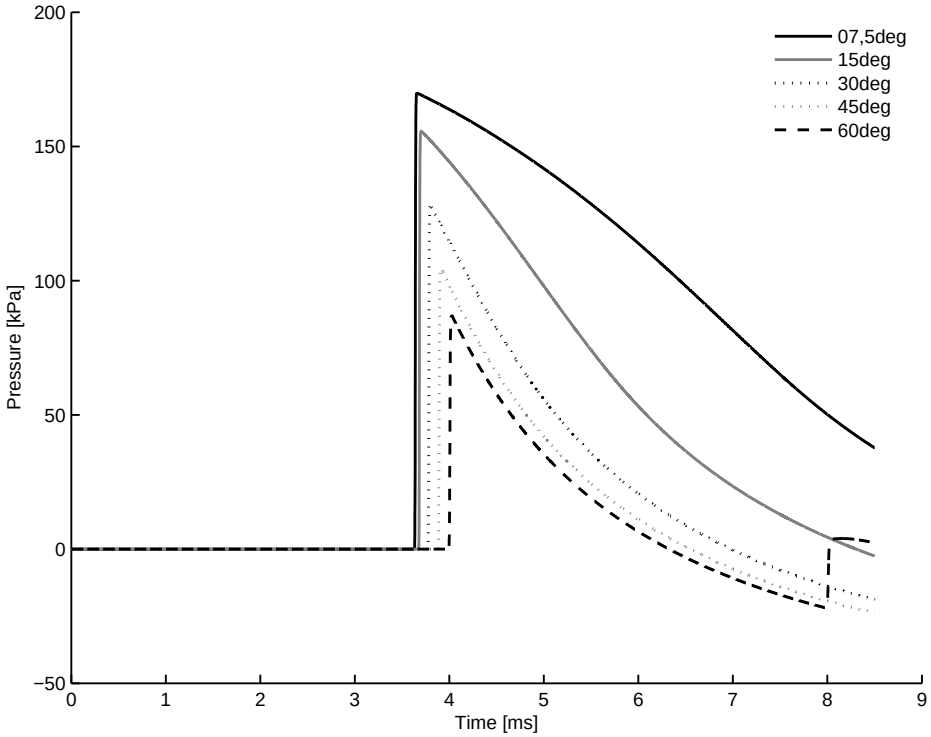
In order to assess the effects of the different linearly diverging driver sections on the blast wave pressure profiles, a comparison of the generated pressure profiles needs to be made. This comparison was performed qualitatively by plotting the pressure profiles generated by the $7,5°$, $15°$, $30°$, $45°$ and $60°$ driver profiles, having drivers pressure of $10bar$, at points $0.50m$, $1.00m$, $2.00m$ and $3.00m$ away from the diaphragm as shown in Figure 4.3.



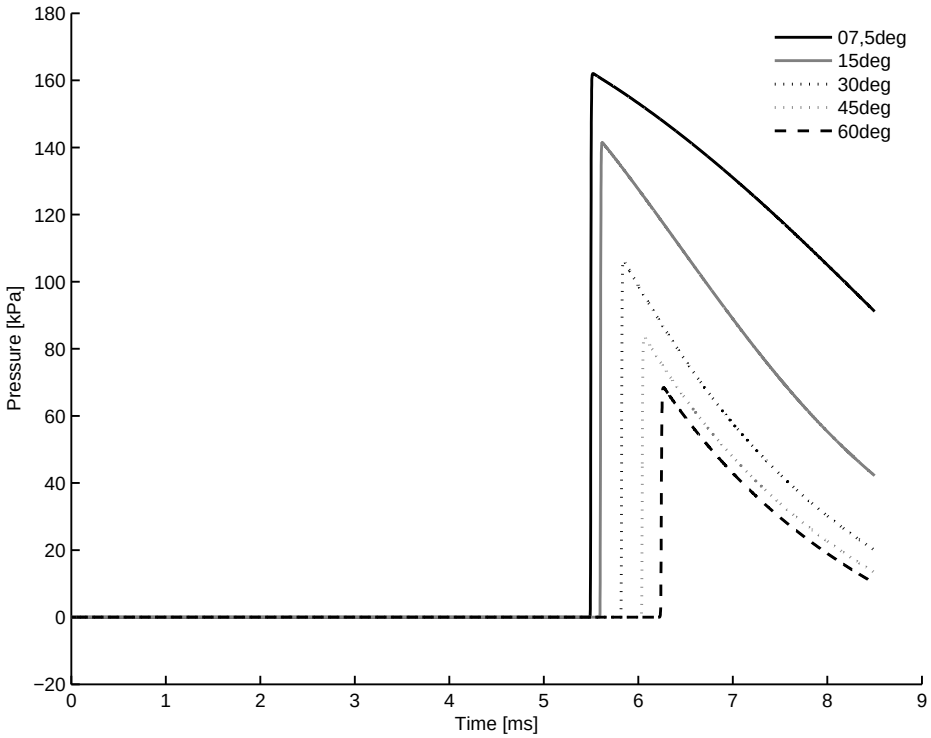
4.3 (a): $0.50m$



4.3 (b): $1.00m$



4.3 (c): $2.00m$



4.3 (d): $3.00m$

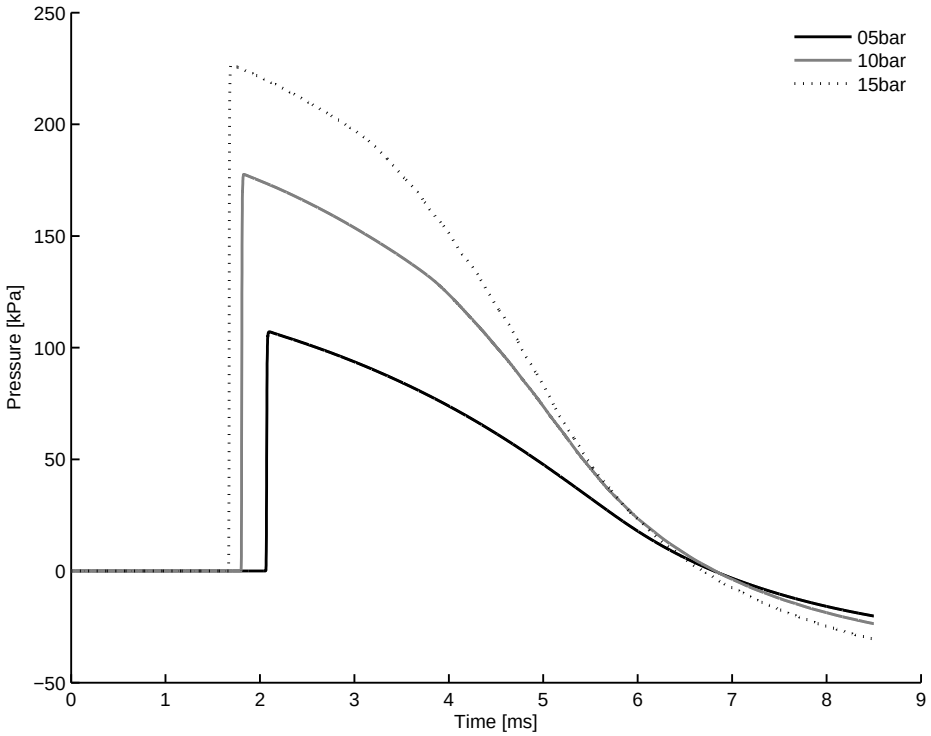
Figure 4.3: The Effect of Driver Divergence Angle on Pressure

Looking at Figure 4.3 it was observed that increasing the angle of divergence of the driver section from $7,5°$ to $30°$ resulted in a marked steepening of the rate at which the decrease in the overpressure trailing the shock front occurred. However it was found that as the shock wave propagated down the length of the expansion section, the difference in pressure gradient was still stark but somewhat lessened as observed in Figure 4.3 (a) and Figure 4.3 (c). In contrast, by examining Figure 4.3 (b) and Figure 4.3 (c), it was noted that the difference in the pressure gradients of the waves generated by the $30°$, $45°$ and $60°$ driver sections, accounting for the different peak overpressures, were almost identical.

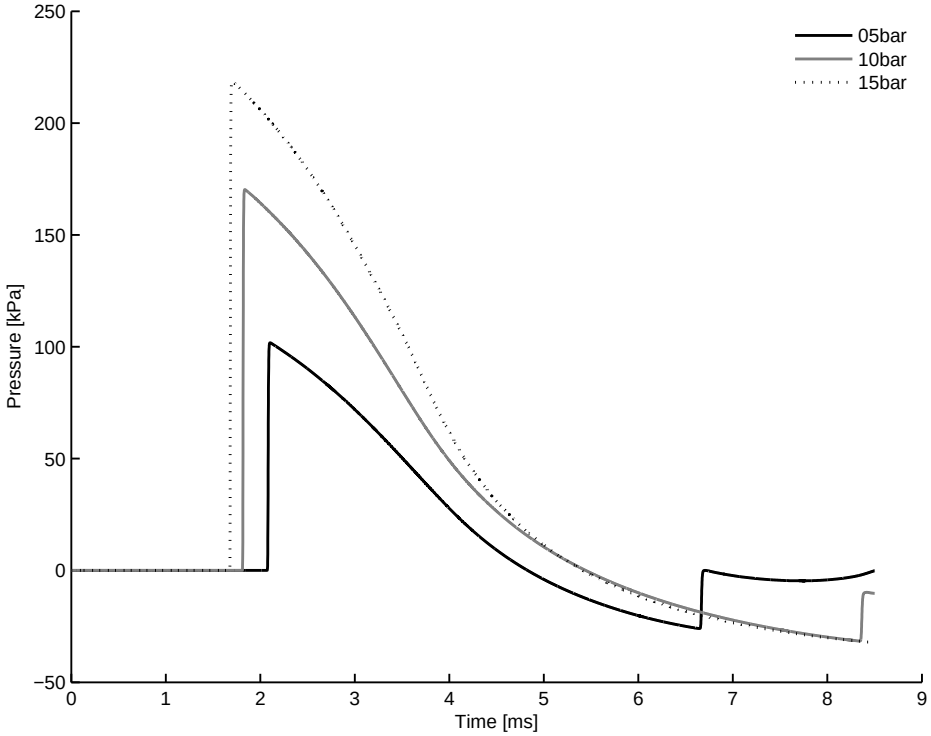
The effect of increasing the angle of divergence on the blast duration can clearly be seen in Figure 4.3 (a) and Figure 4.3 (b) in that an increase in divergence angle results in a reduced blast duration. On the other hand, the duration of the expansion phase of the blast wave decreases with increased divergence angle. It can be seen in Figure 4.3 (a), Figure 4.3 (b) and Figure 4.3 (c) that both the peak-overpressure and minimum expansion pressure of the blast wave decrease as the divergence angle of the driver section is increased. Figure 4.3 shows how the difference in the peak-overpressures and minimum expansions between the different drive sections changes as the blast wave travels down the tube.

By examining all of the sub-figures in Figure 4.3 it can seen that the time between the shock fronts increases with increasing distance down the tube. From this it can be deduced that the velocity of the blast wave is adversely effected by increasing the driver section divergence, in that the velocity of the blast wave reduces more rapidly as the wave propagates through the expansion section. It can also be seen by looking at Figure 4.3 that the rate at which the peak-overpressure of the blast wave deteriorates is greater for the larger divergence angles. Both of these observations imply that the energy of the blast wave reduces with increased divergence angle.

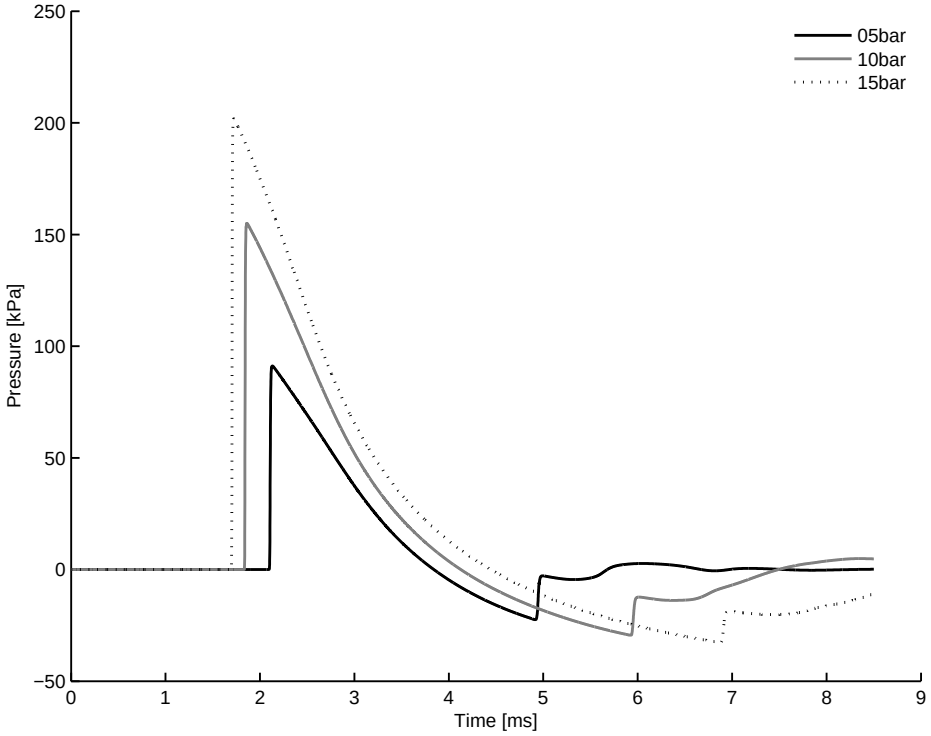
Depicted in Figure 4.4 are plots of the pressures measured at a point along the centre line of the blast tube, $1.00m$ from the diaphragm, for all the linearly diverging sections having driver pressures of $5bar$, $10bar$ and $15bar$. Due to their being in the range of typical experimental driver pressures, these three driver pressures where chosen for numerical analysis.



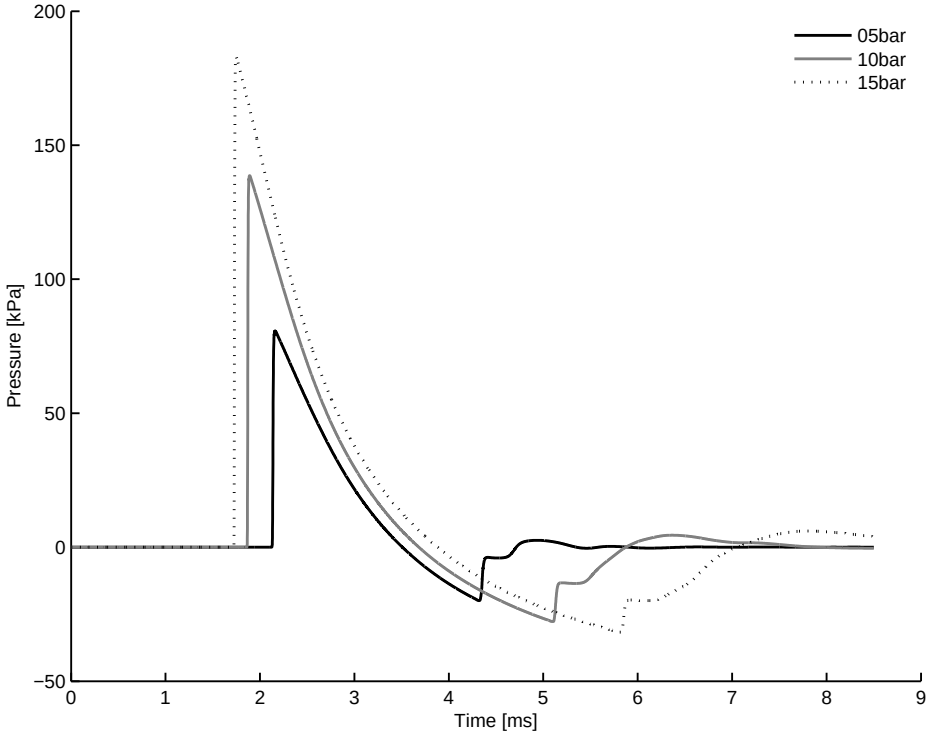
4.4 (a): $7,5°$


05bar
10bar
15bar
Pressure [kPa]
Time [ms]
250
200
150
100
50
0
−50
0
1
2
3
4
5
6
7
8
9

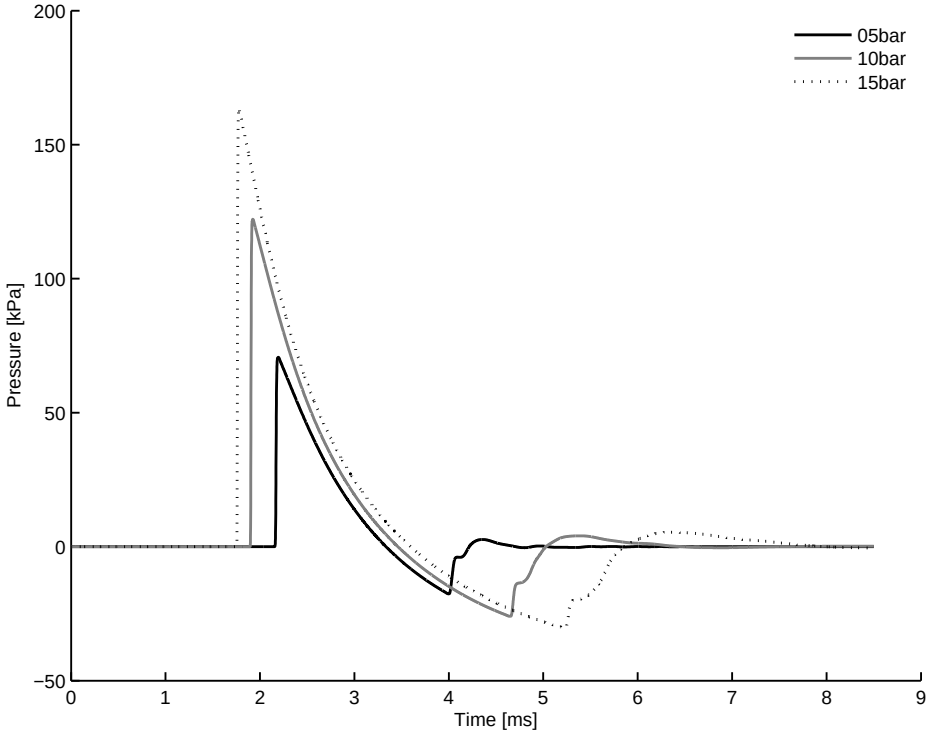
4.4 (b): 15°


05bar
10bar
15bar
Pressure [kPa]
Time [ms]
250
200
150
100
50
0
−50
0
1
2
3
4
5
6
7
8
9

4.4 (c): 30°



4.4 (d): 45°



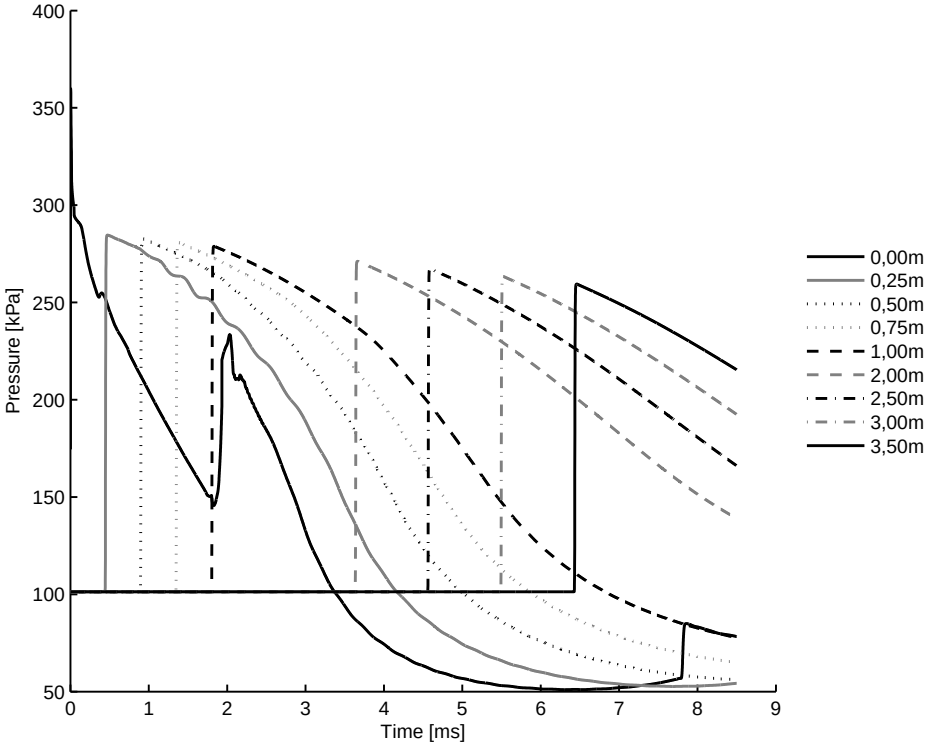
4.4 (e): 60°

Figure 4.4: The Effect of Driver Pressure on Pressure

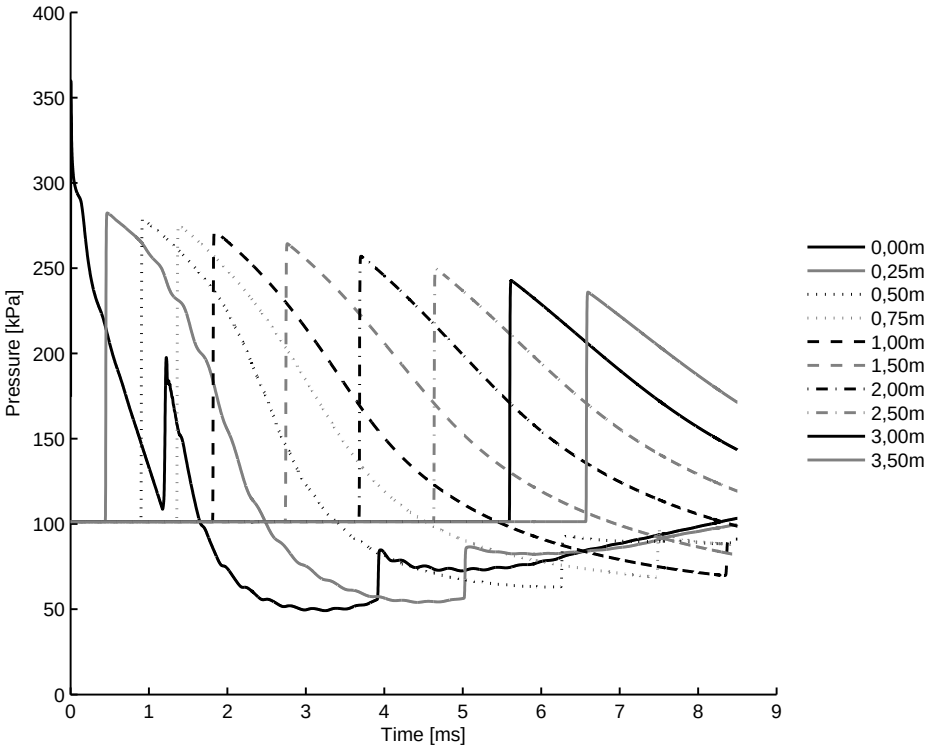
It can be seen in Figure 4.4 that the effects of the varying the driver pressure is much the same for all five driver sections. By examining all the sub-figures in Figure 4.4 it can be observed that the shock fronts induced by the higher driver pressures precede the shock fronts generated by the lower driver pressures. This indicates that the higher the driver pressure that is used, the greater the velocity of the shock front. Another effect of driver pressure on the generated shock wave, as shown in Figure 4.4, is that the higher the driver pressure used, the greater the peak-overpressure of the shock. Both of these characteristics are similar to normal shocks however, using the normal shock equations it can be determined that the magnitude of the difference between the blast waves differs dramatically from the differences in velocity and overpressure arising in normal shocks generated by different driver pressures.

Figure 4.4 shows that increasing the driver pressure results in a steepening of the pressure trace trailing the shock front. This means that the strength of the expansions waves generated are greater for the higher driver pressures. The lower minimum pressure in the expansion phase for the higher driver pressures is also indicative of the strengthened expansion waves. By examining Figure 4.4 (a) and Figure 4.4 (c) it can be seen that the larger driver pressures also result in the expansion waves reaching the shock faster than the cases with the lower driver pressures. Looking at Figure 4.4 it is shown that the duration of both the blast wave and the expansion phase are lengthened as the driver pressure is increased.

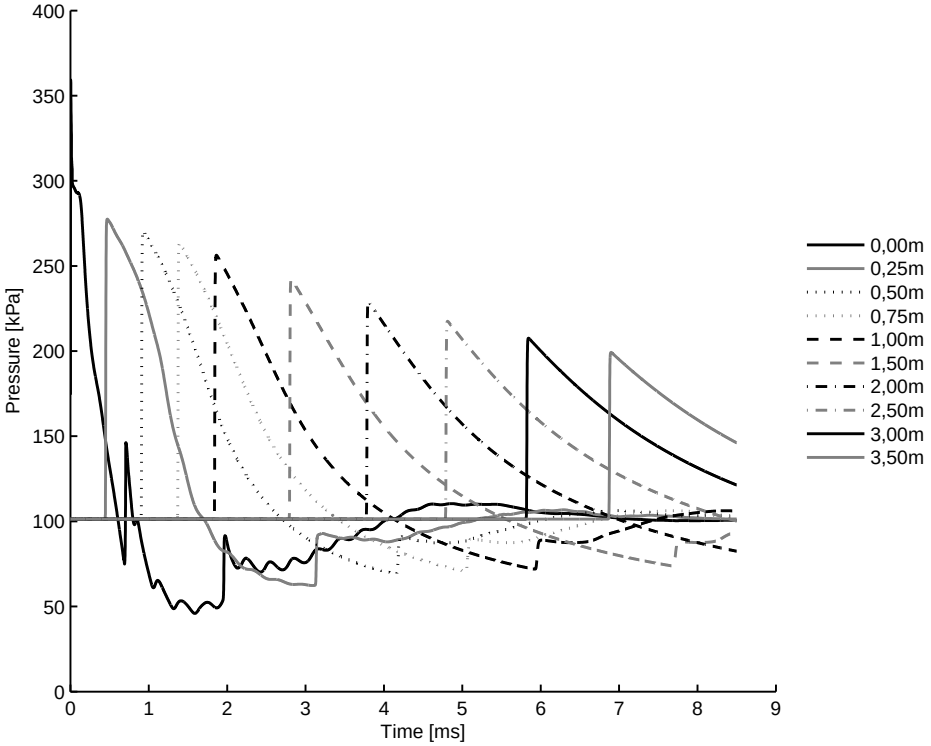
Figure 4.5 displays the pressures measured along the the centreline of the blast tube at distances of $0.00m$, $0.25m$, $0.50m$, $0.75m$, $1,00m$, $1,50m$, $2,00m$, $2,50m$, $3,00m$ and $3,50m$ from the diaphragm. It is important to note that some of the sub-figures in Figure 4.5 are missing some of the measurements due to them being corrupted. The pressure traces measured at $0.00m$ are of an oscillatory nature as the monitor was located at the location of the diaphragm and mesh interface.



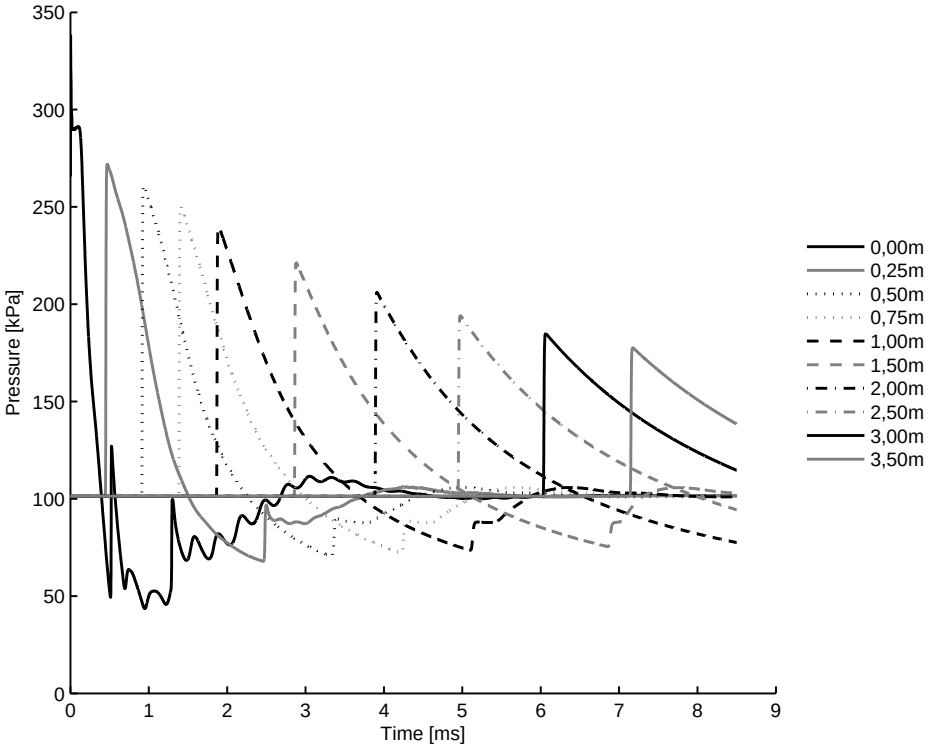
4.5 (a): $7,5°$ $10bar$



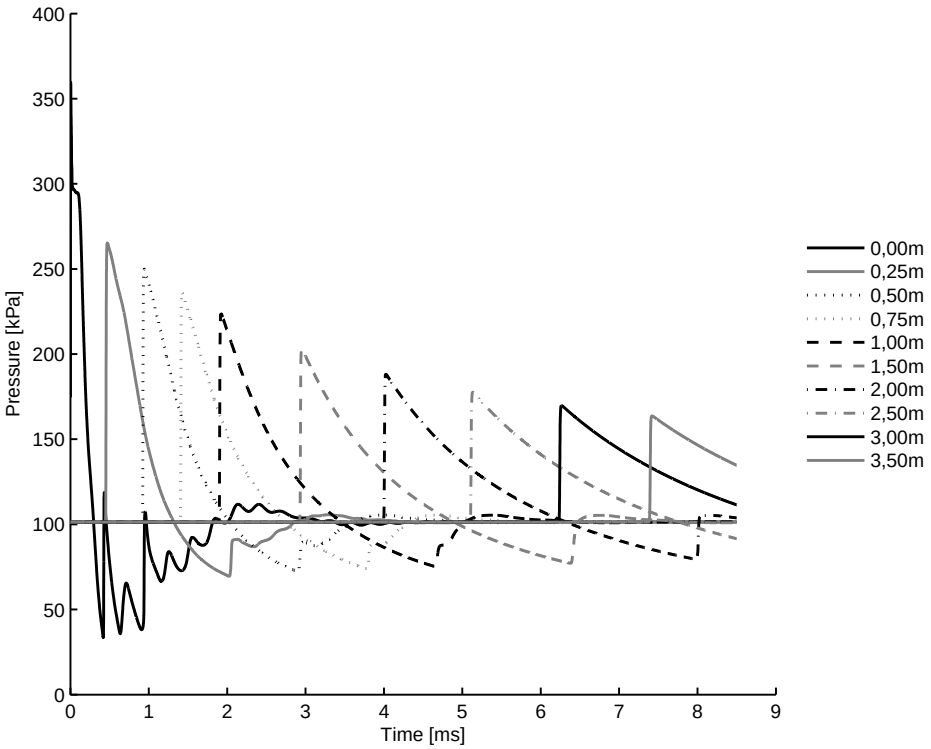
4.5 (b): $15°$ $10bar$



4.5 (c): 30° 10*bar*



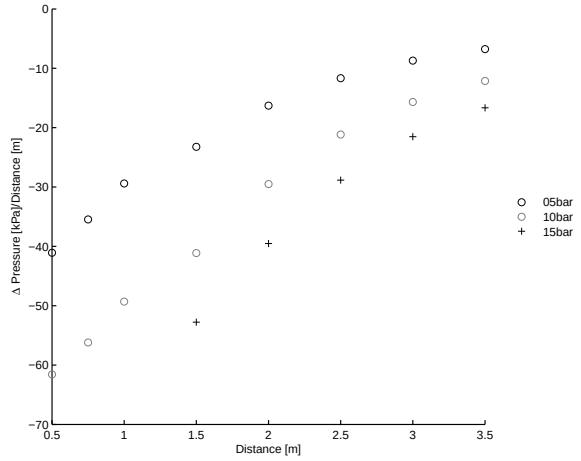
4.5 (d): 45° 10*bar*



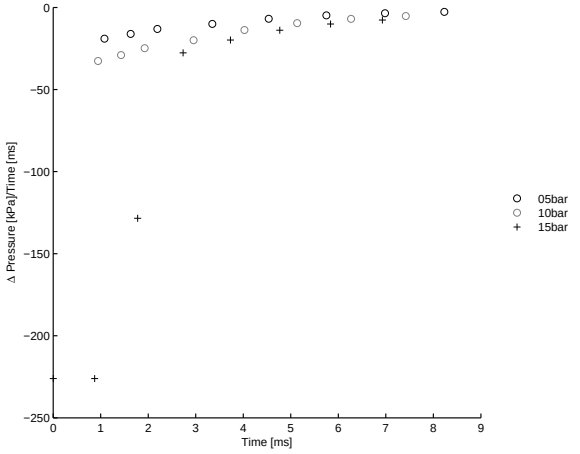
4.5 (e): 60° 10*bar*

Figure 4.5: The Effect of Expansion Section Length on Pressure

Looking at Figure 4.5 it can be seen that for all the linearly diverging driver sections, the peak overpressure of the blast wave decays as the shock front propagates down the tube. What is interesting to note however, by comparing the pressure plots in Figure 4.5 (a), Figure 4.5 (c) and Figure 4.5 (e), is that the rate of decay accelerates as the angle of divergence of the driver section is increased. As shown in Figure 4.5, not only the peak overpressure decays with distance but the magnitude of the minimum pressure also reduces with distance. Another effect distance has on the blast wave is to increase the durations of both the overpressure and expansion phases as the shock front travels further from the burst diaphragm. The last notable effect of distance on the blast wave is the gradient or rate of the decrease in pressure behind the shock front becomes more gradual with increasing distance from the diaphragm. Figure 4.6 shows how increasing the driver pressure initially increases the magnitude of the rate at which the peak overpressure decays with regards to distance and time over the length of the tube. However as the blast wave propagates down the tube, regardless of the driver pressure used, the rate of overpressure decay tends to the same rate. Increasing the angle of divergence of the driver section also increases the rate of of overpressure decay, initially, as can be seen in Figure 4.7, before tending to a similar rate of decay for all the driver sections.

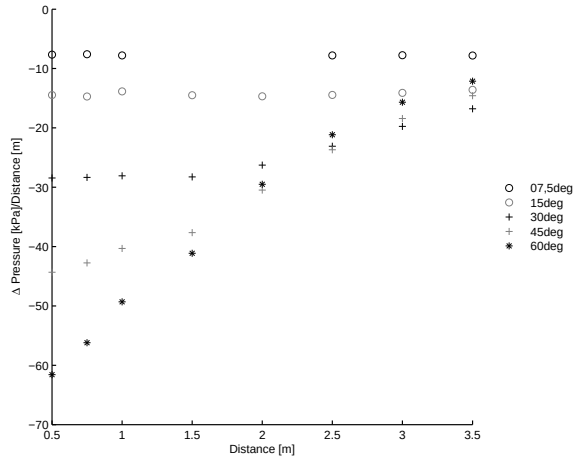


4.6 (a): Rate of Change of Peak Overpressure with Regards to Distance

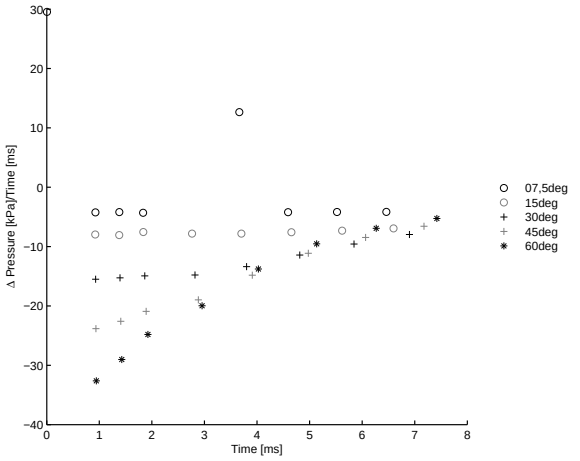


4.6 (b): Rate of Change of Peak Overpressure with Regards to Time

Figure 4.6: Effects of Driver Pressure on Rate of Change of Peak Overpressure for 60° Driver Section



4.7 (a): Rate of Change of Peak Overpressure with Regards to Distance for Diverging Driver Sections

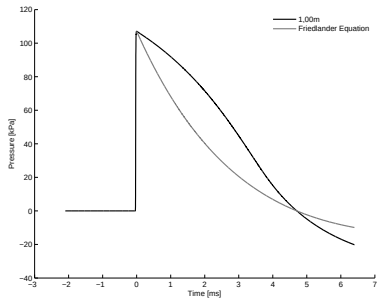


4.7 (b): Rate of Change of Peak Overpressure with Regards to Time for Diverging Driver Sections

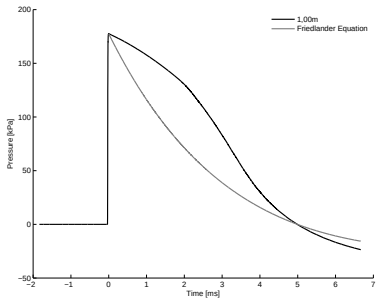
Figure 4.7: Effects of Driver Divergence Angle on Rate of Change of Peak Overpressure

Figure 4.8 shows the blast profiles generate by the linearly diverging driver sections having diverging angles of $7,5°$, $15°$, $30°$, $45°$ and $60°$, and at driver pressures of $5bar$, $10bar$ and $15bar$. On the same plots are the comparative Friedlander profiles for the same peak overpressures and blast durations. The pressure traces plotted in Figure 4.8 were generated by pressure readings taken by monitors located at $1.00m$ from the diaphragm in each blast tube configuration. Looking at Figure 4.8 it can be seen that both increasing the angle of divergence of the driver section as well as increasing the driver pressure both make the decay in the overpressure following the shock front more exponential, which in turn makes the

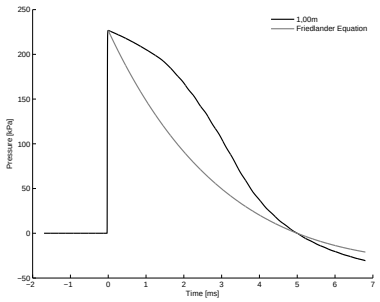
pressure profiles correspond better to the the Friedlander blast profile. Looking at Figure 4.8 (k), Figure 4.8 (l), Figure 4.8 (n) and Figure 4.8 (o) it can be seen that the the best blast profiles were generated by the the 45° and 60° driver sections at high driver pressures as these profiles come closest to match the Friedlander blast profiles. It is important to note however, that upon closer inspection, it can be seen that there is still quite a disparity between the generated blast profiles and comparative Friedlander blast profiles particularly at the middle of the overpressure decay and the expansion phase. By looking at Figure 4.5 above it can also be seen that the profile of the blast wave changes as it propagates down the tube, so although the blast profiles generated in the four above mentioned cases are reasonably good at $1.00m$, at further distances the quality of the blast wave is not as satisfactory.



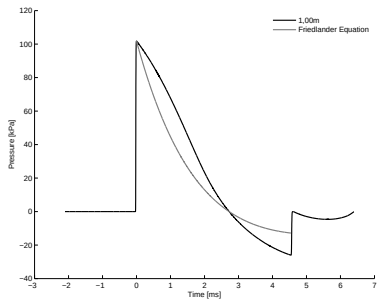
4.8 (a): $7,5°$ $5bar$



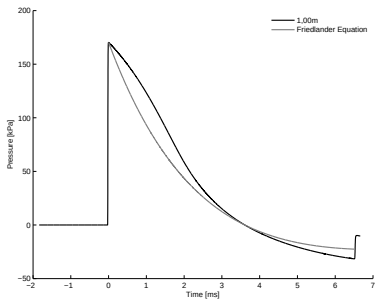
4.8 (b): $7,5°$ $10bar$



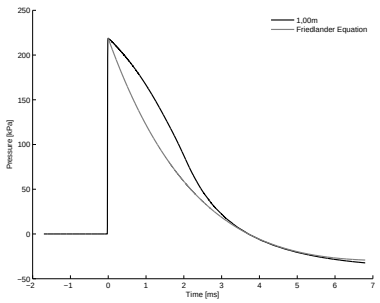
4.8 (c): $7,5°$ $15bar$



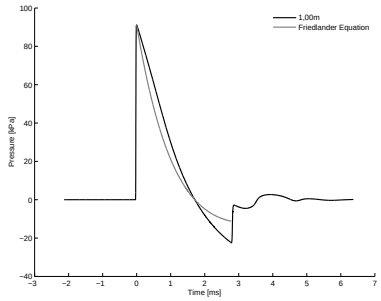
4.8 (d): $15°$ $5bar$



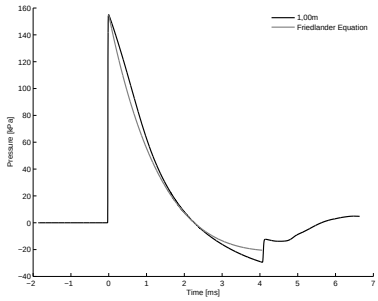
4.8 (e): $15°$ $10bar$



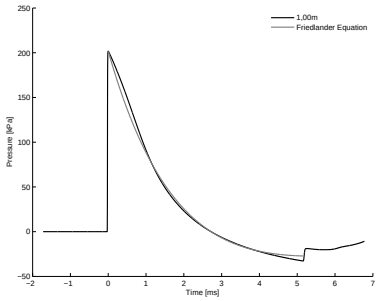
4.8 (f): $15°$ $15bar$



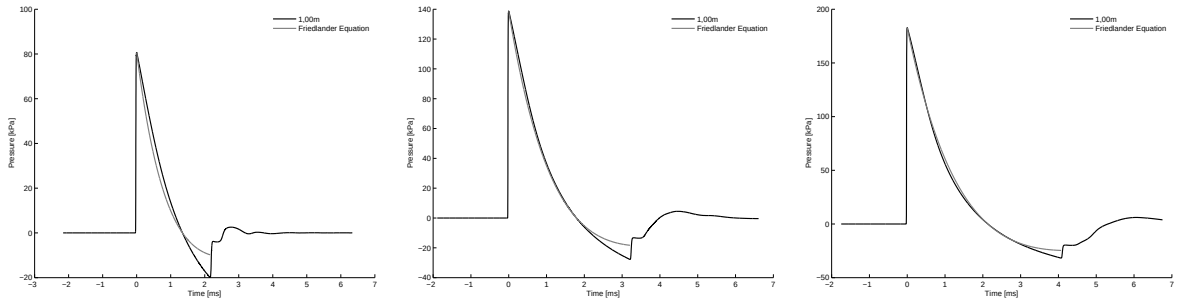
4.8 (g): $30°$ $5bar$



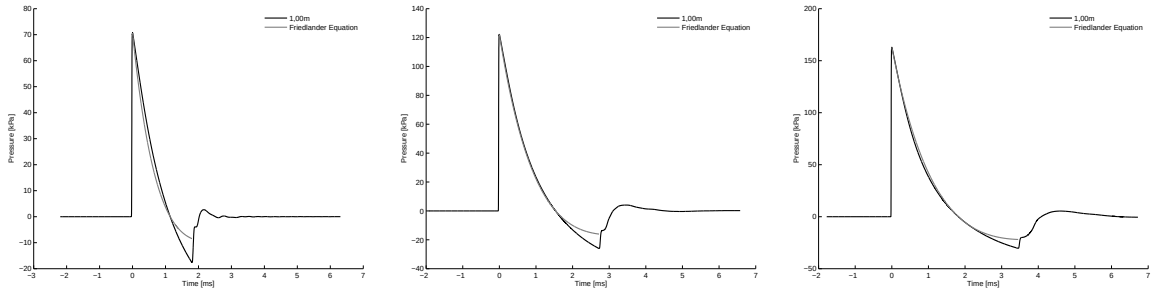
4.8 (h): $30°$ $10bar$



4.8 (i): $30°$ $15bar$



4.8 (j): 45° 5*bar* 4.8 (k): 45° 10*bar* 4.8 (l): 45° 15*bar*



4.8 (m): 60° 5*bar* 4.8 (n): 60° 10*bar* 4.8 (o): 60° 15*bar*

Figure 4.8: Comparing the Effect of Driver Shape and Pressure on Friedlander Pressure Profile

Although the effects of driver divergence angle, driver pressure, travel time and distance on the generated profile have been discussed, the flow features and causes of said effects have not. Looking at the x-t diagrams below in combination with the above pressure plots, an attempt will be made to explain the flow characteristics occurring in the blast tube and the resulting effects on the generated blast profiles. Some of the flow features that will be discussed here were already covered in more detail in section 2.9.

Figure 4.9 shows the variation in pressure along the length of the blast tube for the duration of the simulation. Looking at the bottom left hand corner it can be seen that the initial state of the tube is such that the driver section has a pressure of 10bar, indicated by the dark red, while the expansion section is set to an atmospheric pressure of 101.325kPa, shown in blue. The membrane located at 0.00m then bursts, causing a shock wave to propagate into the expansion section and an expansion wave to travel into the driver section. This can be seen in Figure 4.9, Figure 4.10, Figure 4.11 and Figure 4.12 by the increasing pressure, density, temperature and velocity of the air in the expansion section and the opposite occurring to the air in the driver section.

As the expansion wave travels further into the driver section, the expansion waves reflect off the diverging driver walls and propagate into the the expansion section, reducing the

properties of the air that were raised by the traversing shock wave. This is shown in Figure 4.9 and Figure 4.10 by the darkening of the lighter shade of blue, while in Figure 4.11 and Figure 4.12 it is indicated by the lightening of the darker shade of red behind the shock front. By examining Figure 4.9 it can be deduced that a key difference that altering the angle of divergence makes to the development of the blast wave profile is the extent and rate of the expansion wave reflection that takes place. This can be deduced by inspecting the bands of darkening blue behind the shock wave in Figure 4.9 and Figure 4.10. As the angle of divergence of the driver section is increased, the width of the darkening blue bands decreases and the time it takes the bands to reach the shock front reduces implying that an increase in the angle of driver divergence causes an increase in the rate and magnitude of the reflection of the expansion wave. This in turn will effect the peak overpressure of the blast wave, the rate of decay of the overpressure following the shock front, the blast duration and the minimum pressure in the expansion phase.

Examining the bottom left-hand corner of Figure 4.9, Figure 4.10 and Figure 4.11 it can be seen that there is a line originating at $0.00m$ and $0.00ms$ which tends towards the end of the driver section cubically with time. That line indicates the end of the expansion waves and the beginning of the air effected by the shock wave. Behind or to the left of this line there is a region of darkening blue with time which indicates a lowering in the pressure, density and temperature of the air in this region of the blast tube with time. This is indicative of the expansion wave focusing that takes place due to the linearly diverging nature of the driver section and the expansion wave reflection it induces. It is interesting to note that for all the driver sections, the focusing is so intense it induces a near vacuum at the corner at the rear of the driver section at peak focusing, and the reduction in pressure is so high as to suck the terminal expansion towards the rear corner resulting in ever intensifying expansion focusing. It can be observed by the shortening of this region for increasing divergence angle that increasing the divergence angle of the driver reduces the time it takes for the expansion wave to fully focus. This reduces the time it takes for the blast wave to reach a minimum pressure as well as the magnitude of said minimum pressure.

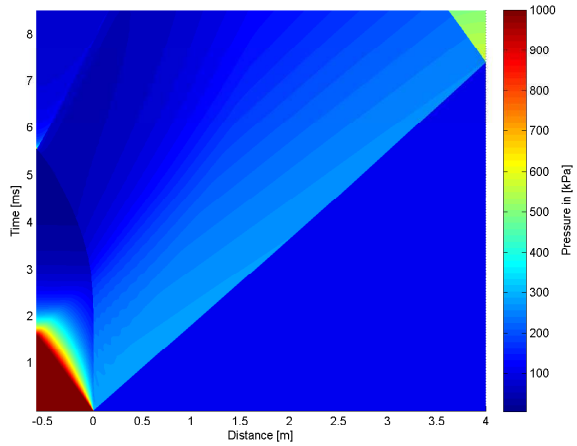
The actual point and moment of expansion focusing is indicated in Figure 4.9, 4.10 and 4.11 by a point directly proceeding the sudden increase in the fluid properties at the back end of the driver section. This point and moment of peak focusing is also marked by a shock wave that emanates from it, as shown in the figures by a straight line trailed by increasing fluid properties, originating at the end of the above mentioned cubic line. The formation of the secondary shock is testament to the intense nature of the focusing that occurs at the end corner as the shock formation is the only means by which the flow can equilibrate. Since increasing the divergence angle reduces the time to peak focusing , increasing the divergence angle of the driver section also reduces the time it takes for the secondary shock to form and

to propagate down the the tube. This is the primary cause for the reduction in the duration of the expansion phase with increasing divergence angle.

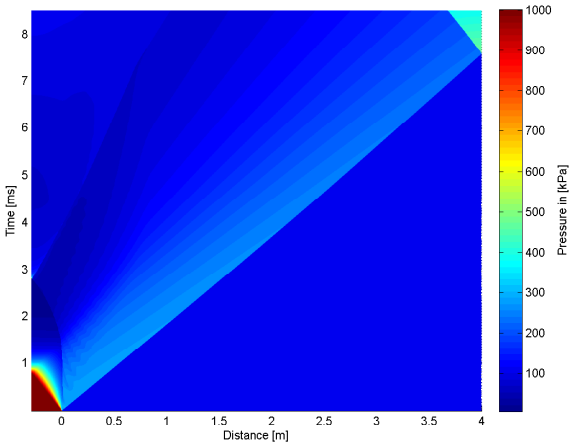
The contact surface that is formed by bursting the diaphragm can be observed in Figure 4.10 and Figure 4.11 but not in Figure 4.9 and Figure 4.12, as the pressure and velocity of the gas on either side of the contact surface are equal. In the Figure 4.10 and Figure 4.11, the contact surface is depicted by the curved line emanating from $0.00m$ and $0.00ms$. The line is trailed by a marked increase in fluid density and a decrease in the temperature of the fluid. The contact surface effects the development of the blast profile in two key ways. The first effect is the reduction in the velocity of the reflected expansions which occurs as the expansion waves pass through the contact surface. This slowing down of the reflected expansion waves can be observed by the increased slope of the colour bands to the left of the contact surface in sub-figures Figure 4.9 (b), Figure 4.10 (b), Figure 4.11 (b) and Figure 4.12 (b). By re-looking at Figure 4.5 it can be deduced that the reduction in the velocity of the reflected expansion waves, reduces the rate at which the pressure decays behind the shock with regards to both time and distance for measurements taken at locations upstream of the contact surface. The cause of the reduced rate of decay downstream of the contact surface is the velocity of the shock being greater than the expansion waves resulting in the shock wave moving further away from the reflect expansion waves as both move down the tube. This is shown in sub-figures in x-t diagrams by the widening of the colour bands behind the shock wave the further both travel down the tube. The second effect of contact surface on the flow is the interaction it has with the secondary shock wave. Just as with the case of the reflected expansion waves, the secondary shock slows before passing through the contact surface. Again this can be deduced by the distinctive kink that occurs in the line delineating the location of the secondary shock with time and distance, at the point where the line intersects with the contact surface. This slowing down of the secondary shock causes the the duration of the expansion phase, for pressure measurements taken upstream of the contact surface, to increase as the shock propagates down the length of the blast tube. The interaction of the secondary shock and the contact surface, in conjunction with the near vacuum formed in the driver section, stops the contact surface from propagating any further along the tube. This can be seen by the vertical line on the left hand side of the sub-figures in the x-t diagrams. By analysing the x-t diagrams it can be seen that the smaller the divergence angle of the driver, the further down the blast tube the contact surface propagates, resulting in the contact surface have a greater influence on the formation of the blast wave.

In normal shock tube relations the velocity of the shock wave is determined by the pressure ratio, that is ratio of the driver pressure to the expansion section pressure. Looking at the x-t diagrams it can be seen that despite having the same driver pressure of $10bar$ for each driver section, the velocity of the shock wave generated by each driver section is different. This

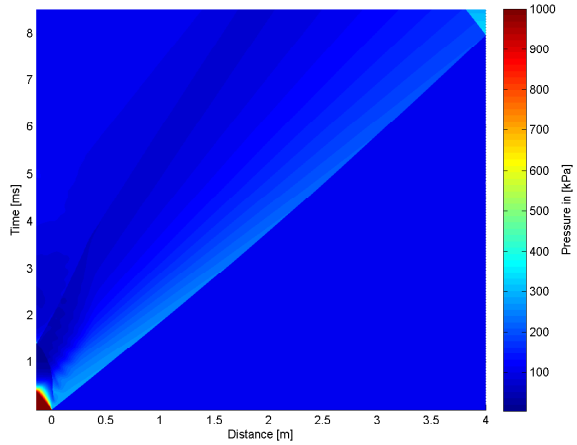
difference in shock velocity for increasing diverging angle is shown in the x-t diagrams by the increased slope, relative to the horizontal axis, of the shock wave line as well as the shock wave reflecting off the end of the expansion section later. This is as a result of the increased rate and magnitude at which the expansion waves reflect, and thereby catch up the shock with increase divergence angle, which reduces the maximum overpressure and velocity of the shock front. This is shown in Figure 4.9 by the darkening blue bands and in Figure 4.12 by the lightening red bands, touching the shock wave earlier and closer to the diaphragm location with increasing divergence angle.



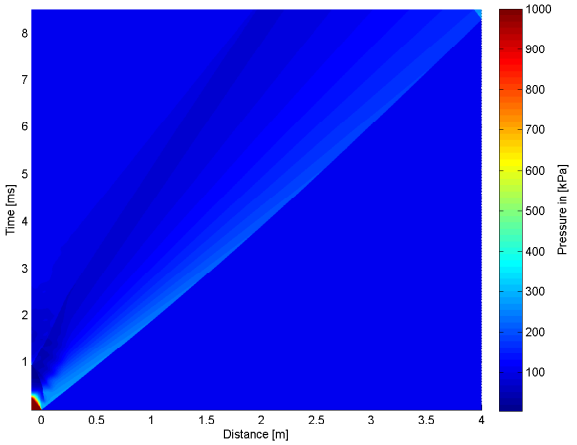
4.9 (a): 07.5° 10*bar*



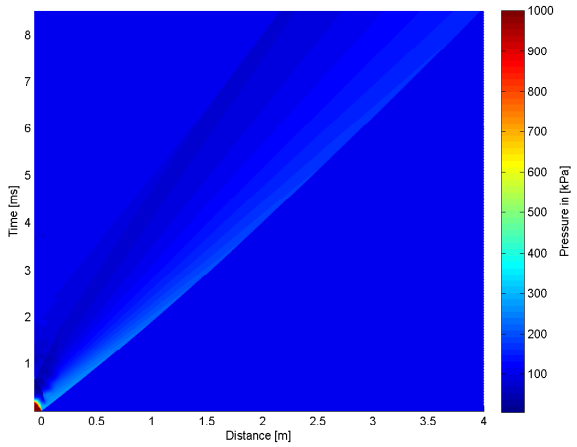
4.9 (b): 15° 10*bar*



4.9 (c): 30° 10*bar*

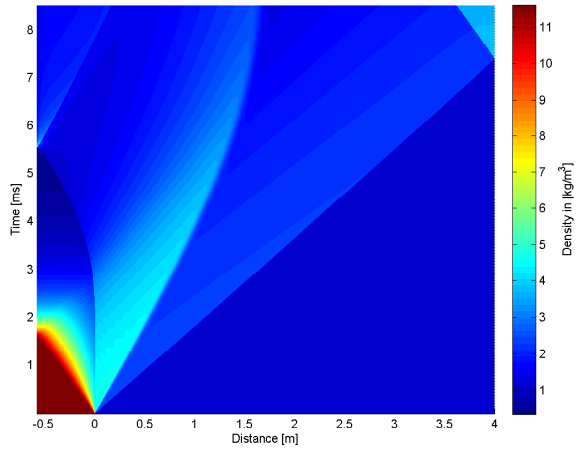


4.9 (d): 45° 10*bar*

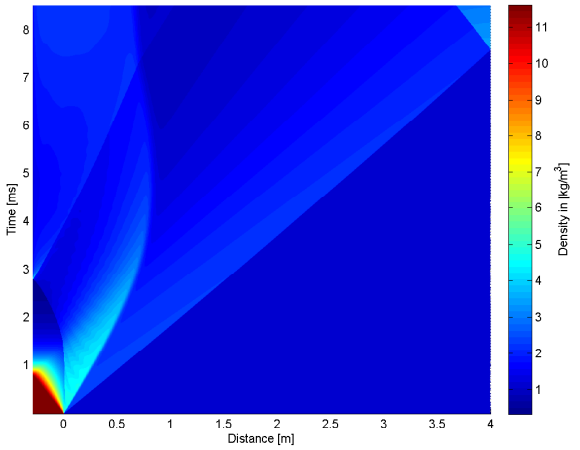


4.9 (e): 60° 10*bar*

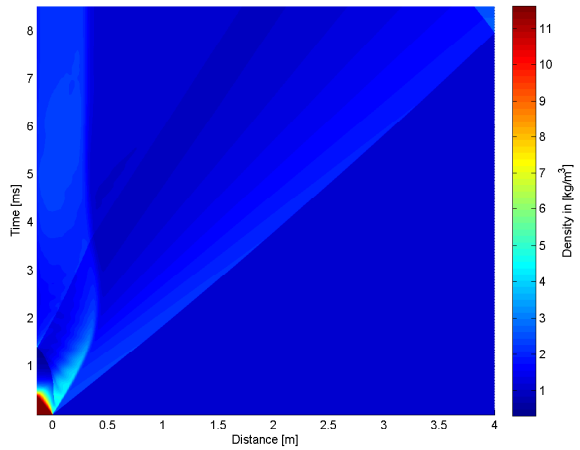
Figure 4.9: X-T Diagram for Linearly Diverging Driver Sections (Pressure)



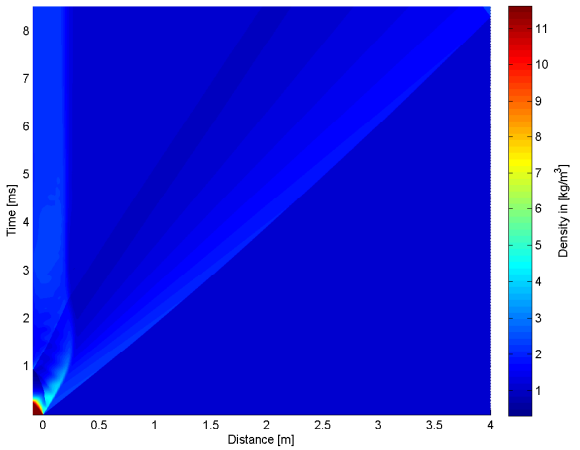
4.10 (a): 07.5° 10*bar*



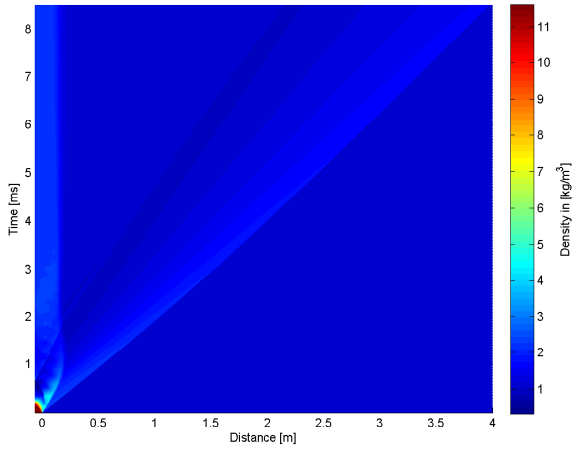
4.10 (b): 15° 10*bar*



4.10 (c): 30° 10*bar*

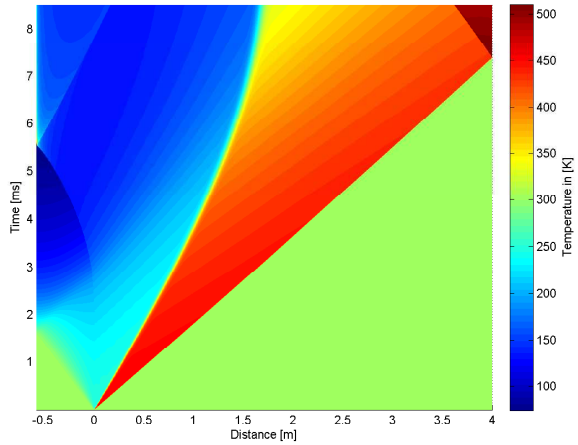


4.10 (d): 45° 10*bar*

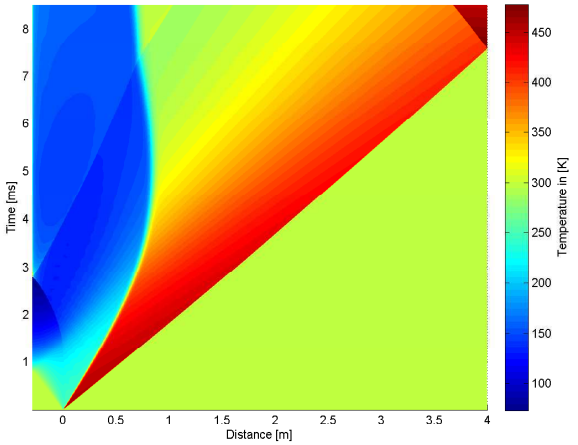


4.10 (e): 60° 10*bar*

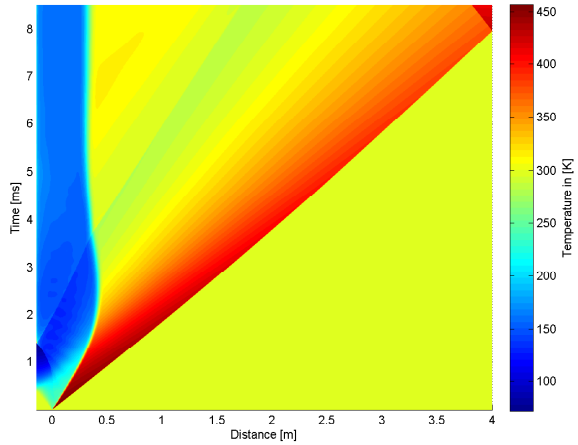
Figure 4.10: X-T Diagram for Linearly Diverging Driver Sections (Density)



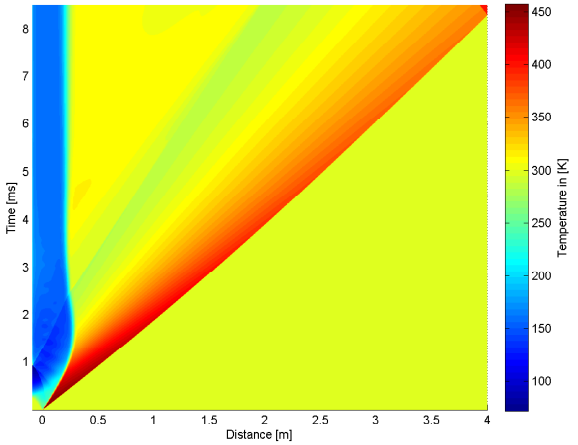
4.11 (a): 07.5° 10*bar*



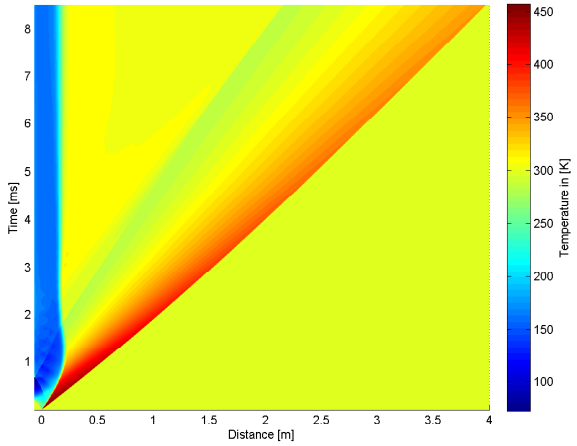
4.11 (b): 15° 10*bar*



4.11 (c): 30° 10*bar*

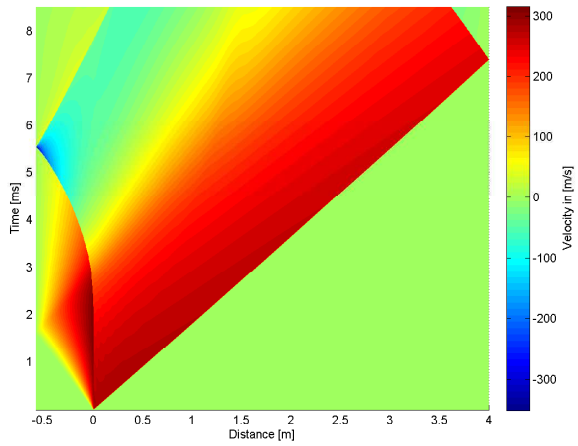


4.11 (d): 45° 10*bar*

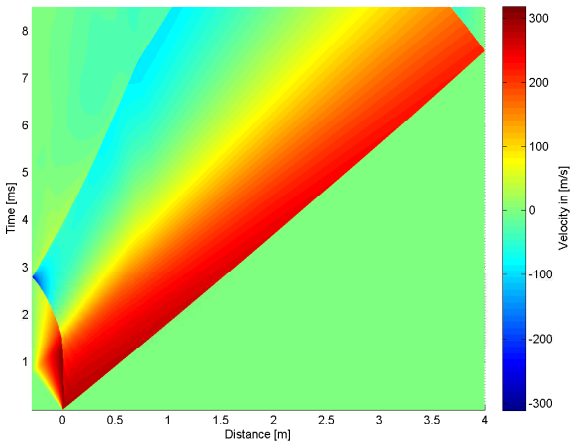


4.11 (e): 60° 10*bar*

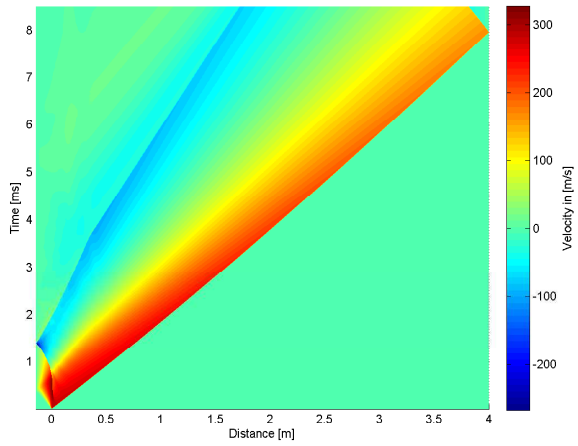
Figure 4.11: X-T Diagram for Linearly Diverging Driver Sections (Temperature)



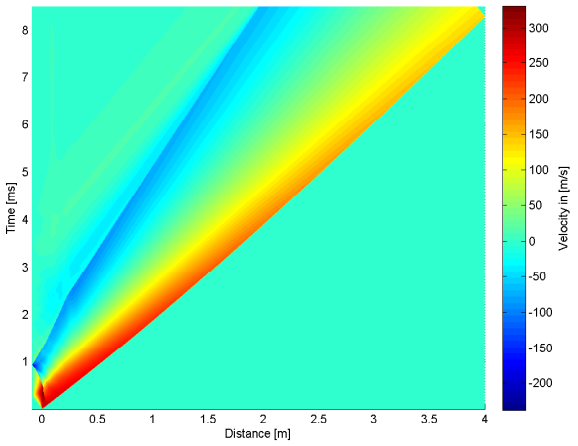
4.12 (a): 07.5° 10*bar*



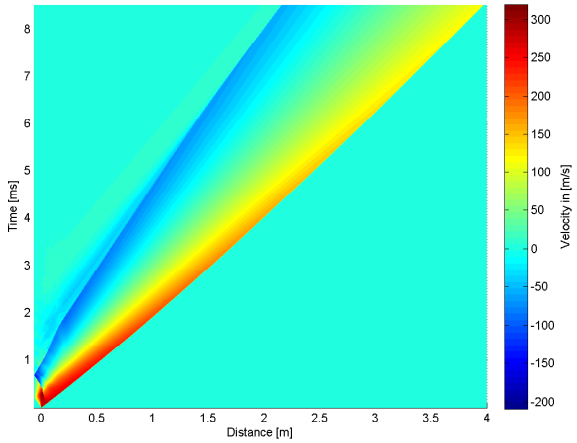
4.12 (b): 15° 10*bar*



4.12 (c): 30° 10*bar*



4.12 (d): 45° 10*bar*



4.12 (e): 60° 10*bar*

Figure 4.12: X-T Diagram for Linearly Diverging Driver Sections (Velocity)

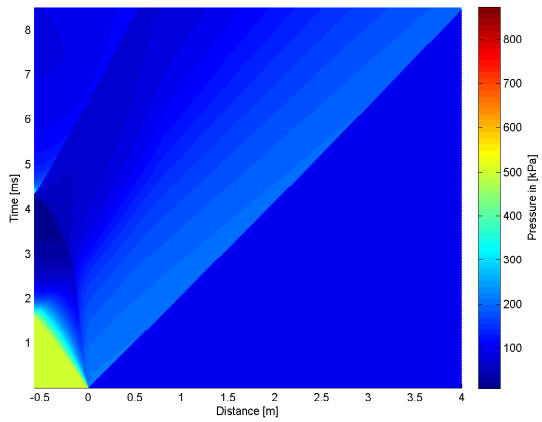
Figure 4.13, Figure 4.14, Figure 4.15 and Figure 4.16 are the x-t diagrams produced by the simulations run for the driver sections having 7.5*deg* and 60*deg* divergence angles at two different driver pressures, namely 5*bar* and 15*bar*. Examination of these x-t diagrams in combination with the x-t diagrams above can be used to assess and explain what effect decreasing and increasing the driver pressure has on the flow and how these effects affect the formation of the blast wave pressure profile.

By observing that the slope of the shock front relative to the horizontal axis has increased in Figure 4.13 and Figure 4.14, while in Figure 4.15 and Figure 4.16 the slope has decreased, it can be ascertained that increasing the driver pressure increases the velocity of the shock front. The first reason for this, is the normal shock relations state that an increase in the ratio between the driver section pressure and the pressure in the expansion section results in a shock of greater velocity. The second reason for the increase in shock velocity with increased driver pressure, can be deduced by looking at the bottom left hand corner of the x-t diagrams and noting that for all three driver pressures the slope of the expansion waves travelling into the driver section are the same. This is to be expected as the temperature, and therefore the speed of sound, in the driver section is the same for all three driver pressures. This means that the speed at which the expansion waves travel into the driver section is the same for all three driver pressures. Consequently, the expansion waves will reflect and travel into the expansion section at the same speed for the three driver pressures but the intensity of the expansion waves will increase with increasing driver pressure. This means that it will take the expansion waves longer to reach the shock front, but when they do, the expansions will reduce the pressure behind the shock front more rapidly and to greater extent for larger driver pressures. This is corroborated by noting that the behind the shock fronts in Figure

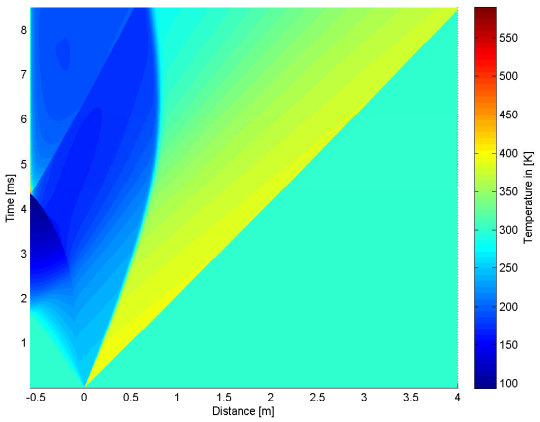
4.15 (a) and Figure 4.16 (a), there are an increased number of and darker shades of blue bands trailing the shock fronts than the shock fronts in Figure 4.13 (a) and Figure 4.14 (a).

Figure 4.13 and Figure 4.15 also show that increasing the driver pressure increases the time it takes for the expansion waves to focus and the secondary shock wave to form. This is because even though the expansion waves reduce the pressure of the gas by a greater percentage for the higher driver pressures, the pressure and density in the driver section after being expanded but before focusing is higher for the higher driver pressures as displayed in sub-figures 4.13 (a), 4.14 (a), 4.15 (a) and 4.16 (a). This means that more expansion focusing is required before the gas in the driver section is fully expanded and the secondary shock forms. The effect this has on the blast wave pressure profile is to increase the time between the primary and secondary shocks as well as to reduce the minimum pressure obtained in the expansion phase.

The last major effect increasing the driver pressure has on the flow features and the blast wave formation is the increasing distance the contact surface propagates down tube for increasing driver pressure. This effect was deduced by comparing the x-t diagrams in Figure 4.13 (b) and Figure 4.15 (b) as well as Figure 4.14 (b) and Figure 4.16 (b) . As discussed earlier, the contact surface slows the speed at which the reflected expansion waves travel into the expansion section due to the reduced temperature of the air behind the contact surface. This inevitably effects the formation of the blast profile as it increases the time it takes the expansion waves to reach the shock front as well as the distribution of the expansion waves trailing the shock front. The less a contact surface propagates down the expansion section, the more desirable, as the effects of the contact surface on the blast wave will be lessened.

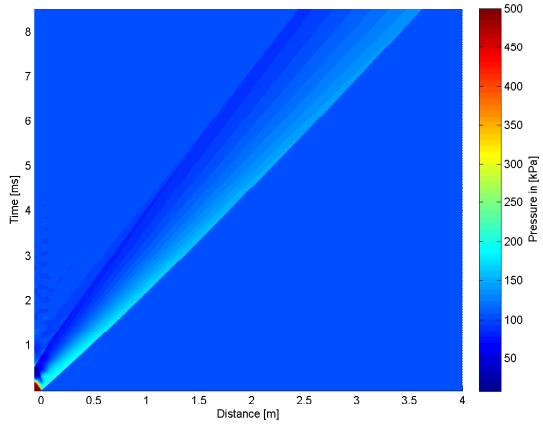


4.13 (a): 7.5° 5*bar* Pressure

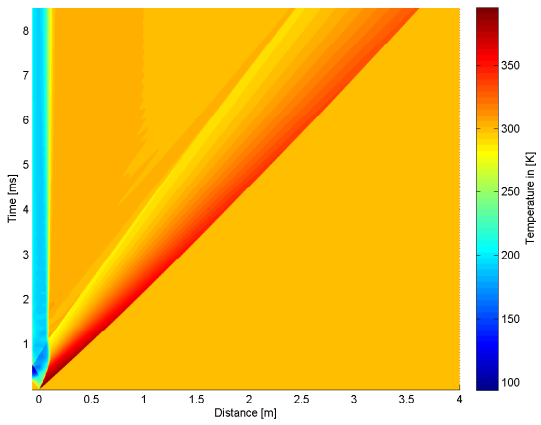


4.13 (b): 7.5° 5*bar* Temperature

Figure 4.13: X-T Diagram for 7.5° Linearly Diverging Driver Section at 5*bar*

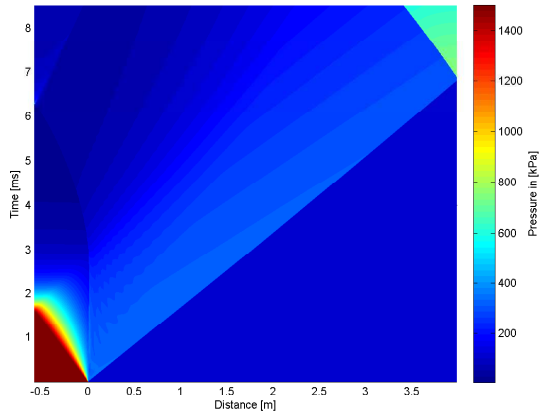


4.14 (a): 60° 5*bar* Pressure

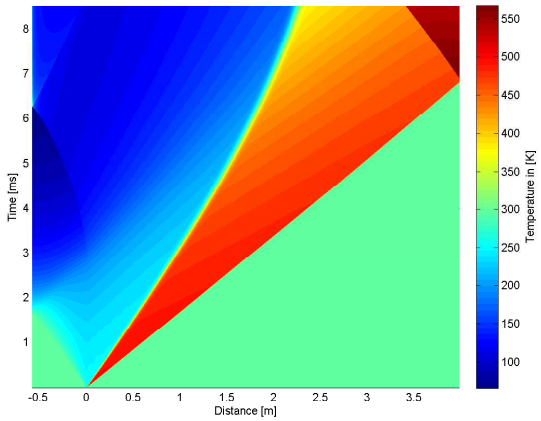


4.14 (b): 60° 5*bar* Temperature

Figure 4.14: X-T Diagram for 60° Linearly Diverging Driver Section at 5*bar*

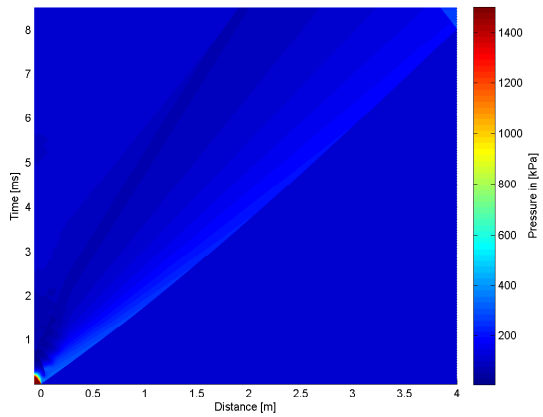


4.15 (a): 7.5° 15*bar* Pressure

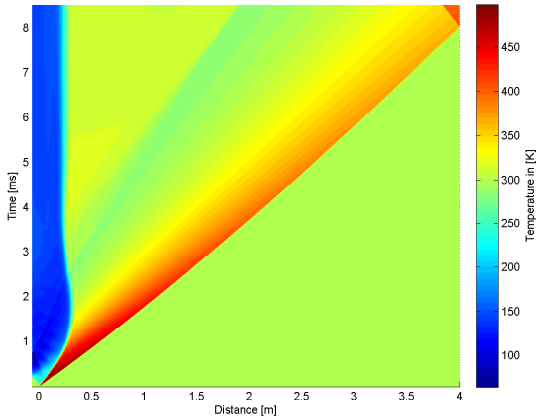


4.15 (b): 7.5° 15*bar* Temperature

Figure 4.15: X-T Diagram for 7.5° Linearly Diverging Driver Section at 15*bar*



4.16 (a): 60° 15*bar* Pressure



4.16 (b): 60° 15*bar* Temperature

Figure 4.16: X-T Diagram for 60° Linearly Diverging Driver Section at 15*bar*

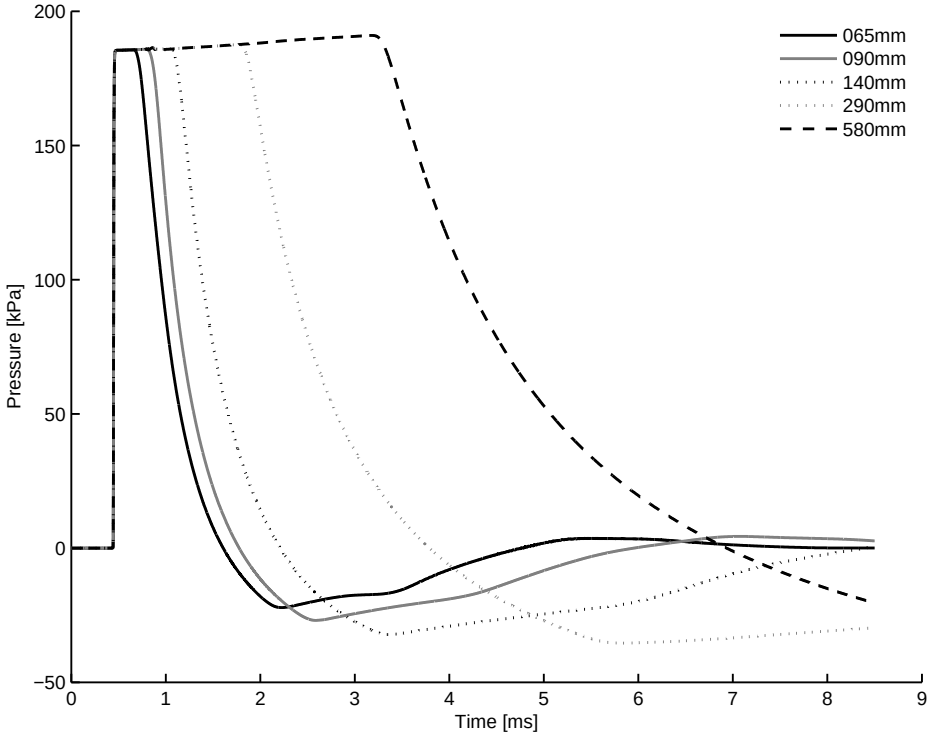
4.1.4 Straight Driver Sections

After analysing the linearly diverging driver sections and determining that none of the linear diverging driver configurations produced Friedlander blast profiles, it was decided that the next stage of the design process would be assessing what blast profiles are generated by shortened straight driver sections, as proposed by Ben-Dor and as are commonly used. The key feature of this analysis would be to make a direct comparison between the linearly diverging driver sections and straight drivers sections having comparative lengths, that is, 7.5° versus $580mm$, 15° versus $290mm$, 30° versus $140mm$, 45° versus $90mm$ and 60° versus $65mm$. The design analysis of the straight driver sections was performed in a similar manner to the linear diverging sections and so, in order to prevent repetition, only differences in the blast wave pressure profiles and flow features will be discussed in detail whereas commonalities between the two configurations will be stated as such and not discussed further. As with the linearly diverging driver sections, the explosive equivalent energy of the different straight driver section configurations was calculated and the results are listed in Table 4.2. By comparing Table 4.1 and Table 4.2 it can be determined that the straight driver section configurations have approximately double the equivalent explosive energy of the comparative linearly diverging driver section configurations. This is as a result of the straight drive sections having larger volumes than the comparative linearly diverging sections.

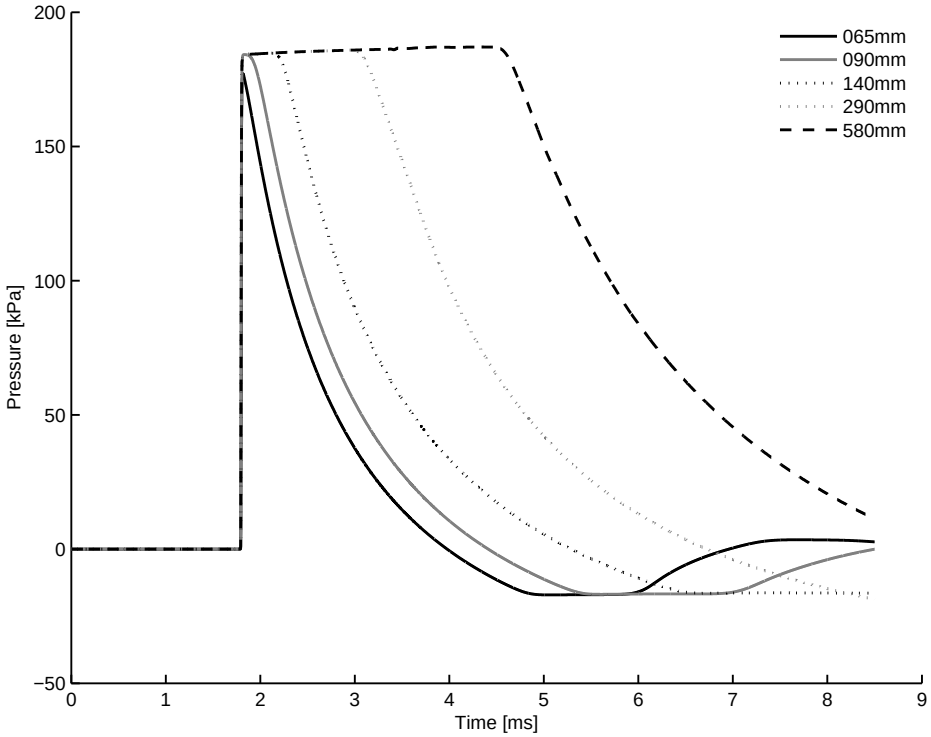
Table 4.2: Straight Driver Pressure TNT Explosive Equivalence

Driver Section Length	5 bar	10 bar	15 bar
$580mm$	$33.38g$	$87.30g$	$146.34g$
$290mm$	$16.69g$	$43.65g$	$73.17g$
$140mm$	$8.06g$	$21.07g$	$35.32g$
$90mm$	$5.18g$	$13.55g$	$22.71g$
$65mm$	$3.74g$	$9.78g$	$16.40g$

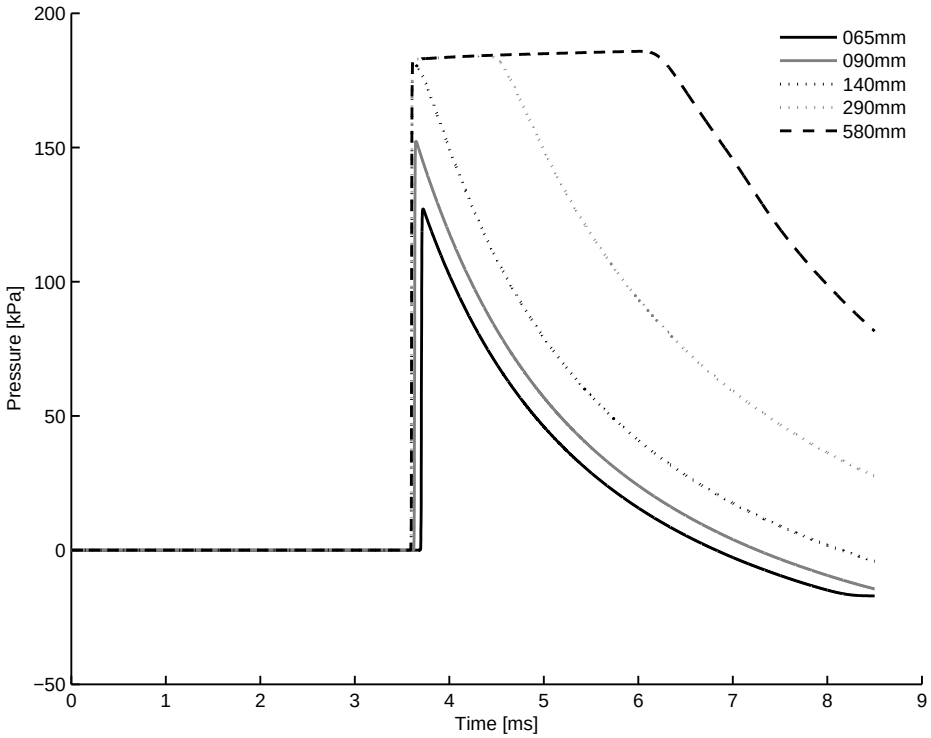
The pressure plots in Figure 4.17 illustrate the effect that the length of the driver section has on the development of the blast wave pressure profile. The pressure plots were generated by setting the driver pressure to $10bar$ for all 5 driver section lengths and placing monitors at $0.25m$, $1.00m$, $2.00m$ and $3.00m$ downstream from the diaphragm.



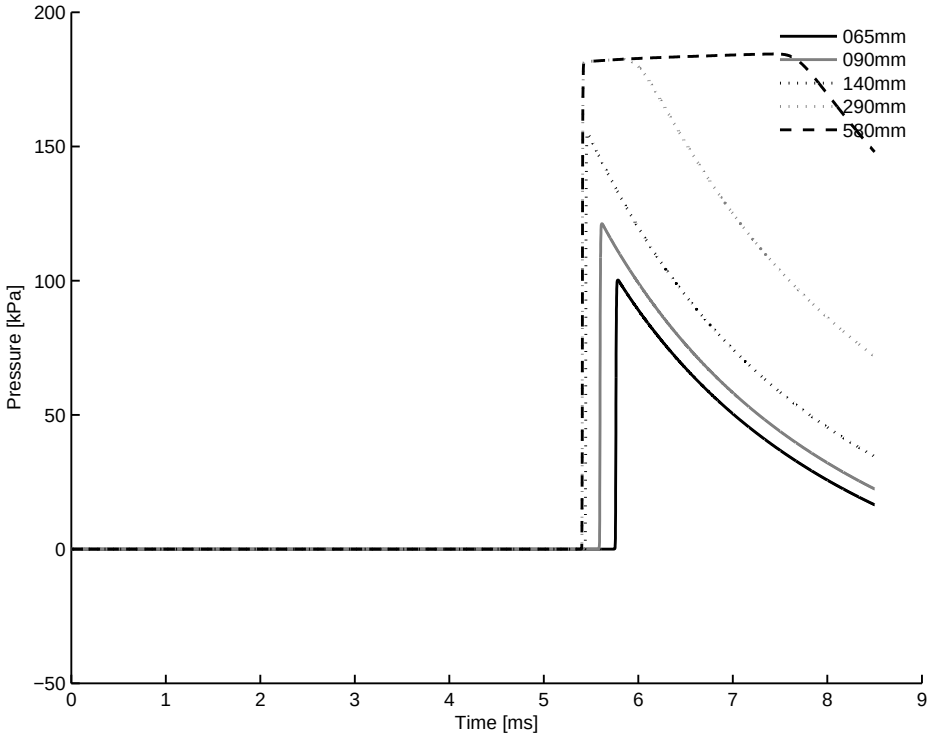
4.17 (a): $0.25m$



4.17 (b): $1.00m$



4.17 (c): $2.00m$



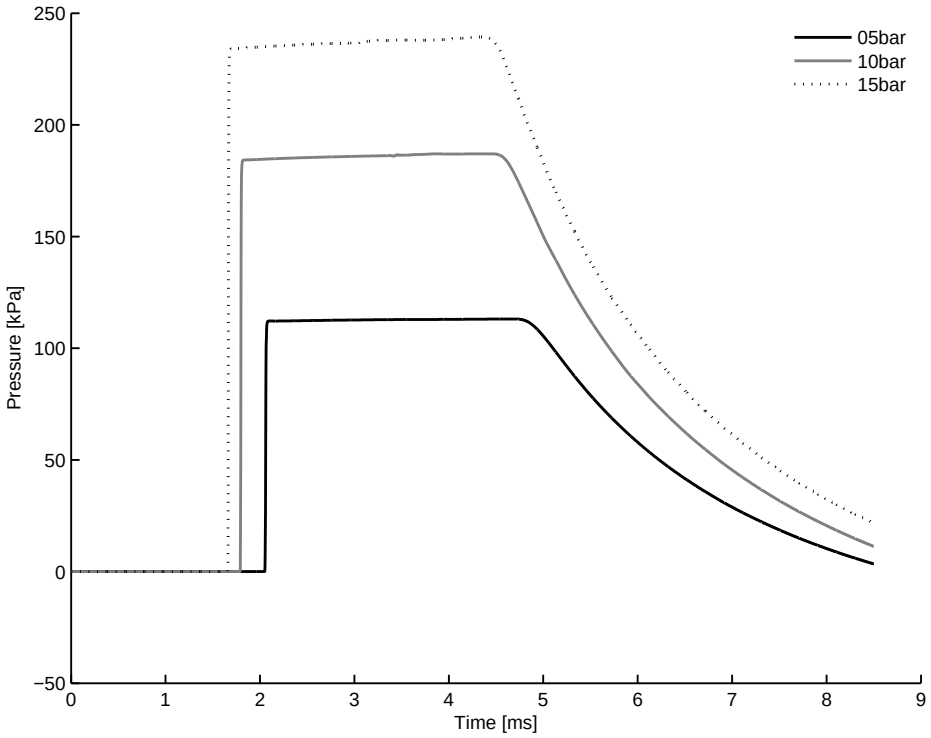
4.17 (d): $3.00m$

Figure 4.17: The Effect of Driver Length on Pressure

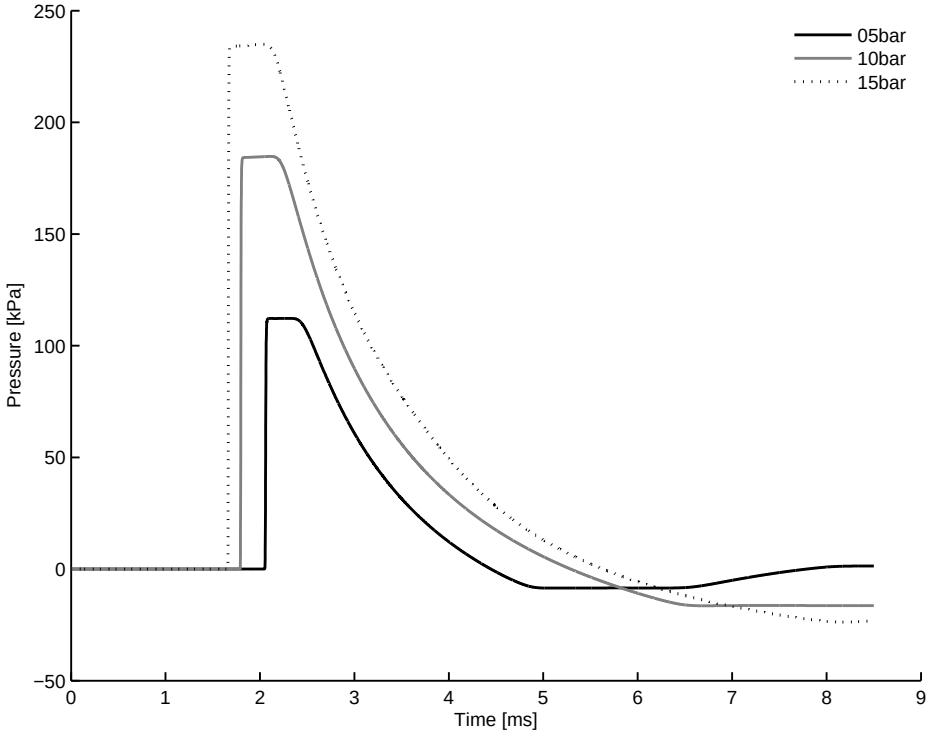
As with the linearly diverging driver sections, a reduction in the length for the straight driver section results in a steepening of the decay in pressure behind the shock front. Initially, unlike the linearly diverging driver sections, the straight driver sections produce normal shock wave pressure profiles which are trailed by an exponentially decaying pressure profile, as depicted in Figure 4.17 (a). Looking at Figure 4.17 (a) it can be seen that decreasing the driver length reduces the duration of the peak shock overpressure. As the shock front travels down the tube, the duration of the peak overpressure reduces, where for the waves generated by the $65mm$, $90mm$ and $140mm$ long driver sections, the overpressure plateau disappears entirely as shown in Figure 4.17 (d). Just as was the case with the linearly diverging sections, the gradient of the pressure decay trailing the shock front is, if accounting for the varying peak overpressure, almost identical for the shock waves induced by the $65mm$, $90mm$ and $140mm$ long driver sections. In Figure 4.17 it is shown that the shorter the driver section length, the quicker the peak overpressure and velocity decay as the shock front travels down the expansion section of the tube.

What is interesting to note from Figure 4.17 (a) and Figure 4.17 (b) is that initially the straight driver sections with longer lengths generate expansion phases having longer durations and lower minimum pressures than comparable shorter straight driver sections. However this situation is not stable and as the shock front travels further down the tube, regardless of driver section length, the minimum pressure in the expansion phase tends to plateau at the same value. The only feature that differs between the expansion phases of the shock waves generated by the different driver sections is the duration of the expansion phase where the duration of the expansion phase increases with increasing driver length.

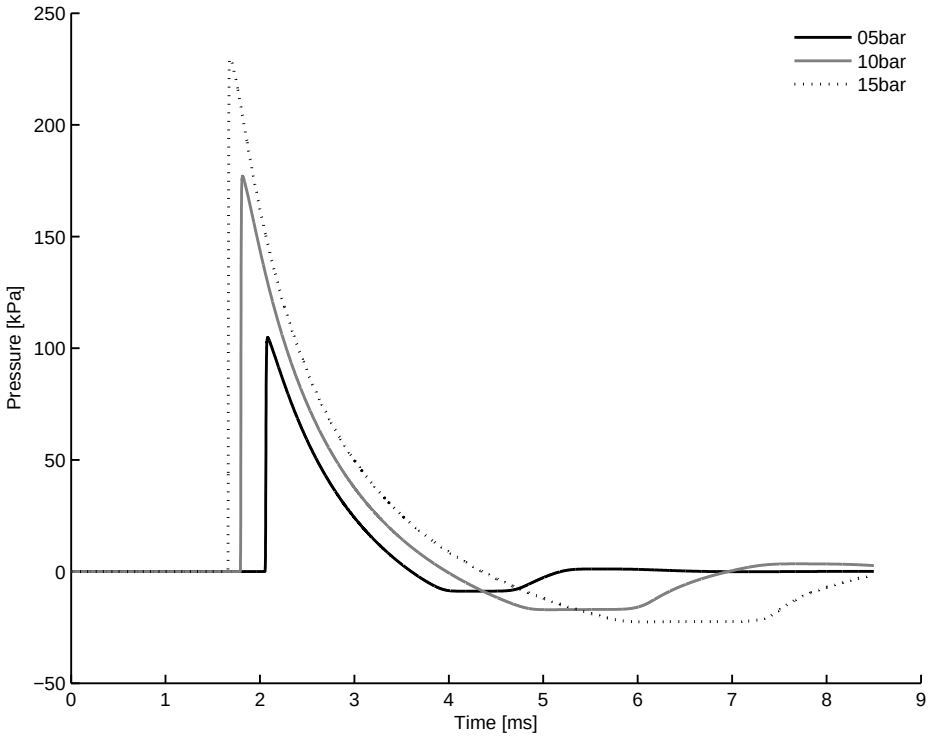
Figure 4.18 shows the shock waves pressure profiles generated by straight driver sections having lengths of $580mm$, $140mm$ and $65mm$, at driver pressures of $5bar$, $10bar$ and $15bar$.



4.17 (e): $580mm$



4.17 (f): $140mm$

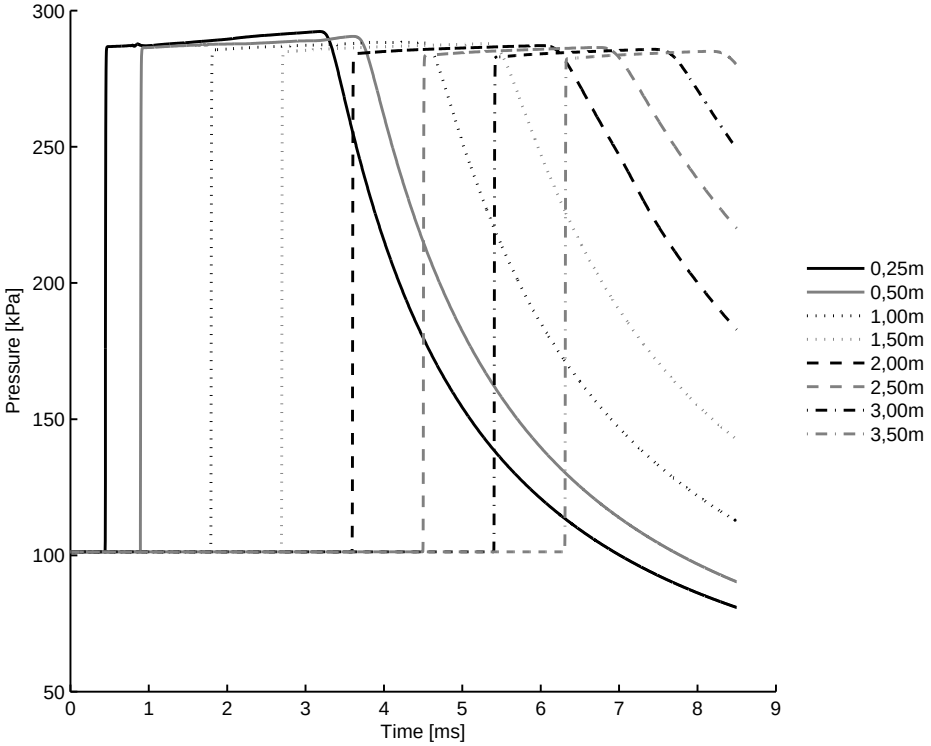


4.18 (a): $65mm$

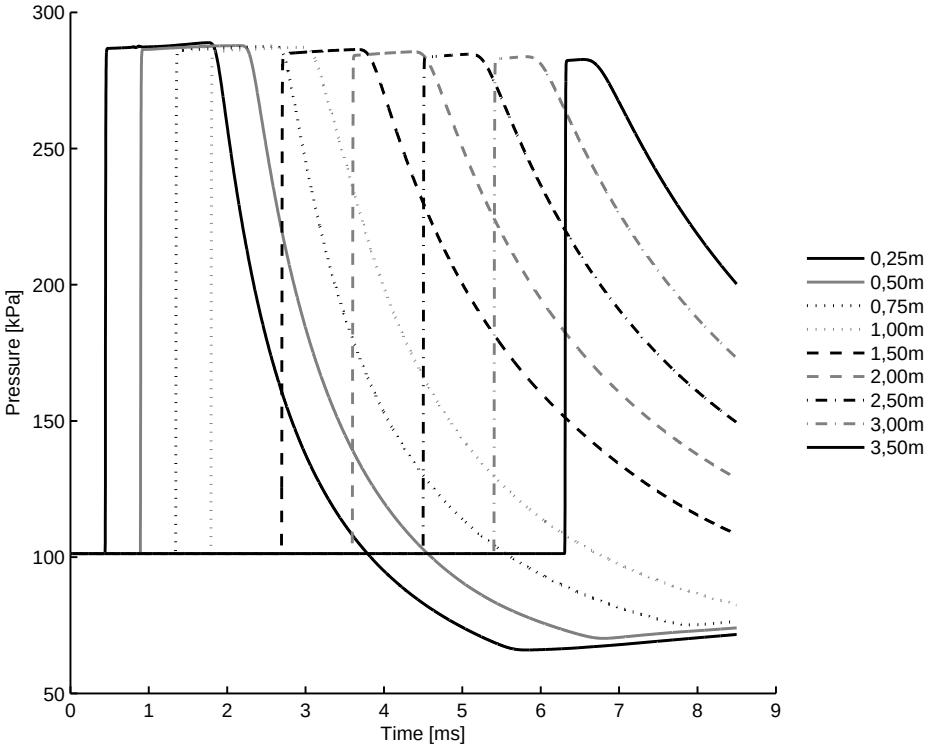
Figure 4.18: The Effect of Driver Pressure on Shock Pressure Profile

By comparing the pressure plots in Figure 4.18 to the pressure plots in Figure 4.4 it can be deduced that the effects that increasing the driver pressure had on the shock waves generated by the straight driver sections are the same as the effects on the linearly diverging driver sections generated blast waves, namely, higher shock velocities, increased peak over pressures, increased blast wave durations, steeper overpressure decay and reduced minimum pressures.

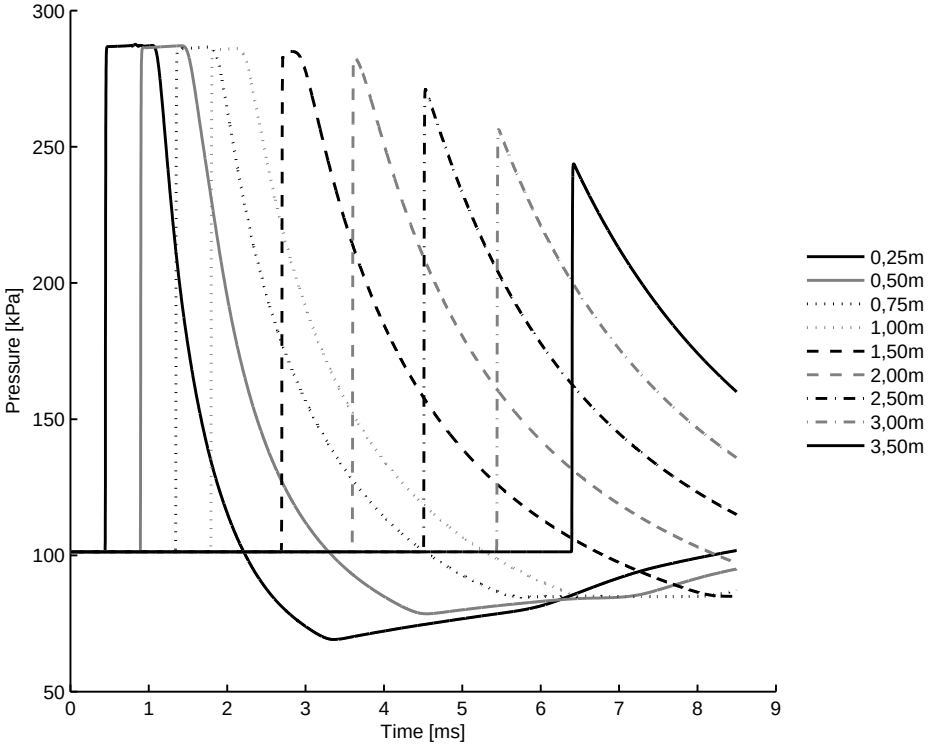
In Figure 4.19 below is shown the development of the blast pressure profiles along the length of the expansion section for blast waves generated by the $65mm$, $90mm$, $140mm$, $290mm$ and $580mm$ long straight driver sections having driver pressures of $10bar$.



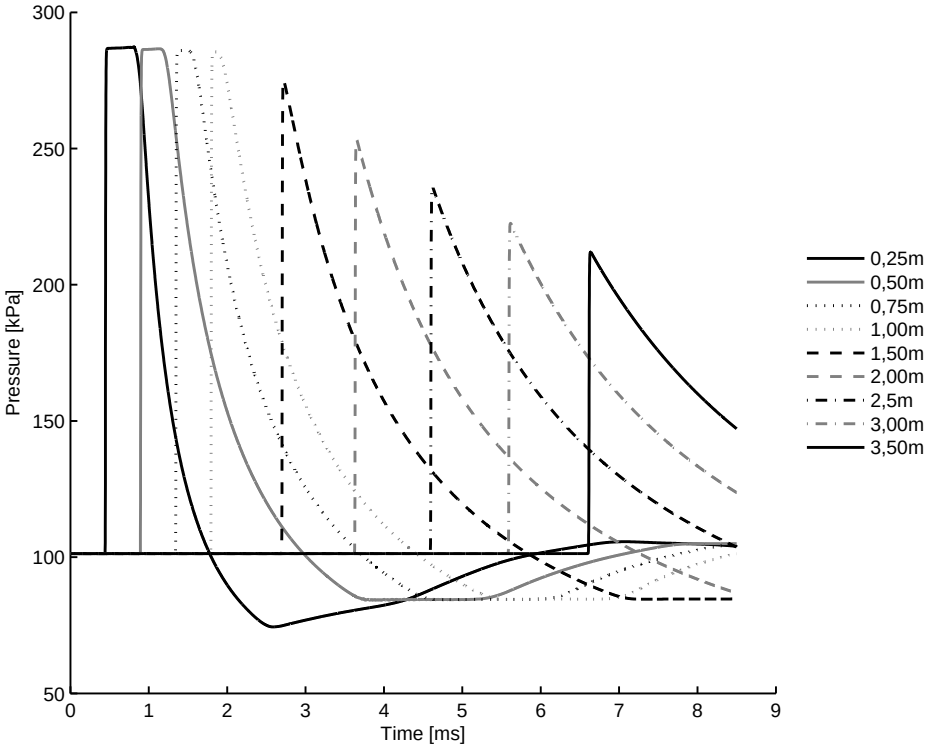
4.19 (a): $580mm$ $10bar$



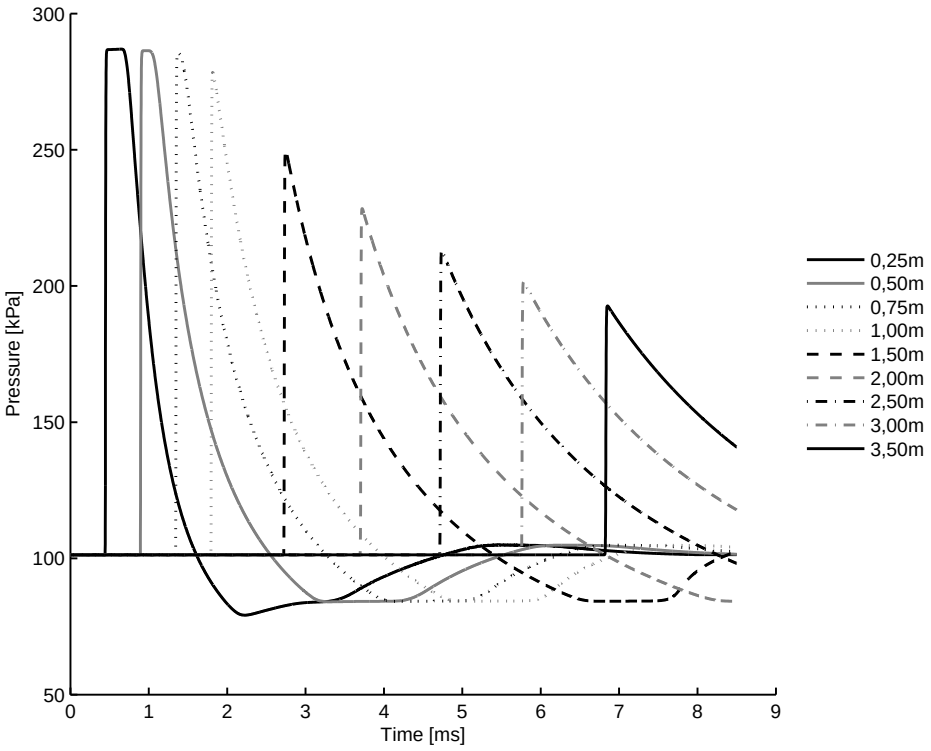
4.19 (b): $290mm$ $10bar$



4.19 (c): $140mm$ $10bar$



4.19 (d): $90mm$ $10bar$



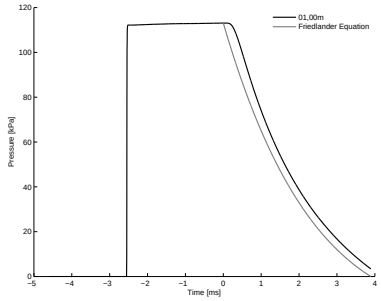
4.19 (e): 65mm 10bar

Figure 4.19: The Effect of Expansion Section Length on Pressure for Straight Drivers

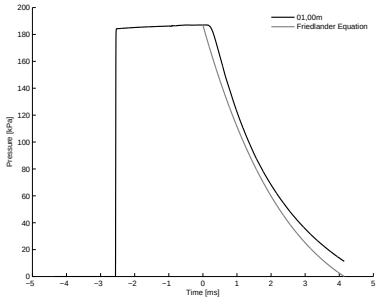
For all the straight driver sections, before the reflected expansion waves catch up with the shock front, the magnitude of the peak overpressure is stable and remains barely unchanged as the shock propagates along the tube. This behaviour is clearly depicted in Figure 4.19 (a), Figure 4.19 (b) and Figure 4.19 (c) and indicates that the shocks generated by the straight driver profiles are indeed shock waves and not blast waves. It can be seen in Figure 4.19 (c), Figure 4.19 (d) and Figure 4.19 (e) that once the reflected expansion waves catch up to the shock front, the peak overpressure decays as the shock front travels further downstream. This behaviour is similar to that exhibited by the shock waves generated by the linearly diverging driver profiles, as shown in Figure 4.5 and is a feature of real world blast waves. Initially the magnitude of the minimum expanded pressure decreases as the shock moves further along the tube, not dissimilar to behaviour exhibited by the waves generated by the linearly diverging driver sections. However it can be seen in Figure 4.19 (d) and Figure 4.19 (e) that, unlike the linearly diverging drivers, the minimum pressure then stabilises, plateaus and remains unchanged as the shock travels further down the expansion section.

Below in Figure 4.20 are plotted the pressure profiles of the shock waves generated by the 580mm, 140mm and 65mm long straight driver sections with the driver pressure being set to pressures of 5bar, 10bar and 15bar. The measurements for this reading were taken by a

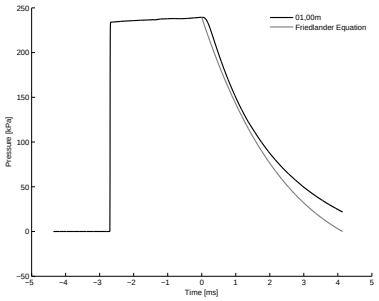
monitor located along the centre line of the tube and at a distance of 1.00m downstream of the diaphragm. On the same axes are plotted the corresponding Friedlander profiles. Looking at Figure 4.20, it can be seen that none of the straight driver sections generated realistic blast wave pressure profiles. This is either due to the expansion waves not being able to catch up to the shock front resulting in a plateaued overpressure trailing the shock front, or due to the plateaued expansion phase. Not dissimilar to the linearly diverging section, Figure 4.20 shows that the shorter the driver section the better the pressure decay following the shock front corresponds to the Friedlander profile. However, unlike the linearly diverging sections, increasing the driver pressures causes the straight driver sections to generate ever worsening pressure decay profiles. The straight driver configuration which generated the most realistic blast wave profile is the 65mm long driver set to a pressure of 5bar, as shown in Figure4.20 (g). However there is a problem with this pressure profile which makes it unsuitable for use in blast testing and simulation, namely the expansion phase, as is the case with the all the waves generated by the straight driver sections, is plateaued and not logarithmic. Another issue, which was raised with the linear diverging case, is that the alignment occurs at 1.00m from the diaphragm and looking at Figure 4.19 it can be deduced that the gradient of pressure decay will becoming more gradual as the wave travels further downstream meaning by the time the wave reaches the test section it will no longer have a Friedlander profile.



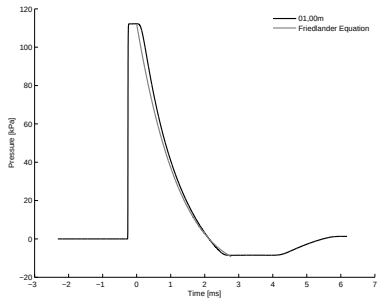
4.20 (a): 580mm 5bar



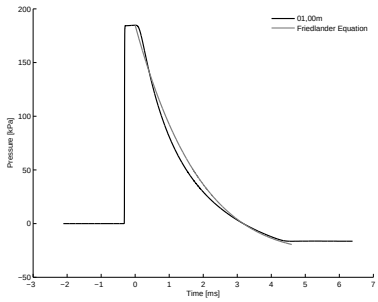
4.20 (b): 580mm 10bar



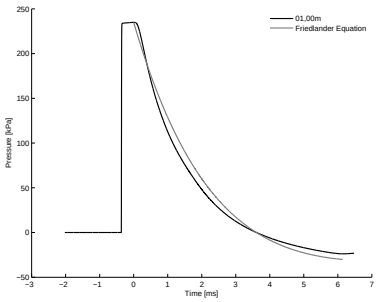
4.20 (c): 580mm 15bar



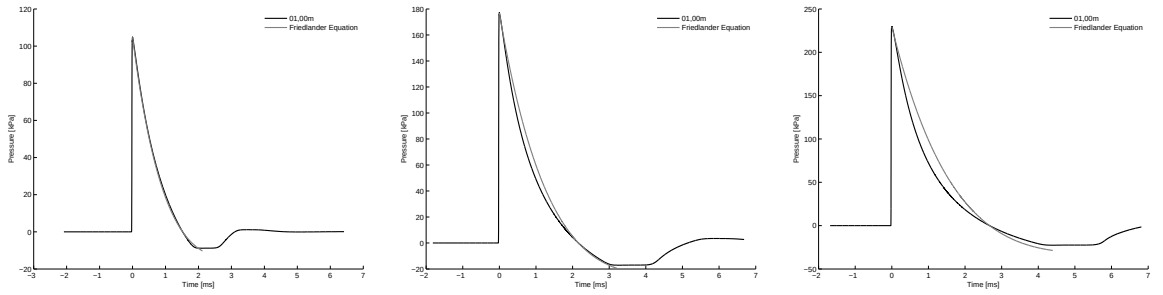
4.20 (d): 140mm 5bar



4.20 (e): 140mm 10bar



4.20 (f): 140mm 15bar



4.20 (g): $65mm$ $5bar$ 4.20 (h): $65mm$ $10bar$ 4.20 (i): $65mm$ $15bar$

Figure 4.20: Comparing the Effect of Driver Length and Pressure on Friedlander Pressure Profile

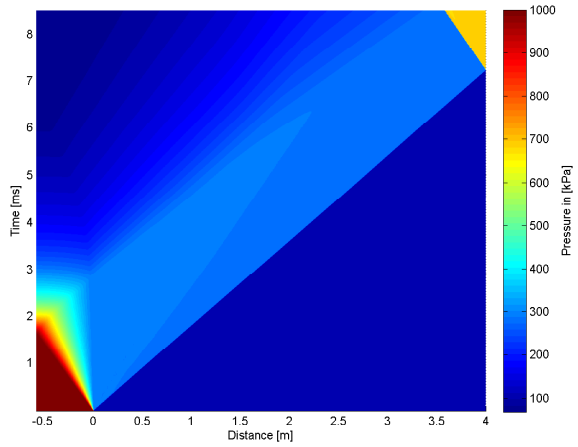
Figure 4.21, Figure 4.22, Figure 4.23 and Figure 4.24 display the x-t diagrams generated by the various straight driver sections when having driver pressures set to $10bar$. Just as was the case with the linearly diverging driver sections, altering the length of the driver section effects the development of the blast wave. Unlike the linearly diverging driver sections which cause the expansion waves to start reflecting downstream of the tube almost immediately after the diaphragm has burst, in the cases having straight driver sections the expansion waves only start reflecting downstream once they impact the back-end of the driver section. The difference this makes on the development of the blast wave is shown starkly by comparing Figure 4.21 and Figure 4.9 where it is observed that the time it takes for the pressure behind the shock front to start reducing is much longer for the straight driver sections than the comparative linearly diverging driver sections. Even by comparing the different straight driver sections, the effect that the increased distance and time that the reflected expansions waves have to travel to reach the shock front on the development of the blast wave can clearly be seen by comparing the sub-figures in Figure 4.21. Comparing Figure 4.21 (a) to Figure 4.21 (c) to Figure 4.21 (e) it is deduced that the shorter the driver section, the quicker the reflected expansion waves can reach the shock front, indicated in the x-t diagrams by the darkening shades of blue behind the shock front, which in turn reduces the duration of the plateaued peak overpressure, indicated by the light blue band behind the shock front, inducing a more realistic blast pressure profile sooner.

A key difference between the formation of the blast waves generated by the straight and linearly diverging sections is the lack of expansion focusing that occurs when the straight driver sections are utilised. This becomes clearly apparent after examining and comparing the bottom left hand corner of Figure 4.9, Figure 4.10 and Figure 4.11 to the bottom left hand corner in Figure 4.21, Figure 4.22 and Figure 4.23 and noting that the x-t diagrams for the straight drivers do not display, unlike the x-t diagrams for the linearly tapered drivers, a region in the driver section where there is a rapid decrease in the fluid properties. This lack of

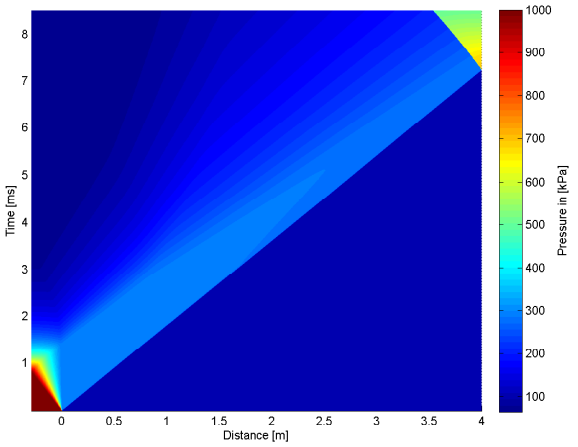
expansion focusing explains why the expansion phase of the waves generated by the straight driver sections plateau, the minimum pressures have large magnitudes than the comparative linearly diverging pressure profiles and why the straight driver section pressure profiles lack secondary shock waves.

Contrasting Figure 4.22 and Figure 4.23 with Figure 4.10 and Figure 4.11 it can be seen that the contact surface generated by the straight driver section exhibits similar behaviour to the contact surface generated by the linearly diverging sections in that the longer the driver section, the further downstream the contact surface travels. A key difference between the contact surfaces generated by the straight and linearly tapered driver section is the how far along the tube they travel, with the straight driver generated contact surfaces travelling further than the comparative linearly diverging generated contact surfaces. This is to be expected though as the straight driver sections contain nearly double the volume of gas than the comparative linearly diverging section and also do not induce expansion focusing or secondary shocks.

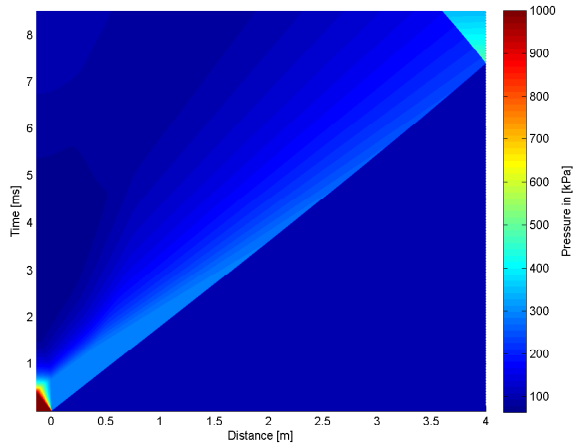
Just as was the case with the linearly diverging driver sections, the x-t diagrams below show that despite having the same driver pressures, the length of the driver section effects the velocity of the shock wave as it propagates along the tube, where the shorter the straight driver sections the lower the velocity of the shock wave generated. The reason for this is that the reflected expansion waves require less time and distance to reach the shock front where upon reaching the shock they reduce the peak overpressure and velocity of the shock.



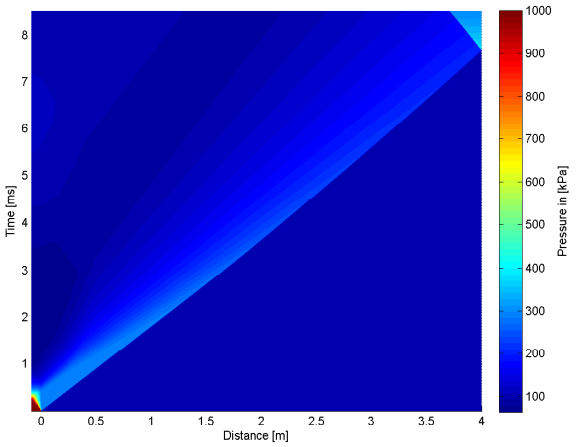
4.21 (a): 580mm 10bar



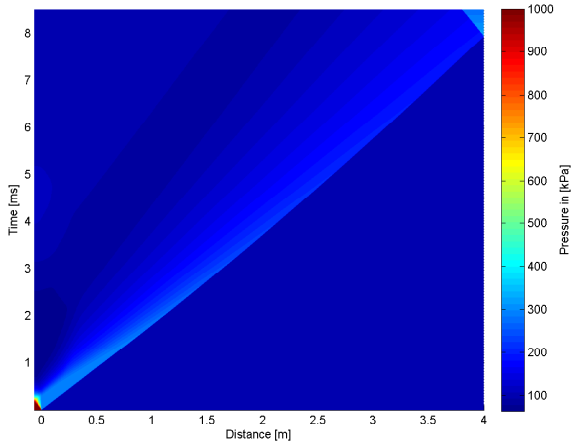
4.21 (b): 290mm 10bar



4.21 (c): $140mm$ $10bar$

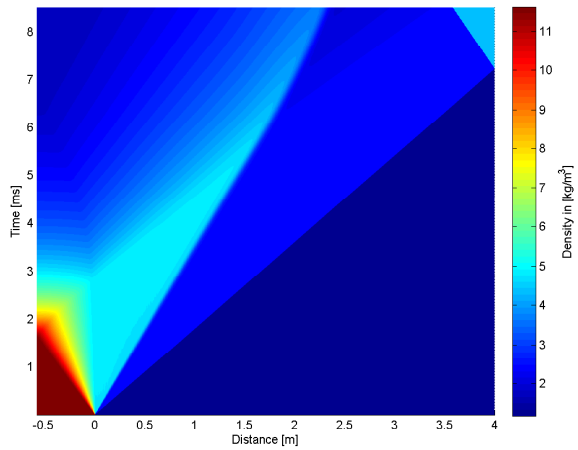


4.21 (d): $90mm$ $10bar$

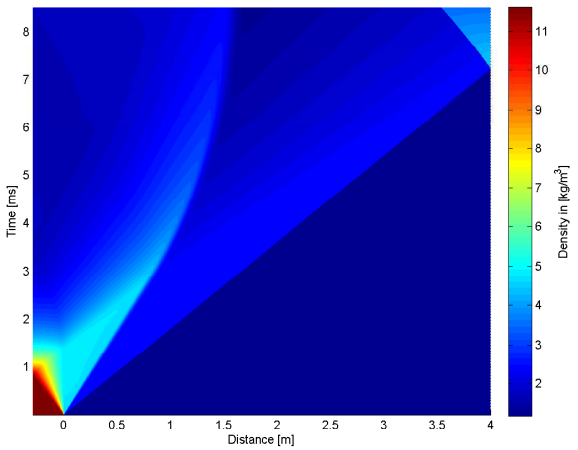


4.21 (e): $65mm$ $10bar$

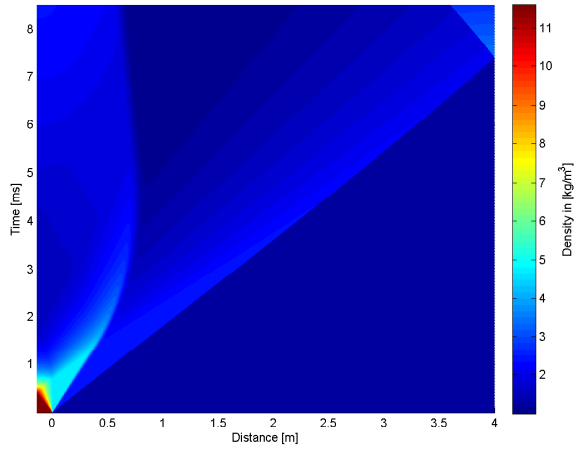
Figure 4.21: X-T Diagram for Straight Driver Sections (Pressure)



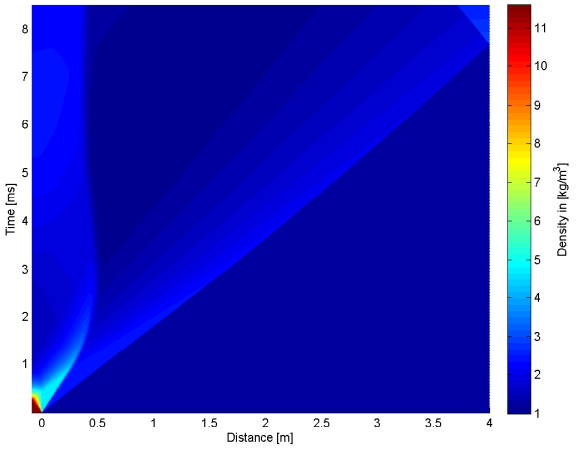
4.22 (a): $580mm$ $10bar$



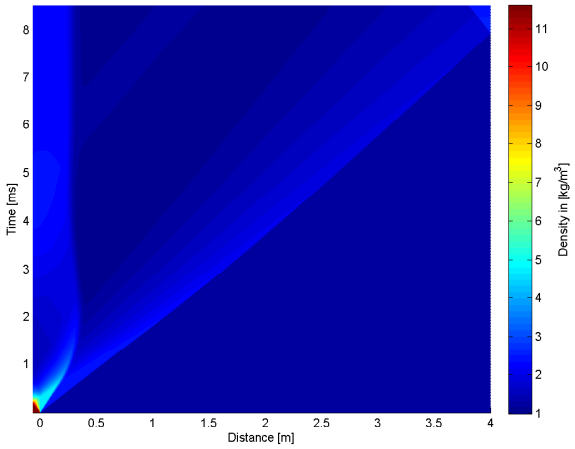
4.22 (b): $290mm$ $10bar$



4.22 (c): $140mm$ $10bar$

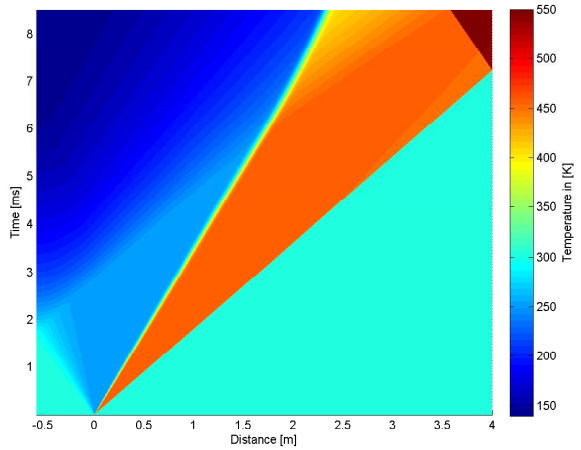


4.22 (d): $90mm$ $10bar$

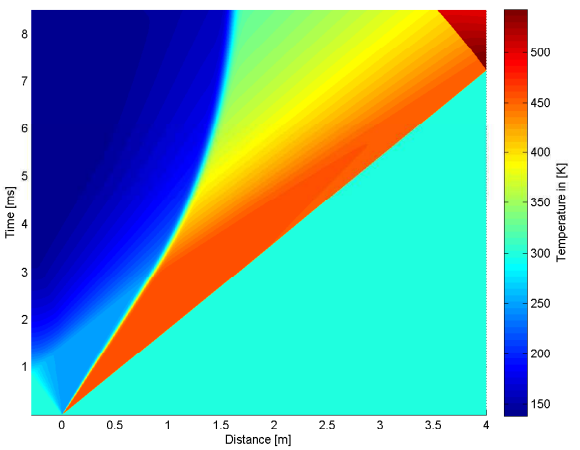


4.22 (e): $65mm$ $10bar$

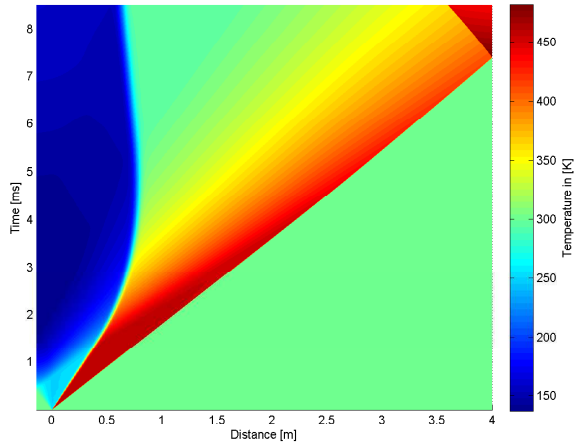
Figure 4.22: X-T Diagram for Straight Driver Sections (Density)



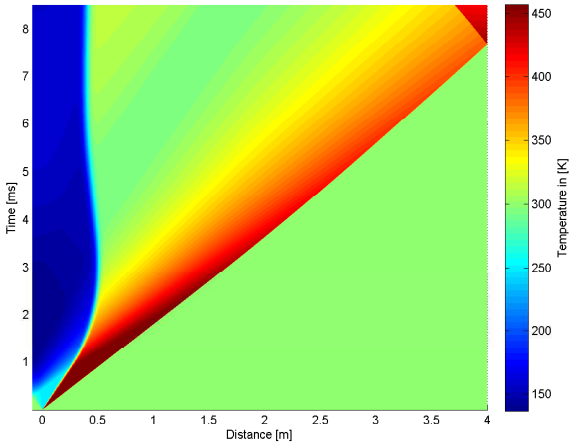
4.23 (a): $580mm$ $10bar$



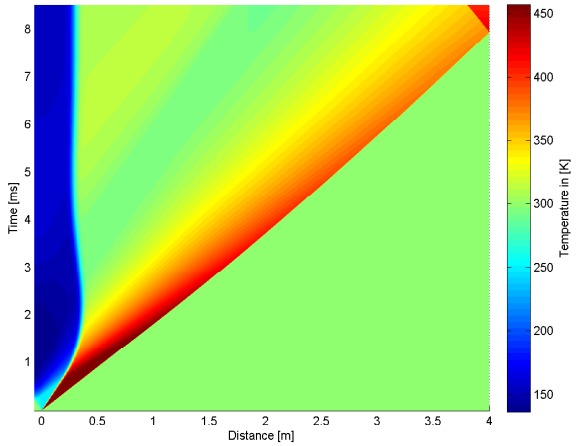
4.23 (b): $290mm$ $10bar$



4.23 (c): $140mm$ $10bar$

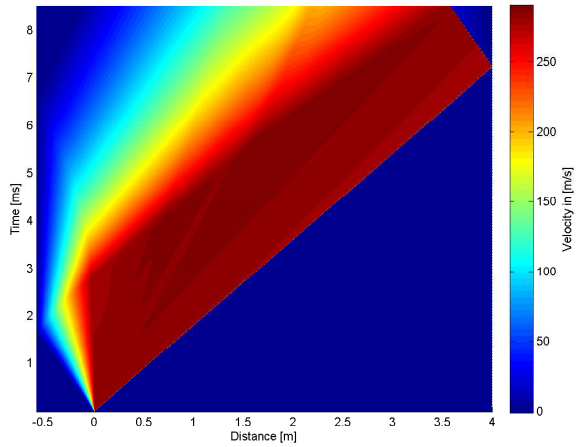


4.23 (d): $90mm$ $10bar$

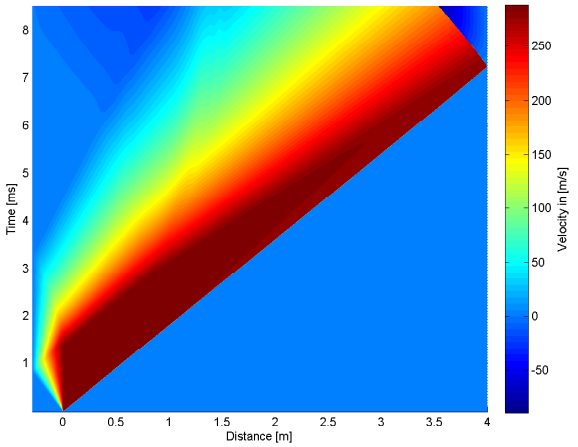


4.23 (e): $65mm$ $10bar$

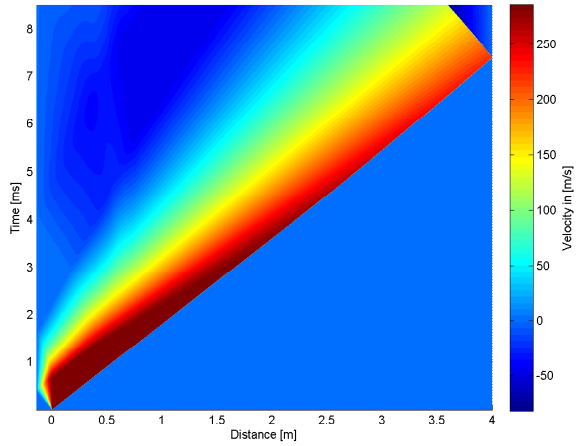
Figure 4.23: X-T Diagram for Straight Driver Sections (Temperature)



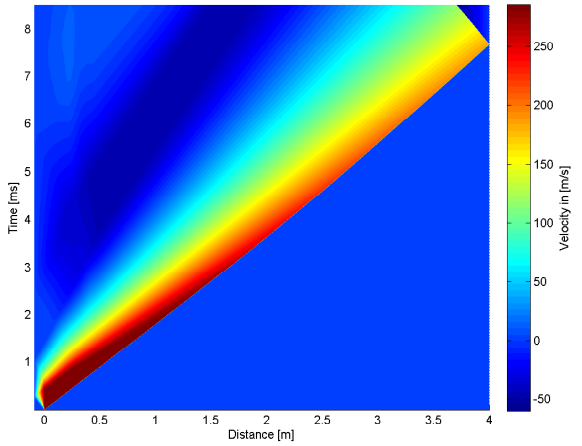
4.24 (a): $580mm$ $10bar$



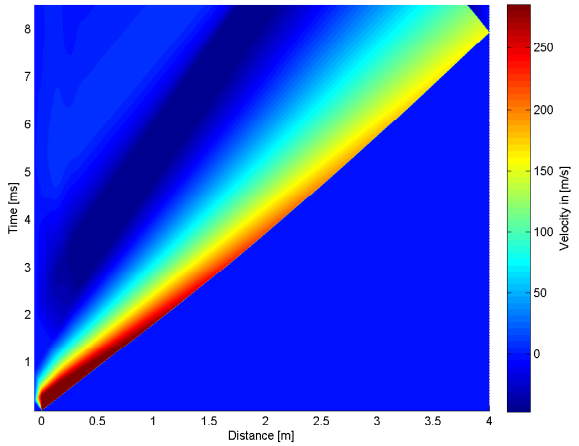
4.24 (b): $15°$ $10bar$



4.24 (c): $140mm$ $10bar$



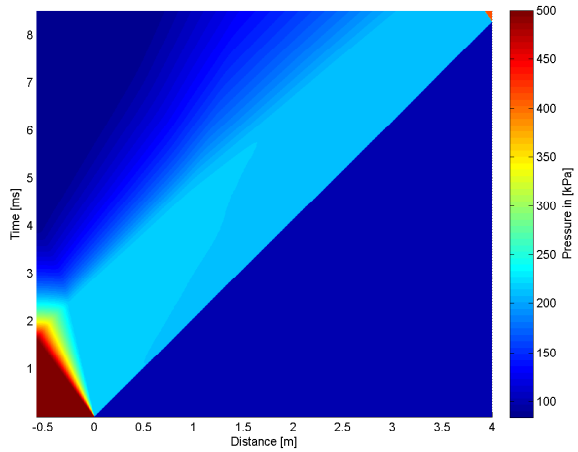
4.24 (d): $90mm$ $10bar$



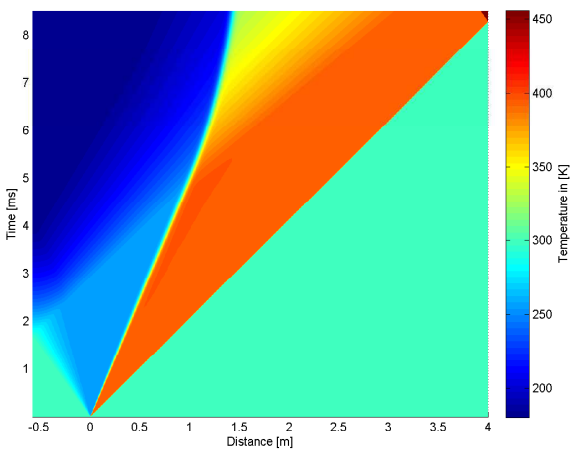
4.24 (e): $65mm$ $10bar$

Figure 4.24: X-T Diagram for Straight Driver Sections (Velocity)

Figure 4.25, Figure 4.26 show the effects of reducing the driver pressure on the flow characteristics while Figure 4.27 and Figure 4.28 show the effects of increasing driver pressure. As was the case with the linearly diverging drivers, increasing the driver pressure results in the shock having a greater velocity, as shown by the steeper angle of the shock fronts in Figure 4.27 and Figure 4.28. Increasing the driver pressure also causes the contact surface to travel a further distance along the expansion of the tube as was the case with the linearly diverging sections.

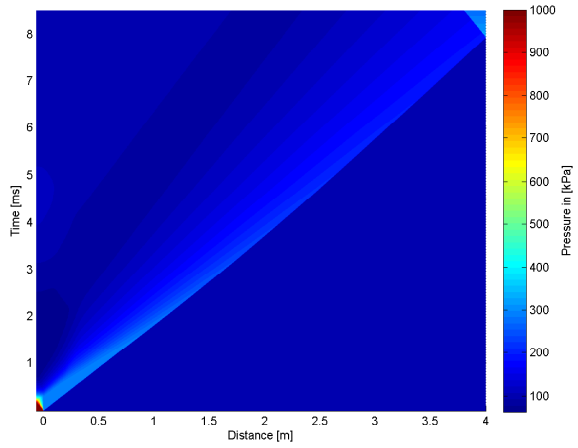


4.25 (a): 580mm 5bar Pressure

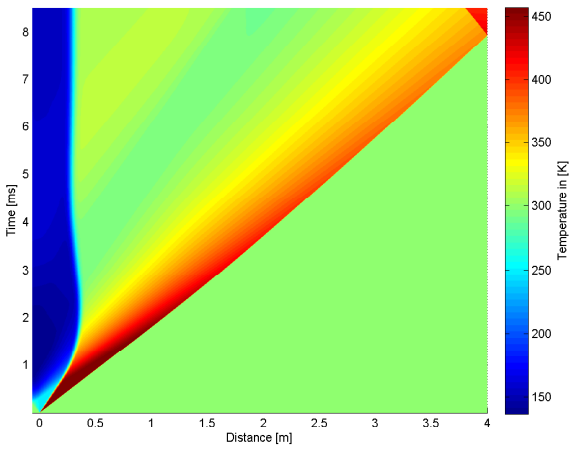


4.25 (b): 580mm 5bar Temperature

Figure 4.25: X-T Diagram for 580mm Straight Driver Section at 5bar

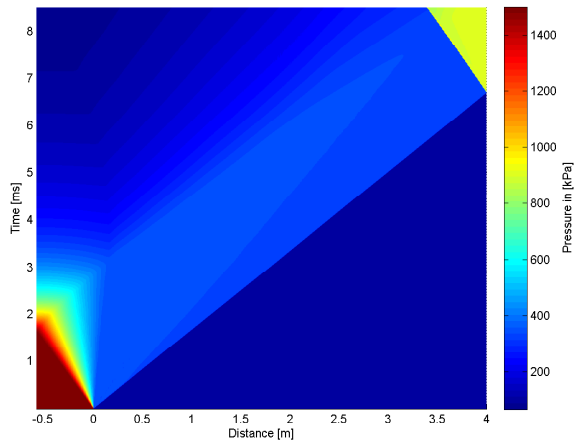


4.26 (a): 65mm 5bar Pressure

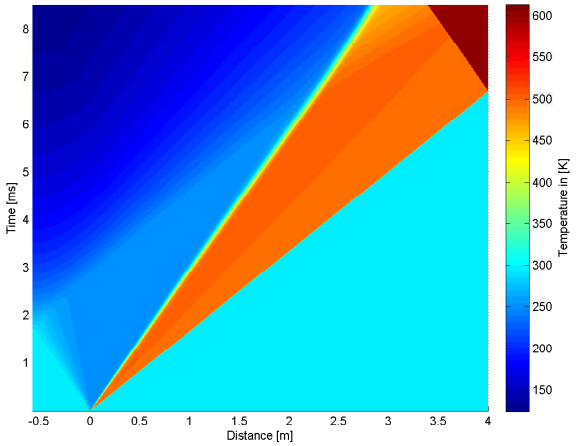


4.26 (b): 65mm 5bar Temperature

Figure 4.26: X-T Diagram for 65mm Straight Driver Section at 5bar

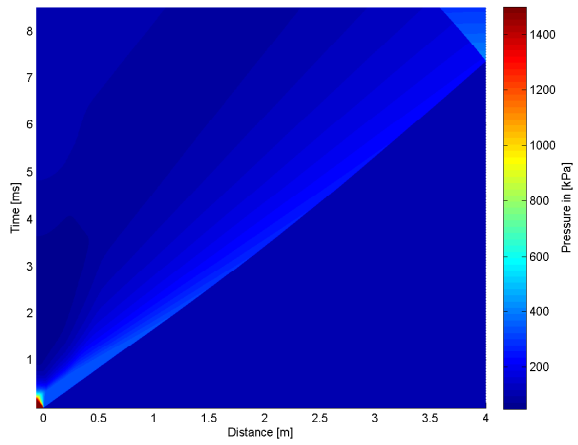


4.27 (a): 580mm 15bar Pressure

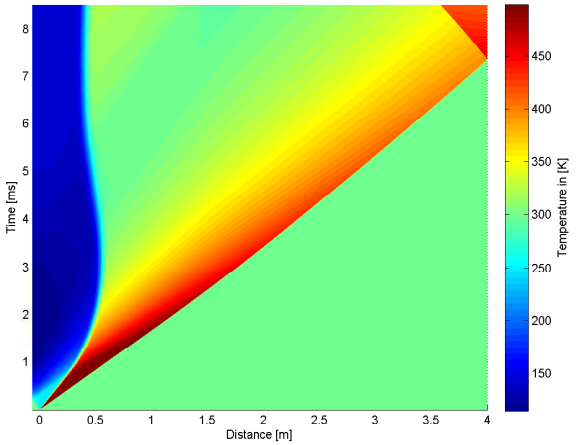


4.27 (b): 580mm 15bar Temperature

Figure 4.27: X-T Diagram for 580mm Straight Driver Section at 15bar



4.28 (a): 65mm 15bar Pressure



4.28 (b): 65mm 15bar Temperature

Figure 4.28: X-T Diagram for 65mm Straight Driver Section at 15bar

4.1.5 Polynomial Driver Sections

Based on the results and analysis performed in the subsection 4.1.3 and subsection 4.1.4 as well as the research carried out by Whalley (2016), it was deduced that a driver section requires a few key features in order to generate a blast wave with a realistic Friedlander pressure profile. The features are as follows:

- The driver section must end in a sharp corner in order to enable expansion focusing to occur.
- The walls of the driver section must be divergent to cause the expansion waves to reflect downstream almost immediately after the diaphragm bursts as well to drive the expansion focusing.
- The walls of the driver section must transition smoothly, that is without a corner, into the expansion section walls.
- The walls of the driver section must be curved in order to induce smooth and continuous expansion wave reflection and focusing.

After some tests were carried out on a few iterations of driver section shapes, three shapes were settled on, namely a concave driver, a linear driver and a convex driver as shown in Figure 4.29. To help with the analysis, Figure 4.30 shows the angle of inclination of the driver walls at each point along the length of the drivers. In order to enable further optimisation and to freeze the design, it was decide that the length of the driver section would be set to $500mm$.

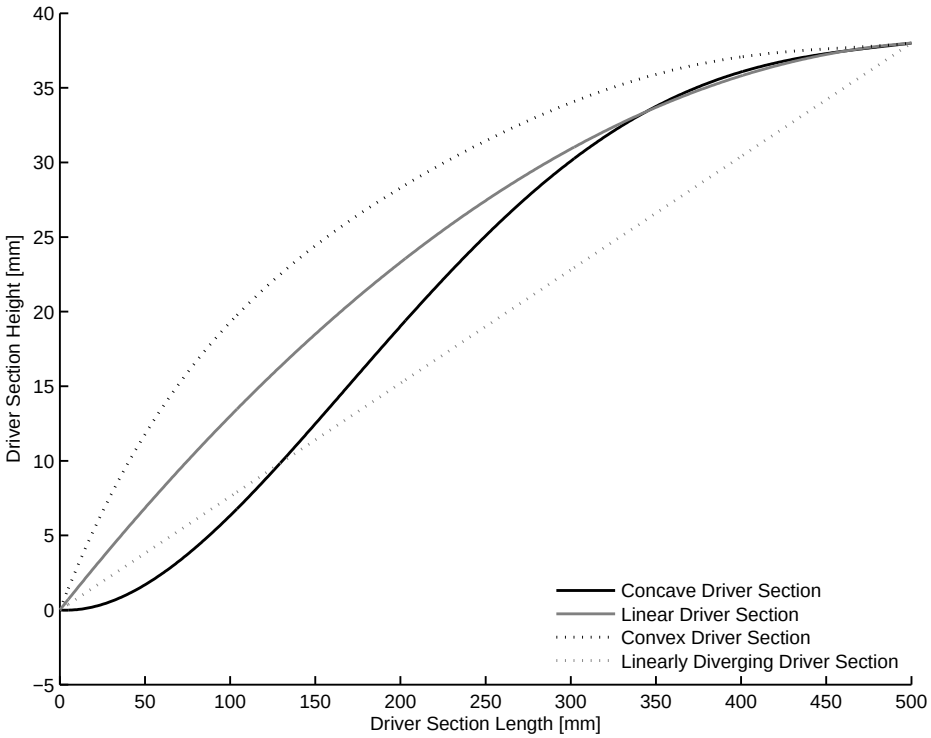


Figure 4.29: The 3 Driver Section Profiles Designed for Further Testing

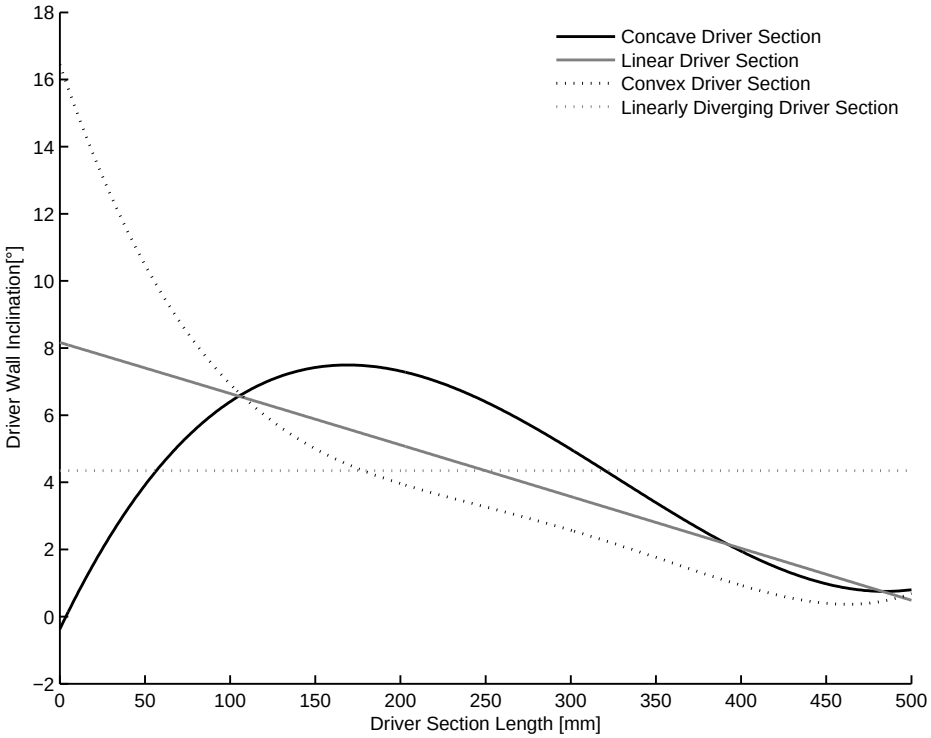


Figure 4.30: The Angle of Inclination of the 3 Driver Section Profiles

4.1.6 Varying Diaphragm Location

The next stage of the design development process of the blast tube driver section was assessing what effect the location of the diaphragm had on the formation of the blast wave pressure profile. Moving the location of the diaphragm from the point where the driver section and expansion sections met, to further upstream in the driver section, led to a section of the walls of the expansion section to be diverging. This diverging expansion section was titled the transition section and the effects the length of said section has on the blast formation will be addressed in this and the next section. All the the varying diaphragm simulations were run with the driver pressure being set to $10bar$. Table 4.3 lists the equivalent explosive energy of the driver shaping and pressure configurations that were tested. By comparing the data in Table 4.3 to the data listed in Table 4.1 it can be seen that the explosive equivalent energies for the varying diaphragm simulations are in the range of the tapered driver simulations explosive equivalents.

Table 4.3: Varying Diaphragm Location TNT Explosive Equivalence

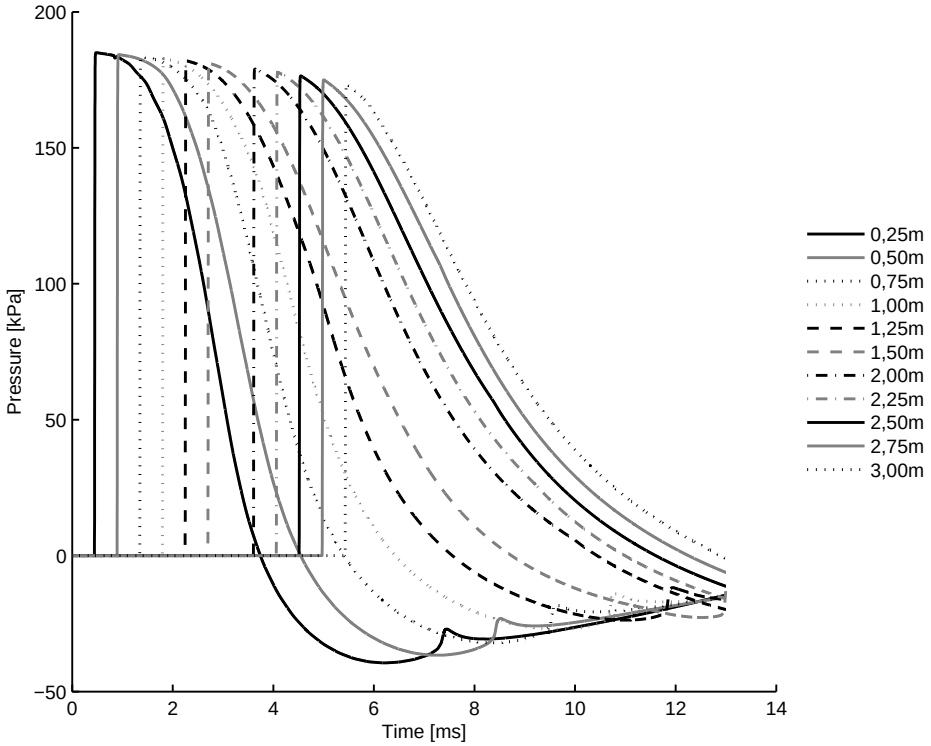
Driver	25%	50%	75%	100%
Concave Driver	$1.63g$	$10.21g$	$25.45g$	$43.71g$
Linear Driver	$4.09g$	$14.98g$	$30.56g$	$48.76g$
Convex Driver	$6.43g$	$19.90g$	$36.91g$	$55.44g$

It was noted that the effects of varying the location of the diaphragm was much the same for all three driver sections and therefore only the data from the concave driver simulations will be examined in depth and the data for the linear and convex drivers are contained in Appendix A and will be referred to as required. Figure 4.31 shows that as was the case with the linearly diverging driver sections, the further upstream the diaphragm is located and therefore the shorter the driver section, the quicker the decay of the overpressure with distance. It is challenging making a direct comparison between the varying diaphragm simulations and the linearly tapering simulations as neither the lengths nor the diverging angles of the drivers correspond. However by comparing Figure 4.31 (a) to Figure 4.5 (a), Figure 4.31 (b) to Figure 4.5 (a) and Figure 4.5 (b), Figure 4.31 (c), Figure 4.5 (b) and Figure 4.31 (d) to Figure 4.5 (d) some distinctions can be made.

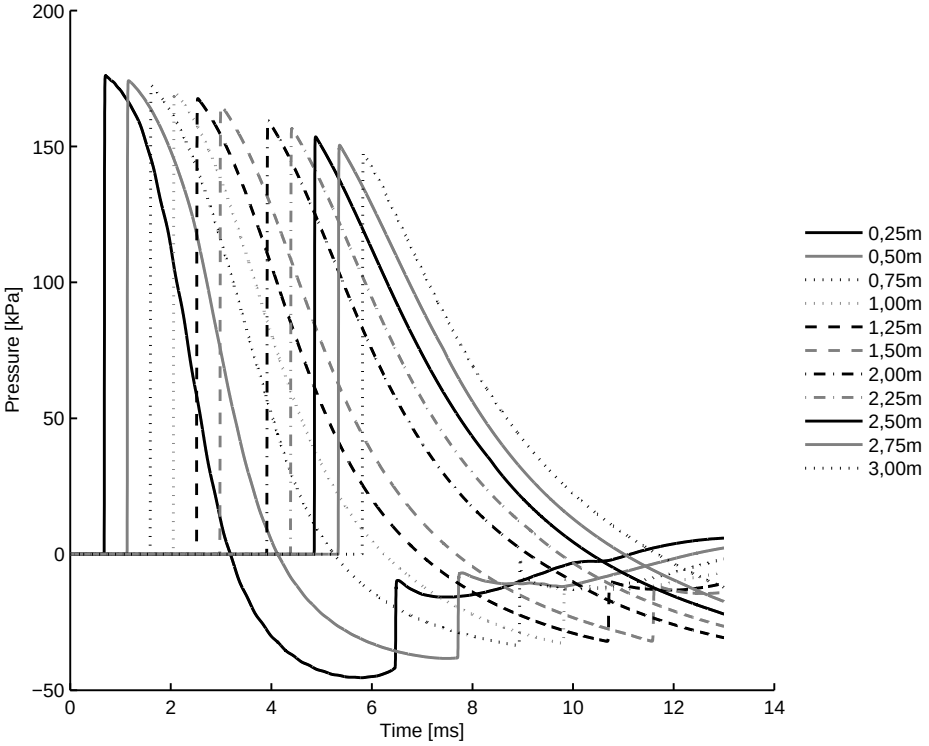
Looking at Figure 4.31 it can be seen that due them having the same driver pressure as the linearly diverging driver sections, the concave driver sections produce blast waves with similar peak overpressures. However as the length of the driver section is reduced, a difference in the peak overpressures with distance is noted. This also holds true for the linear and convex driver profiles as can be seen in Figure A.1 and Figure A.8. This difference in peak overpressure with

distance is indicative of the improved expansion wave reflection induced by the polynomial driver sections which results in the expansion waves catching up to the shock front faster and with greater intensity. This difference becomes more marked as the percentage driver length locating the diaphragm is reduced. The reason for this is, unlike the the linearly diverging profiles which undergo a constant rate of cross-section area change, the rate of cross-section area change of the polynomial driver sections increases the further upstream the location. The concave profile is slightly different to the linear and convex profiles in this regard in that it attains a maximum area rate change at 33% of the driver length.

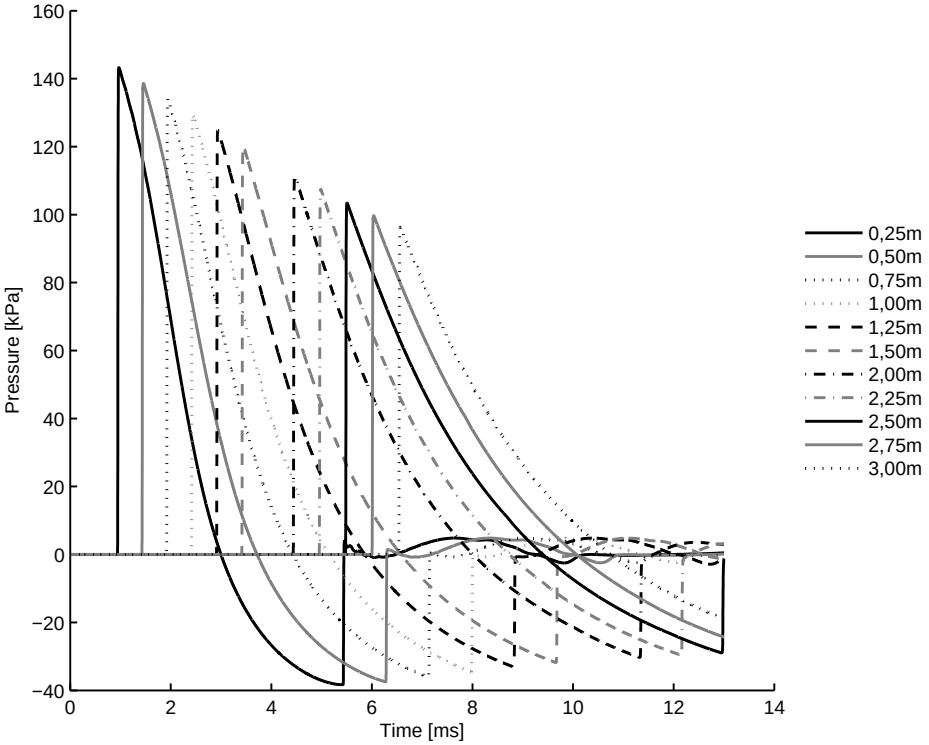
Although the concave driver sections produce blast waves having similar overpressure and expansion phase durations to those generated by the comparative linearly diverging driver sections, that is where the similarities end. The pressure decay of the blast waves produced by the polynomial driver sections are much smoother and more rapid than the comparative linearly diverging waves. Another difference between the two sets of driver sections is the magnitude of the secondary shocks are much larger for the waves generated the polynomial driver section. Both these differences are indicative of the improved expansion reflection and focusing taking place in the polynomial drivers.



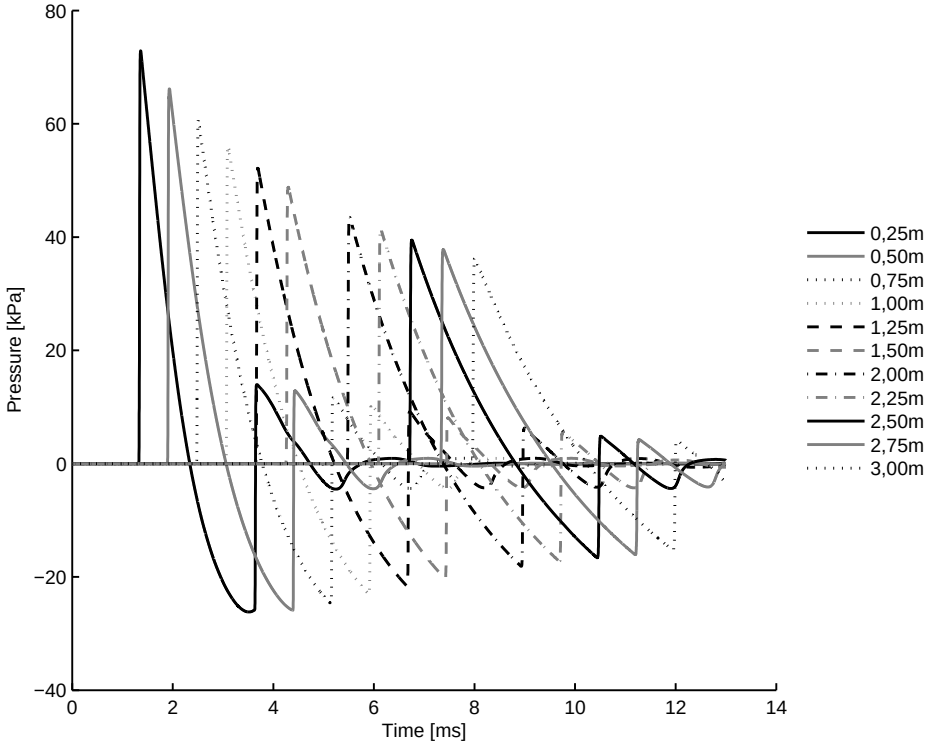
4.31 (a): 100% of Concave Driver Length 10*bar*



4.31 (b): 75% of Concave Driver Length 10*bar*



4.31 (c): 50% of Concave Driver Length 10*bar*

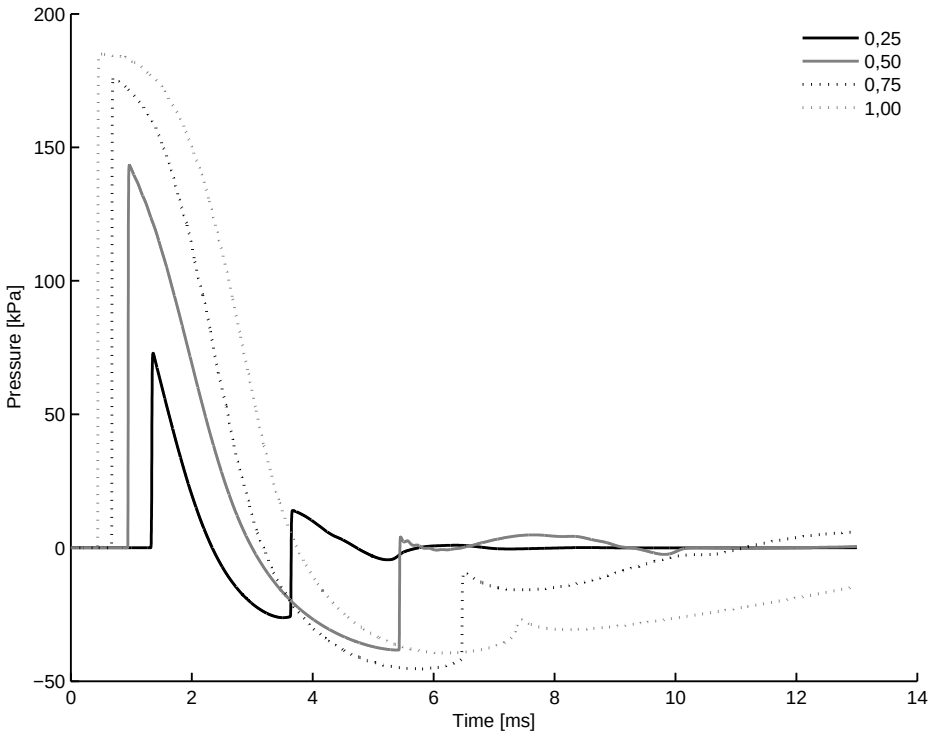


4.31 (d): 25% of Concave Driver Length 10*bar*

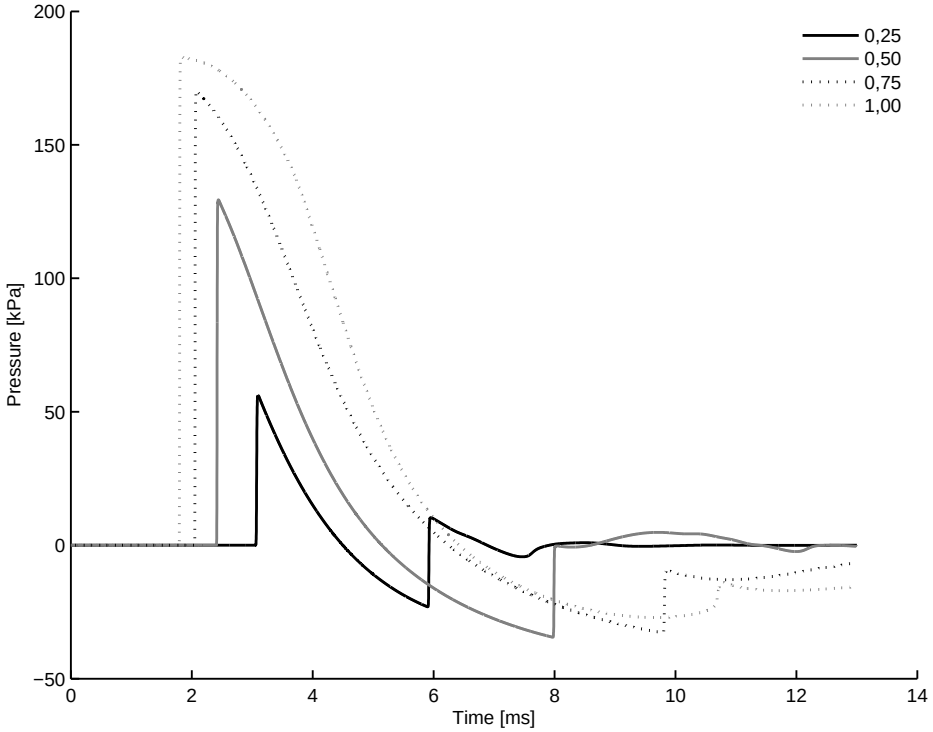
Figure 4.31: The Development of the Blast Pressure Profile for Varying Diaphragm Locations in Concave Driver Section

To determine what effects reducing the percentage driver length of the diaphragm location had on the generation of the blast waves, the pressure traces measured at locations $0.25m$, $1.00m$, $2.00m$ and $3.00m$ from the end of the transition section for each diaphragm location were plotted on the same axes and are displayed in Figure 4.32. Comparing Figure 4.32 to Figure 4.3 it can be seen that the effects of moving the diaphragm location upstream has similar effects on the blast wave generation to increasing the divergence angle of the linearly diverging driver sections. This is due to both alterations resulting in a decrease in the length of the driver section. Looking at the sub-figures in Figure 4.32 it can bee seen that the further upstream the location of the diaphragm is moved, the lower the peak overpressure of the generated blast wave. It can also be seen that moving the diaphragm upstream reduces the durations of both the overpressure and expansion phases of the blast wave. Reducing the driver length and increasing the transition length induces a blast wave with a sharper peak overpressure as well as faster and smoother pressure decay after the peak over pressure. Comparing Figure 4.32 (a) to Figure 4.32 (a) it is observed that the distance between the shock fronts increases as the waves propagate along the length of the tube which is indicative of the increased rate at which the velocity of the blast wave decays as the diaphragm placement is

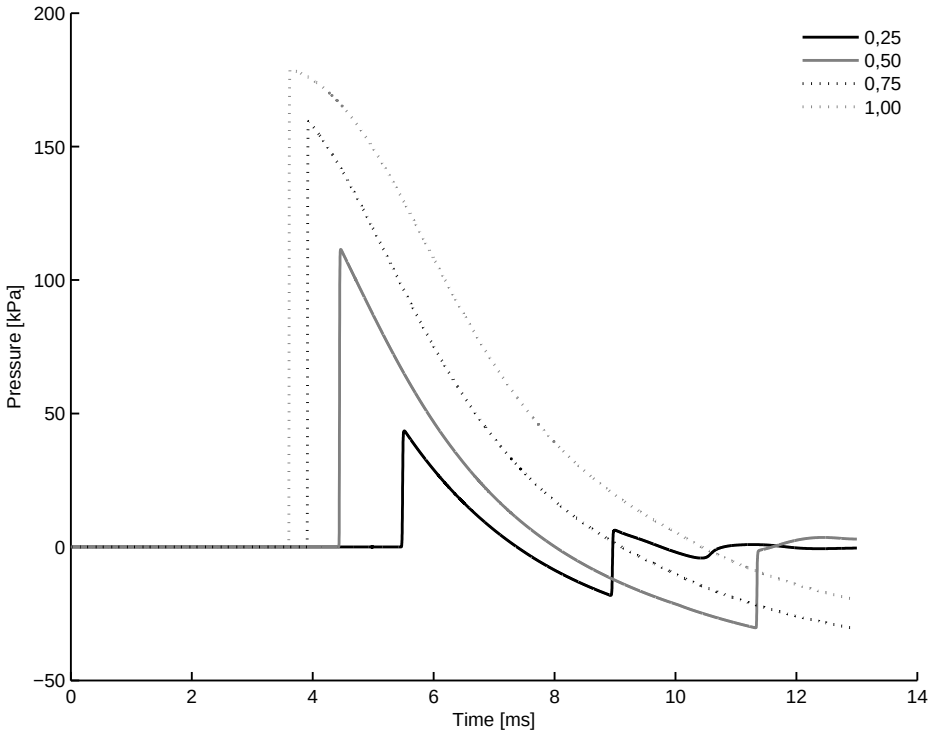
shifted upstream. Figure A.2 and Figure A.9 show that the same effects are are induced for the linear and convex driver sections.



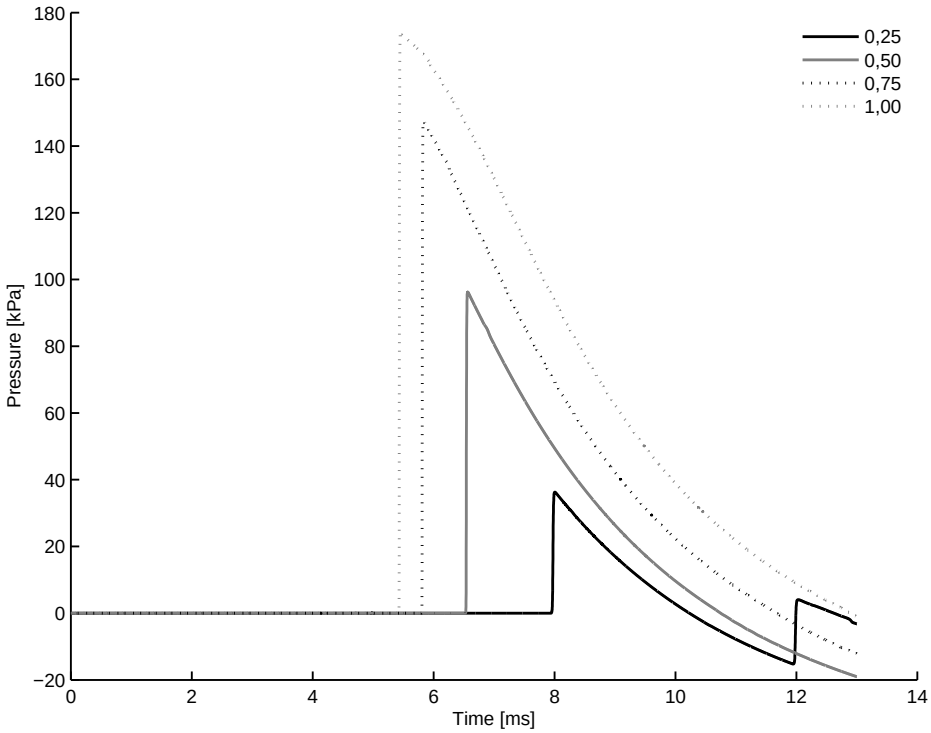
4.32 (a): $0.25m$ $10bar$



4.32 (b): $1.00m$ $10bar$



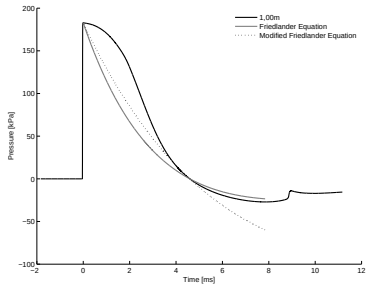
4.32 (c): $2.00m$ $10bar$



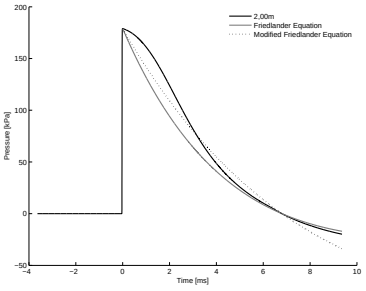
4.32 (d): $3.00m$ $10bar$

Figure 4.32: The Effect of Varying Diaphragm Locations in the Concave Driver Section on the Pressure Profile

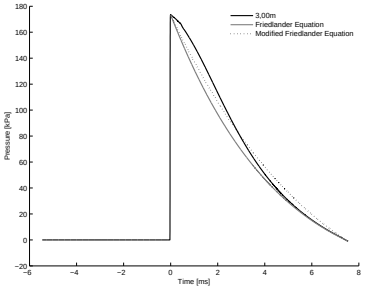
In order to determine whether or not the polynomial driver sections generated blast waves with realistic blast profiles, the pressures measured by monitors located at distances of $1.00m$, $2.00m$ and $3.00m$ from the end of the transition section for each of the diaphragm locations were plotted against the comparative Friedlander and Modified Friedlander plots. The resulting plots are displayed in Figure 4.33. Looking at Figure 4.33 (j), Figure 4.33 (g), Figure 4.33 (g) and Figure 4.33 (j) it was observed that the difference between the expansion sections of the measured pressures and the corresponding Friedlander expansion sections increased with decreasing percentage of driver length diaphragm placement. This is probably due to the inability of the Friedlander equation to account for the the large secondary shock. Examining the sub-figures in Figure 4.33 it can be deduced that for the diaphragm locations simulated, the further upstream the diaphragm is located, the better the pressure decay behind the shock front matches the Modified Friedlander pressure profile. However, after some iterative analysis, it was determined that the best overall blast profile was generated by a driver section having the diaphragm located at 33% of the combined driver section and transition section length. Both of these properties were also observed to be true with the linear and convex drivers as shown in Figure A.3 and Figure A.10.



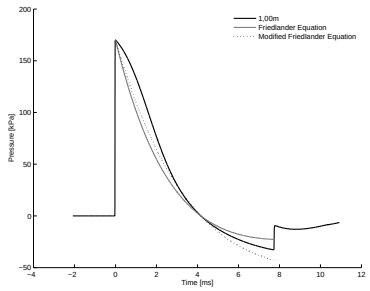
4.33 (a): 100% of Concave Driver Length $10bar$ $1.00m$



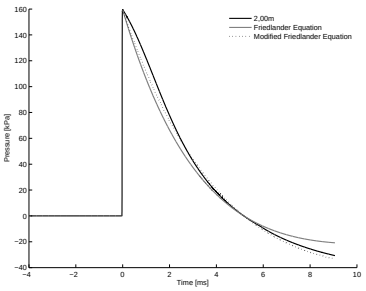
4.33 (b): 100% of Concave Driver Length $10bar$ $2.00m$



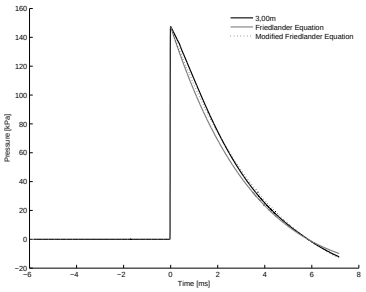
4.33 (c): 100% of Concave Driver Length $10bar$ $3.00m$



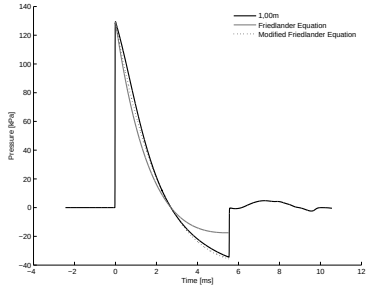
4.33 (d): 75% of Concave Driver Length $10bar$ $1.00m$



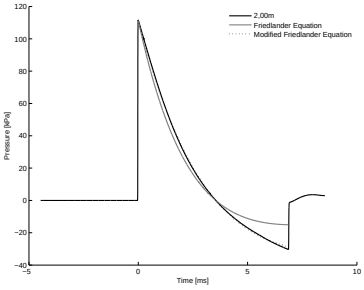
4.33 (e): 75% of Concave Driver Length $10bar$ $2.00m$



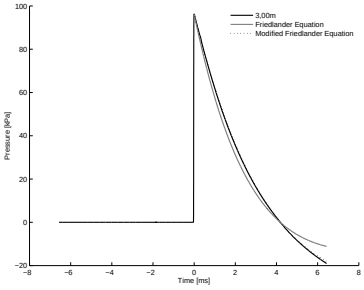
4.33 (f): 75% of Concave Driver Length $10bar$ $3.00m$



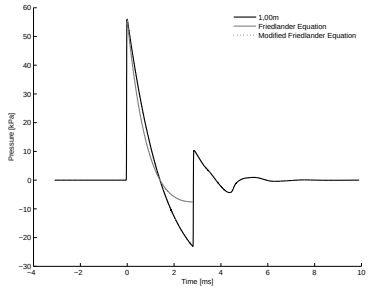
4.33 (g): 50% of Concave Driver Length 10*bar* 1.00*m*



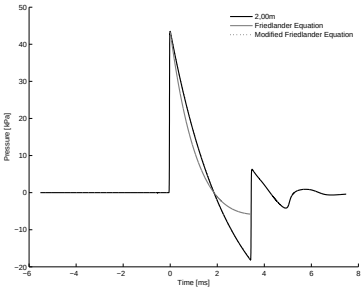
4.33 (h): 50% of Concave Driver Length 10*bar* 2.00*m*



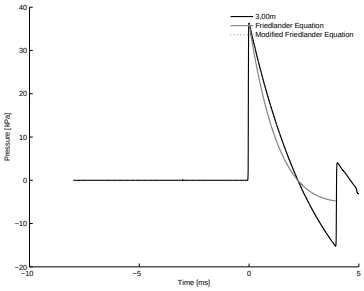
4.33 (i): 50% of Concave Driver Length 10*bar* 3.00*m*



4.33 (j): 25% of Concave Driver Length 10*bar* 1.00*m*



4.33 (k): 25% of Concave Driver Length 10*bar* 2.00*m*



4.33 (l): 25% of Concave Driver Length 10*bar* 3.00*m*

Figure 4.33: Comparing the Effect of Varying Diaphragm Location in the Concave Driver Section on Friedlander Pressure Profile

The pressure, density, temperature and velocity x-t diagrams generated by the simulations of the varying diaphragm locations in the concave driver profile are plotted in Figure 4.34, Figure 4.35, Figure 4.36 and Figure 4.37 respectively. As was the case with the linearly diverging profiles, the polynomial driver sections induce expansion wave reflection almost immediately after the diaphragm bursts. As was observed with the linearly diverging cases, this expansion reflection is shown by the reduction in flow properties behind the shock front which is indicated by the darkening bands of blue behind the shock front in Figure 4.34 and Figure 4.35. Comparing the linearly diverging cases in Figure 4.9, to the concave profile cases in Figure 4.34, it can be seen that the reduction in the flow properties behind the shock front in the concave profile cases is smoother and more rapid as indicated by the comparatively smaller colour bands. Looking at Figure 4.34 (a), Figure 4.34 (b), Figure 4.34 (c) and Figure 4.34 (d) it can be seen that the width and number of the darkening blue bands behind the shock front reduces as the diaphragm location is moved upstream. This is similar to what was observed with increasing divergence angle of the linearly diverging driver and it is indicative of an increased rate and magnitude of expansion wave reflection. In the concave driver this increased rate and magnitude are induced by the increasing rate of area change of the driver

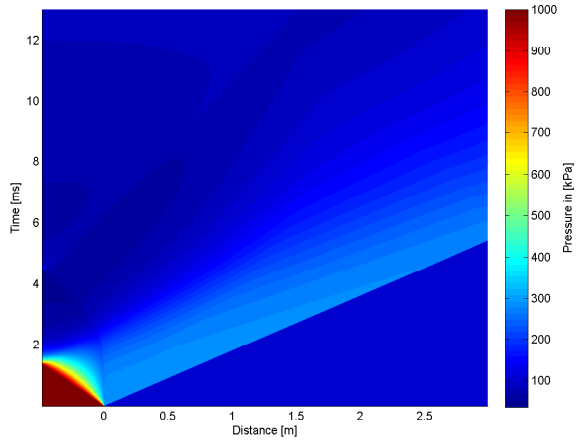
with decreasing distance from the end corner. Figure A.4 and Figure A.11show that improved expansion wave reflection and focusing also occur in the linear and convex driver sections.

Like the linearly diverging driver sections the concave driver sections induce expansion wave focusing as shown by the dark blue region in the bottom left-hand corner of Figure 4.34, Figure 4.35 and Figure 4.36. What differs between the two cases is the intensity of the focusing and the behaviour of the trailing expansion wave. Unlike the cases of linearly diverging drivers where the intensity of the expansion focusing was almost the same for all driver divergence angles, with the concave driver cases, the intensity of the focusing increased as the diaphragm was located further upstream. This is depicted in Figure 4.35 and Figure 4.36 by the increasing intensity and thickness of the line marking the secondary shock as the diaphragm is located further upstream. This intensified expansion focusing is as a result of the increased rate and magnitude of expansion reflection induced by the increasing rate of area change of the driver cross-section with reduced distance from the end corner. Figure 4.35 (a), Figure 4.35 (b) Figure 4.35 (c), and Figure 4.35 (d) show that as the diaphragm is moved further upstream the further downstream the trailing expansion travels before being sucked back to the end corner. Looking at Figure 4.37 it can be deduced that the behaviour of the trailing expansion waves is caused by the increasing flow velocity that arises as the location of the diaphragm is moved further upstream. This can be only a partial explanation as the linearly diverging drivers generate similar flow velocities but the trailing expansion remains in the diaphragm location before being sucked to the corner as shown in Figure 4.12. The other explanation for the behaviour of the trailing expansion wave must be the shaping of the transition section which becomes more effectual as the diaphragm is located further upstream. The same trailing expansion wave behaviour occurs in the linear and convex drivers as observed in Figure A.5 and Figure A.12.

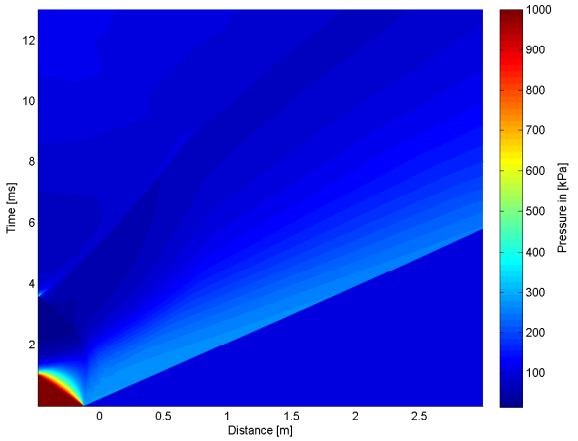
The observed behaviour of the contact surface generated by the concave driver sections is almost identical to that of the comparative linearly diverging drivers. Comparing Figure 4.35 and Figure 4.36 to Figure 4.10 and Figure 4.11 it can be seen that the contact surfaces generated by the concave drivers exhibit similar behaviour in that the contact surfaces propagate some distance down the tube, before being sucked back upstream by the region of expansion and then remaining stationary for the remainder of the simulation after interacting with the secondary shock. There are slight differences in the behaviour of the concave driver generated contact surfaces in that these contact surfaces tend to travel less down the tube and get sucked back further upstream before interacting with the secondary shock than the comparative contact surfaces generated by the linearly diverging driver sections. The increased pull pack of the contact surface is an effect of the improved expansion wave reflection and focusing induced by the concave shaping of the drive section. Figure A.6 and Figure A.13

show that the contact surfaces generated by the linear and convex drivers act in much the same way.

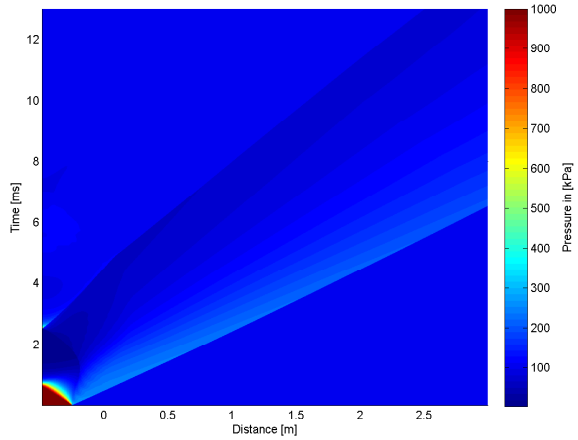
Just as was the case with the linearly diverging driver sections, it was noted that the further upstream the diaphragm was placed the quicker the reflected expansion waves would catch up with the shock front and the slower the shock front would become. This is indicated in Figure 4.37 by the reducing thickness of the red colour band behind the shock front with decreasing driver length caused by the diaphragm being placed further upstream as well as by the increasing slope of the line marking the location of the shock front relative to the horizontal axes.



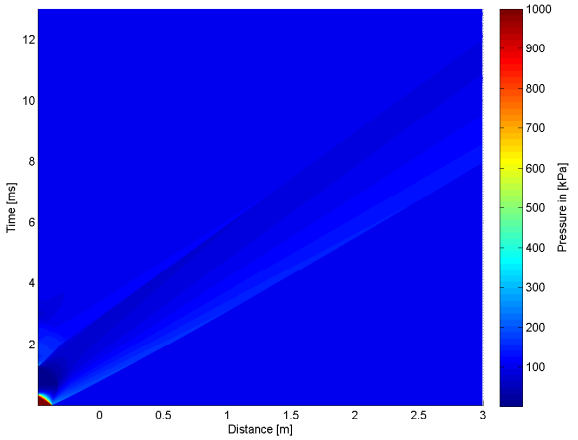
4.34 (a): 100% of Concave Driver Length 10*bar*



4.34 (b): 75% of Concave Driver Length 10*bar*

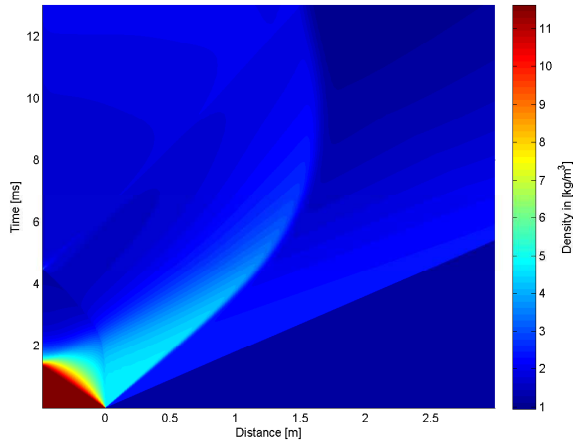


4.34 (c): 50% of Concave Driver Length 10*bar*

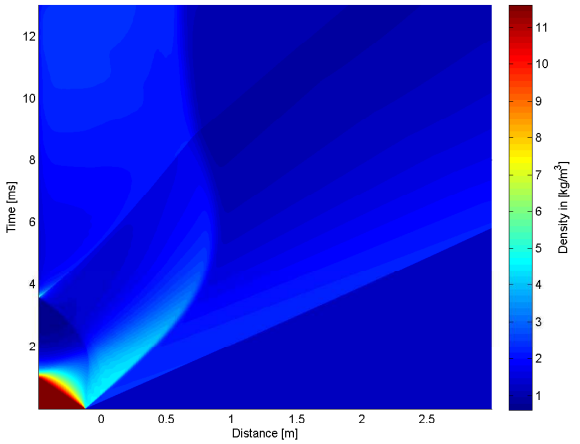


4.34 (d): 25% of Concave Driver Length 10*bar*

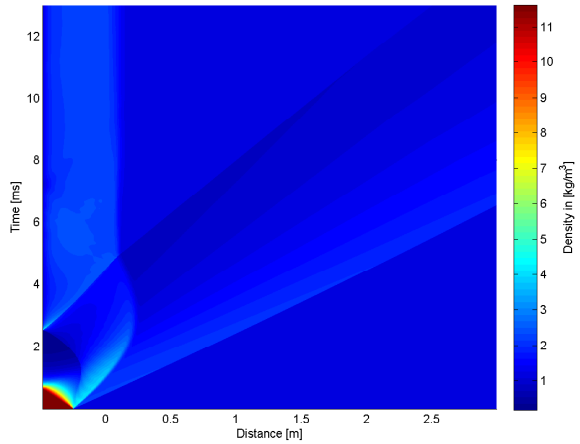
Figure 4.34: X-T Diagram for Varying Diaphragm Locations in the Concave Driver Section (Pressure)



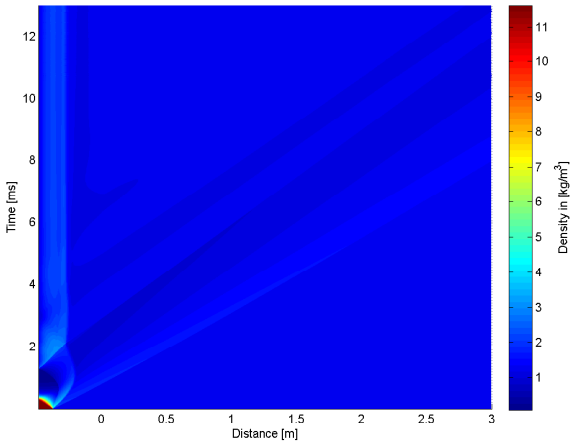
4.35 (a): 100% of Concave Driver Length 10*bar*



4.35 (b): 75% of Concave Driver Length 10*bar*

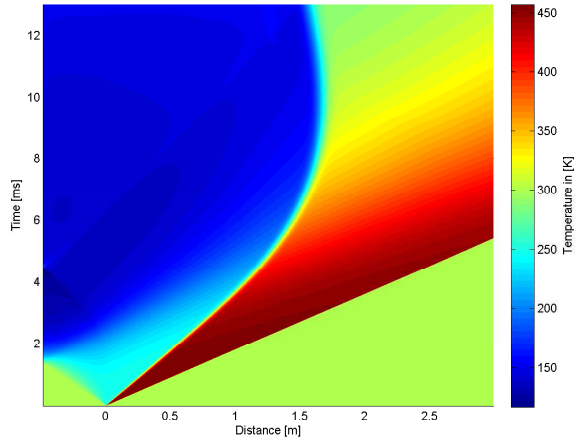


4.35 (c): 50% of Concave Driver Length 10*bar*

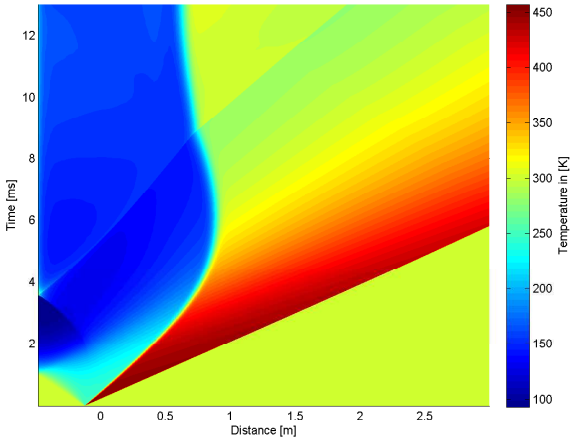


4.35 (d): 25% of Concave Driver Length 10*bar*

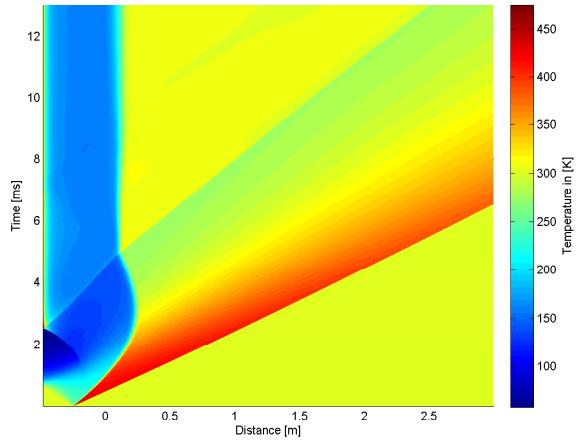
Figure 4.35: X-T Diagram for Varying Diaphragm Locations in the Concave Driver Section (Density)



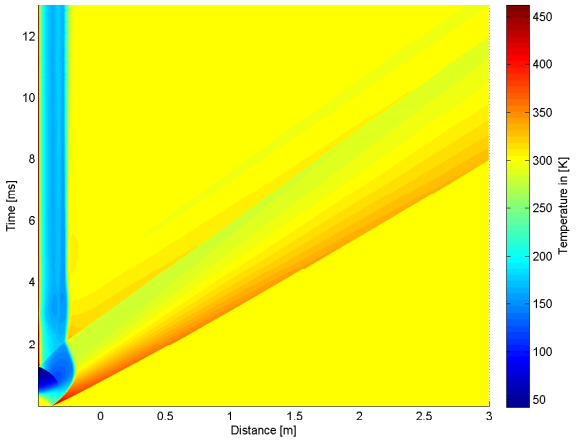
4.36 (a): 100% of Concave Driver Length 10*bar*



4.36 (b): 75% of Concave Driver Length 10*bar*

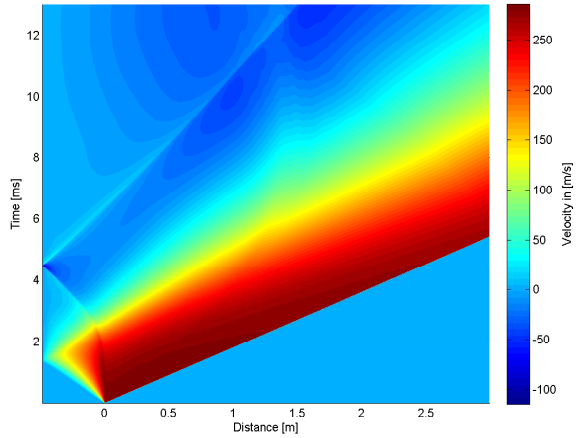


4.36 (c): 50% of Concave Driver Length 10*bar*

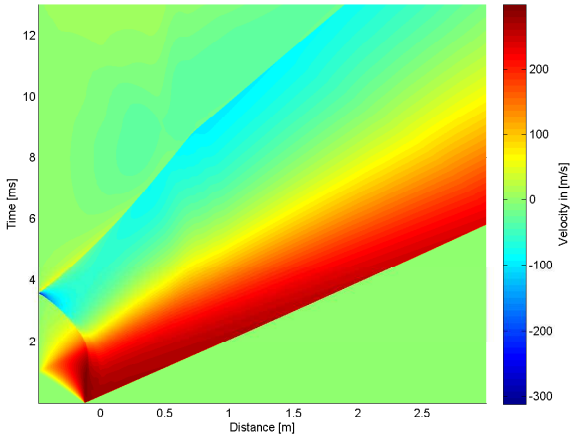


4.36 (d): 25% of Concave Driver Length 10*bar*

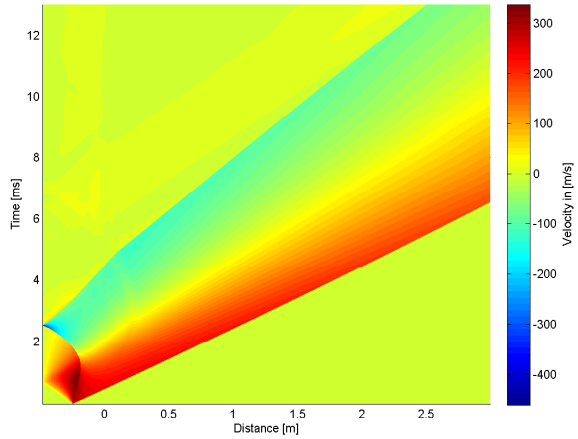
Figure 4.36: X-T Diagram for Varying Diaphragm Locations in the Concave Driver Section (Temperature)



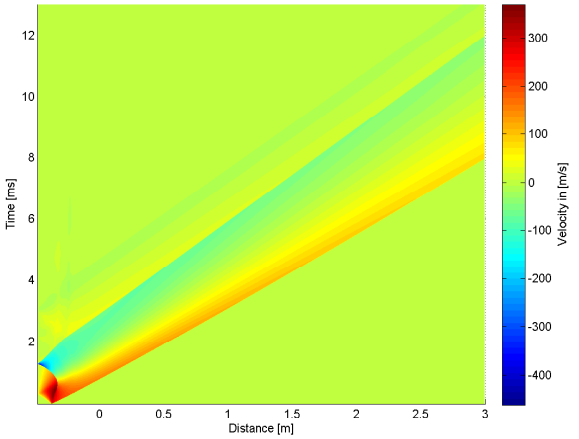
4.37 (a): 100% of Concave Driver Length 10*bar*



4.37 (b): 75% of Concave Driver Length 10*bar*



4.37 (c): 50% of Concave Driver Length 10*bar*



4.37 (d): 25% of Concave Driver Length 10*bar*

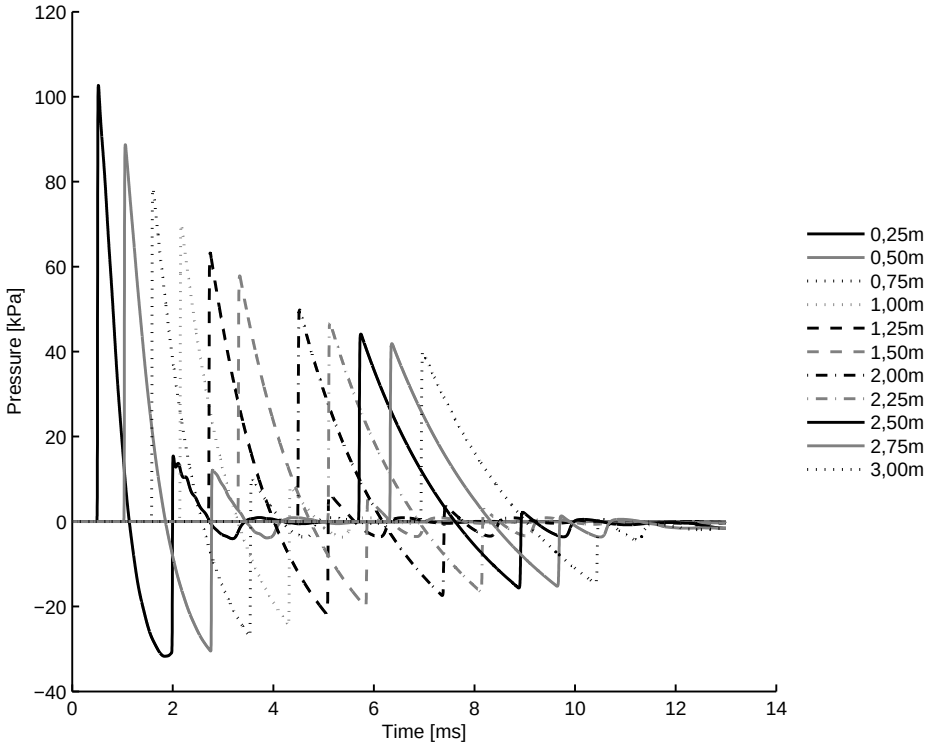
Figure 4.37: X-T Diagram for Varying Diaphragm Locations in the Concave Driver Section (Velocity)

4.1.7 Varying Driver Section and Transition Section Lengths

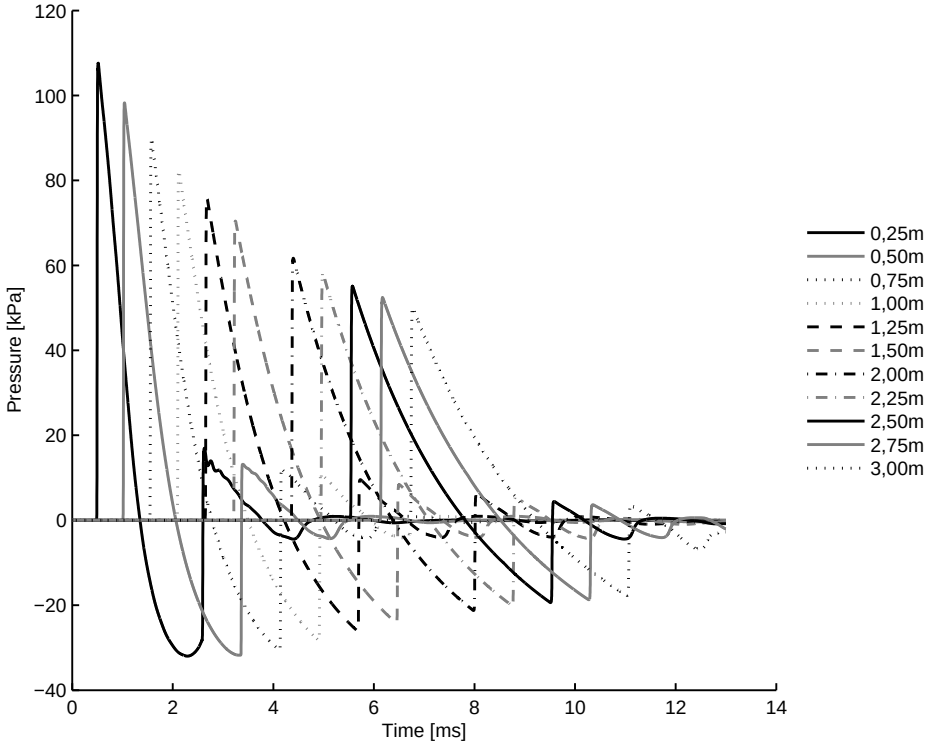
Once the best relative location of the diaphragm was determined, it was decided that the effects of increasing both the length of the driver section and the transition sections, while keeping the relative diaphragm location fixed, on the generation of blast waves should be assessed. This assessment was performed by simulating driver and transition sections having combined lengths of 50%, 75%, 100%, 125%, 150% of the 500mm length of the driver tested in the previous section, subsection 4.1.6 and with the diaphragm located at 33% of this length. As with the varying diaphragm location simulations, the varying driver section and transition section length simulations were run with the initial driver pressure being set to 10bar.

The flow characteristics induced by varying the driver and transition lengths was much the same for the concave, linear and convex driver sections, as was the case for the vary diaphragm simulations, and therefore, as before, only the data from the concave driver simulations will be examined in this section while the data from the linear and convex simulations is presented in Appendix B. Again it was challenging to make a direct comparison between the linearly diverging, vary diaphragm location and varying driver and transition section length cases as the angles and lengths don't directly correlate. However by comparing Figure 4.38 (a) to Figure 4.5 (d), Figures 4.38 (b) and 4.38 (c) to Figure 4.5 (c) and Figure 4.38 (e) to Figure 4.5 (b) some attempt can be made to compare the varying driver and transition section lengths cases to the linearly diverging cases. The same can be done for the varying diaphragm location cases by comparing Figures 4.38 (b) and 4.38 (e) to Figure 4.31 (d) and Figure 4.31 (c) respectively.

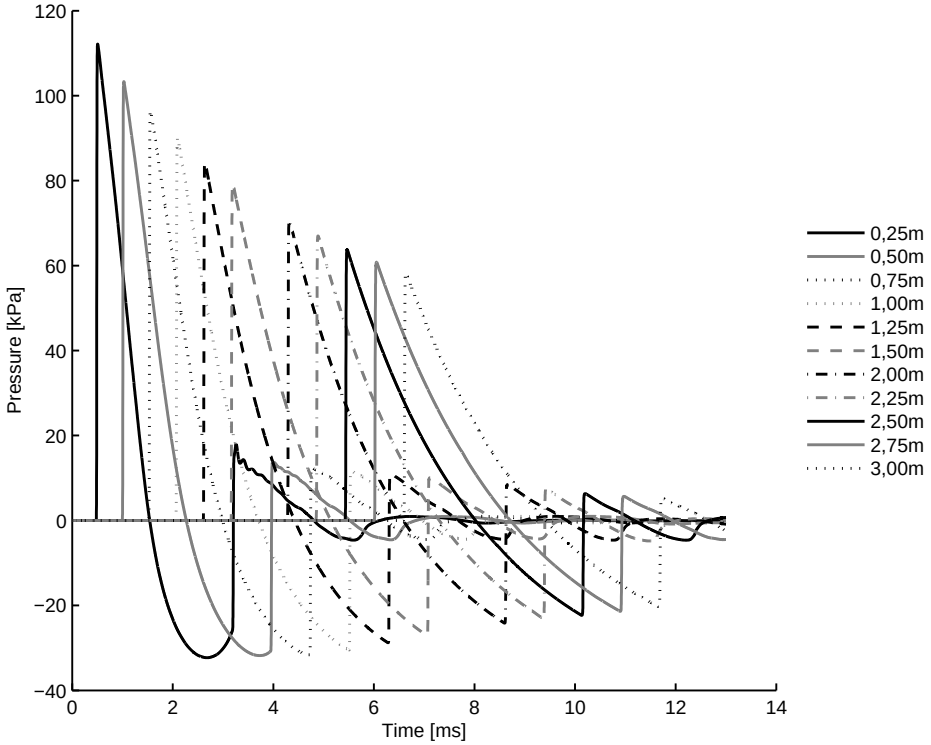
Looking at the pressure plots in Figure 4.38 and comparing them to the pressure plots in Figure 4.5, immediately it becomes apparent that unlike all the previous cases, despite having the same driver pressure and comparable driver lengths to the linearly diverging sections, the concave shaped section with varying driver a transition lengths produces blast waves having peak overpressures much lower than the comparable linear diverging drivers. Another major difference between the varying driver and transition section length simulations and the previous cases as was observed in Figure 4.38 and Figure 4.39, was that reducing the length of the driver section, as in the previous cases, reduces the peak overpressure of the blast wave however, unlike the previous cases, the extent to which it does so is much reduced. Comparing Figures 4.38 (e), 4.31 (c) and 4.5 (b) it can be seen that despite having similar lengths, the elongated concave profile process a blast wave having the lowest peak overpressure, steepest pressure decay following the shock front, the shortest duration overpressure, the highest minimum pressure and the largest magnitude secondary shock. This is indicative of the improved expansion reflection and focusing that takes place when the the diaphragm is located at 33% of the combined driver and transition section lengths. Similar observations were made when comparing Figures 4.38 (b), 4.31 (d) and 4.5 (c) however in that comaprison the configuration with the diaphragm located at 25% of the driver length produced the blast wave with the lowest peak overpressure. This reduced overpressure is as a result of the increased rate of area change that occurs further upstream of the driver section profile. Looking at the Figure B.1 and Figure B.8 in Appendix B it can be seen that similar observations can be made for the linear and convex profiles.



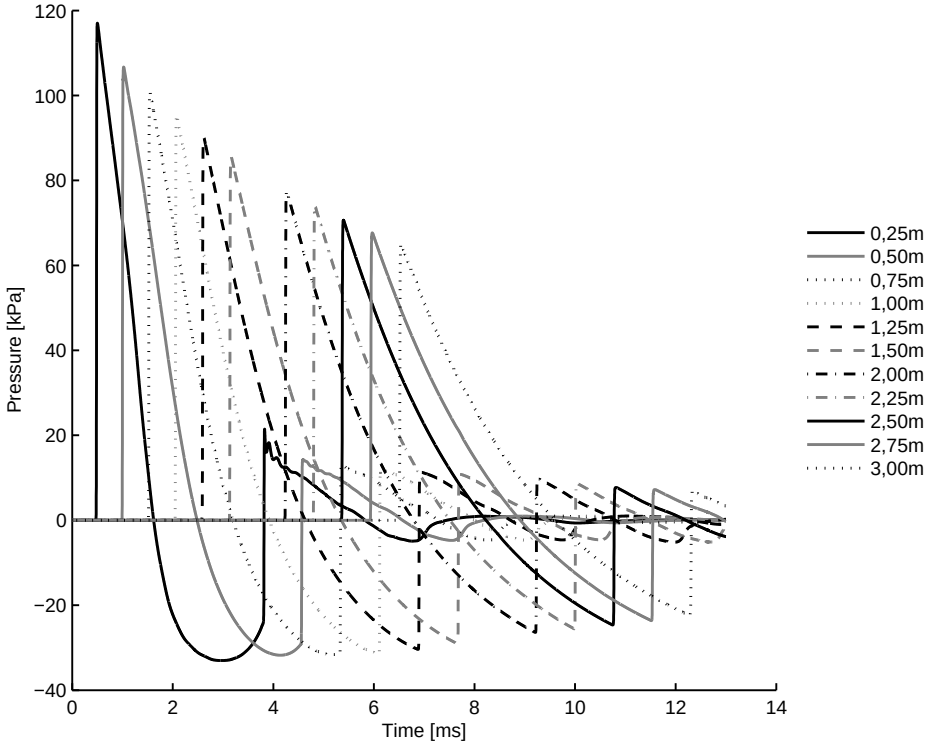
4.38 (a): 50% of Concave Driver and Transition Length 10*bar*



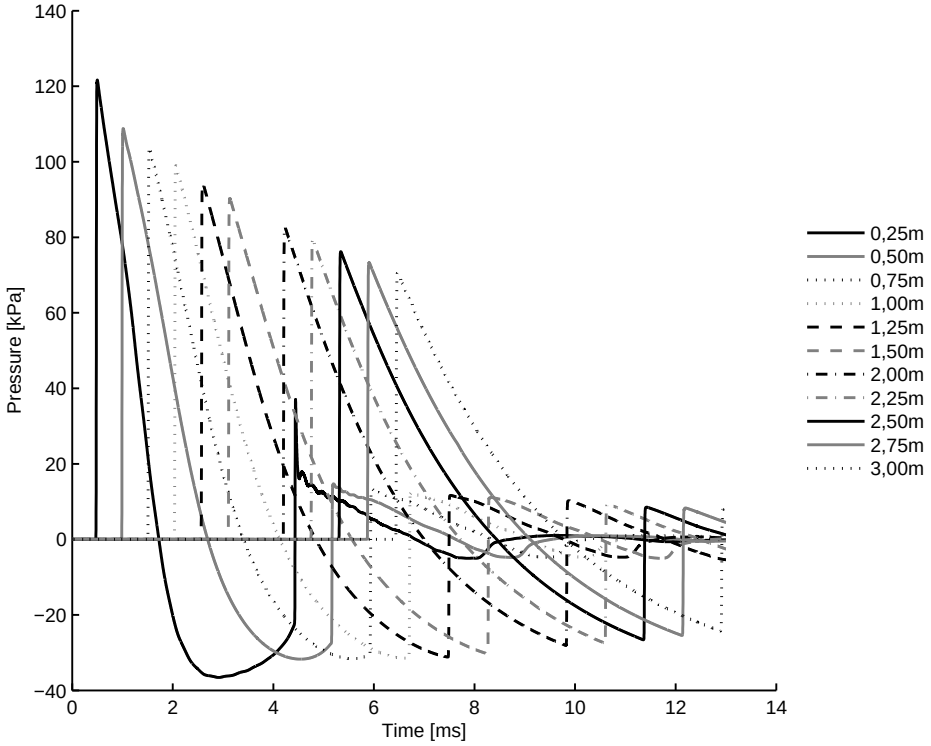
4.38 (b): 75% of Concave Driver and Transition Length 10*bar*



4.38 (c): 100% of Concave Driver and Transition Length 10*bar*



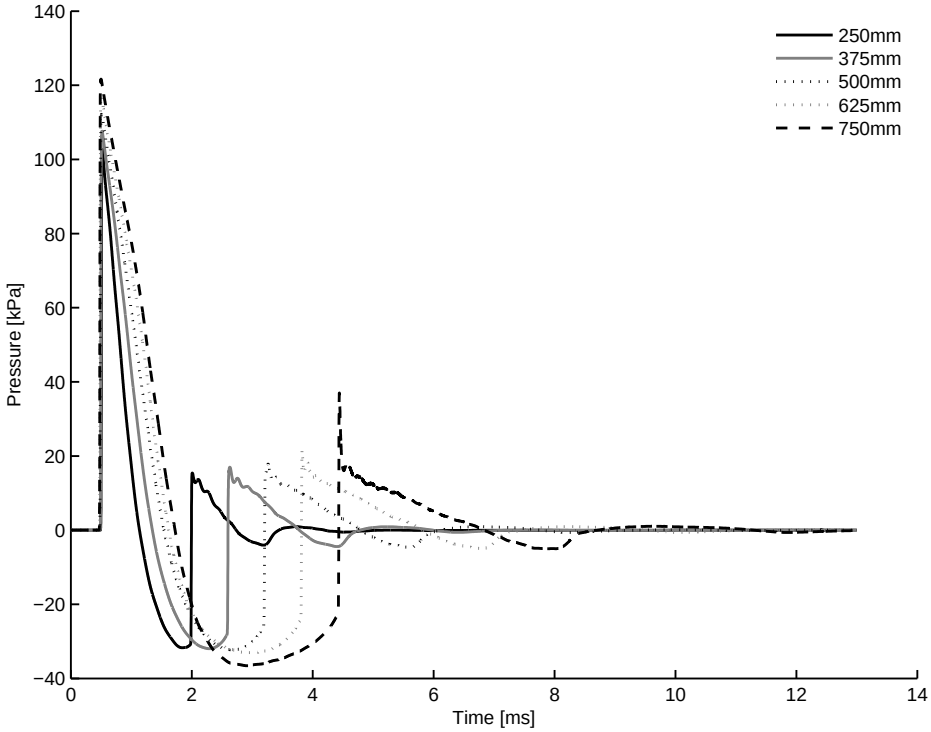
4.38 (d): 125% of Concave Driver and Transition Length 10*bar*



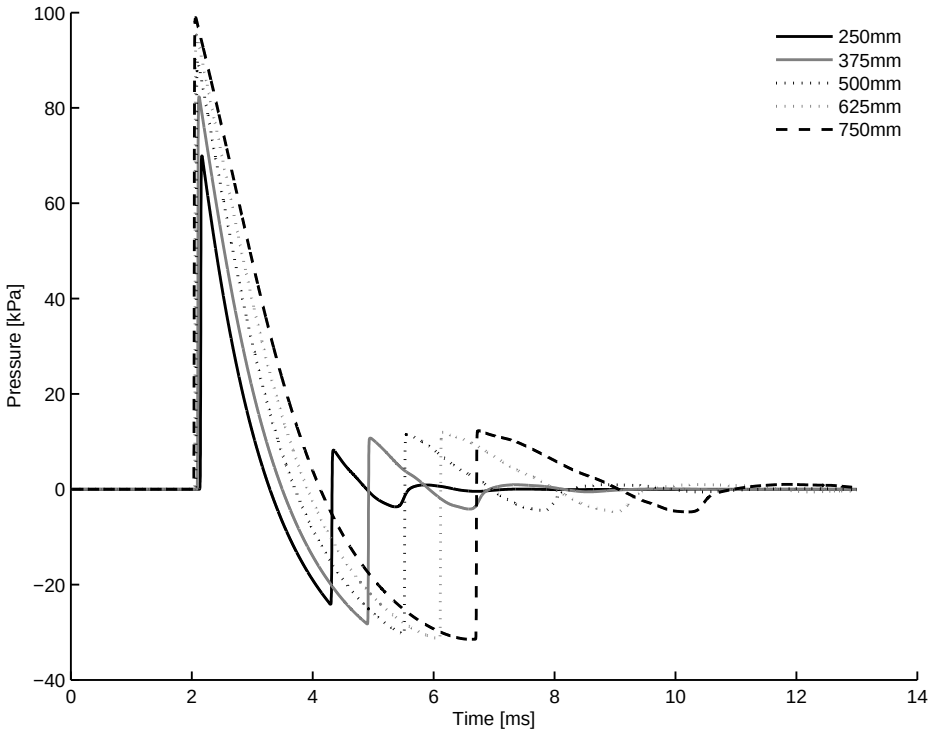
4.38 (e): 150% of Concave Driver and Transition Length 10*bar*

Figure 4.38: The Development of the Blast Pressure Profile for Varying Concave Driver and Transition Length

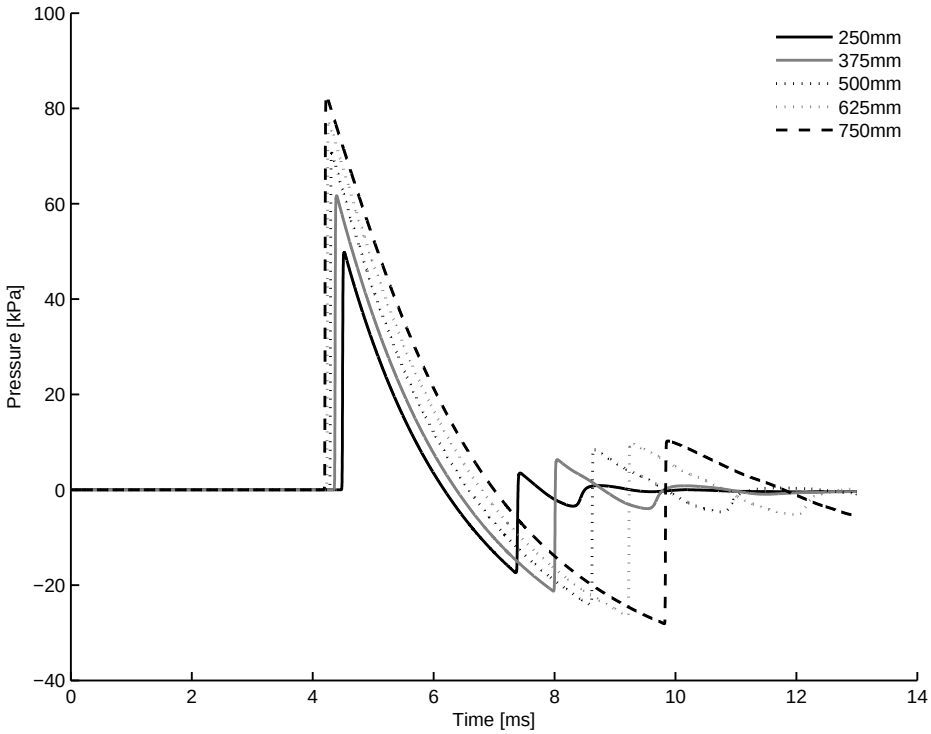
Figure 4.39 shows the pressures measured by monitors placed $0.25m$, $1.00m$, $2.00m$ and $3.00m$ downstream of the diaphragm for all five driver section and transition section length configurations plotted on the same set of axes. Figure 4.39 can be used to make a comparison between various driver and transition length configurations to ascertain what effect varying the length of the driver and transition sections has on the blast wave generation and development. Looking at the sub-plots in Figure 4.39 it can be seen that decreasing the length of the driver and transition sections has the tendency to steepen the gradient of the pressure decay trailing the shock front as well as to reduce the duration of both the overpressure and expansion phases of the blast wave. This is similar to the behaviour exhibited by increasing the angle of divergence of the linearly diverging drivers, as shown in Figure 4.3, however, the effect is much less marked in the case of the varying driver and transition section lengths. Looking at Figures 4.39 (c) and 4.39 (d) other similarities to the linearly diverging driver cases were noted in that it can be seen that as the generated blast waves propagate down the tube, the shorter the driver and transition sections, the quicker the velocity of the blast wave decays, the lower the peak overpressure of the blast wave, the higher the minimum expansion pressure and the smaller the magnitude of the secondary shock wave. Again however, the differences are markedly less for the varying driver and transition section length simulations than the comparable linearly diverging driver section and varying diaphragm location simulations. If one accounts for the increased peak overpressures and reduced minimum expansion pressures, the five different driver and transition length produce blast waves having almost identical pressure decays and overall shapes. The same behaviour can be observed for the linear and convex drivers in Figure B.2 and Figure B.9.



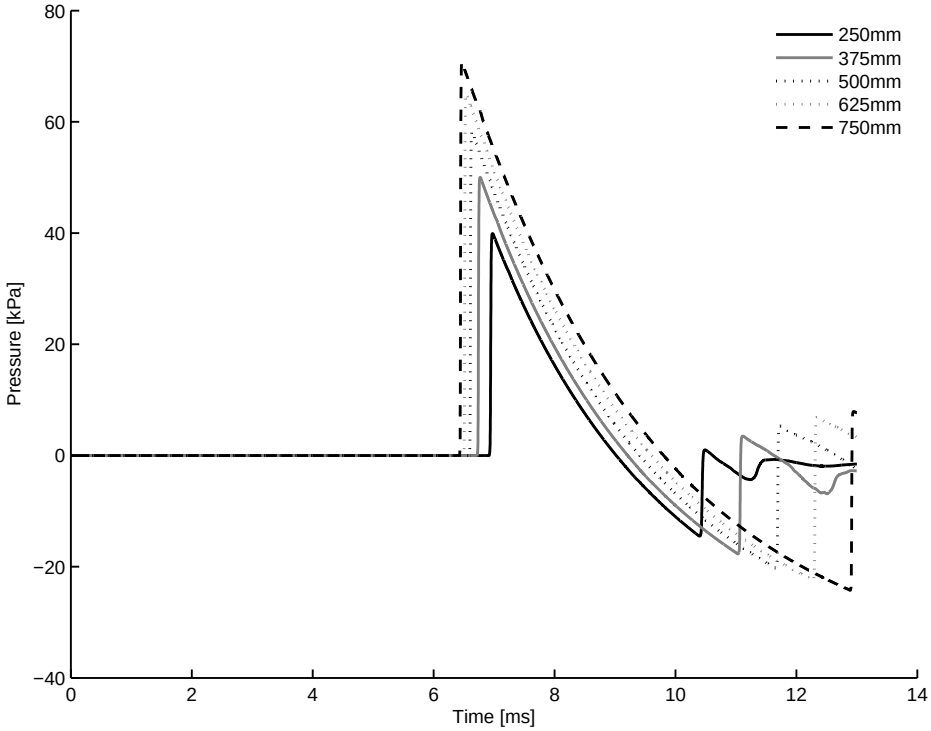
4.39 (a): $0.25m$ $10bar$



4.39 (b): $1.00m$ $10bar$



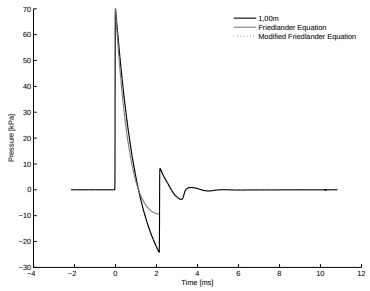
4.39 (c): $2.00m$ $10bar$



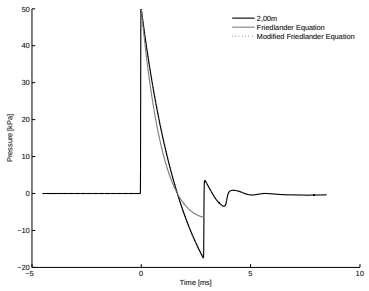
4.39 (d): $3.00m$ $10bar$

Figure 4.39: The Effect of Varying the Concave Driver and Transition Section Length on the Pressure Profile

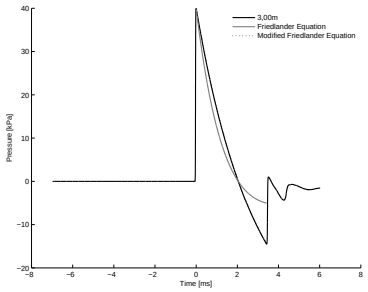
In Figure 4.40, the blast wave pressure profiles generate by the driver and transition sections having combined lengths of 50%, 75%, 100%, 125%, 150% are plotted against the comparative Friedlander and Modified Friedlander pressure profiles. As was the case with the varying diaphragm location, it can be seen in Figure 4.40 that there is a disparity between the generated blast wave pressure profiles and the Friedlander pressure profile due to the inability of the Friedlander equation to account for secondary shocks. Looking at Figures 4.40 (c), 4.40 (f), 4.40 (i), 4.40 (l) and 4.40 (o) it can be seen that all 5 driver and transition section lengths generated realistic blast waves which is inferred by the almost perfect alignment of the generated pressure profiles with the corresponding Modified Friedlander profile. This implied that as long the diaphragm location of approximately 33% as well as the overall shape of the profile is maintained, various blast wave configurations can be generated by a similarly shaped driver profile by increasing the length of both the driver and transition section proportionally. This makes varying the driver and transition sections lengths, along side varying the driver pressure, the best methods for obtaining the desired blast wave pressure profile. The linear and convex shaped drivers, regardless of length, also produced realistic blast wave as can be seen in Figure B.3 and Figure B.10.



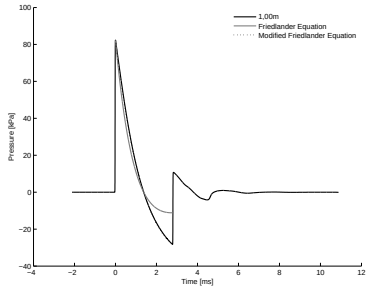
4.40 (a): 50% of Concave Driver and Transition Length 10bar 1.00m



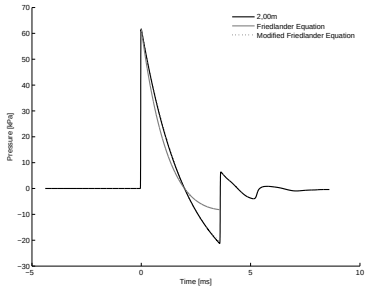
4.40 (b): 50% of Concave Driver and Transition Length 10bar 2.00m



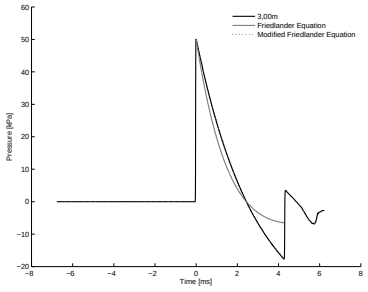
4.40 (c): 50% of Concave Driver and Transition Length 10bar 3.00m



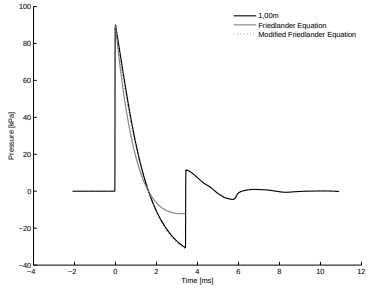
4.40 (d): 75% of Concave Driver and Transition Length 10bar 1.00m



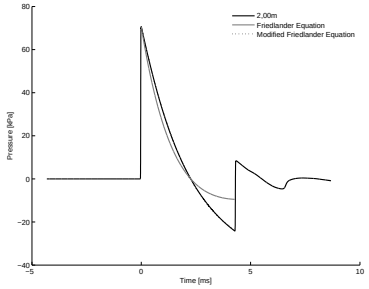
4.40 (e): 75% of Concave Driver and Transition Length 10bar 2.00m



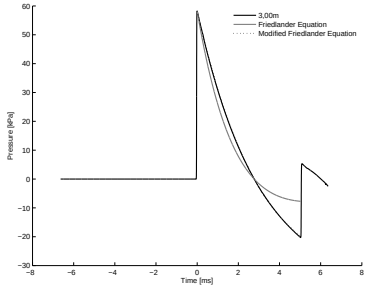
4.40 (f): 75% of Concave Driver and Transition Length 10bar 3.00m



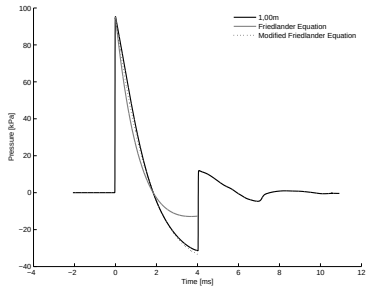
4.40 (g): 100% of Concave Driver and Transition Length 10bar 1.00m



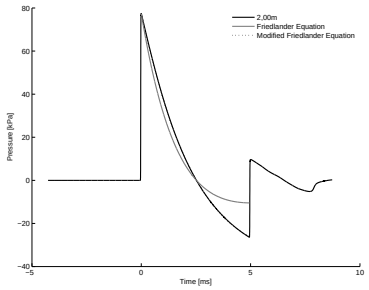
4.40 (h): 100% of Concave Driver and Transition Length 10bar 2.00m



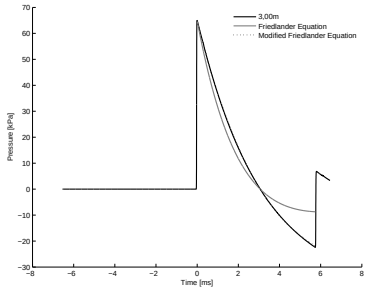
4.40 (i): 100% of Concave Driver and Transition Length 10bar 3.00m



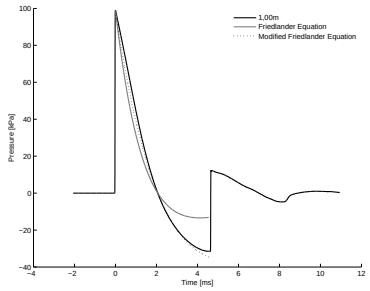
4.40 (j): 125% of Concave Driver and Transition Length 10bar 1.00m



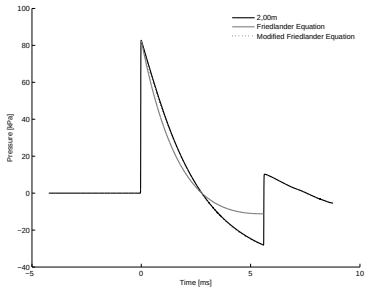
4.40 (k): 125% of Concave Driver and Transition Length 10bar 2.00m



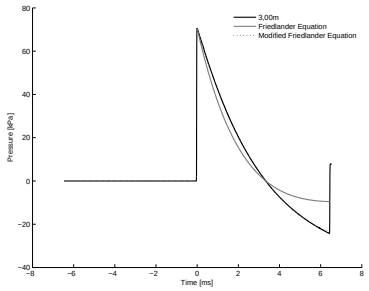
4.40 (l): 125% of Concave Driver and Transition Length 10bar 3.00m



4.40 (m): 150% of Concave Driver and Transition Length 10bar 1.00m



4.40 (n): 150% of Concave Driver and Transition Length 10bar 2.00m



4.40 (o): 150% of Concave Driver and Transition Length 10bar 3.00m

Figure 4.40: Comparing the Effect of Varying the Concave Driver and Transition Section Length on the Friedlander Pressure Profile

The x-t diagrams plotting the effects on pressure, density, temperature and velocity induced in the flow by varying the driver and transition lengths of the concave shaped section are plotted in Figure 4.41, Figure 4.42, Figure 4.43 and Figure 4.44. Looking at Figure 4.41 it can be seen that just as was observed with the varying diaphragm simulations, the x-t pressure plots for which are shown in Figure 4.34, regardless of the driver and transition

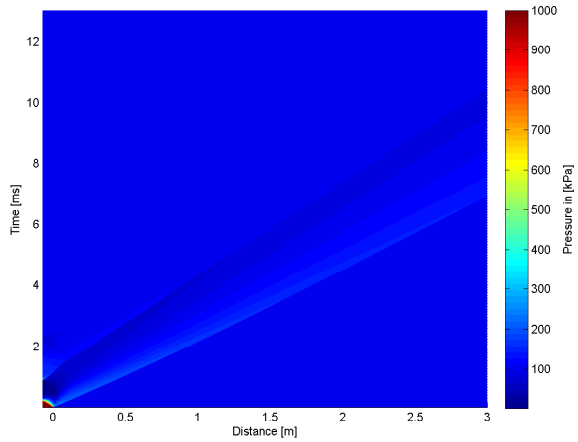
section lengths, expansion reflection and focusing is induced in the driver section almost immediately after the diaphragm is burst and a smooth pressure decay results behind the shock front as shown by the darkening blue band behind the shock front. Looking at and comparing the darkening blue bands behind the shock front in each of the different driver and transition section length cases in Figure 4.34, it can be seen that regardless of the driver and transition length the spacing of the colour bands does not change but rather the number of bands changes. The corroborates the blast pressure profiles in Figure 4.39 in that it shows that keeping the concave shape and driver and transition sections proportional while increase the lengths of both sections results in almost identical decay profiles as a result of very similar expansion reflection and focusing. Like the varying diaphragm location simulations having the diaphragm location set at 50% and 25%, where it was observed that the further upstream the diaphragm location and therefore the shorter the driver section, the further downstream the trailing expansion would travel, for the various driver and transition lengths the trailing expansion travelled downstream and the distance was proportional to the length of the driver section. Again this motion of the trailing expansion is induced by both the high velocities induced in the flow at this location as observed in Figure 4.44 as well as the concave shaping of the driver and transition sections. Similar behaviour was exhibited by the linear and convex profiles as shown in Figure B.7 and Figure B.14.

Upon comparing the temperature x-t diagrams in Figure 4.43 to the temperature x-t diagrams for the linear diverging driver section and vary diaphragm location cases contained in Figure 4.11 and Figure 4.36 respectively it was immediately noticed that unlike the two aforementioned cases, were there were stark flow differences between the various diverging angle driver section cases and diaphragm location cases, the flow features observed for the varying driver and transition section cases looked almost identical. The reasons for this are twofold. The first reason being that the range of the lengths of the drivers simulated in the varying driver and transition lengths analysis is about half of that of the the linear diverging driver sections and varying diaphragm sections. The second reason is that as mentioned above, keeping the concave shape of the driver and transition sections while proportionally increasing the length of these sections induces similar expansion reflection and focusing features.

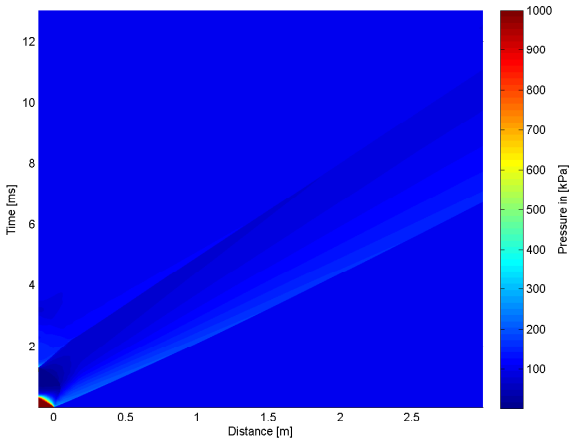
Looking at Figure 4.42 and Figure 4.43, it can be seen that the focusing that takes place in the varying driver and transition lengths simulations is slightly different to that observed occurring in the different varying linearly diverging driver, as shown in Figure 4.43 by the increasing temperature at the focus point, and varying diaphragm location cases in that as the driver and transition sections are lengthened, the intensity of the focusing that occurs increases and the magnitude of induced secondary shock is increased as well a result, which is depicted in Figure 4.42 by the increase size and lightening of the blue band trailing the

secondary shock wave. This is due to the increased distance and therefore time the expansion waves have to reflect in combination with the improved expansion reflection induced by the concave shaped driver profile.

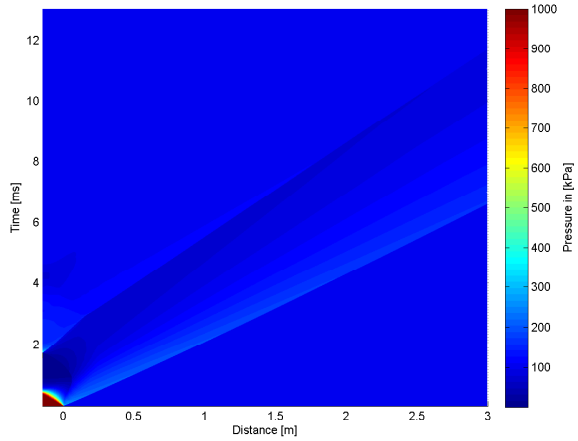
The behaviour of the contact surface for all five driver and transition length cases, which can be seen in Figure 4.42 and Figure 4.43 was found to be much the same as the contact surface generated by the varying diaphragm location cases where the diaphragm was located at 25% and 50% which are shown in Figure 4.36 (d) and Figure 4.36 (d) respectively, in that it travelled downstream, got sucked back upstream and then remained stationary upon interacting with the secondary shock. Again, the distance the contact surface travelled down the blast tube increased with increasing driver section length.



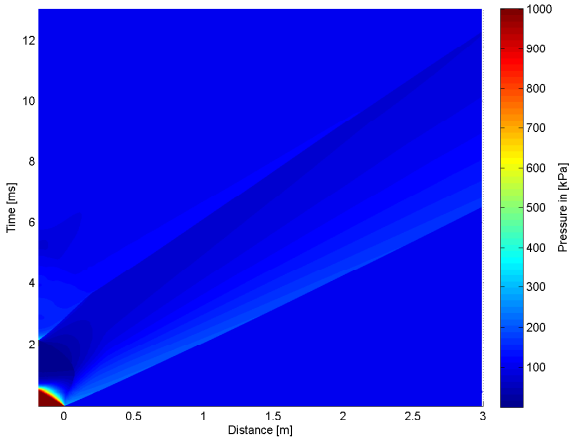
4.41 (a): 50% of Concave Driver and Transition Length 10*bar*



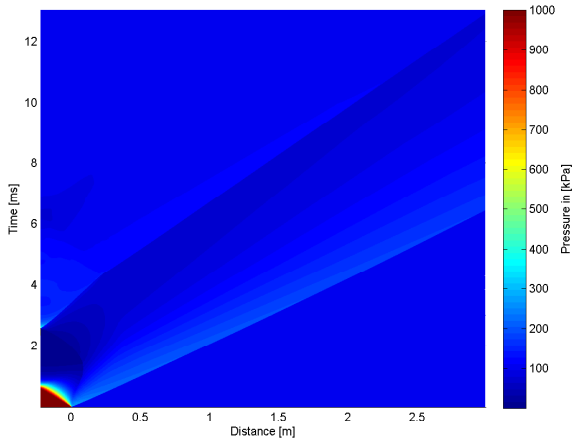
4.41 (b): 75% of Concave Driver and Transition Length 10*bar*



4.41 (c): 100% of Concave Driver and Transition Length 10*bar*

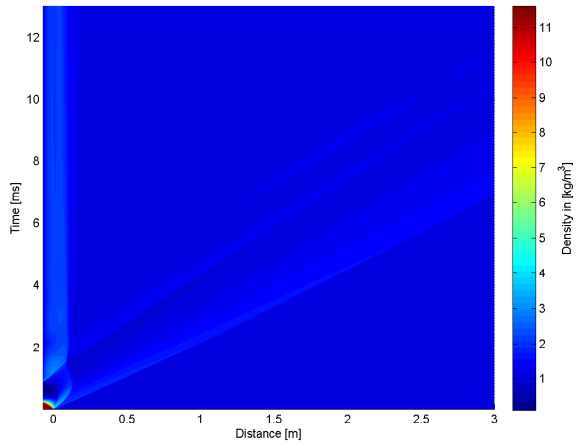


4.41 (d): 125% of Concave Driver and Transition Length 10*bar*

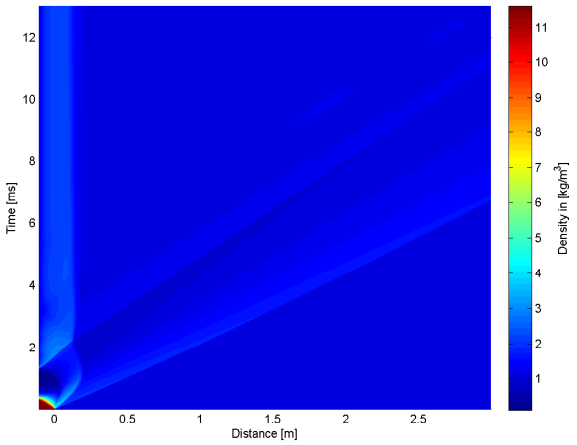


4.41 (e): 150% of Concave Driver and Transition Length 10*bar*

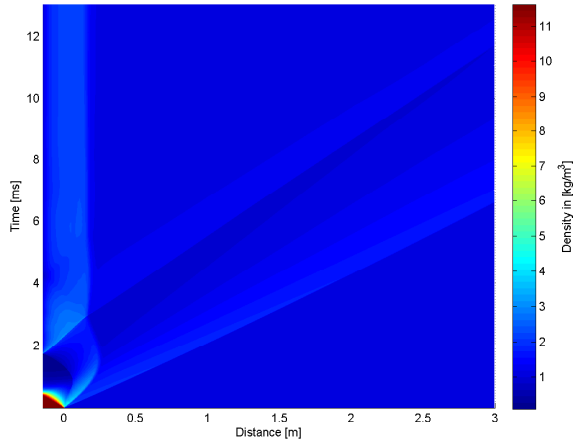
Figure 4.41: X-T Diagram for Varying the Concave Driver and Transition Section Length (Pressure)



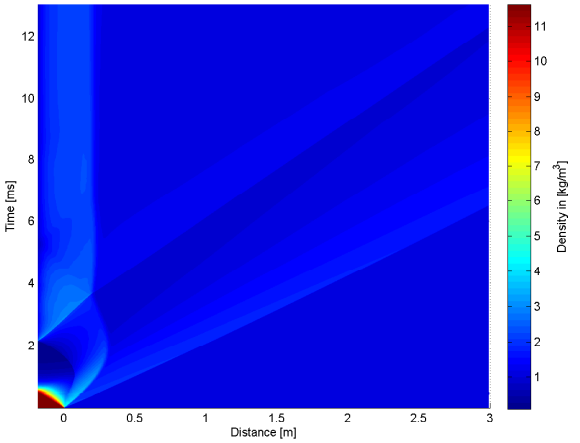
4.42 (a): 50% of Concave Driver and Transition Length 10*bar*



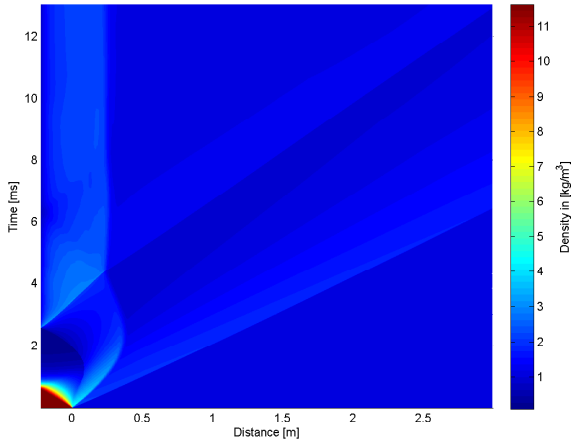
4.42 (b): 75% of Concave Driver and Transition Length 10*bar*



4.42 (c): 100% of Concave Driver and Transition Length 10*bar*

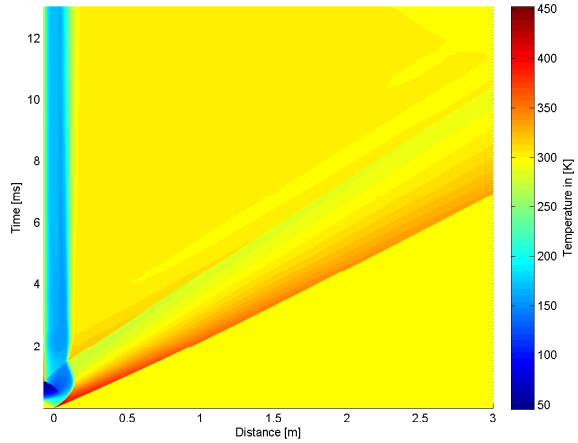


4.42 (d): 125% of Concave Driver and Transition Length 10*bar*

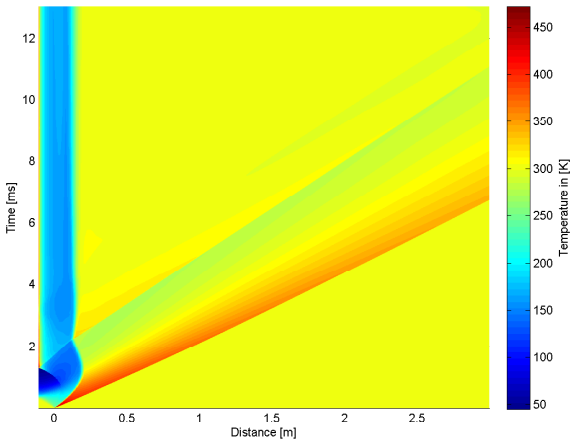


4.42 (e): 150% of Concave Driver and Transition Length 10*bar*

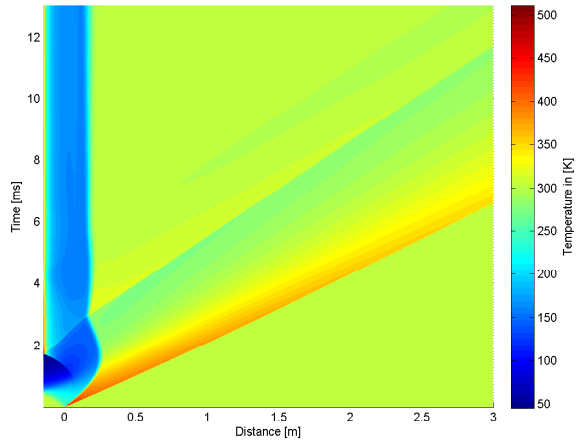
Figure 4.42: X-T Diagram for Varying the Concave Driver and Transition Section Length (Density)



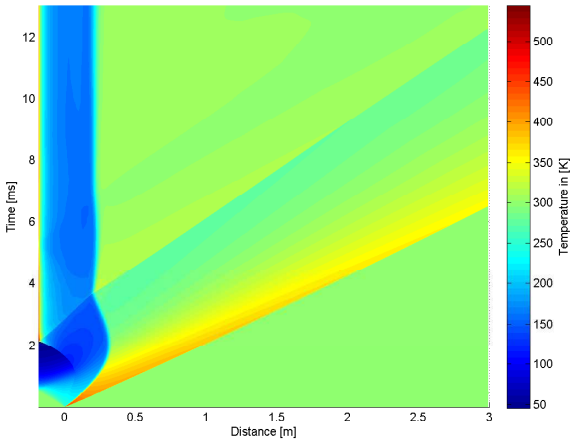
4.43 (a): 50% of Concave Driver and Transition Length 10*bar*



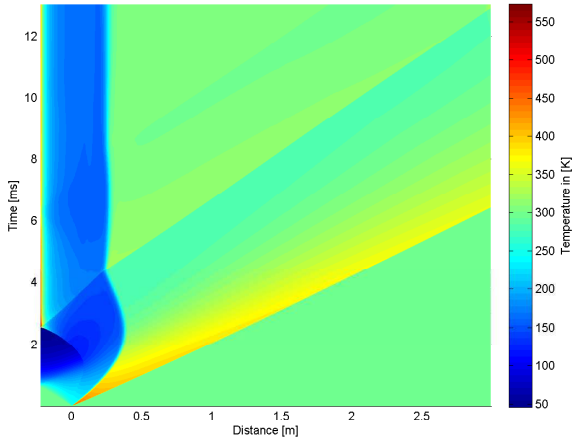
4.43 (b): 75% of Concave Driver and Transition Length 10*bar*



4.43 (c): 100% of Concave Driver and Transition Length 10*bar*

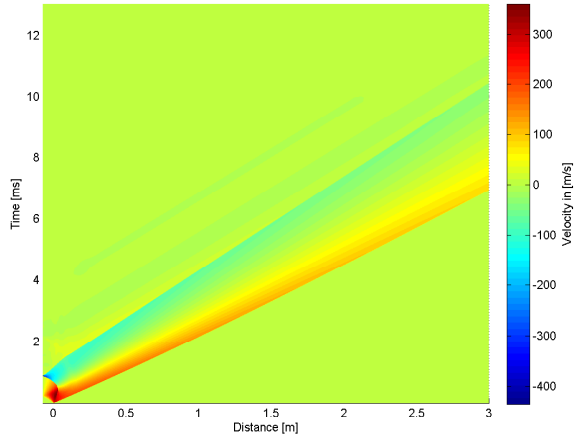


4.43 (d): 125% of Concave Driver and Transition Length 10*bar*

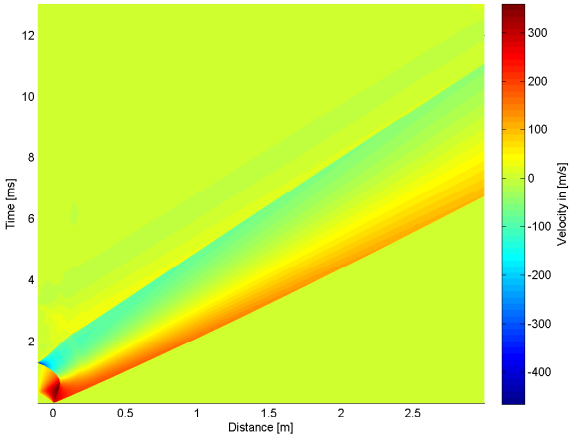


4.43 (e): 150% of Concave Driver and Transition Length 10*bar*

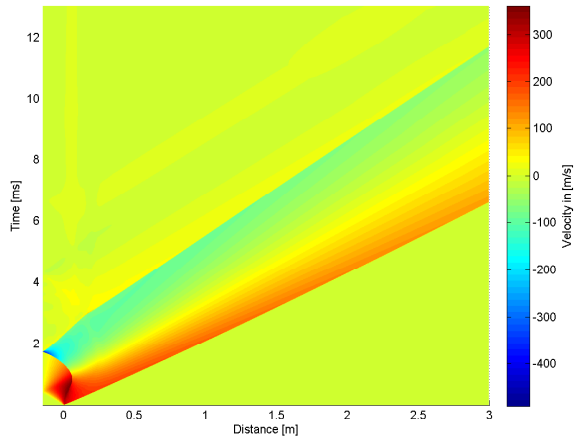
Figure 4.43: X-T Diagram for Varying the Concave Driver and Transition Section Length (Temperature)



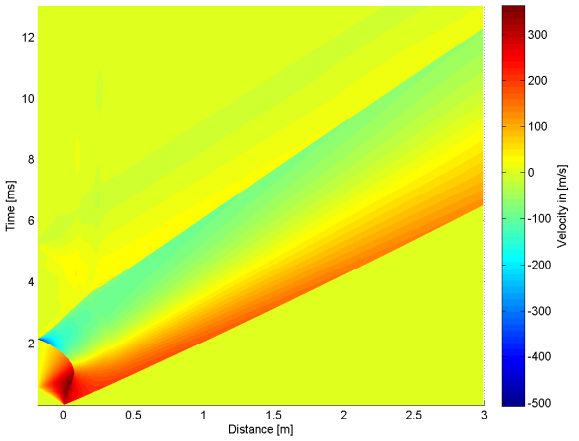
4.44 (a): 50% of Concave Driver and Transition Length 10*bar*



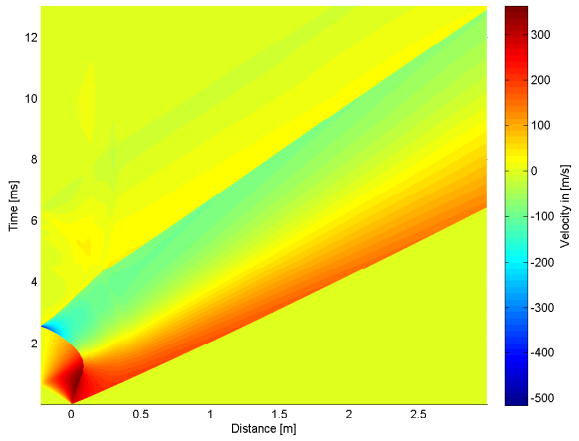
4.44 (b): 75% of Concave Driver and Transition Length 10*bar*



4.44 (c): 100% of Concave Driver and Transition Length 10*bar*



4.44 (d): 125% of Concave Driver and Transition Length 10*bar*



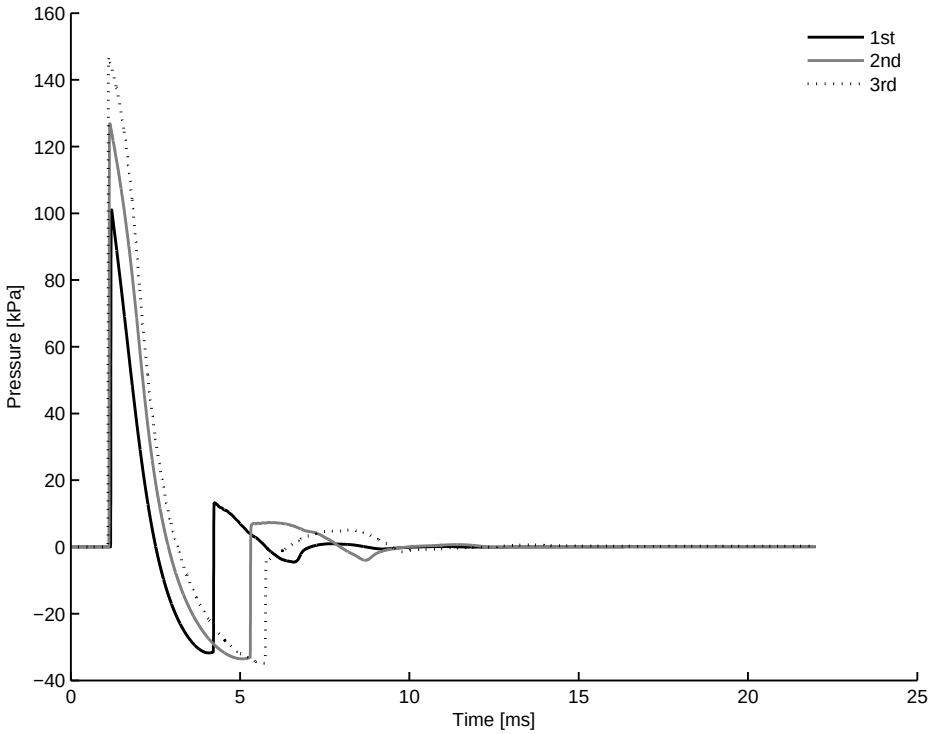
4.44 (e): 150% of Concave Driver and Transition Length 10*bar*

Figure 4.44: X-T Diagram for Varying the Concave Driver and Transition Section Length (Velocity)

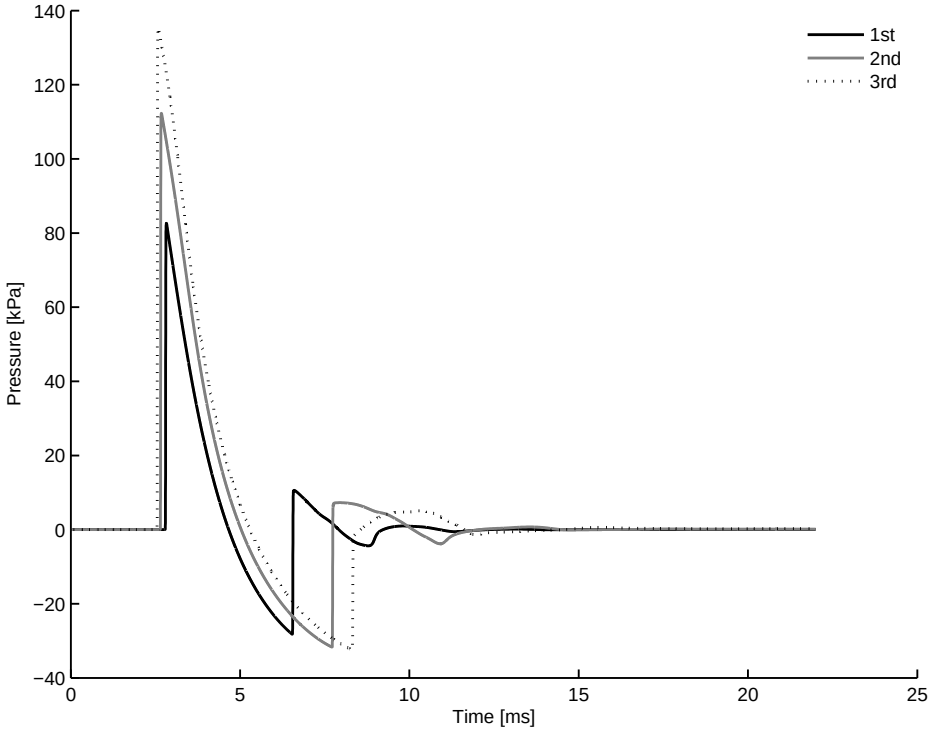
4.1.8 Effect of Blast Tube Length

Upon settling on a driver and transition length having a combined length of 500mm and diaphragm located at 33% for carry out the experimentation and validation of the blast tube design, it was decided to assess what the difference, if any, between the blast waves generated by the concave, linear and convex driver at three different driver pressures of $5bar$, $10bar$ and $15bar$ were. It was also decided to assess what effect the length of the expansion section would have on the development of the blast wave, even though the expansion section used for experimentation and validation of the blast tube design was limited to $3480mm$. The affects of expansion section length were assessed by simulating a blast tube having a $5m$ long open ended expansion section and placing monitors at $0.25m$ increments along the lengthwise centreline of the tube.

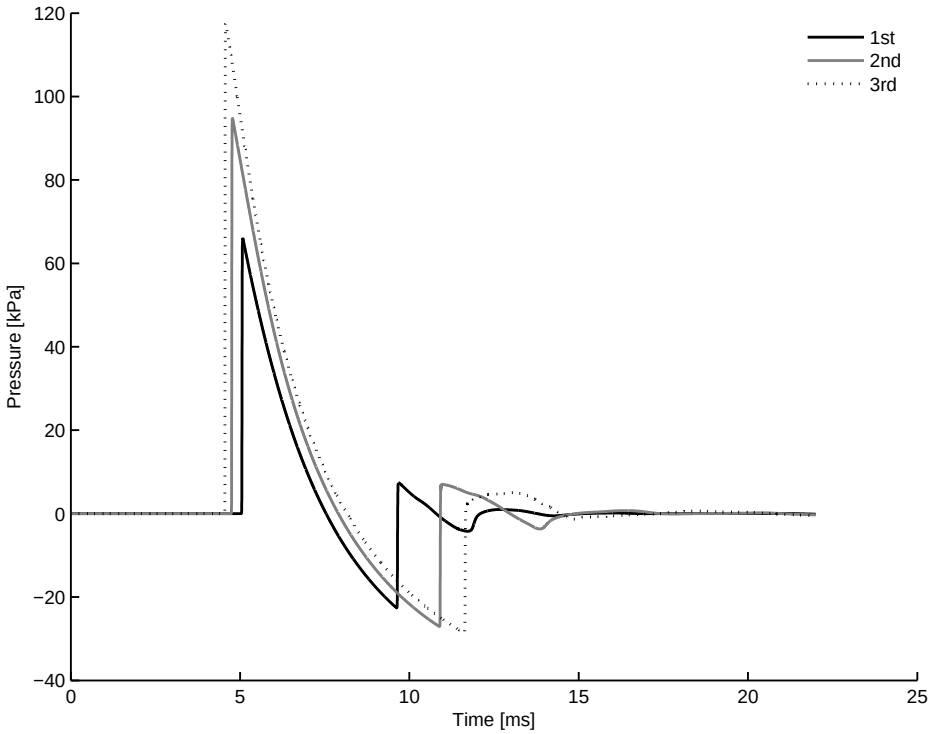
A comparison of the development of pressure profiles of the blast waves generated by the concave, linear and convex driver profiles having driver pressures of $10bar$ is displayed in Figure 4.45. The first notable thing in Figure 4.45 is the difference in peak overpressure of the three blast waves, with the convex driver producing a blast wave with the the highest peak overpressure while the concave driver generates a blast wave having the lowest peak overpressure of the three waves. Looking at Figure 4.30 it can be deduced that this as a result of the concave driver having the highest angle of inclination at the diaphragm location while the concave driver has the lowest. Another notable difference between the three blast waves was the blast and expansion phase durations with the blast wave generate by the convex driver profile having the longest overpressure and expansion phase durations while the blast wave induced by the concave profile had the shortest of both. This is due to the convex profile initially having the lowest angle of inclination but ending up with the highest at the back end while the concave profile has the highest angle of inclination at the diaphragm location but the lowest angle of inclination at the back corner. Similar to what was mentioned previously, this is due to the convex profile generated the more intense reflections at the back-end of the blast pressure profile thereby inducing a stronger shock front and a expansion phase. Accounting for the different peak overpressures, minimum expansion pressures and blast durations it was observed in Figure 4.45 that all three driver profiles produce waves with almost identical pressure decay profiles.



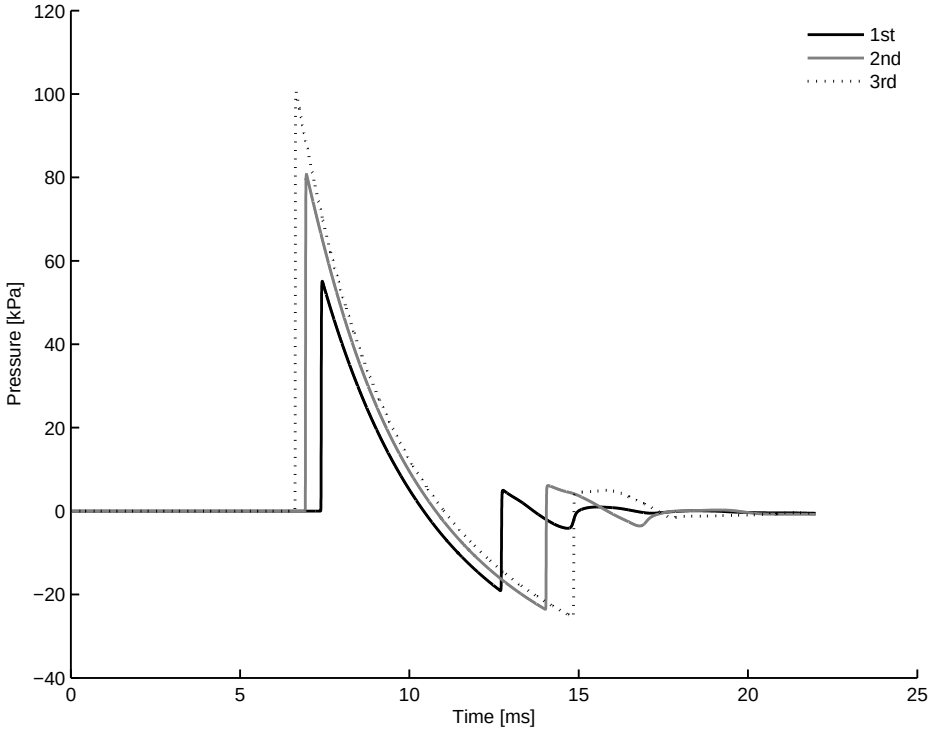
4.45 (a): $0.25m$



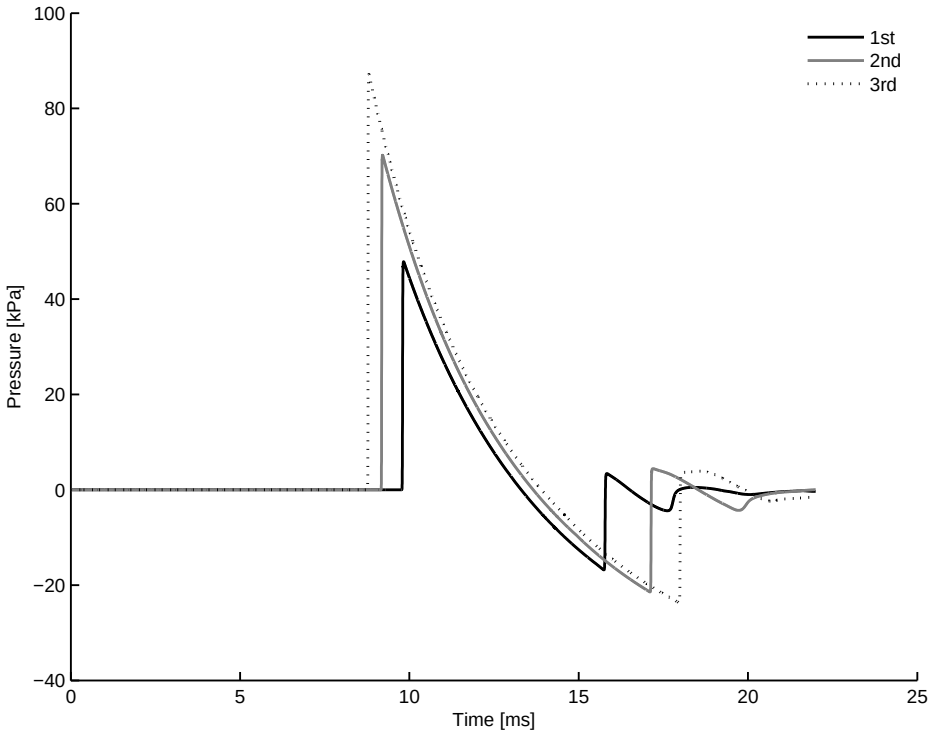
4.45 (b): $1.00m$



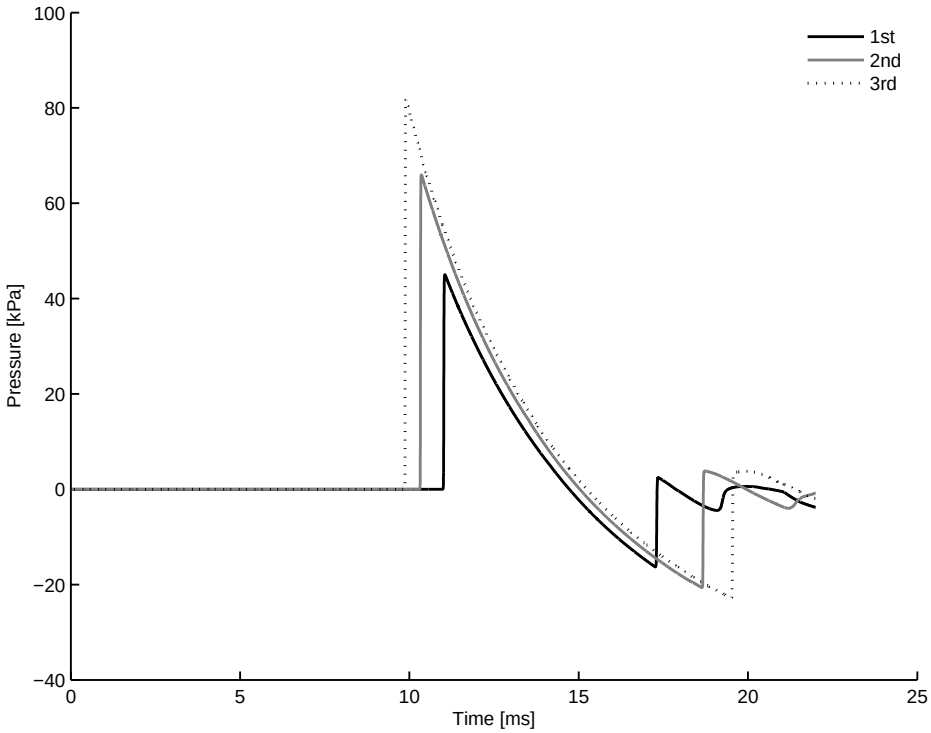
4.45 (c): $2.00m$



4.45 (d): $3.00m$



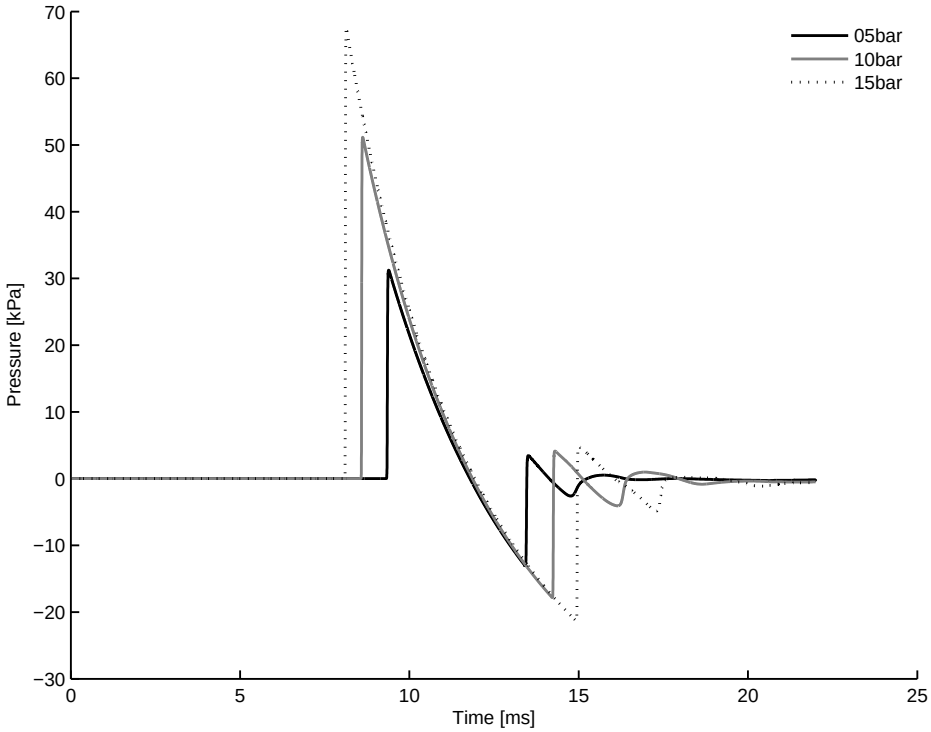
4.45 (e): $4.00m$



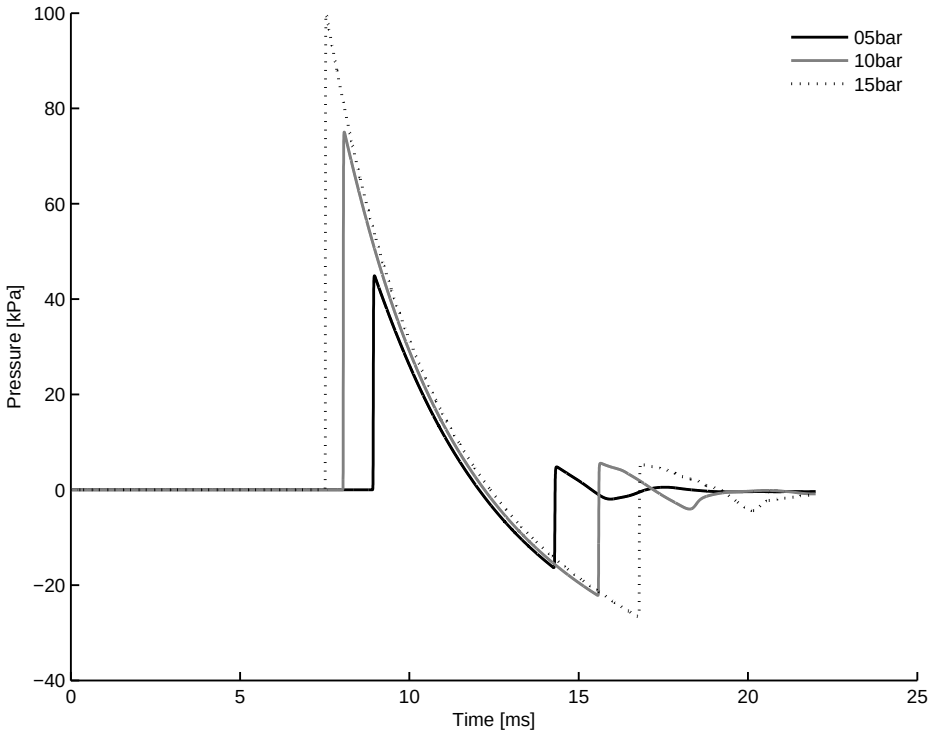
4.45 (f): $5.00m$

Figure 4.45: The Effect of Driver and Transition Section Shaping on Blast Pressure Profile

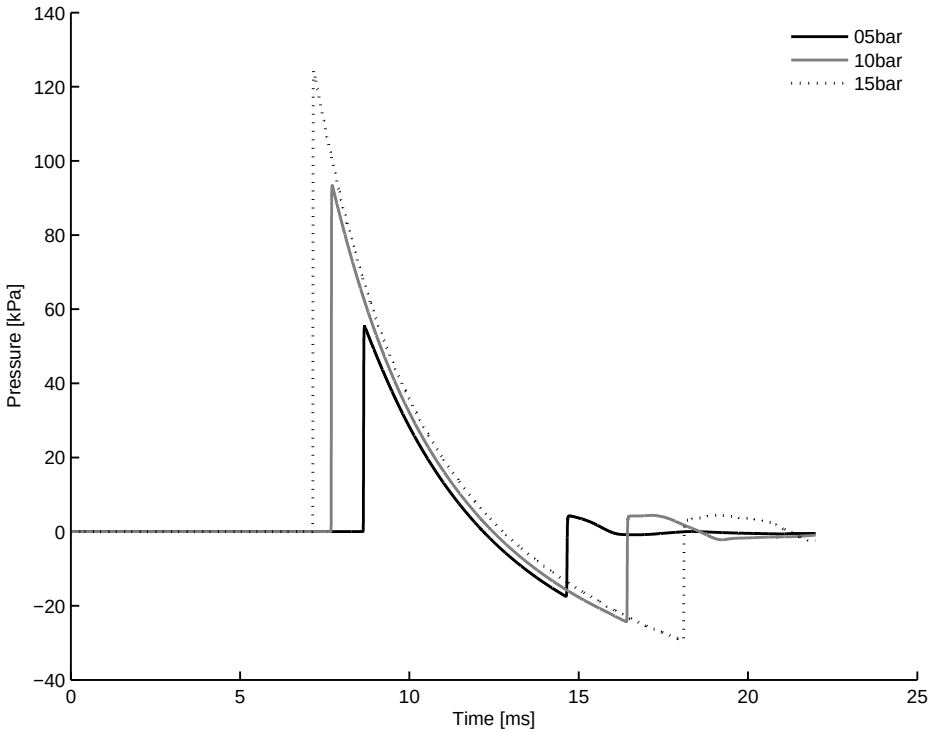
Just as was observed in the previous sections, Figure 4.46 shows that the effect of increasing the driver pressure of the concave, linear and convex drivers on the pressure profile was to increase the peak overpressure, blast duration, expansion phase duration, secondary shock strength and reduce the minimum expansion pressure. What was noticed in Figure 4.46 was that regardless of driver pressure the blast waves generated had almost identical decay profiles.



4.46 (a): Concave Profile 3.50m



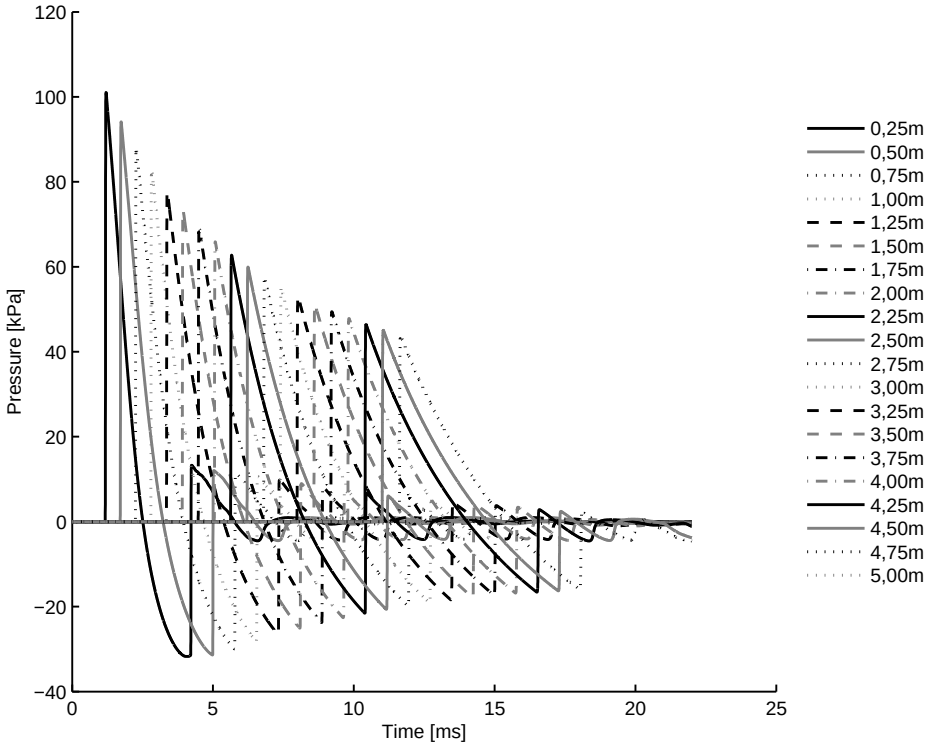
4.46 (b): Linear Profile 3.50m



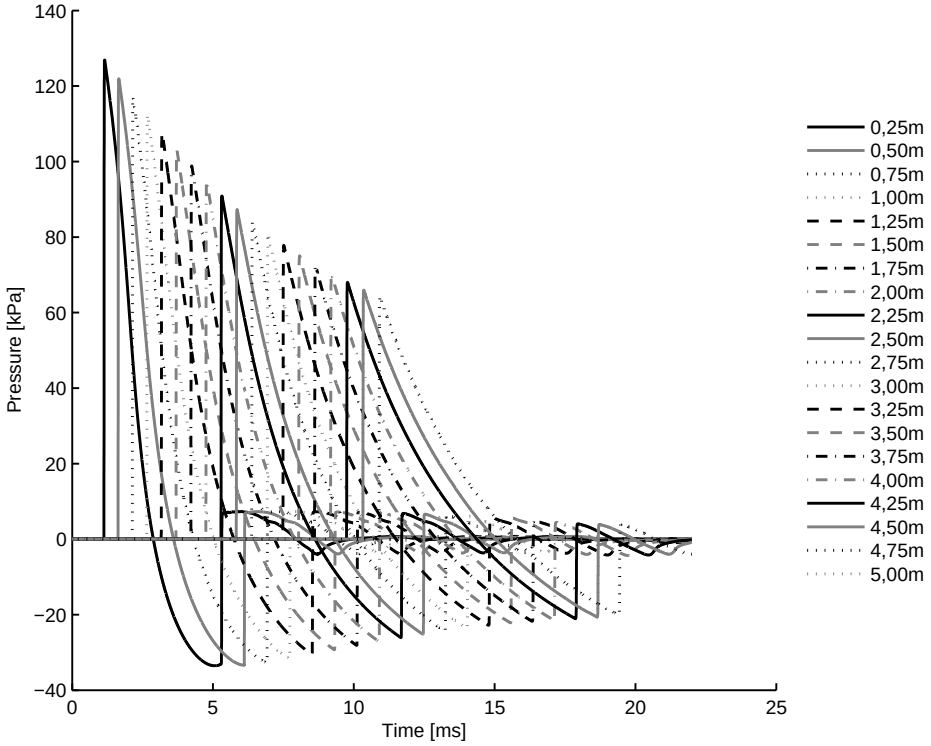
4.46 (c): Convex Profile 3.50m

Figure 4.46: The Effect of Driver Pressure on Pressure for Concave, Linear and Convex Shaped Profiles

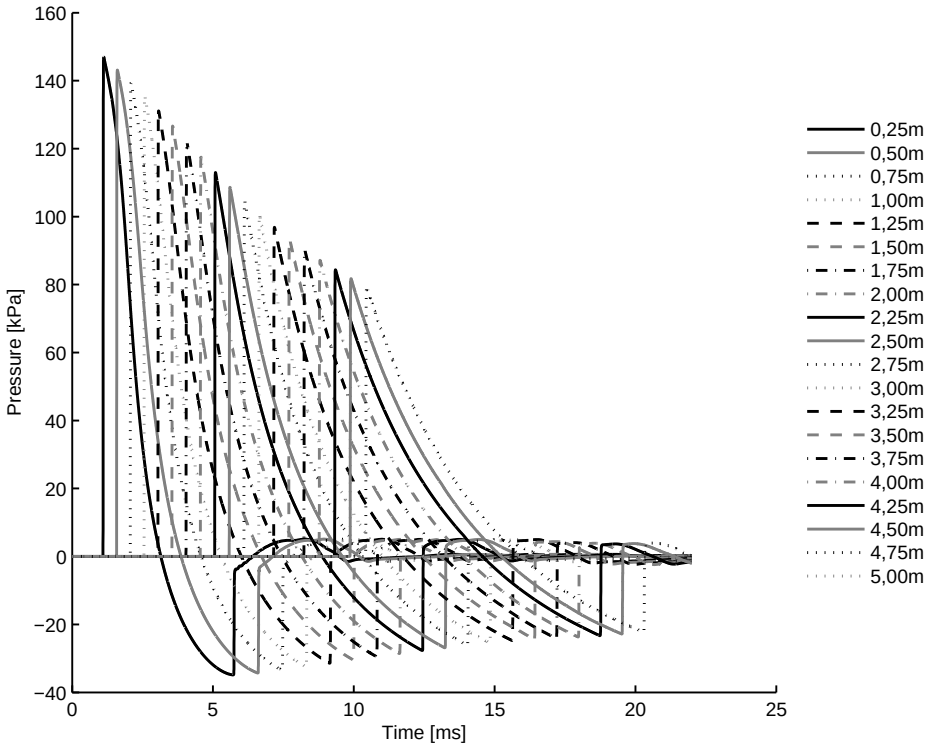
Figure 4.47 shows all the pressure traces generated by the monitors along the length of the blast tube for the blast waves generated by the concave, linear and convex drivers sections having driver pressures of $10bar$. It was noted that initially, the concave generated blast wave had the highest rate of pressure decay while the blast wave generated by the lowest rate of peak overpressure decay. It was noticed however that this situation reversed itself at some point between $3ms$ and $4ms$ and stayed that way for the remainder of the simulation.



4.47 (a): Concave Profile $10bar$



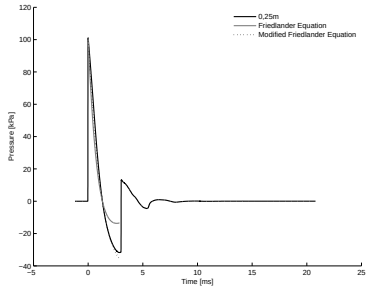
4.47 (b): Linear Profile 10*bar*



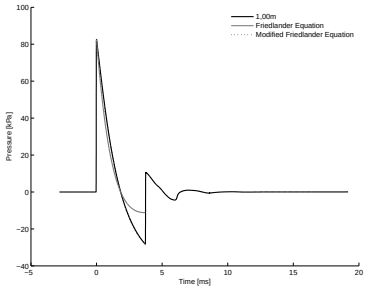
4.47 (c): Convex Profile 10*bar*

Figure 4.47: The Effect of Expansion Section Length on Pressure for Concave, Linear and Convex Shaped Profiles

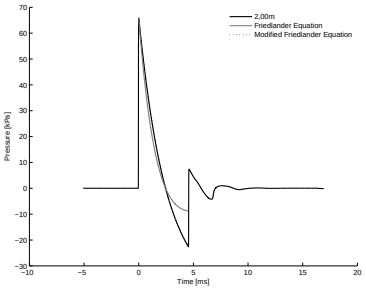
Looking at the blast pressure profiles for the blast waves generated by the concave, linear and convex drivers having driver pressures of $10bar$ and the corresponding Friedlander and Modified Friedlander pressure profiles plotted on the same set of axes as displayed in Figure 4.50, it can be seen that all three drivers produce waves which from $1.00m$ downstream of the diaphragm perfectly match the Modified Friedlander profile. This implies that along with driver pressure and driver shaping, altering the length of the driven section is another property of the blast tube that can be modified in order to produce the desired blast wave pressure profile and impulse.



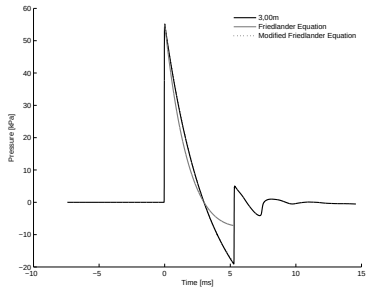
4.48 (a): Concave Profile $10bar$ $0.25m$



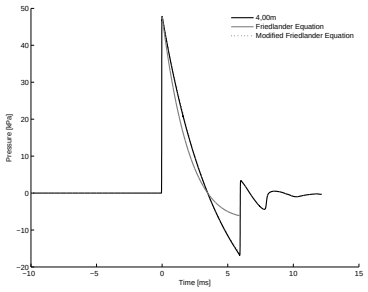
4.48 (b): Concave Profile $10bar$ $1.00m$



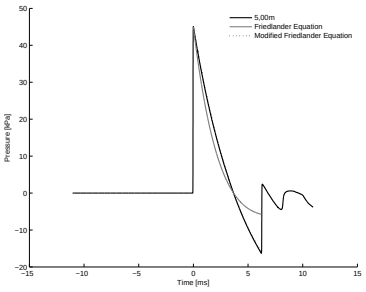
4.48 (c): Concave Profile $10bar$ $2.00m$



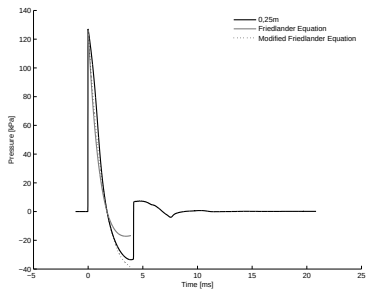
4.48 (d): Concave Profile $10bar$ $3.00m$



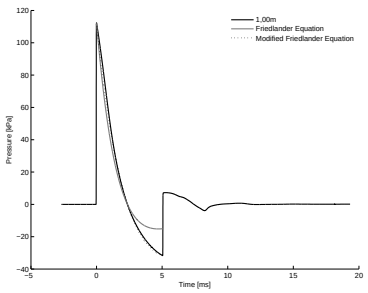
4.48 (e): Concave Profile $10bar$ $4.00m$



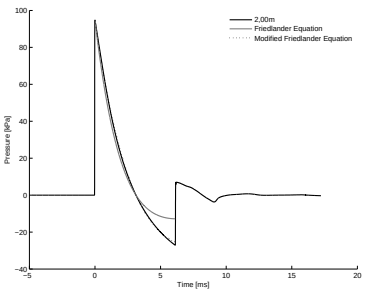
4.48 (f): Concave Profile $10bar$ $5.00m$



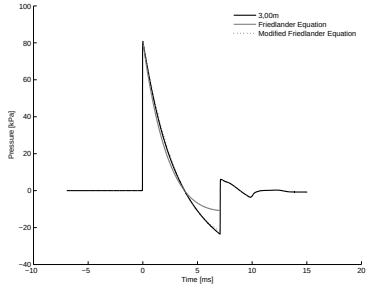
4.49 (a): Linear Profile $10bar$ $0.25m$



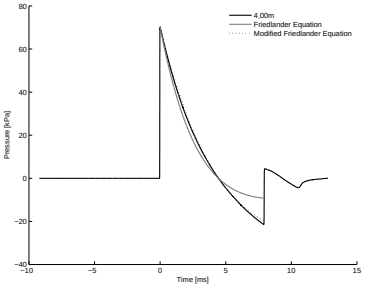
4.49 (b): Linear Profile $10bar$ $1.00m$



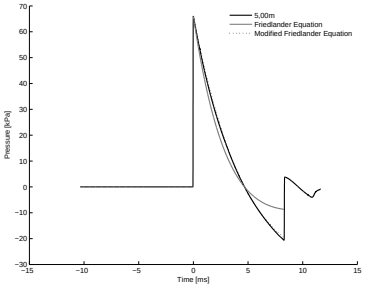
4.49 (c): Linear Profile $10bar$ $2.00m$



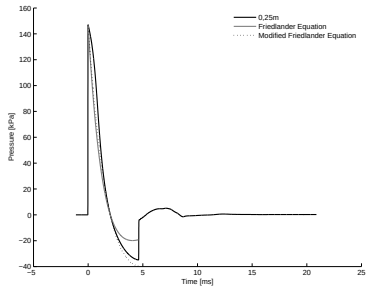
4.49 (d): Linear Profile 10*bar* 3.00*m*



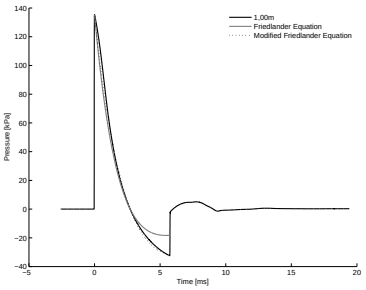
4.49 (e): Concave Profile 10*bar* 4.00*m*



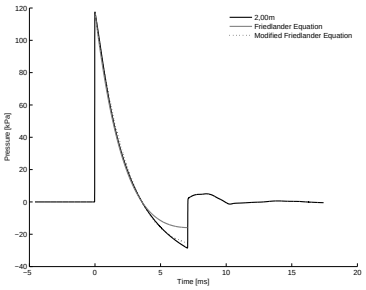
4.49 (f): Linear Profile 10*bar* 5.00*m*



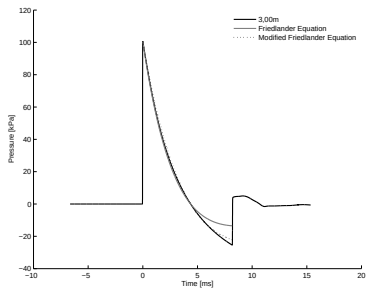
4.50 (a): Convex Profile 10*bar* 0.25*m*



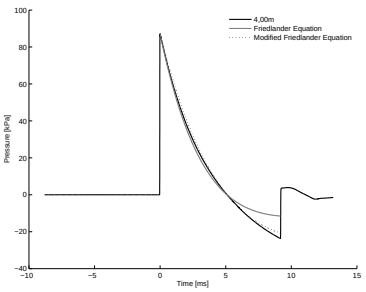
4.50 (b): Convex Profile 10*bar* 1.00*m*



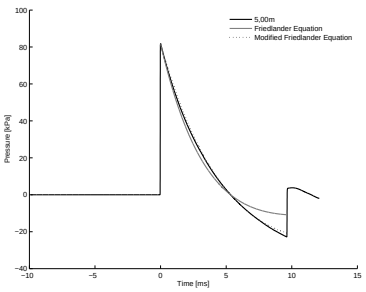
4.50 (c): Convex Profile 10*bar* 2.00*m*



4.50 (d): Convex Profile 10*bar* 3.00*m*



4.50 (e): Convex Profile 10*bar* 4.00*m*

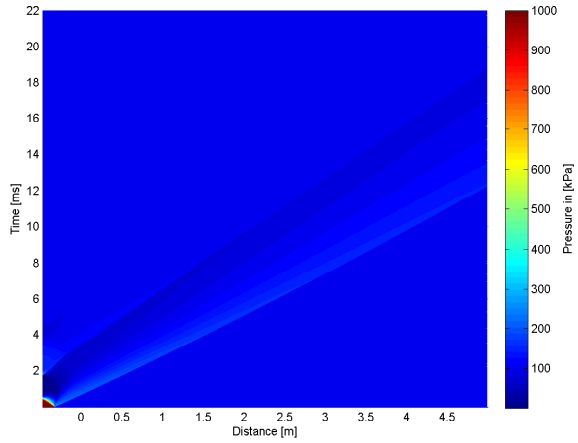


4.50 (f): Convex Profile 10*bar* 5.00*m*

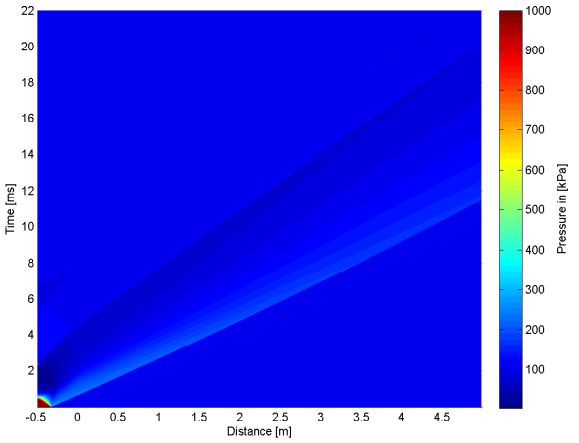
Figure 4.50: Comparing the Effect of Blast Tube Length on the Friedlander Pressure Profile

Looking at the pressure, density, temperature and velocity x-t diagrams in Figure 4.51, Figure 4.52, Figure 4.53 and Figure 4.54 it can be seen that the blast wave remains stable as it propagates down the length of the blast tube, apart from the increasing duration between the primary shock and secondary shock as well as the decay in peak over pressure with increasing distance travelled, which is similar to the behaviour observed in explosively generated blast waves. Figure 4.52 and Figure 4.53 show that the contact surface for all three driver shapes barely travels out of the transition section implying that the test section can be placed anywhere from about 1.00*m* from the end of the transition section and onwards without any fear

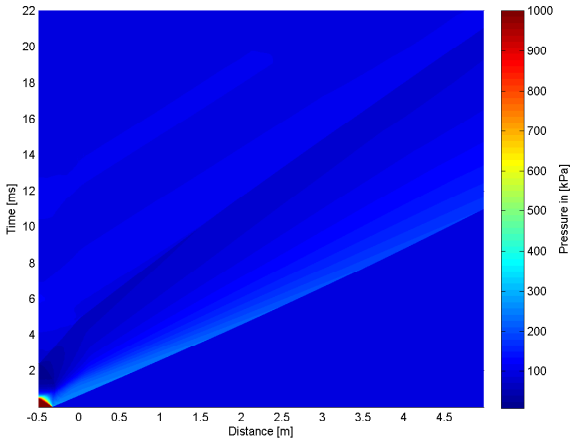
of the contact surface interacting with the test section which would compromise the results due to the increased density and reduced temperature of the gas trailing the contact surface.



4.51 (a): Concave Profile 10*bar*

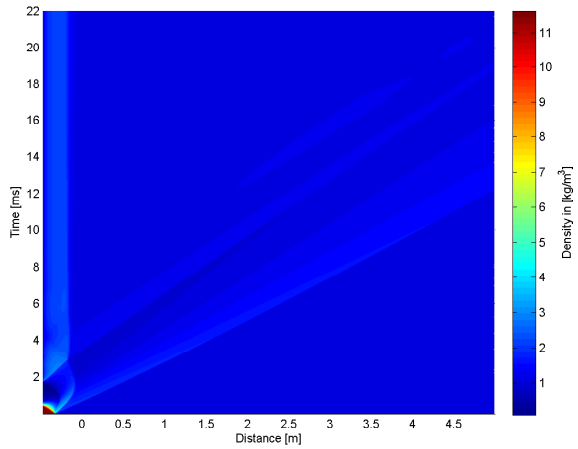


4.51 (b): Linear Profile 10*bar*

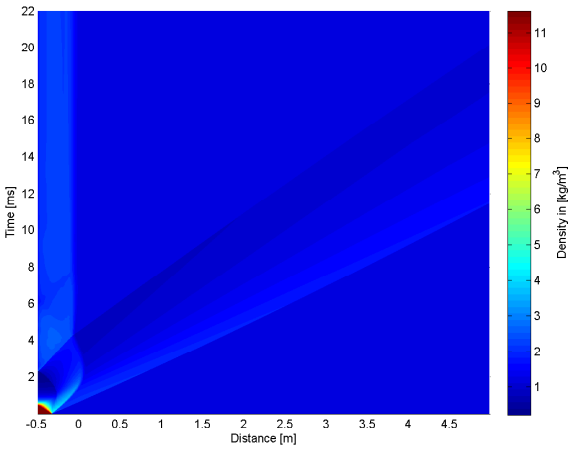


4.51 (c): Convex Profile 10*bar*

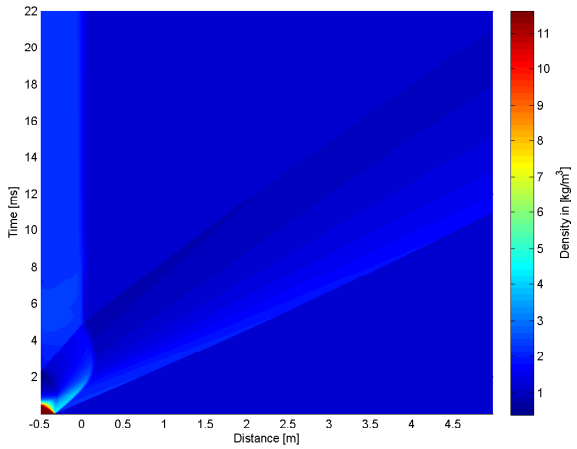
Figure 4.51: X-T Diagram for Effect of Blast Tube Length Simulations (Pressure)



4.52 (a): Concave Profile 10*bar*

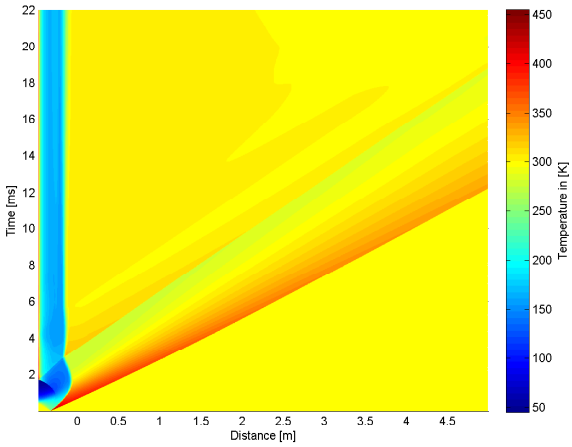


4.52 (b): Linear Profile 10*bar*

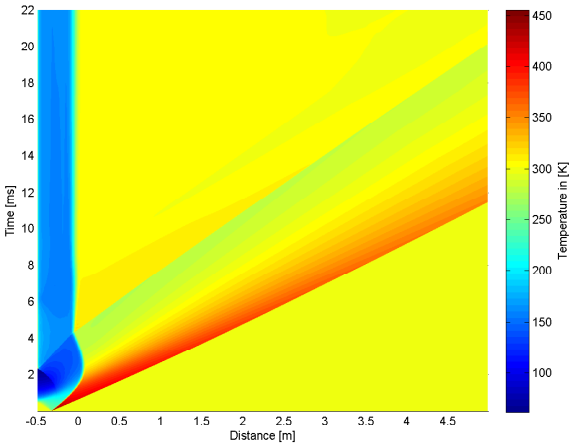


4.52 (c): Convex Profile 10*bar*

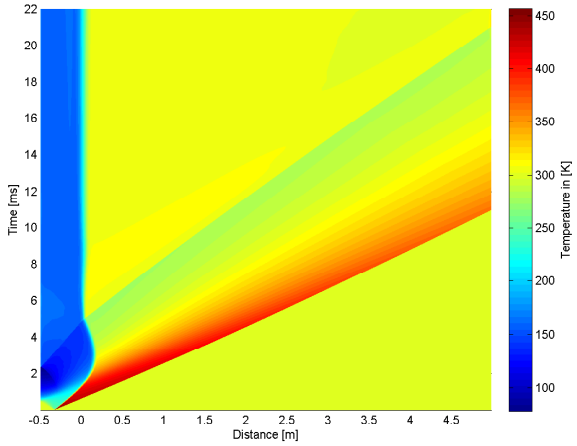
Figure 4.52: X-T Diagram for Effect of Blast Tube Length Simulations (Density)



4.53 (a): Concave Profile 10*bar*

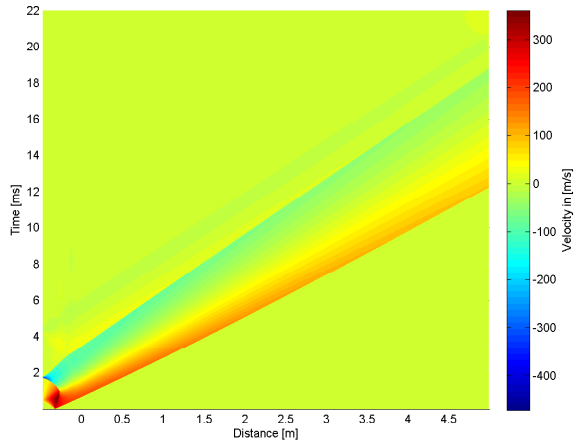


4.53 (b): Linear Profile 10*bar*

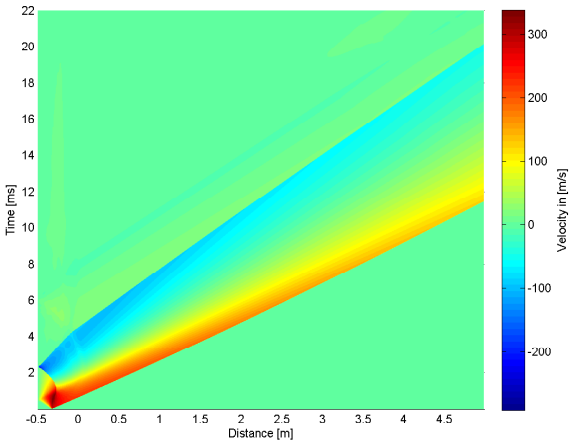


4.53 (c): Convex Profile 10*bar*

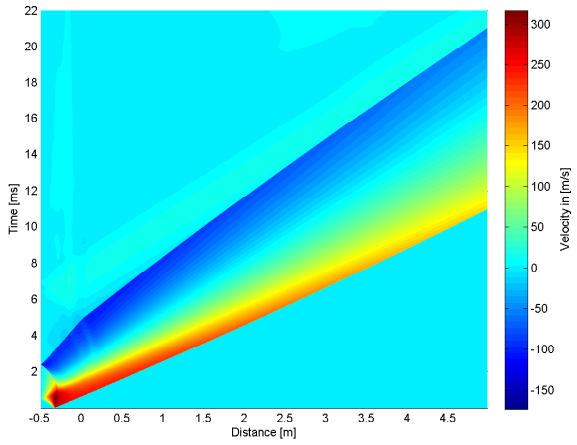
Figure 4.53: X-T Diagram for Effect of Blast Tube Length Simulations (Temperature)



4.54 (a): Concave Profile 10*bar*



4.54 (b): Linear Profile 10*bar*



4.54 (c): Convex Profile 10*bar*

Figure 4.54: X-T Diagram for Effect of Blast Tube Length Simulations (Velocity)

4.1.9 Final Blast Tube Design and Specification

4.1.9.1 Driver Section

The final driver section design is shown in Figure 4.55. Despite not having to be certified as a pressure vessel due it having been designed to be inserted into a pre-certified pressure vessel, the driver section was designed to meet pressure vessel standards. With this in mind the driver section was designed to contain air compressed up to 20*bar* at a safety factor of 4. The driver section consists of a 30*mm* thick flange onto which the side plates and concave, linear and convex shaped driver sections bolted onto. The construction of the driver section was designed such that the concave, linear and convex shaped driver sections could be interchanged quite easily. In each of the driver section side plates were placed direct-loaded

poppet valves. The original design was such the the driver section would be pressurised by first pressurising the pressure vessel containing it and then once the pressure differential was high enough the valves would open allowing the pressurised air into the driver section where upon reaching the desired pressure the valves would again close. However due to unforeseen complications arising with the pneumatic pricker, this methodology for pressurising the driver section was found to be flawed as it was found that the valves would open due to the pressure differential arising from the expansion focusing and inability to evacuate the pressure vessel before commencing a test. The valves opening during testing caused high pressure air to flow into the driver section which adversely effected the expansion focusing and formation of the blast wave pressure profile. Detailed Engineering Drawings of the driver section are contained in Appendix C section C.3.

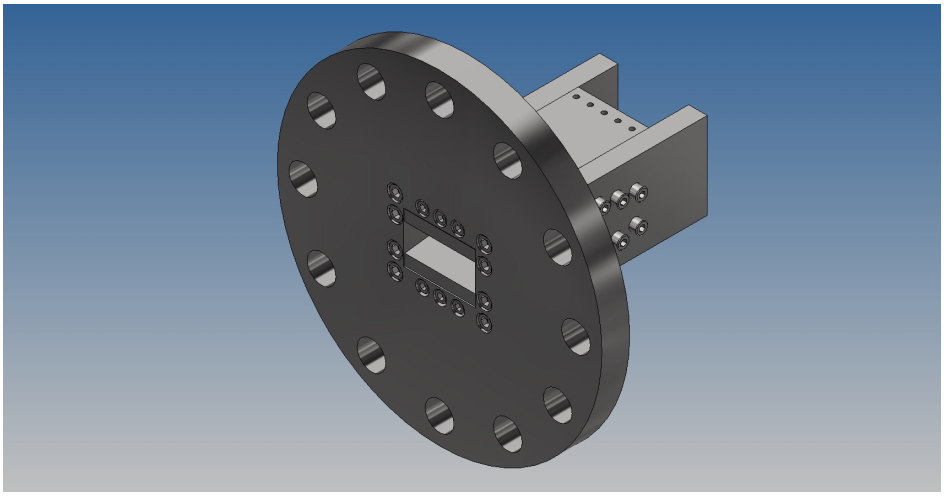


Figure 4.55: Driver Section Assembly

4.1.9.2 Transition Section

Figure 4.56 shows the design of the transition section that was used for experimentation. The transition section consisted of two flanges and four plates which upon assembly created a tube into which the concave, linear and convex shaped transition section pieces were inserted as required. The one flange was used to connect the transition section to the driver section and pressure vessel while the the other flange was used to connect the section to the expansion section of the blast tube. Despite not needing to be a pressure vessel, the walls of the transition section where designed using complementary energy analysis for square pressure vessels and were designed to withstand $20bar$. The Engineering Drawings of the transition section are displayed in Appendix C section C.4.

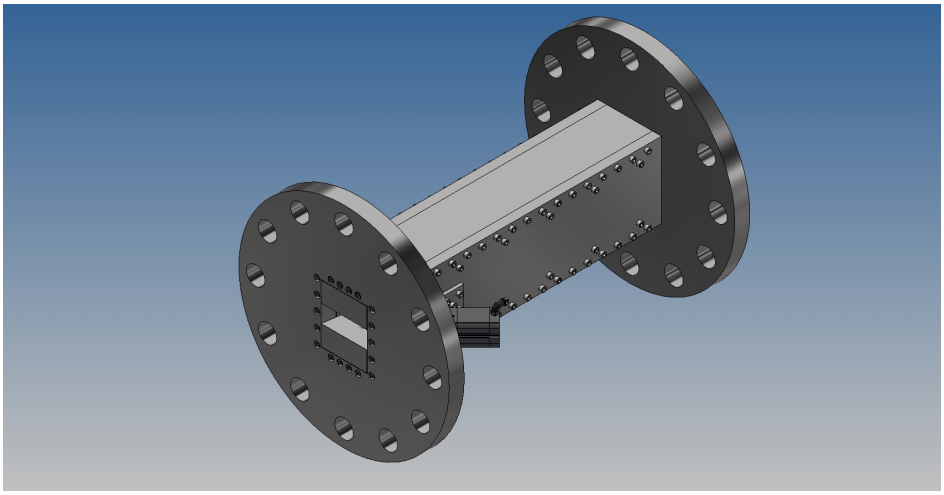


Figure 4.56: Driver Section Assembly

Chapter 5 Experimental Method

5.1 Experimental Facilities

5.1.1 Blast Tube Facility

The Blast Tube, once fabricated and assembled, consisted of a pressure vessel, driver section, transition section, driven section and test section. . The driver section, along with wooden inserts, were placed inside the pressure vessel. The wooden inserts were placed inside the pressure vessel to decrease the pressure vessel volume so as to reduce the time required to pressurise the driver section for each test. The pressure vessel was mounted onto a specially designed trolley which enabled it to be easily rolled away from the transition section and a new diaphragm placed at the interface between the driver section and the transition section before each test. The driver section was bolted to the transition section and in turn the transition section was bolted to the driven section by 12 $M30$ bolts that were tightened at loosened using a hand operated wrench. The driven section of the blast tube was salvaged from a previous shock tube assembly and consisted of three $635mm$ long and one $1m$ long steel square tubes with internal dimensions of the driven section being $76mm$ x $76mm$. The test section was then attached to the end of the driven section with the test section having internal dimensions of 76mm wide, a height of 232mm and a length of 295mm. The viewing windows of the test section were $235mm$ in diameter and were mounted securely in the doors of the test section which allowed the windows to be cleaned in between tests. The test pieces were bolted to the test section by means of three $M6$ cap screws. In order to prevent the windows being scratched as well as to create an air tight seal between the test piece and the windows, a few layers of double sided tap were placed on the ends of the test pieces. The blast tube was operated manually by means of a single diaphragm , natural burst technique. To run a test a diaphragm having thickness of either 50μ or $100\mu m$ was placed between the driver section and the transition section and then affixed by the bolting together of these two sections. The driver was then pressurised to the required driver pressure to run the test which was approximately the point at which the diaphragm burst naturally. Upon bursting

a blast wave forms which propagates down the driven section and into the test section. A schematic of the blast tube facility used is shown Figure 5.1 with a list of components in Table 5.1.

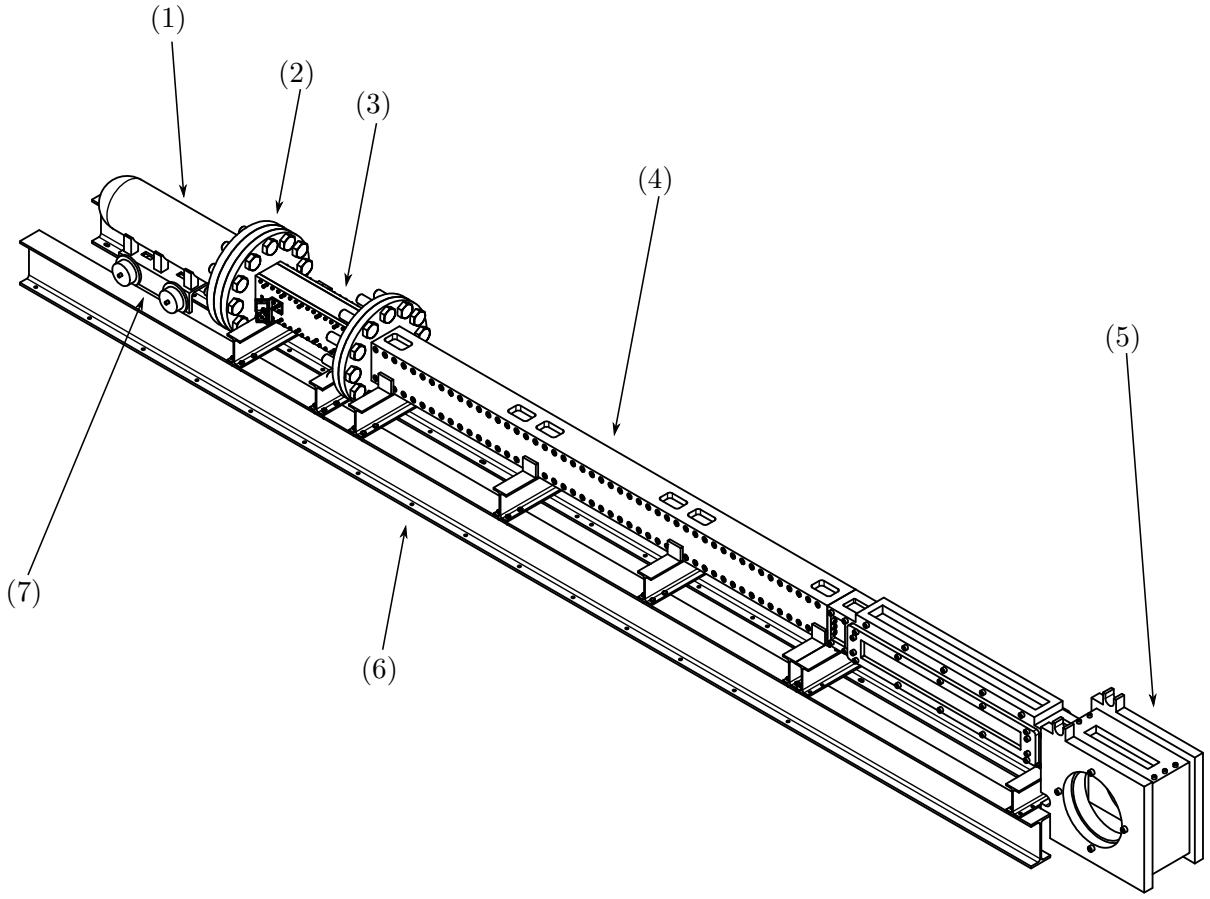


Figure 5.1: Schematic of the Blast Tube Facility

Table 5.1: Blast Tube Facility Component List

Label Number	**Component**
(1)	Pressure Vessel
(2)	Driver Section
(3)	Transition Section
(4)	Driven Section
(5)	Test Section
(6)	Support Structure
(7)	Trolley

5.2 Experimental Procedures and Precautions

5.2.1 Air Storage Vessel Pressurisation Procedure

The compressed air used to pressurise the driver section of the blast tube was sourced from a pressure vessel located in the lab. In order to obtain the desired driver pressures it was required that said pressure vessel was pressurised to between $1.1MPa$ and $1.4MPa$ before each experimentation session commenced. The procedure for pressurising the pressure vessel is as follows:

1. Check that the air dryer unit is switched off.
2. Close the air dryer bleed valves by first closing the receiver tank valve and then the heater valve.
3. Turn on the solenoid for the pressure vent system.
4. Turn on the water sump supply valve.
5. Open the cooling water valve.
6. Turn on the air compressor.

Upon the air in the pressure vessel reaching the maximum storage pressure of $1.4MPa$, the compressor turns off automatically so as to ensure that safety requirements are met. Before testing can commence the pressurisation system must be turned of and the shut down procedure is as follows:

1. Turn off the air compressor.
2. Close the cooling water supply valve.
3. Turn off the water supply sump pump.
4. Turn off the solenoid for the pressure vent system.
5. Bleed the air dryer unit by slowly opening the receiver tank valve and vent the air until the pressure gauge attached to the unit reads $0lb/in^2$.
6. Open the heater valve.

5.2.2 Blast Tube Pre-Testing Procedure

1. Turn on laptops being used to record photographic and pressure data.
2. Turn on all instrumentation: signal conditioner, oscilloscope and delay box.
3. Check to make sure that the Volt/Division and Time/Division of the oscilloscope are set to the correct values for the planned experimentation.
4. Using the channel selector on the signal conditioner box, ensure that the pressure transducers have been connected correctly.
5. Turn on the high speed camera and light source.
6. Take the parabolic mirror covers off of the mirrors.

5.2.3 Blast Tube Testing Procedure

1. Detach the driver section and pressure vessel from the transition section by loosening and removing the bolts attaching the two sections.
2. Roll the driver section away from the transition section.
3. Remove the burst diaphragm from between the driver section flange and the transition section flange.
4. If required, open the doors of the test section and insert the high pressure hose into the tube opening by the transition section flange, blowing out any diaphragm fragments stuck in blast tube. Remember to close the doors of the test section before proceeding further.
5. Using masking tape, place and affix a new diaphragm of the desired thickness in between the driver section flange and transition section flange.
6. Roll the driver section back to the transition section such that the flanges of both sections are flat against each other and sandwiching the fresh diaphragm.
7. Bolt the driver section, pressure vessel and transition section flanges together.
8. Inspect the blast tube to make sure that all components and pipes bolted and attached securely.
9. Close the door to the the blast tube lab.
10. Set the delay of the trigger box to the required value for the experiment being run where the units of the delay are in microseconds.

11. Arm the trigger box and oscilloscope.
12. Set the oscilloscope and high speed camera software to record upon being triggered.
13. Ensure that all the valves on the control panel are closed.
14. Open the valve on the high pressure line supplying compressed air from the lab pressure vessel.
15. Open the safety valve on the control panel.
16. While monitoring the pressure gauge, slowly open the supply valve located on the control panel. This will cause the pressure vessel and in turn the driver section to start pressurising.
17. Note the pressure displayed on the pressure gauge when the diaphragm bursts and close the supply valve on the control panel.
18. Close the supply valve on the high pressure line.
19. Open the release valve on the control panel to the vent the compressed air remaining in the pressure vessel.
20. Close the release valve and safety valve on the control panel.
21. Note the difference in time between the recording of the shock front at the first pressure transducer and the recording of the shock front at the second pressure transducer,Δt , in order to determine the Mach number of the generated blast wave.
22. Record the burst pressure, Δt, room temperature and atmospheric pressure.
23. Save and store the oscilloscope pressure readings as well as the photographs and videos taken by the high speed camera.
24. Repeat steps 1 through 23 for each successive test.

5.2.4 Blast Tube Shut Down Procedure

1. Ensure that all the valves on the control panel as well as the supply valve on the high pressure line are closed.
2. Turn off the high speed camera and light source.
3. Replace the parabolic mirror covers back onto the mirrors.
4. Turn off all instrumentation: signal conditioner, oscilloscope and delay box.

5. Turn off laptops being used to record photographic and pressure data.
6. Open the test section doors.

5.2.5 Precautions

The following precautions must be taken notice of and practised while operating the blast tube:

- In order to prevent hearing loss, hearing protection must be worn while bleeding the air dryer unit.
- Due to the loud noises produce during operation, hearing protection must be worn for the duration of the testing procedure.
- The transition, expansion and test sections of the blast tube must be inspected for any foreign bodies or debris before being sealed up and a test run.
- Every effort must be made to ensure that the optical equipment is not moved during the testing procedure so as to avoid images of poor quality being taken.
- The utmost care must be taken to ensure that the optical mirrors and glass test section windows are not scratched or otherwise damaged.
- The glass test section windows as well as the parabolic mirrors should be cleaned with a soft cloth and acetone between tests to ensure that clear images are captured.
- When changing the driver section and transition section inserts as well as the test pieces, make sure to inspect and tighten the bolts to ensure that the the inserts and pieces are affixed securely.
- Make sure to blow the warning whistle before testing so as to alert other lab workers that a test is about to be carried out and that they should protect their ears accordingly
- Ensure that the test section doors are opened at the end of the days testing to prevent the glass windows from cracking due to temperature change induced expansion and contraction.

5.3 Flow Visualisation

In order to validate the numerical method and to verify that the blast tube produced blast waves of good visual quality, experimental flow field images of the test section were taken using

Schlieren flow visualisation techniques. The optical set-up that was used was the standard z-configuration as shown in Figure 5.2. Initially two rails were placed on either side of the test section at angles of approximately 10° to the centreline of the test section, where the one rail support the light source while the other support the high-speed camera. Two 317.5mm diameter parabolic mirrors having focal lengths of 1905mm were placed on either side of the test section and were used for all testing. The light source, mirrors, test section and camera were aligned using a laser which was attached to one of the rails. In order to avoid poor image quality due to optical misalignment, every effort was made to ensure that the mirrors were place such that the light beam entered the test section perpendicular to the test section windows. A continuous Short-arc Xenon lamp, a Megaray MR2000LAB, was used as the light source as this would allow numerous images as well as video to be taken of the flow field during each test. The light from the Xenon lamp was passed through a bi-convex lens which converged the light to a point, at which a knife-edge cut-off slit was placed. The distance of the knife-edge from the parabolic mirror was equal to the focal length of the mirror. In front of the double-slit located on the light source side a plano-concave cylindrical lens was placed in order to minimise a astigmatism in the horizontal plane. The light was then shone into the parabolic mirror which collimated the light and directed it through the test section. Upon passing through the test section the paralleled light reflected off the other parabolic mirror which focused the light to a point at a distance from the mirror equal to the focal length of the second mirror. At this focal length a pin hole was placed. A pin whole was used rather than a conventional knife-edge so as to produce axi-symmetric Schlieren flow visualisation. The light from the pin hole was then directed into another bi-convex converging lenses which converged the light towards the sensor of the high-speed camera, a Photron Fastcam SA5, which then captured images and video of the flow field.

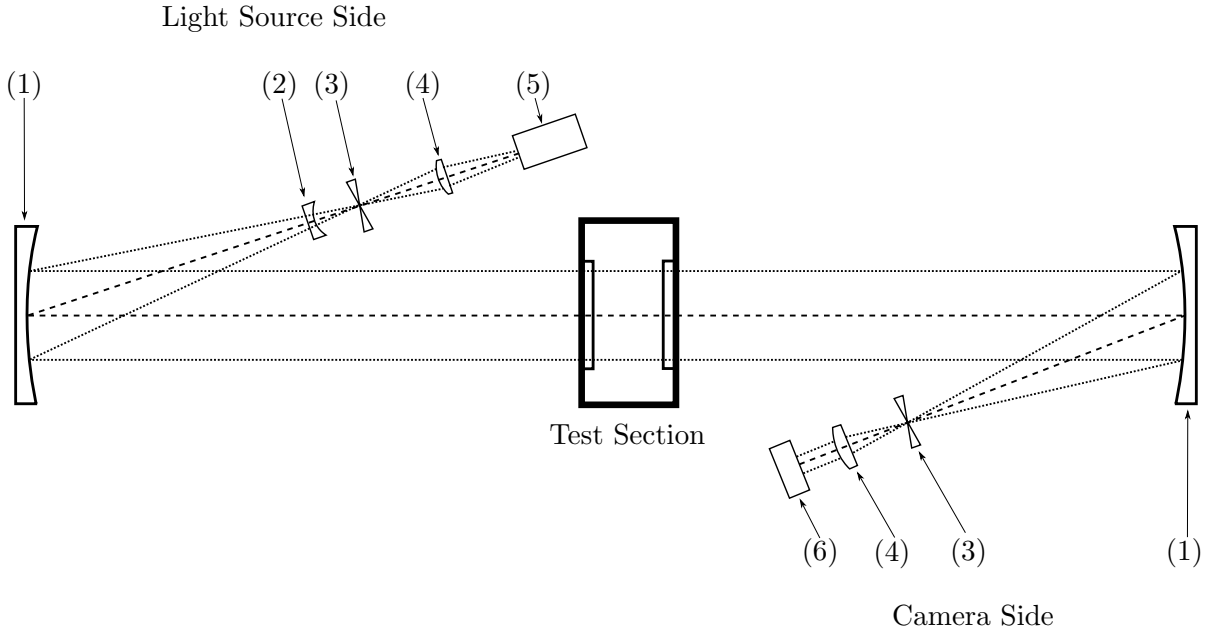


Figure 5.2: Uni-Directional Schlieren Flow Visualisation Set-up

Table 5.2: Uni-Directional Schlieren Visualisation Set-up Parts List

Part Label	**Part Description**
(1)	Parabolic Mirror
(2)	Cylindrical Lens
(3)	Cut-Off
(4)	Converging Lens
(5)	Light Source
(6)	Camera

Four transducers located in the expansion section of the blast tube, at distances of $2310mm$, $2730mm$, $2980mm$ and $3230mm$ from the diaphragm, measured the arrival time, pressure and velocity of the generated blast wave. The signal generated by the blast wave passing the first transducer was transmitted to the oscilloscope which outputted the signal to the delay box. The delay box, upon receiving this signal then triggered the camera to record the flow field.

Chapter 6 Calibration

6.1 Pneumatic Pricker

The initial design of the blast tube had intended that the diaphragm be burst by a pneumatic pricker which would be control by the operator, allowing the pressure vessel containing the driver section to be evacuated before the diaphragm was burst and a test initiated. However, after a few preliminary tests of the blast tube facility were run it, was found that due to the size as well as the aspect ratio of the internal opening of the tube at the driver-transition section interface, the pricker could not reliably and effectively burst the diaphragm. It was thereafter decided that all the tests would be run with the diaphragm bursting naturally. The reliability issues with the pricker in combination with the issues arising with the direct-loaded poppet valves and the blast wave not following the normal shock relations meant that it was very difficult to ascertain what the driver pressure was at each test. It was therefore decide that the best properties with which to characterise the blast waves was the Mach number and peak overpressure of the wave.

6.2 Blast Tube Calibration Data

Unlike normal shocks, where the Mach number of the shock wave can be determined by applying the normal shock relations if the pressure ratio between the gas in the driver section and the expansion section is known, this same cannot be done to determine the Mach number of a blast wave. Therefore, before testing could be carried out with the blast tube, the blast tube needed to be calibrated in order to ascertain what blast waves were produced by what combination of diaphragm thickness and shaped driver and transition section inserts. The data from the calibration runs of the blast tube are listed in the Table 6.1, Table 6.2 and Table 6.3. It is important to note that the burst pressures listed in the below tables are the pressures measured in the pressure vessel containing the driver section and not the pressures in the driver section itself at the time of diaphragm rupture. Using the valve equations it

was estimated that the when the $50\mu m$ thick diaphragm was used the driver pressure at diaphragm rupture ranged from $220KPa$ to $330KPa$ while the driver pressure was between $440KPa$ and $620KPa$ when the $100\mu m$ thick diaphragm was used. Looking at the below table it is observed that the convex driver has the a much lower burst pressure than both the concave and linear drivers. The most likely cause of this phenomena is the increased cross-sectional area and reduction in aspect ratio of the internal blast tube dimensions by the diaphragm location.

Table 6.1: Calibration of Blast Tube with Concave Shaped Driver and Transition Installed

Test Number	Diaphragm Thickness $[\mu m]$	Burst Pressure $[kPa]$	Shock Velocity $[m/s]$	Mach Number	Peak Overpressure $[kPa]$
1	50	560	396.23	1.16	47.14
2	50	540	430.33	1.26	44.69
3	50	560	430.33	1.26	50.42
4	50	400	396.23	1.16	34.90
5	50	480	396.23	1.16	39.80
6	50	520	415.84	1.22	47.97
7	50	530	411.76	1.21	44.69
8	50	530	415.84	1.22	47.97
9	50	600	422.54	1.24	51.22
10	100	1010	458.02	1.34	74.08
11	100	1010	450.64	1.32	66.74
12	100	990	438.41	1.28	67.54
13	100	1000	446.33	1.31	69.18
14	100	880	415.84	1.22	68.38
15	100	910	440.25	1.29	62.65
16	100	1000	440.25	1.29	66.74

Table 6.2: Calibration of Blast Tube with Linear Shaped Driver and Transition Installed

Test Number	Diaphragm Thickness $[\mu m]$	Burst Pressure $[kPa]$	Shock Velocity $[m/s]$	Mach Number	Peak Overpressure $[kPa]$
41	50	580	430.33	1.26	55.31
42	50	590	430.33	1.26	58.56
43	50	540	430.33	1.26	52.03
44	50	600	430.33	1.27	56.12
45	50	600	430.33	1.27	56.95
46	100	890	482.76	1.42	92.06
47	100	1020	482.76	1.42	89.61
48	100	1030	473.51	1.39	88.78
49	100	920	464.09	1.36	79.80
50	100	1000	473.51	1.39	85.53

Table 6.3: Calibration of Blast Tube with Convex Shaped Driver and Transition Installed

Test Number	Diaphragm Thickness $[\mu m]$	Burst Pressure $[kPa]$	Shock Velocity $[m/s]$	Mach Number	Peak Overpressure $[kPa]$
61	50	500	446.33	1.31	61.84
62	50	490	438.41	1.29	59.40
63	50	400	438.41	1.29	59.40
64	50	440	438.41	1.29	54.50
65	50	440	430.33	1.26	55.31
66	100	740	473.51	1.39	86.33
67	100	740	482.76	1.41	89.61
68	100	620	455.04	1.33	68.38
69	100	600	438.41	1.28	63.48
70	100	590	455.04	1.33	74.08
71	100	520	464.09	1.36	81.44
72	100	620	455.04	1.34	73.27

Chapter 7 Results and Discussion

7.1 Data Processing

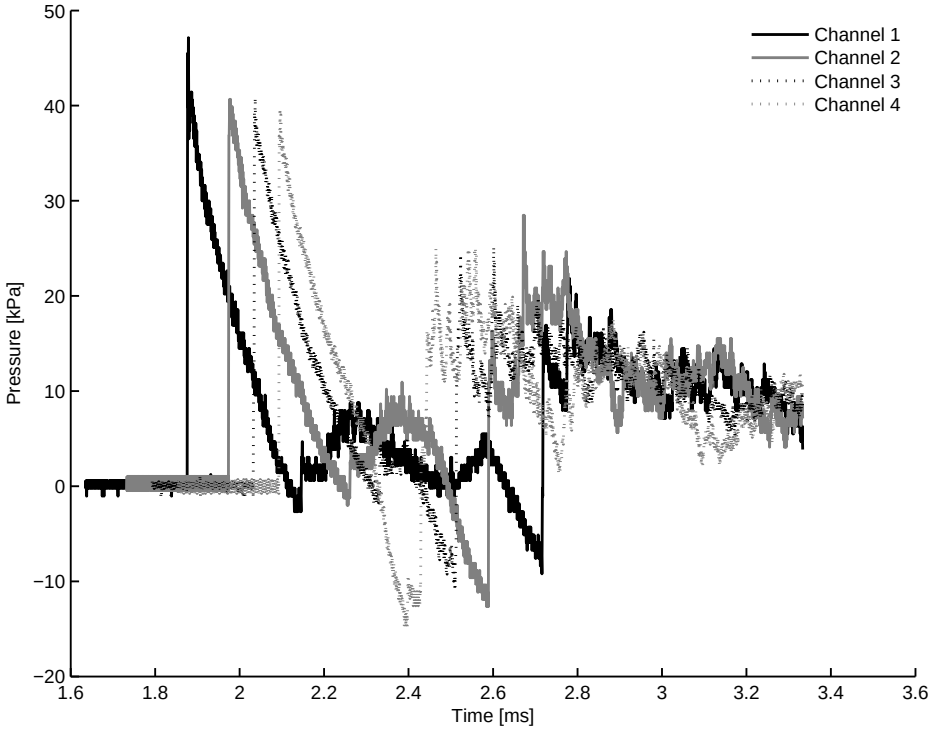
The pressure traces that were measured by the transducers were processed using code written and run in MATLAB while the schlieren images were edited using GIMP photo editing software.

7.2 Validation Numerical Design and Analysis

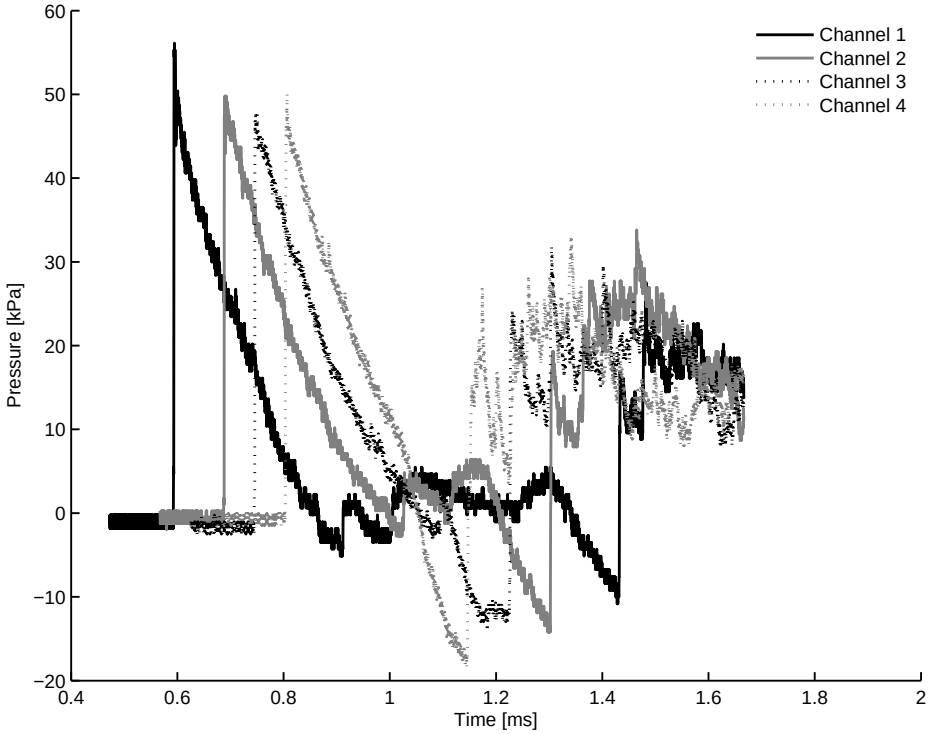
There were two main objectives of the design of the blast tube, namely to design a blast tube that could generate blast waves having realistic blast wave pressure decay profiles and blast waves of good visual quality so as to allow visual experimentation to be performed with the blast tube. Once the blast tube design had been completed and the tube fabricated and assembled a few tests of the tube were performed and pressure data from the four transducers was collected and axisymmetric schlieren photographs were taken, the results of which are shown below in Figure 7.1, Figure 7.2 and Figure 7.3.

Figure 7.1 shows the pressure traces measured by all four transducers on the same plot. It immediately becomes apparent when looking at by observing that the fourth channel measures the secondary shock first and then the third channel second and so on, such that it was deduced the secondary shock shown in the pressure plots Figure 7.1 is in fact the reflected blast wave and not the secondary shock generated by the expansion focusing as observed in the blast tube design simulations and described in detail section 4.1. The reflected blast wave prevents the development of the full blast wave pressure profile and it is therefore recommend that any further iterations of this blast tube design has an open ended test section with a diffuser connected to the downstream end so as to prevent a strong blast wave reflection from travelling back upstream which in turn will allow the full blast wave pressure profile to develop. Looking at Figure 7.1 it can be seen that all four pressure transducers measure similarly shaped pressure profiles and that the peak overpressure decays slightly while the

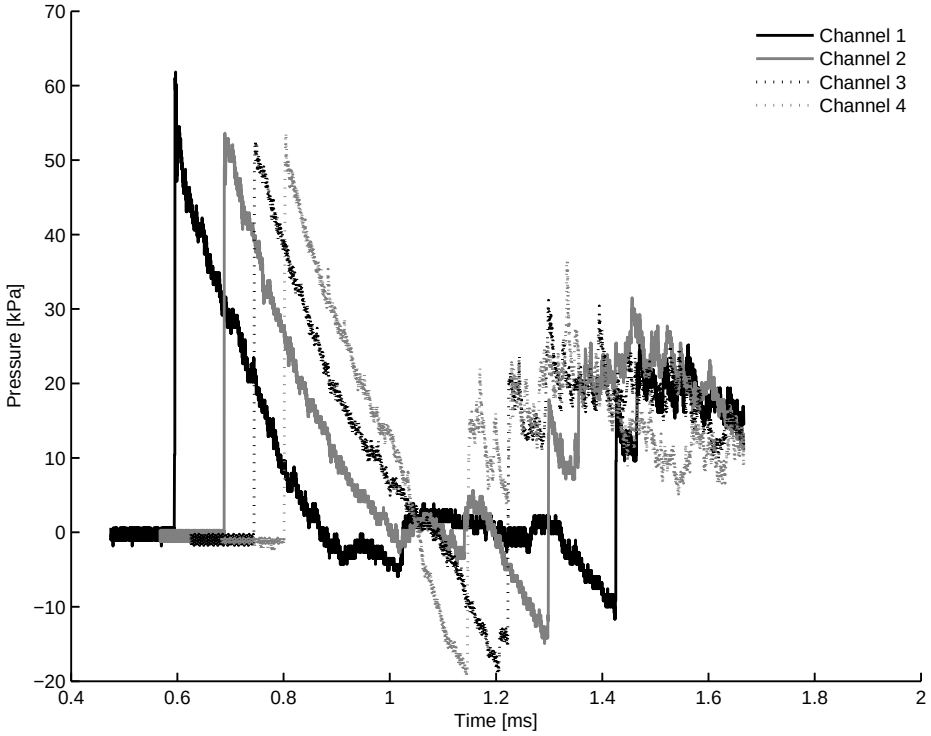
overpressure duration increases slightly as as the blast wave propagates down the tube which correlates with the findings in section 4.1.



7.1 (a): Concave Profile $\approx 560kPa$



7.1 (b): Linear Profile $\approx 600kPa$

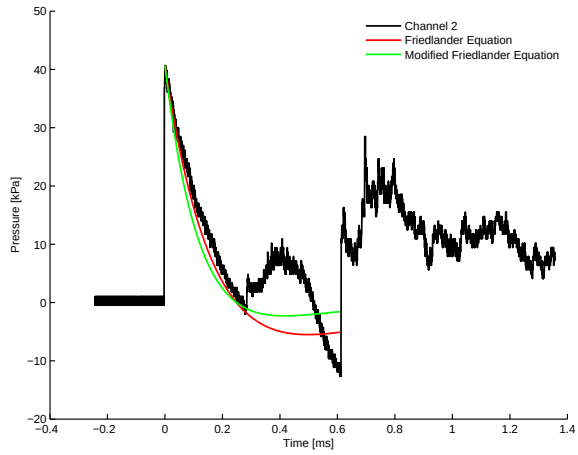


7.1 (c): Convex Profile $\approx 500kPa$

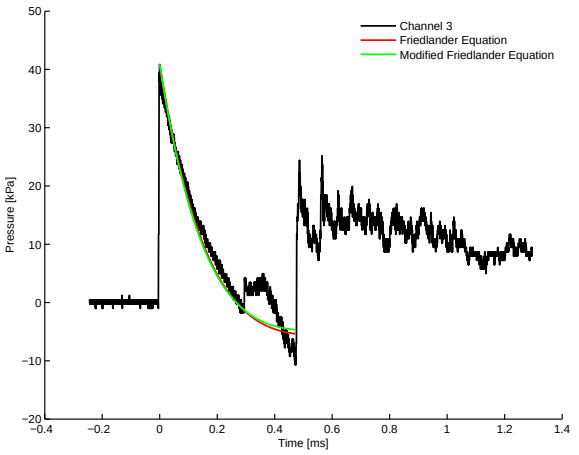
Figure 7.1: The Pressure Traces for the Experimental Validation of the Blast Tube having Concave, Linear and Convex Shaped Profiles

Figure 7.2 shows the pressure traces produced by the second and third transducers for all the blast tube configurations tested namely, the concave, linear and convex driver and transition sections with $50\mu m$ and $100\mu m$ diaphragms being used. On the same set of axes are plotted the corresponding Friedlander and Modified Friedlander pressure profiles which enable the determination of whether or not the blast tube, for all the configurations tested, did in fact produce realistic blast waves. Looking at all the sub-figures in Figure 7.2 it can be deduced that the blast tube does in fact produce realistic blast waves as the pressure profiles produced by the transducers for all the configurations correspond almost perfectly with the Friedlander and Modified Friedlander pressure profiles. A discrepancy was noticed, for all the measured blast waves, between the measured pressure trace and the corresponding Friedlander and Modified Friedlander pressure profiles starting from when the measured blast wave pressure reached just below atmospheric pressure and ending when the reflected blast wave was measured. The behaviour of the discrepancy, being a sudden steady increase in pressure before decaying again is most likely due to the pressure differential which arises between the driver section and the pressure vessel which causes the direct-loaded poppet valves to open letting in high pressure air into the driver section which disrupts the expansion focusing process and in turn the blast wave formation. It is recommended that any further design of the blast

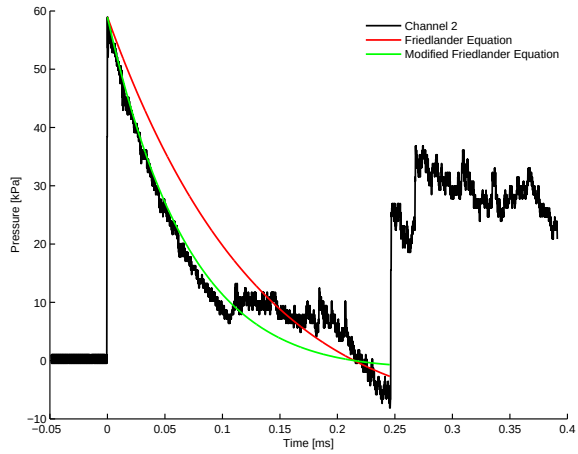
tube take this flaw of the direct-loaded poppet valves into account and an alternative filling method be generated.



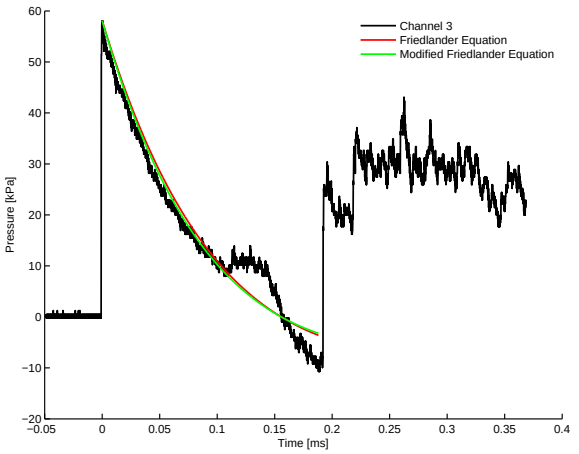
7.2 (a): Concave Profile $50\mu m \approx 560kPa$ $2.73m$



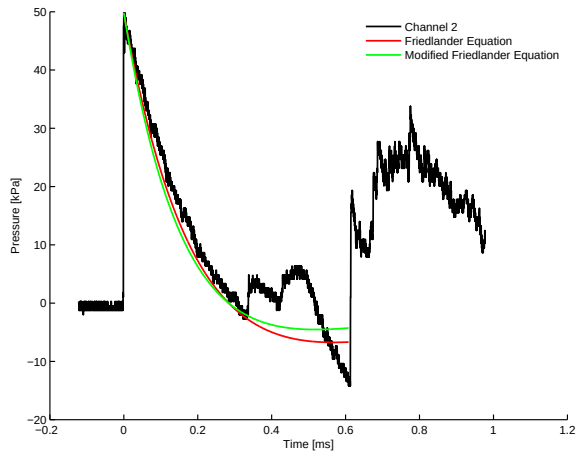
7.2 (b): Concave Profile $50\mu m \approx 560kPa$ $2.98m$



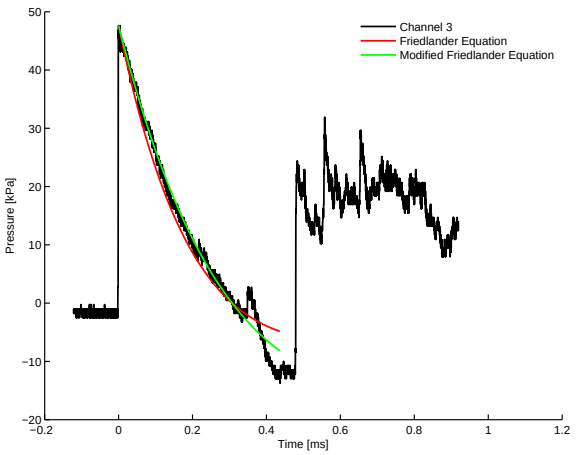
7.2 (c): Concave Profile $100\mu m \approx 1000kPa$ $2.73m$



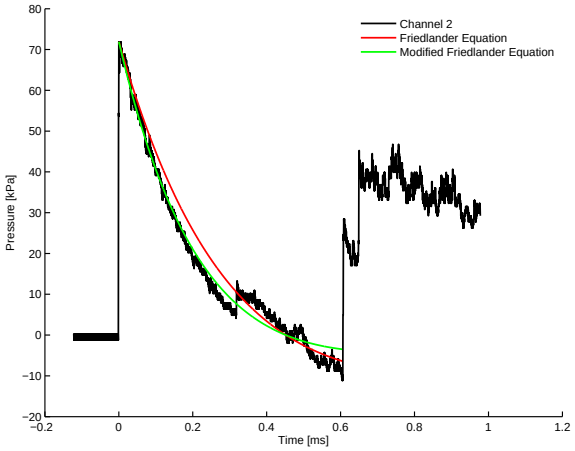
7.2 (d): Concave Profile $100\mu m \approx 1000kPa$ $2.98m$



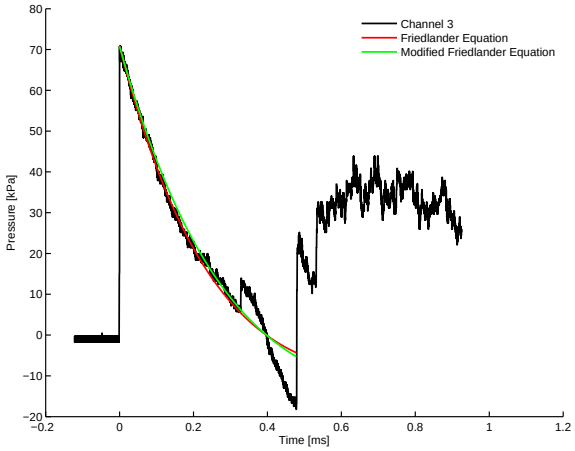
7.2 (e): Linear Profile $50\mu m \approx 600kPa$ $2.73m$



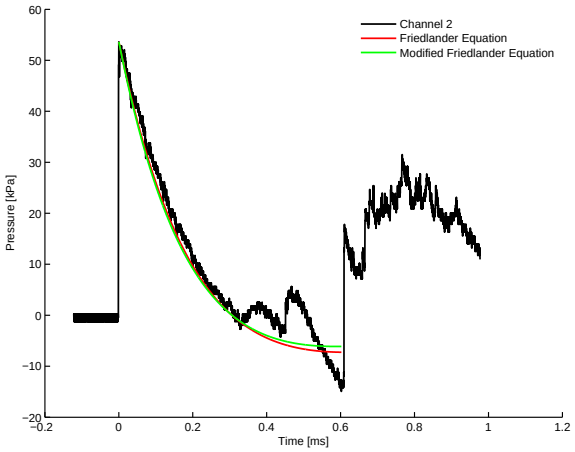
7.2 (f): Linear Profile $50\mu m \approx 600kPa$ $2.98m$



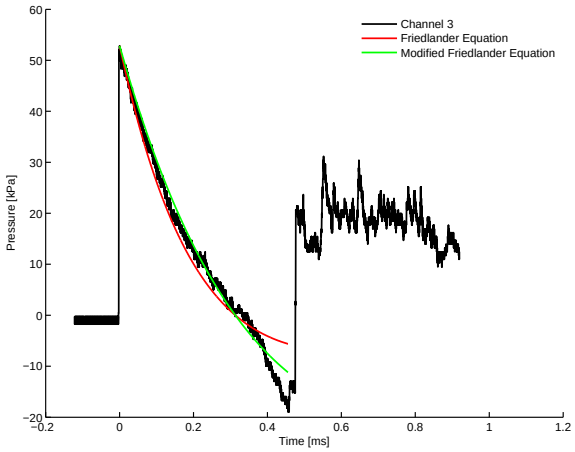
7.2 (g): Linear Profile $100\mu m \approx 1000kPa$ $2.73m$



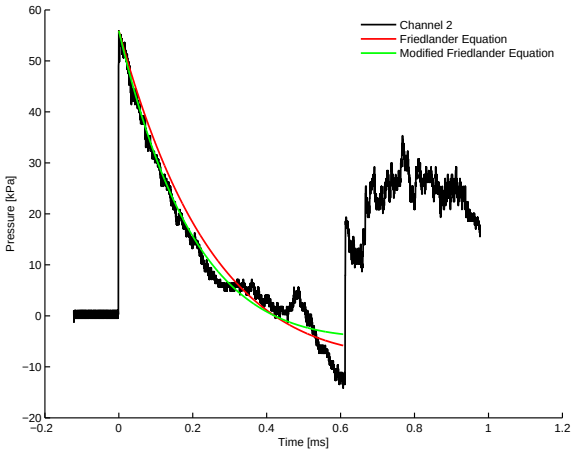
7.2 (h): Linear Profile $100\mu m \approx 1000kPa$ $2.98m$



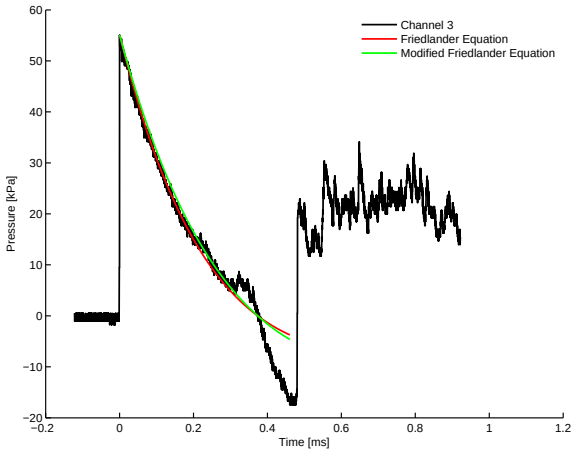
7.2 (i): Convex Profile $50\mu m \approx 500kPa$ $2.73m$



7.2 (j): Convex Profile $50\mu m \approx 500kPa$ $2.98m$



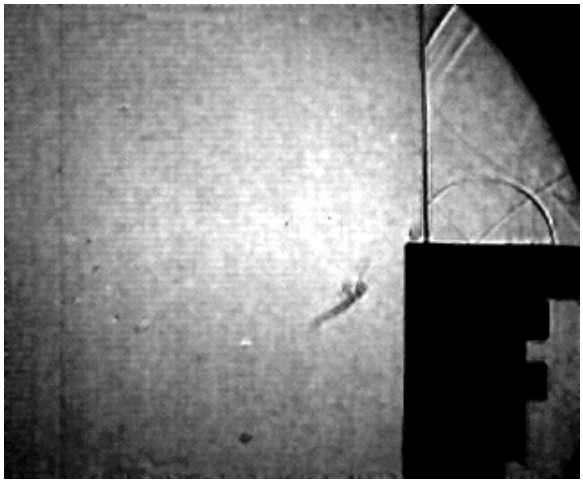
7.2 (k): Convex Profile $100\mu m \approx 600kPa$ $2.73m$



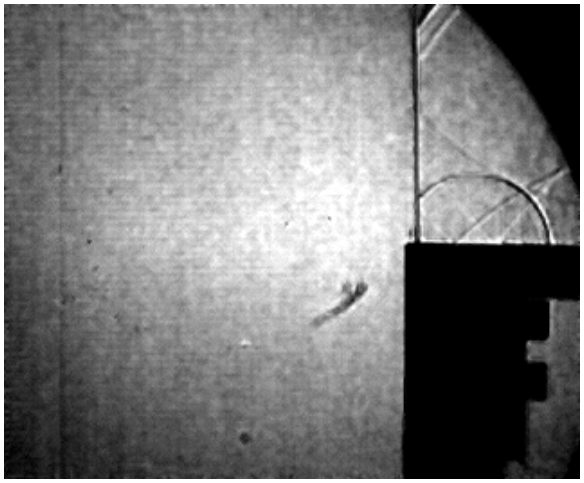
7.2 (l): Convex Profile $100\mu m \approx 600kPa$ $2.98m$

Figure 7.2: Transducer Pressure Profiles produced by the Experimental Validation of the Blast Tube with Concave, Linear and Convex Driver and Transition Section Inserts with Comparable Friedlander Pressure Profile

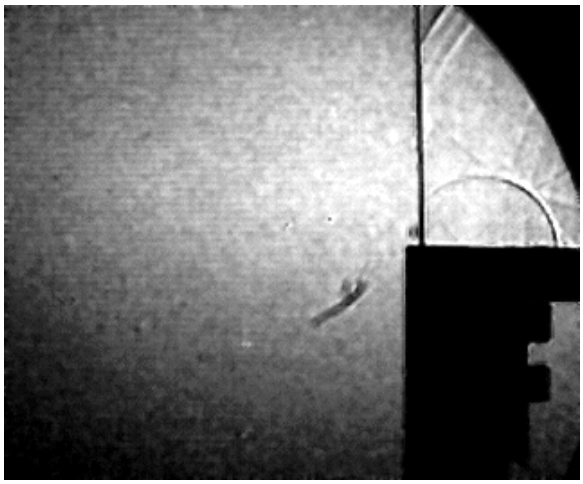
Having verified that the blast tube does in fact produce realistic blast waves, the last characteristic that needs to be verified is the visual quality of the generated blast waves. Figure 7.3 contains schlieren images of each of the blast waves generated by the the blast tube having the concave, linear and convex driver and transition sections installed. Looking at the subfigures in Figure 7.3 it can be seen that all the blast tube configurations produce blast waves of high visual quality as the blast wave shock fronts are flat, perpendicular to the direction of travel and clearly seen in the schlieren images. It was observed in Figure 7.3 that there are a diffracting waves at the bottom of each of the blast wave shock fronts as well as transverse waves trailing the shock fronts. These are all due to notches and steps that occur in the blast tube where the different sections of the blast tube join as well as where the test piece is connected to the test section. It is recommended that the next blast tube be designed with as few sections, and therefore joints, as possible to eliminate this problem.



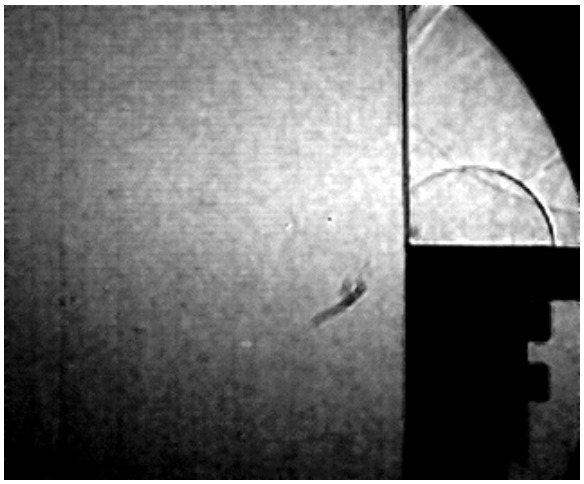
7.3 (a): Concave Profile $50\mu m$ $M = 1.253$



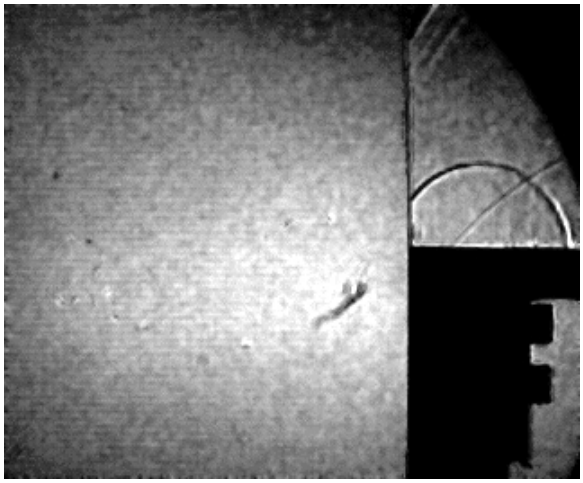
7.3 (b): Concave Profile $100\mu m$ $M = 1.338$



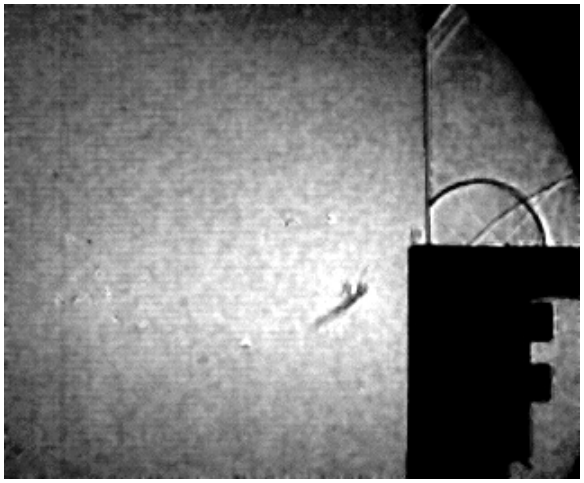
7.3 (c): Linear Profile $50\mu m$ $M = 1.287$



7.3 (d): Linear Profile $100\mu m$ $M = 1.362$



7.3 (e): Convex Profile $50\mu m$ 1.240

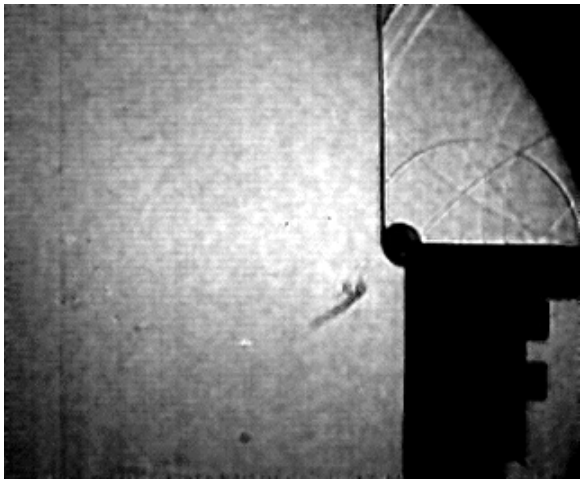


7.3 (f): Convex Profile $100\mu m$ 1.335

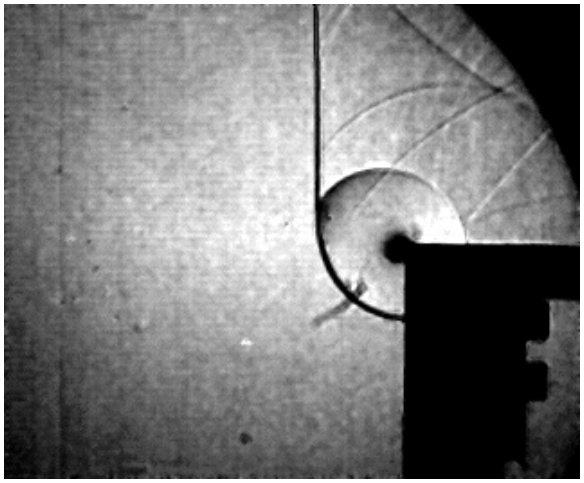
Figure 7.3: Verifying Visual Quality of Blast Tube with Concave, Linear and Convex Inserts

7.3 Blast Wave Diffraction

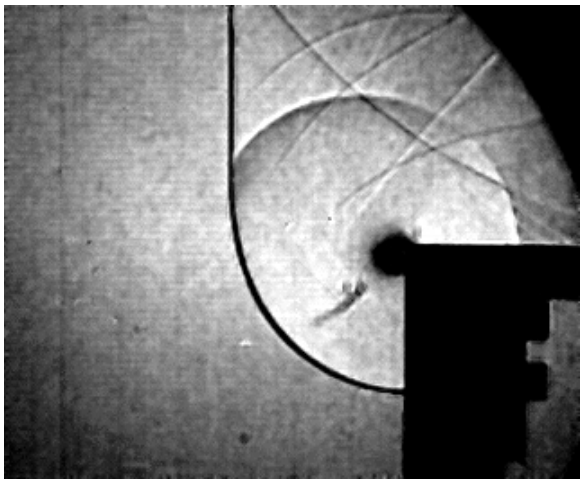
Figure 7.4 shows the development of a blast wave diffracting around a 90° corner. Looking at Figure 7.4 (a) it was observed that as the incident blast wave travels past the corner of the test piece it starts to diffract. This results in a diffracted blast wave travelling down the side of the test piece while a sound wave travels back upstream. The density gradients of the region of the flow encapsulated by the diffracted blast wave and reflected sound wave is very high as indicated by the black region located at the corner in Figure 7.4 (a). After some time has passed the diffracted blast travels further down the side of the test piece while the reflected sound wave travels further upstream. It can also be observed, by noting the black dot at the corner of the test piece in Figure 7.4 (b), that a vortex forms at the corner of the test piece. As even more time passes the vortex grows in size and the diffracted blast wave and continue to propagate away from the test piece corner. As this happens, the length of the straight incident blast wave shrinks while the length of the diffracted blast wave increases. Looking at Figure 7.4 (c) and Figure 7.5 (a) it can be seen that no contact surface was generated. This is due to the generated blast waves having Mach numbers of between 1.2 and 1.4 which mean that they are weak shocks and do not induce a high enough entropy change to create a contact surface.



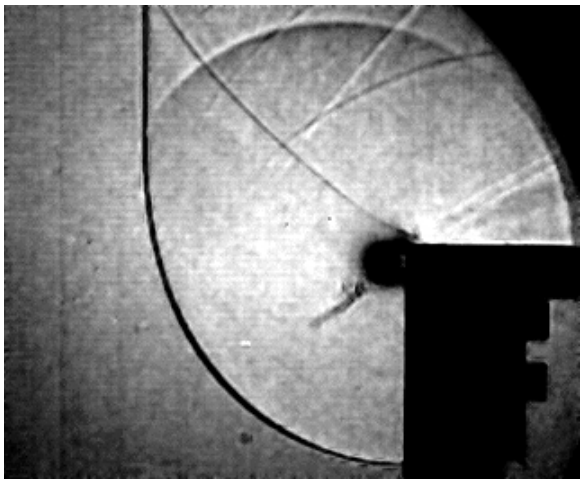
7.4 (a)



7.4 (b)



7.4 (c)



7.4 (d)

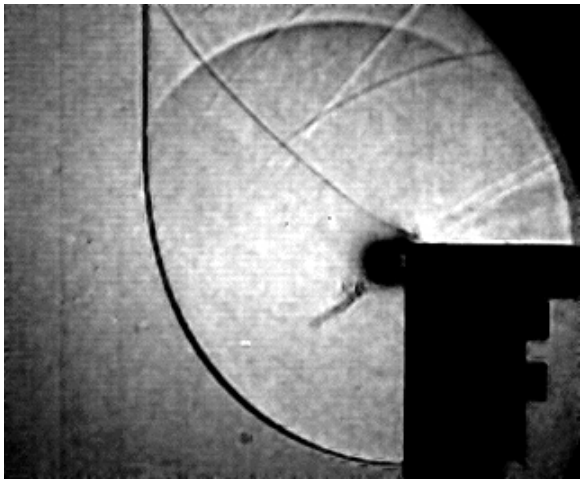
Figure 7.4: Development of a Diffracted Blast Wave generated by the Blast Tube having Concave Driver Section $50\mu m$ $M_0 = 1.253$

The diffraction around a 90° corner of the blast waves generated by the blast tube having the concave, linear and then convex driver and transition section inserts installed is shown in Figure 7.5. Comparing Figure 7.5 (a), Figure 7.5 (c) and Figure 7.5 (e) to Figure 7.5 (b), Figure 7.5 (d) and Figure 7.5 (f) it can be observed that increasing the Mach number of the generated blast wave causes the induced vortex at the corner to increase in size. Looking at the sub-figures in Figure 7.5 it would appear that another difference between the blast waves having lower Mach number and the blast waves having higher Mach numbers is the distance that the reflected sound wave travels upstream, with the reflected sound waves of the lower Mach number blast waves travelling further upstream than the comparative higher Mach number blast waves. However, this is not in fact the case but rather that the diffracted blast wave generated by the higher Mach number incident blast wave has travelled

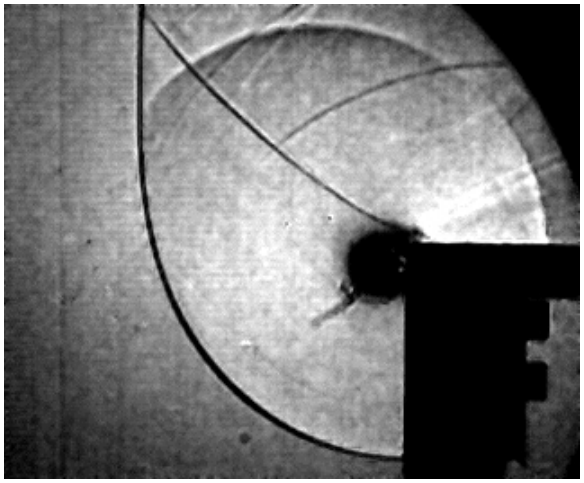
down the side of the corner piece quicker than the comparative diffracted blast wave induced by the lower Mach number incident blast wave. This is not the full explanation of this phenomena as the temperature behind the higher Mach number incident wave will be higher than the comparative lower Mach number incident wave thus increasing the speed of sound in the gas trailing the shock front which in turn will cause the reflected sound wave to travel with a higher velocity upstream, thereby compensating for the reduced travel time. This understanding of the flow field can be verified by the fact that it can be seen in the sub-figures in Figure 7.5 that at the top of each of the images, the reflected sound waves for both the higher and lower Mach number cases is in approximately the same location and the only differences in the distance travelled by the reflected sound wave start to occur further upstream in the flow. The most probable cause for this is that the higher Mach number wave undergoes a higher rate of decay in pressure, density and temperature behind the shock front than the lower Mach number wave thus the speed of sound of the gas will reduce quicker resulting in the reduced velocity at which the reflected sound wave travels and therefore a reduction in the perceived distance that the reflected shock travels upstream.

Looking at Figures 7.5 (a) and 7.5 (b) and comparing them to Figures 7.5 (c) and 7.5 (d) and Figures 7.5 (d) and 7.5 (f) it can be seen that the there is no discernible difference in the characteristic and nature of the blast wave diffraction around the 90° between the blast waves generated by the different driver and transition shapes. This is to be expected because as shown in the pressure plots in Figure 7.2 the blast wave generated have similar characteristics to one another namely, similar peak overpressure values and pressure decay profiles which follow the Modified Friedlander pressure profiles.

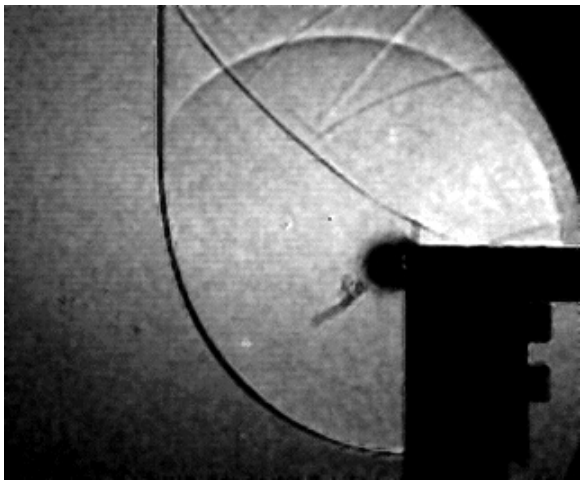
Comparing Figure 7.5 to schlieren images of 90° diffraction of a normal shock wave produced by Skews (1966), it was observed that the only perceivable difference between the blast wave and the normal shock diffraction was the behaviour of the reflected sound wave where the reflected sound wave generated by the normal shock wave has a much more circular path than the comparative blast wave induced reflected sound wave. This is to be expected as the gas properties immediately behind the normal shock front are constant whereas the properties behind the blast wave vary exponentially.



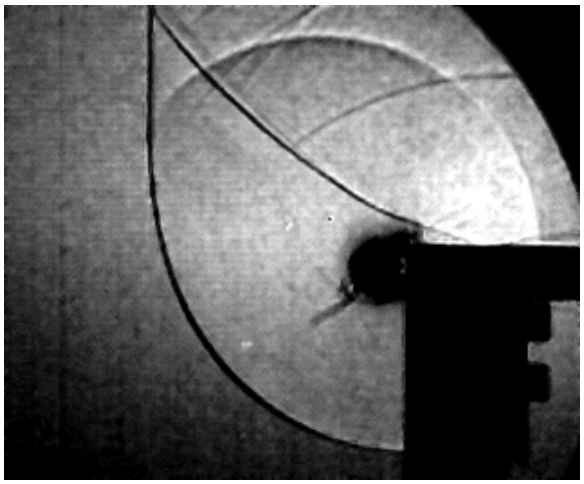
7.5 (a): Concave Profile $50\mu m$ $M_0 = 1.253$



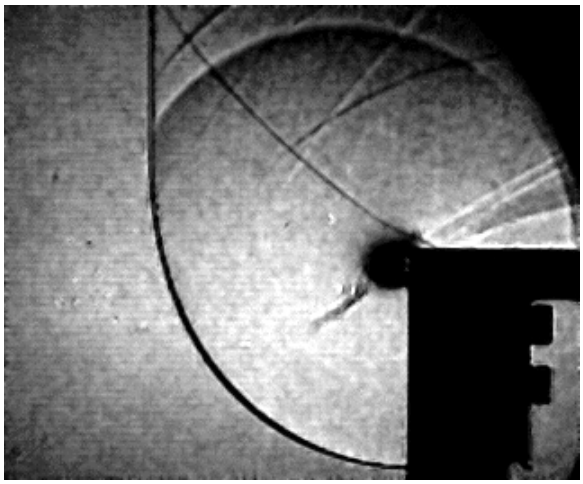
7.5 (b): Concave Profile $100\mu m$ $M_0 = 1.338$



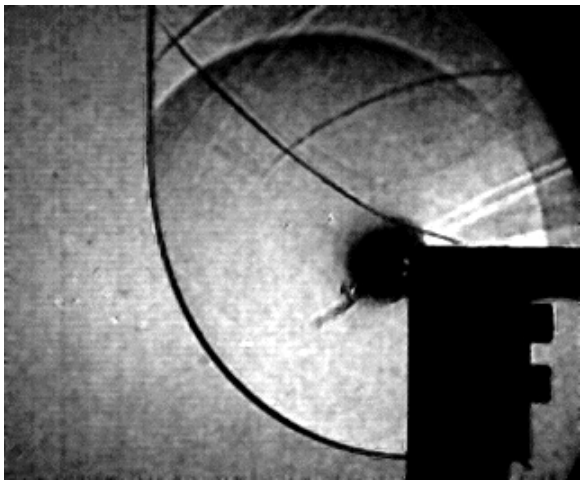
7.5 (c): Linear Profile $50\mu m$ $M_0 = 1.287$



7.5 (d): Linear Profile $100\mu m$ $M_0 = 1.362$



7.5 (e): Convex Profile $50\mu m$ $M_0 = 1.253$



7.5 (f): Convex Profile $100\mu m$ $M_0 = 1.335$

Figure 7.5: Comparison of a Diffracted Blast Wave generated by the Blast Tube having Concave, Linear and Convex Driver Section

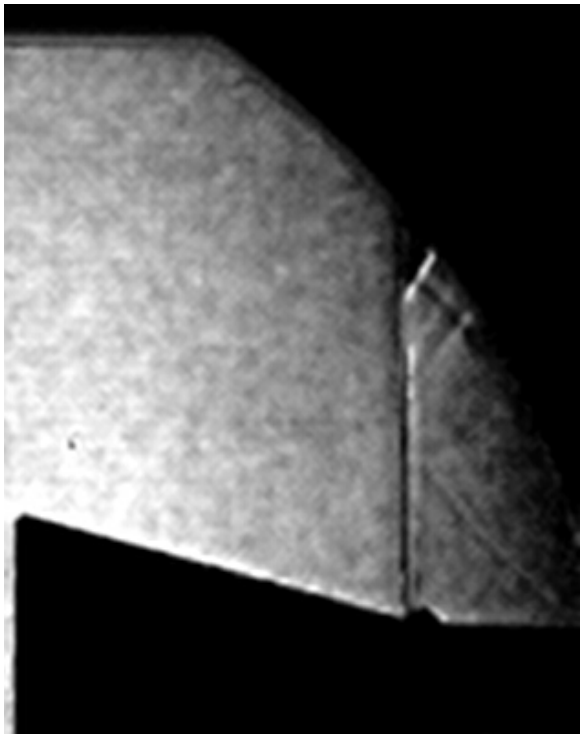
7.4 Blast Wave Reflection

7.4.1 15° Reflection

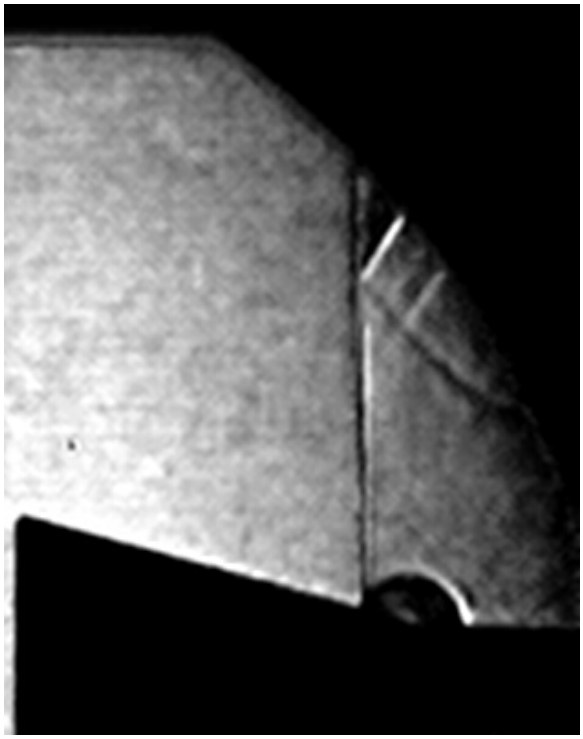
The development of the reflection of a blast wave, induced by the blast wave impinging a 15° wedge is shown in Figure 7.6. Figure 7.6 (b) shows the first step of the blast wave reflection, where it is observed that as soon as the incident blast wave impinges the corner of the wedge a reflected wave is induced. Looking at Figure 7.8 (c) it can be seen that a Mach stem has formed and the reflected wave has propagated slightly further from the wedge corner. It can also be deduced by the dark shade of grey behind the reflected blast wave that there are strong density gradients trailing the reflected blast wave. The remaining sub-figures in Figure 7.6 show that as the incident blast wave propagates further downstream across the 15° wedge that the height or length of the Mach stem increases while the distance the reflected blast wave has travelled from the corner also increases. The increased length of the Mach stem means that the triple point is moving further from the wedge with time, implying that the reflection induced is DiMR. It was also noted in the sub-figures in Figure 7.6 that there is a very high density gradient behind the Mach stem, indicated by the dark grey smear trailing the Mach stem, which reduces in intensity as the incident blast wave travels further downstream. Figure 7.6 (i) and Figure 7.7 (a) show that despite the density gradient behind the rest of the reflected blast wave reducing, the section of the reflected blast wave travelling upstream still induces a high density gradient. This could be due to the high density gradient in the upstream flow induced by the incident blast wave. What is curious is that none of the images in Figure 7.6 indicate the presence of a slipstream. This could be due to the use of unidirectional schlieren to capture the images.



7.6 (a)



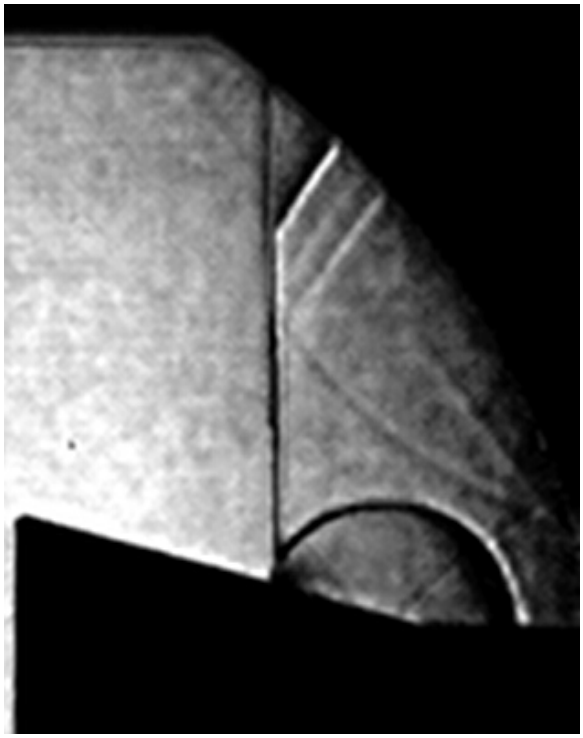
7.6 (b)



7.6 (c)



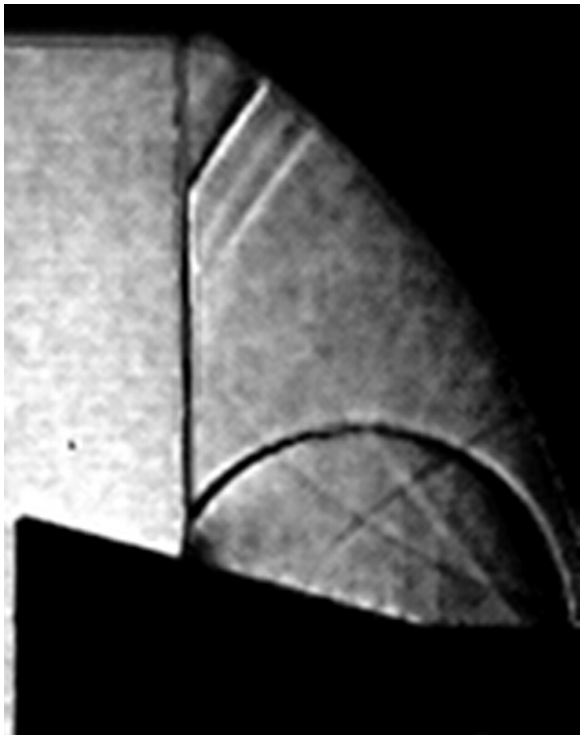
7.6 (d)



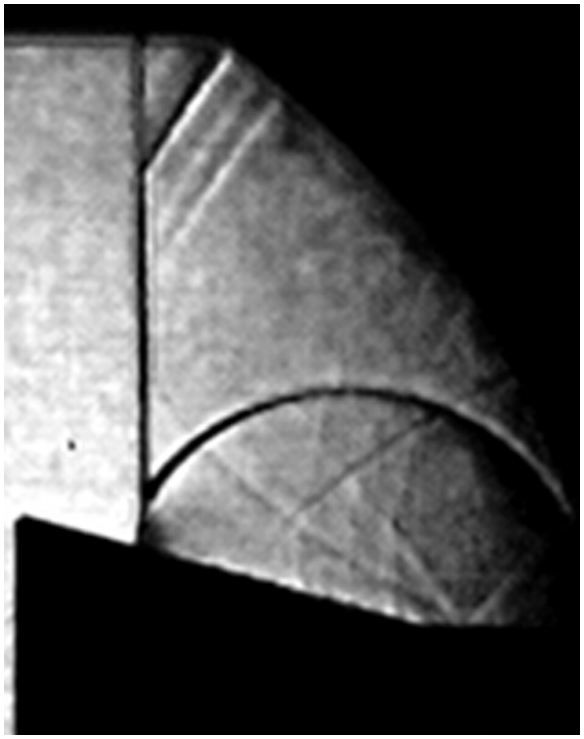
7.6 (e)



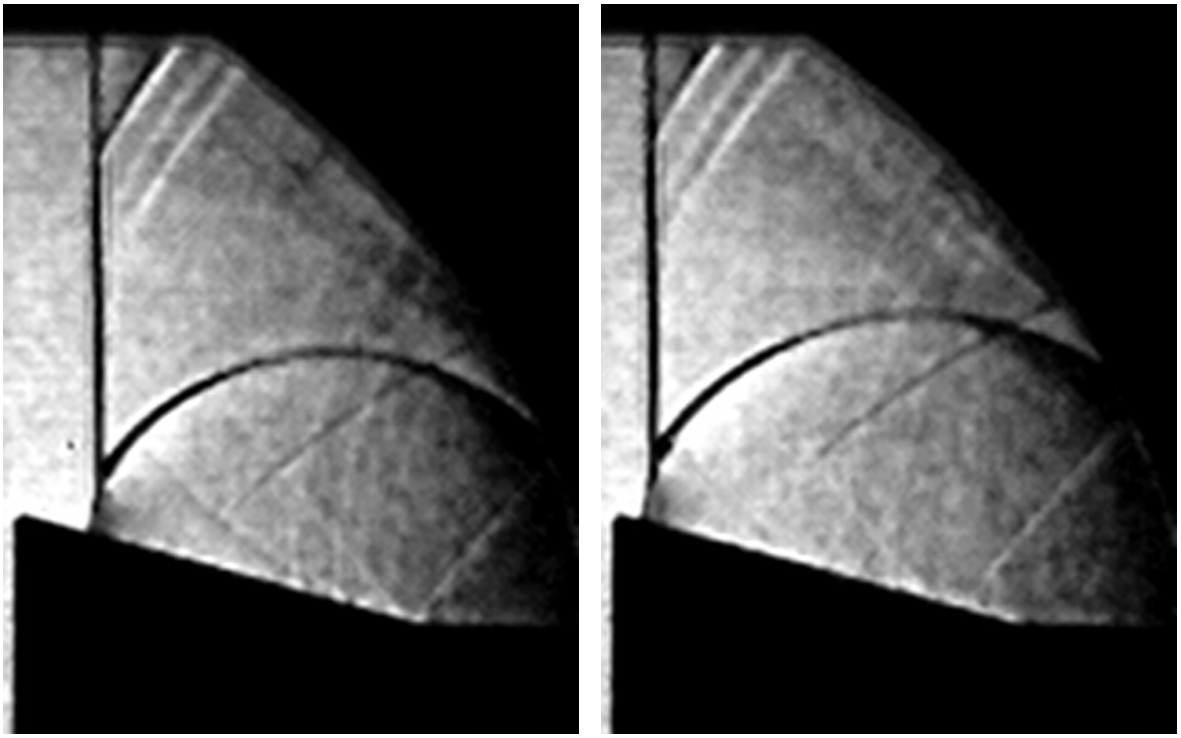
7.6 (f)



7.6 (g)



7.6 (h)



7.6 (i) 7.6 (j)

Figure 7.6: Development of a 15° Reflected Blast Wave generated by the Blast Tube having Concave Driver Section $50\mu m$ $M_0 = 1.240$

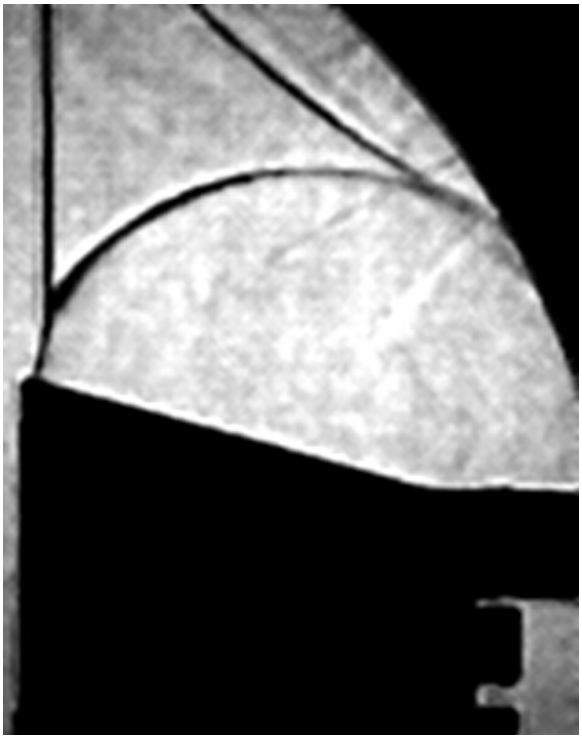
A comparison of the reflections induced by the the differently generated blast waves impinging a 15° wedge can be made by examining the sub-figures in Figure 7.7. Looking at the sub-figures 7.7 (a), 7.7 (c) and 7.7 (e) for the reflections induced by the blast waves generated with the $50\mu m$ thick diaphragm and comparing them to the reflections of the $100\mu m$ thick diaphragm generated blast waves shown in sub-figures 7.7 (b), 7.7 (d) and 7.7 (f) it is observed that the higher Mach number blast waves induce a slightly longer Mach stem then the comparative lower Mach number blast wave. The reflected blast wave in the higher Mach number cases are much darker and thicker than the lower Mach number cases indicating that the higher Mach number blast waves induce stronger reflected waves. Another notable difference between the different Mach number waves is the appearance of a slipstream behind the Mach stem of the reflection of the higher Mach number blast wave. This implies that the differences in velocities, densities and temperatures between the region behind the reflected blast wave and the Mach stem are larger for the higher Mach number blast wave than the comparable lower Mach number blast wave. Comparing Figure 7.7 (a) and 7.7 (b) to Figure 7.7 (c) and 7.7 (d) and Figure 7.7 (e) and 7.7 (f) it was observed that there were no obvious discernible differences between the reflections induced by the concave, linear and convex generated blast waves.



7.7 (a): Concave Profile $50\mu m$ $M_0 = 1.240$



7.7 (b): Concave Profile $100\mu m$ $M_0 = 1.335$



7.7 (c): Linear Profile $50\mu m$ $M_0 = 1.263$



7.7 (d): Linear Profile $100\mu m$ $M_0 = 1.390$



7.7 (e): Convex Profile $50\mu m$ $M_0 = 1.240$

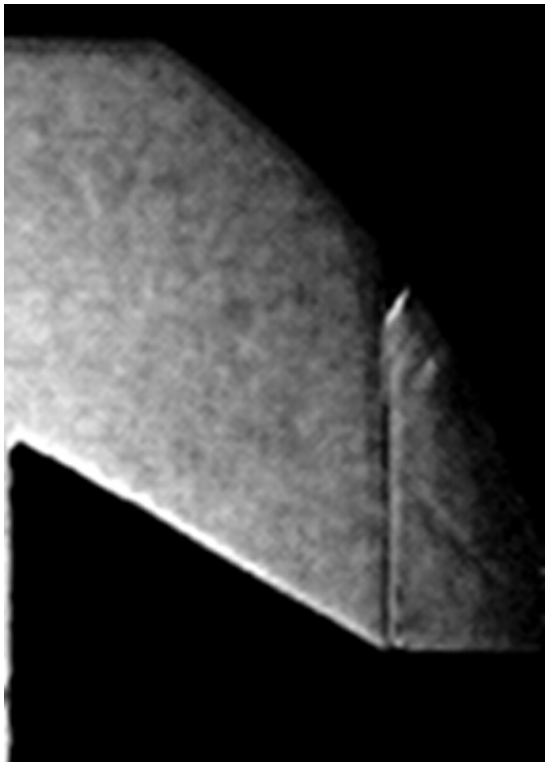


7.7 (f): Convex Profile $100\mu m$ $M_0 = 1.362$

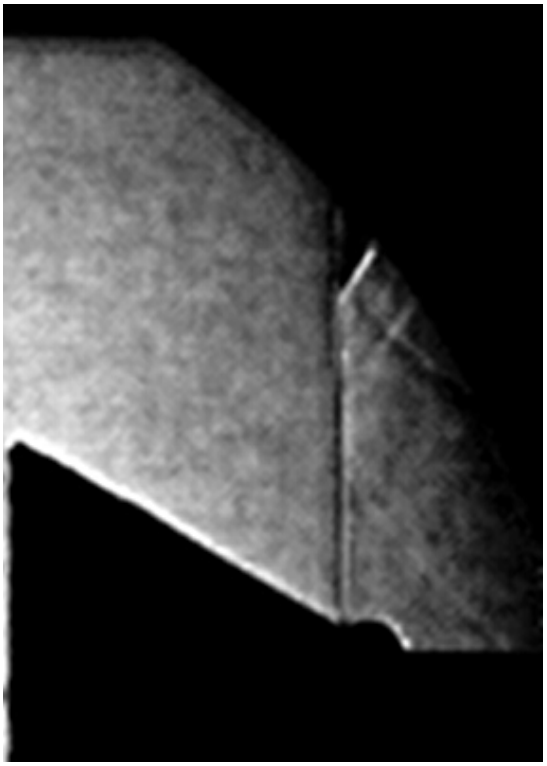
Figure 7.7: Comparison of a 15° Wedge Blast Wave Reflection generated by the Blast Tube having Concave, Linear and Convex Driver Section

7.4.2 30° Reflection

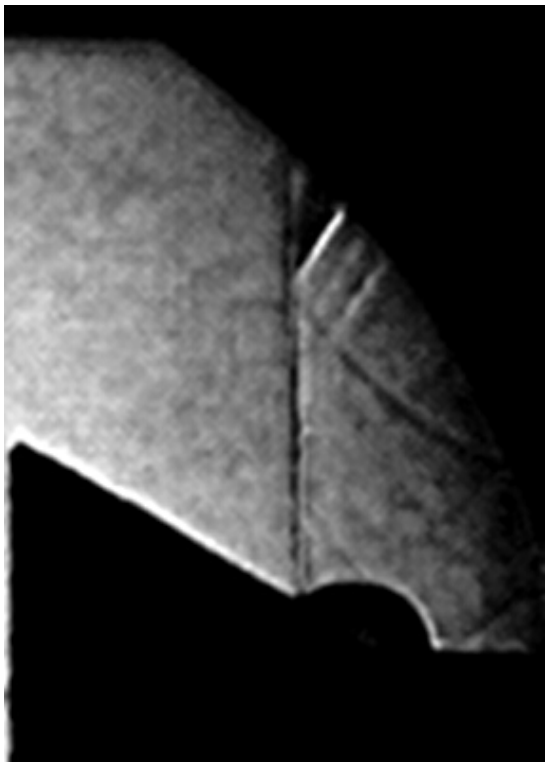
Figure 7.8 shows the development of the the blast wave reflection induced when the blast wave impinges a 30° convex wedge. Looking at Figure 7.6 and comparing it to Figure 7.8 it can be seen that the development of the 30° blast wave reflection is much the same as the 15° blast wave reflection. There are two key differences between the two different blast reflections namely, the 30° wedge reflection induces a much shorter Mach stem that has a much higher density gradient trailing it, and the reflected wave induced by the blast wave impinging the 30° wedge has higher density gradients trailing it than the comparative 15° reflected wave.



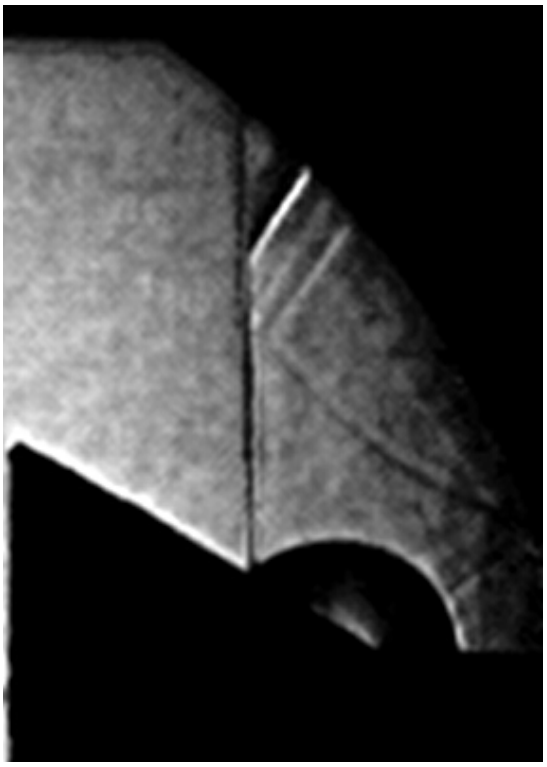
7.8 (a)



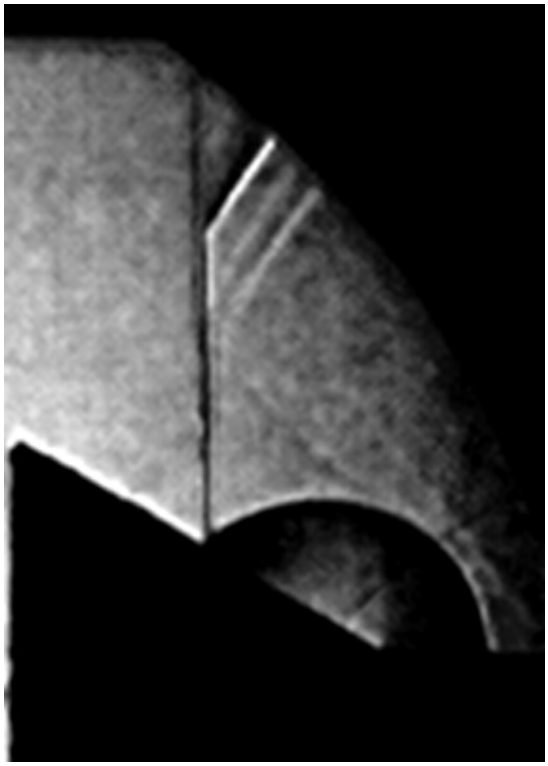
7.8 (b)



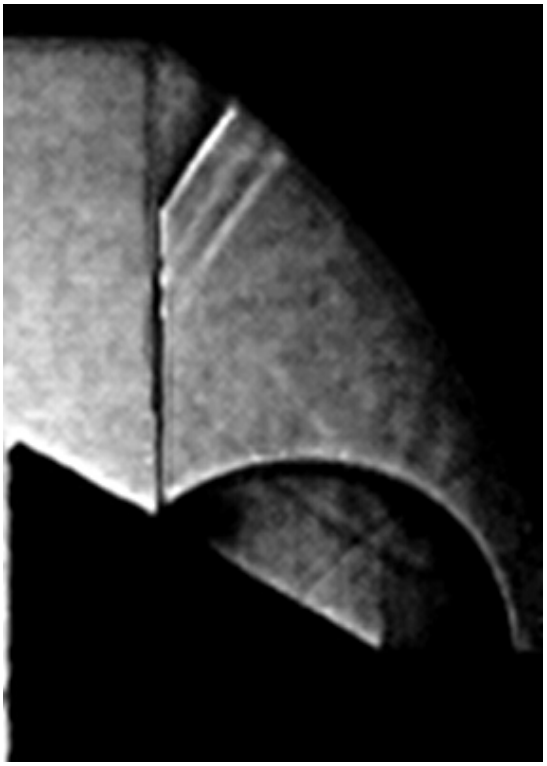
7.8 (c)



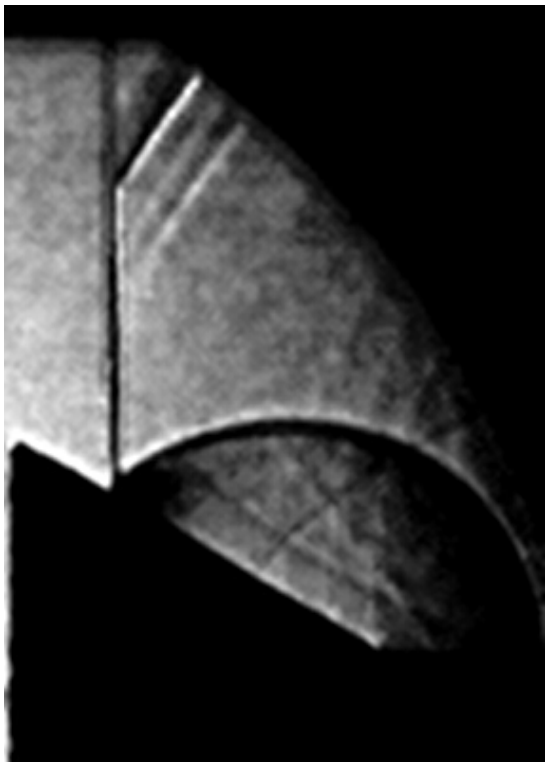
7.8 (d)



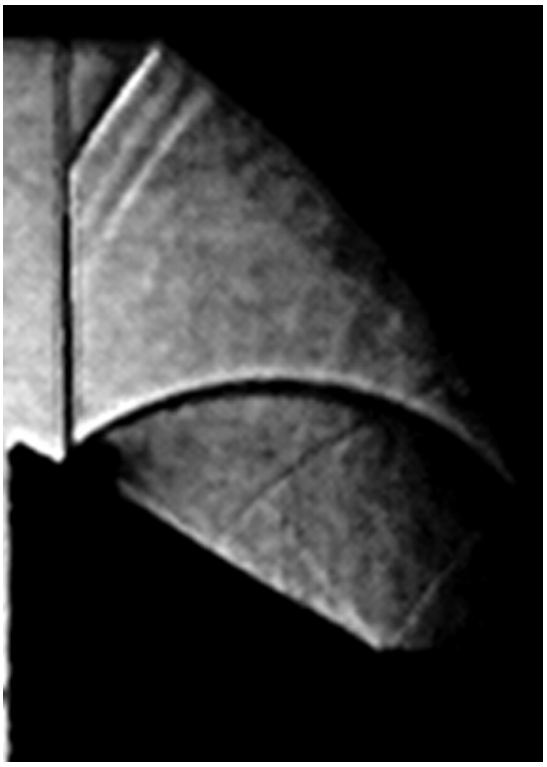
7.8 (e)



7.8 (f)



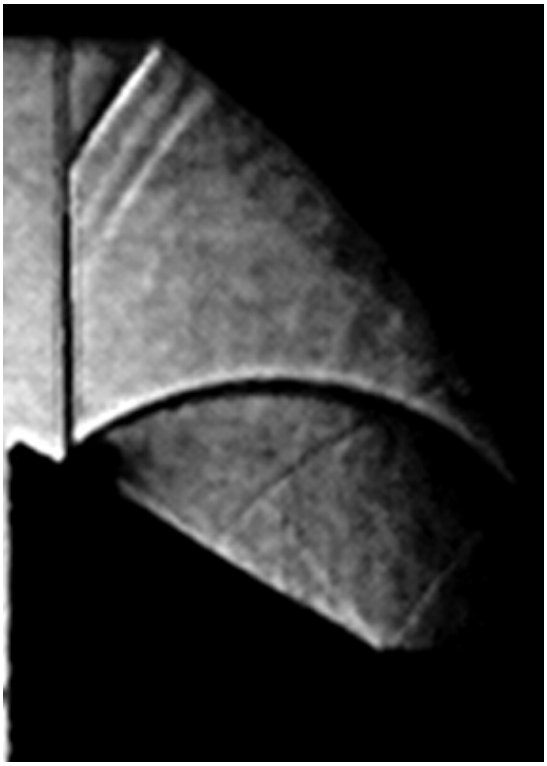
7.8 (g)



7.8 (h)

Figure 7.8: Development of a 30° Wedge Blast Wave Reflection generated by the Blast Tube having Concave Driver Section $50\mu m$ $M_0 = 1.265$

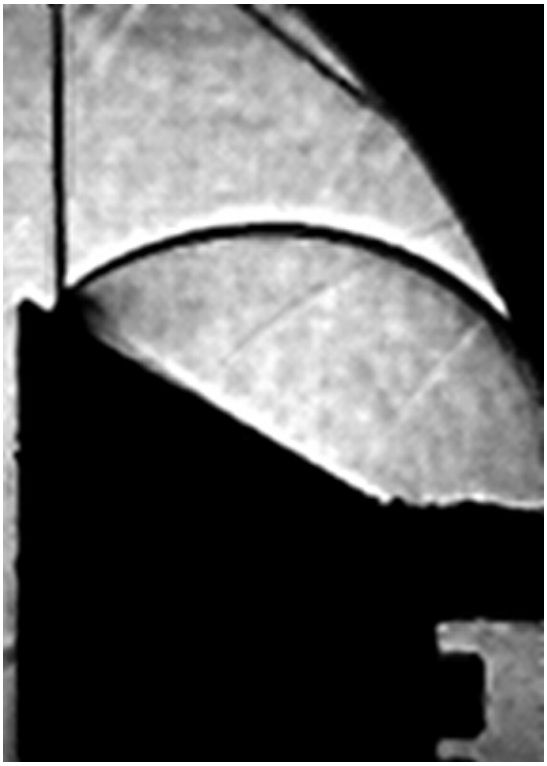
Comparing Figure 7.9 (a) to Figure 7.9 (b) it can be that, as was the case with the 15° blast wave reflection, increasing the driver pressure and in turn the Mach number of the incident blast wave causes the pressure gradient behind the Mach stem and reflected blast wave to increase in intensity. Increasing the Mach number of the incident blast wave also causes the length of the Mach stem to increase. The last notable difference that was observed between the lower and higher Mach number blast waves is the appearance of a very prominent slipstream, indicated by the black triangular shaped region trailing the Mach stem and just above the surface of the 30° wedge in Figure 7.9 (b). Similar observations were made for the 30°reflections of the blast waves generated by the linear and convex driver sections as shown in sub-figures 7.9 (c), 7.9 (d), 7.9 (e) and 7.9 (f). Looking at Figure 7.9, no blatant differences between the 30° reflections of the blast waves generated by the concave, linear and convex driver and transition section profiles were noted.



7.9 (a): Concave Profile $50\mu m$ $M_0 = 1.265$



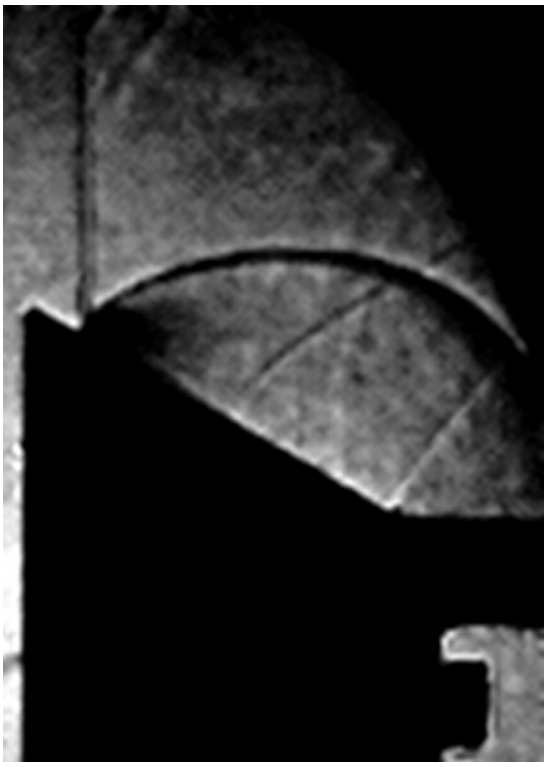
7.9 (b): Concave Profile $100\mu m$ $M_0 = 1.338$



7.9 (c): Linear Profile $50\mu m$ $M_0 = 1.263$



7.9 (d): Linear Profile $100\mu m$ $M_0 = 1.390$



7.9 (e): Convex Profile $50\mu m$ $M_0 = 1.239$

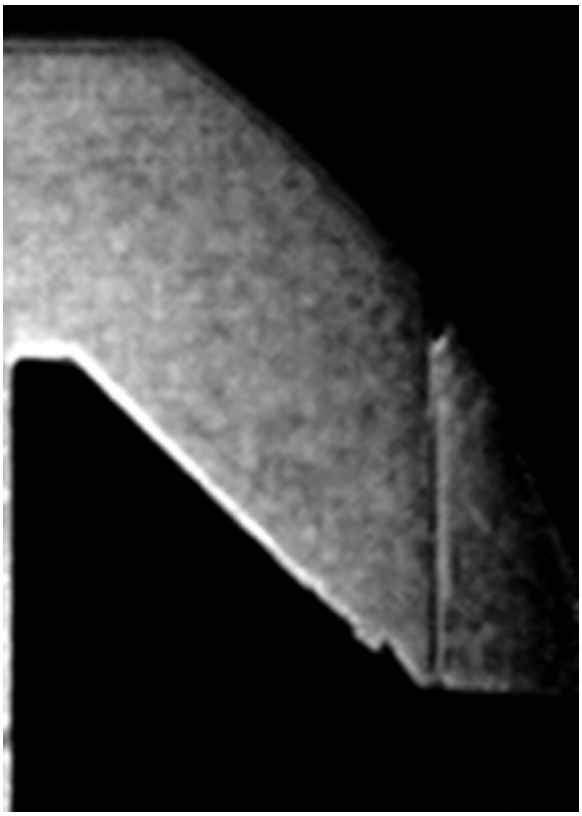


7.9 (f): Convex Profile $100\mu m$ $M_0 = 1.334$

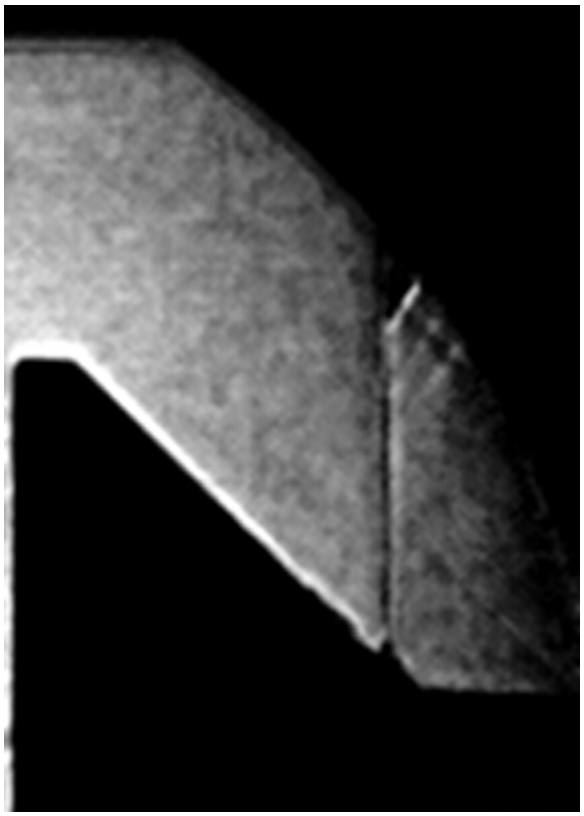
Figure 7.9: Comparison of a 30° Wedge Blast Wave Reflection generated by the Blast Tube having Concave, Linear and Convex Driver Section

7.4.3 45° Reflection

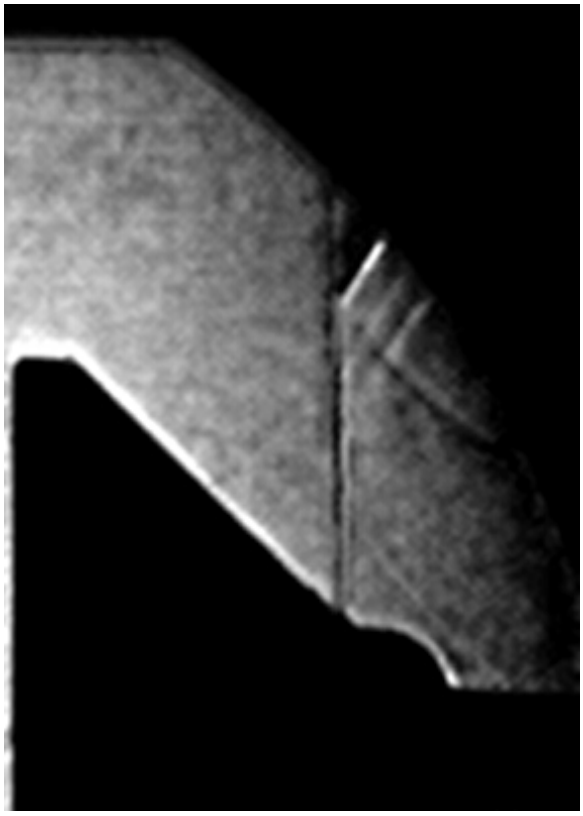
The development of the 45° blast wave reflection, as shown in Figure 7.10, differs substantially from the 15° reflection and 30° reflection in that, unlike those two previous cases, no Mach stem is induced by the 45° wedge but rather the 45° wedge induces regular oblique reflection. The reflected blast wave induced upon the incident blast wave impinging the 45° wedge is straight near the reflection point and then curves towards the bottom surface of the blast tube channel before ending at and perpendicular to the bottom surface. It was noted that the reflected blast wave induces very high density gradients in the flow trailing the reflected wave. Looking at the sub-figures in Figure 7.10 it can be seen that the reflected blast wave grows linearly with time.



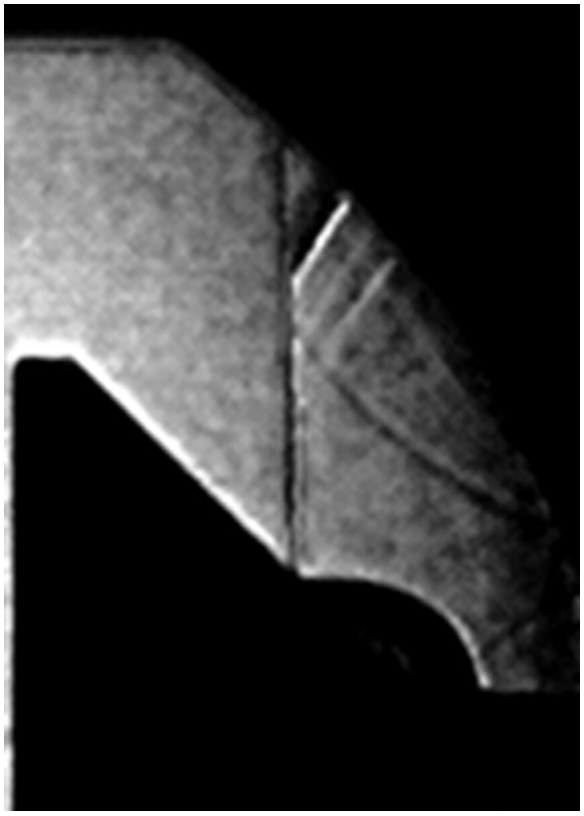
7.10 (a)



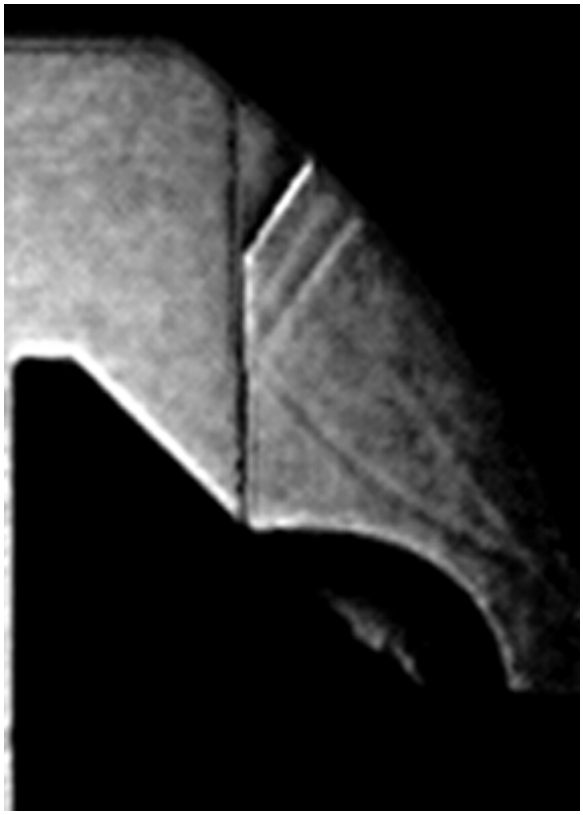
7.10 (b)



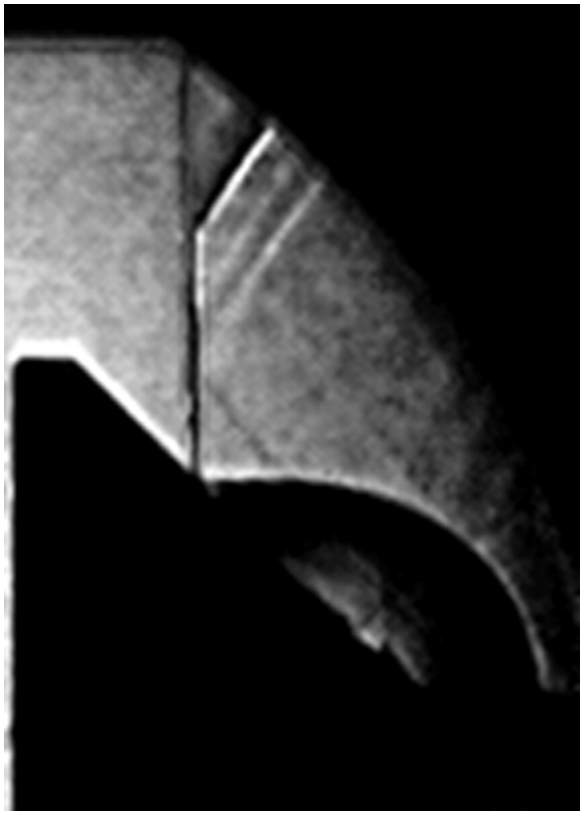
7.10 (c)



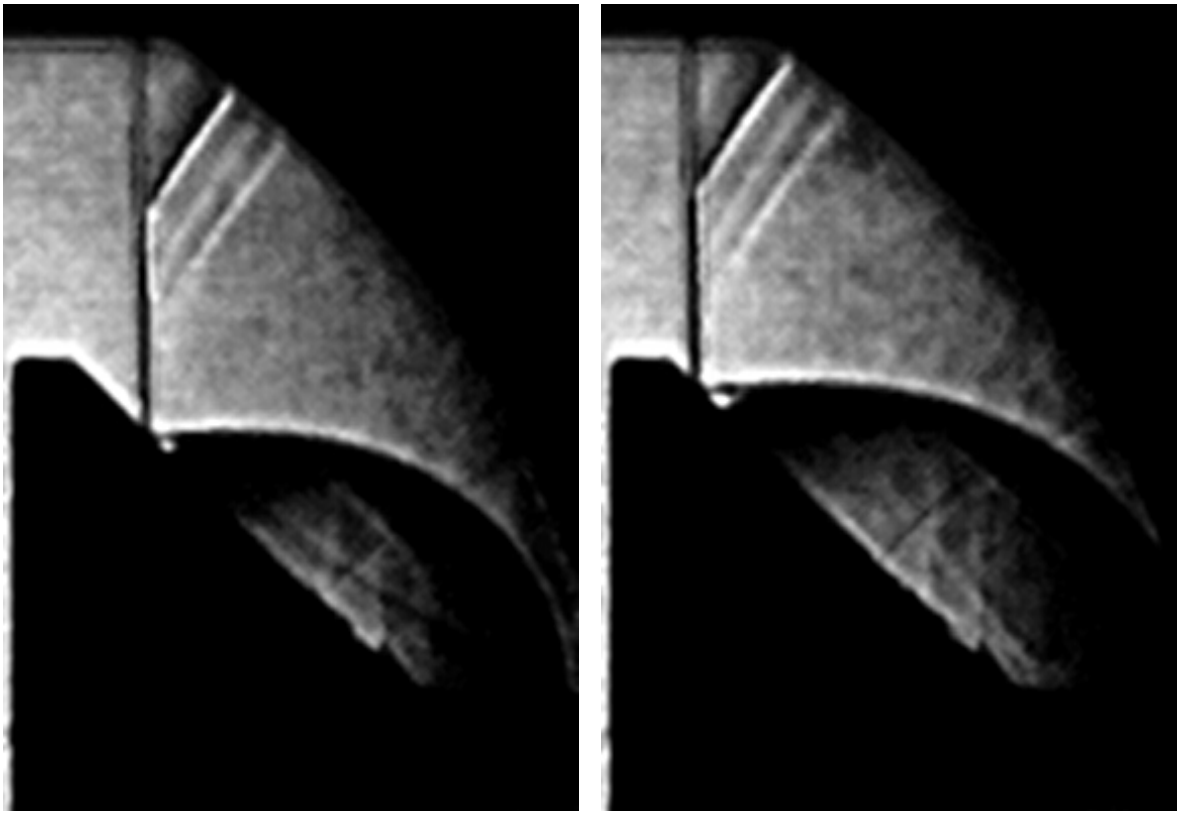
7.10 (d)



7.10 (e)



7.10 (f)



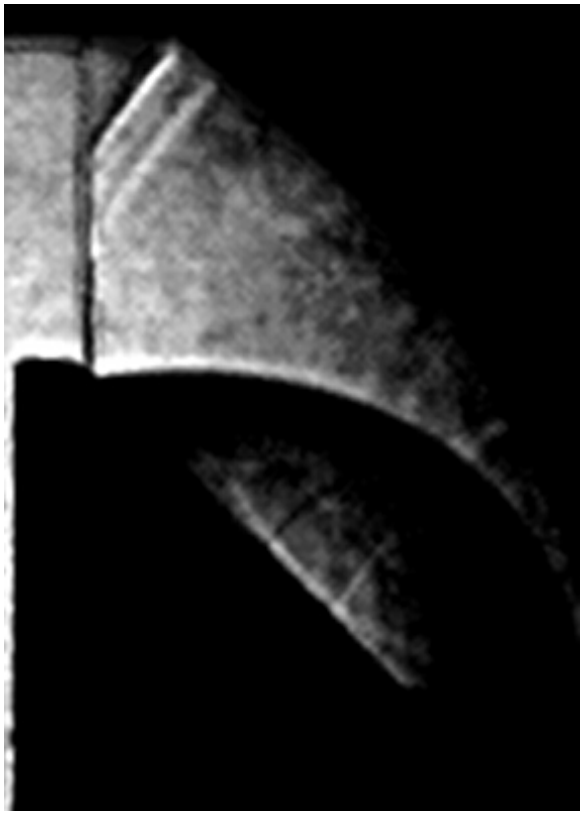
7.10 (g) 7.10 (h)

Figure 7.10: Development of a 45° Reflected Blast Wave generated by the Blast Tube having Concave Driver Section $50\mu m$ $M_0 = 1.242$

Much like the 15° and 30° blast wave reflections, the key difference that is observed between the 45° reflections induced by the lower Mach number incident blast wave and the higher Mach number incident blast wave is the increased intensity of the density gradient behind the reflected blast wave. Looking at Figure 7.11 (a) and Figure 7.11 (b) it can be seen that the higher Mach number incident blast wave induces a reflected wave with a shorter straight section by the point of reflection, than the comparative lower Mach number incident wave. Comparing Figure 7.11 (c) to Figure 7.11 (d) and Figure 7.11 (e) to Figure 7.11 (f) it can be seen that this holds true for the blast waves generated using the linear and convex driver and transition sections as well. As was the case with the 30° blast wave reflection, it can be seen by looking at that there are discernible differences in the 45° reflections induced by the concave, linear and convex generated blast waves.



7.11 (a): Concave Profile $50\mu m$ $M_0 = 1.242$



7.11 (b): Concave Profile $100\mu m$ $M_0 = 1.311$



7.11 (c): Linear Profile $50\mu m$ $M_0 = 1.262$



7.11 (d): Linear Profile $100\mu m$ $M_0 = 1.388$



7.11 (e): Convex Profile $50\mu m$ $M_0 = 1.285$



7.11 (f): Convex Profile $100\mu m$ $M_0 = 1.387$

Figure 7.11: Comparison of a 45° Wedge Blast Wave Reflection generated by the Blast Tube having Concave, Linear and Convex Driver Section

7.4.4 Comparison of Blast Wave Reflection to Normal Shock Wave Reflection

A basic comparison between the flow characteristics of blast wave reflection and normal shock wave reflection induced by the waves impinging 15°, 30° and 45° wedges was performed by using the blast wave reflection images in subsection 7.4.1, subsection 7.4.2 and subsection 7.4.3 and comparing them to the images of normal shock wave reflection produced by Skews (1966) for the doctoral thesis *Shock Wave Diffraction*. Looking at the 15° blast wave reflection in Figures 7.7 (a), 7.7 (c) and 7.7 (e) and comparing them to the images of the normal shock reflection taken by Skews (1966), it was observed that there was no discernible difference in flow features between the two types of wave reflections. The same deduction was made regarding the comparison between the 30° blast wave reflection, as shown in Figures 7.9 (a), 7.9 (c) and 7.9 (e) and the 30° normal shock wave reflection. The only difference in flow features between the blast and shock wave reflection was seen when comparing the 45° reflections where it was observed that the normal shock wave reflection had a longer straight section trailing the point of reflection than the comparative straight section of the reflected blast wave. It is important

to note however that the images used for this comparison where taken on different test rigs and with a small test section. It is therefore recommended that if a thorough comparison between blast wave and normal shock wave reflections is to be undertaken, that it be done so on the same test rig and with a larger test section that allows for longer durations for the reflected shock to develop, that is in the thousands of microseconds instead of in the hundreds of microseconds.

Chapter 8 Conclusions

A numerical design and analysis of a non-explosively driven blast tube was carried out in order to determine what effects shaping, length, the addition of a transition section and the diaphragm location have on the ability of the blast tube to generate realistic blast waves. The different driver configurations that were analysed were linearly diverging drivers, straight drivers and polynomial drivers. The CFD Simulations for the numerical analysis were performed using ANSYS Fluent. The analysis was carried out using driver pressures of $5bar$, $10bar$ and $15bar$. Upon completing the blast tube design, a prototype of the the blast tube was fabricated and assembled and the quality of the blast waves generated by the blast tube was validated experimentally. After being validated the blast tube was used to examine the diffraction of the blast wave around a 90° corner and the reflection of the blast wave induced upon impinging wedges having angles of 15°, 30° and 45°. The blast wave diffraction and reflection experimentation were carried out in the $1.2 < M_s < 1.4$ domain. Below are the conclusions drawn from the design section in chapter 4 and results section in chapter 7.

8.1 Diverging Driver Sections

The angles of divergence of the driver sections that were chosen to be examined were $7,5°$, 15°, 30°, 45° and 60°. It was observed that increasing the angle of divergence of the driver section resulted in: a marked reduction in the peak overpressure of the blast wave, a decrease in the blast over pressure and expansion phase durations, an increase in the rate of pressure decay trailing the shock front, a decrease in the velocity of the shock front and an increase in the rate at which the peak overpressure value decays with distance and time. It was noted from the numerical analysis that increasing the driver pressure from $5bar$ to $15bar$ caused: the peak overpressure value to increase, the velocity of the shock front to increase and the rate of pressure decay behind the shock front to increase. Analysing the CFD simulation data it was deduced that the effects of increasing distance on the blast wave profile was: to reduce the peak overpressure and the magnitude of the minimum expanded pressure, to increase the durations of the overpressure and expanded pressure and reduce the rate of pressure decay

behind the shock front. The pressure profiles of the blast waves generated by the linearly diverging profiles were compared to the Friedlander pressure profiles and it was found that although increasing the driver pressure and driver divergence angles produced waves with more realistic pressure decay profiles, none of the generated blast waves accurately replicated the Friedlander pressure profile.

8.2 Straight Driver Sections

After analysing the linearly diverging driver sections and determining that none of the linear diverging driver configurations produced Friedlander blast profiles, it was decided that the next stage of the design process was to assess what blast wave profiles were generated by shortened straight driver sections. The key feature of this analysis was to make a direct comparison between the linearly diverging driver sections and straight drivers sections having comparative lengths, that is, 7.5° versus $580mm$, 15° versus $290mm$, 30° versus $140mm$, 45° versus $90mm$ and 60° versus $65mm$. Like the linearly diverging driver section, it was observed that shortening the driver section resulted in an increased rate of pressure decay trailing the shock front however with the waves generated by the straight sections the pressure decay was preceded by a plateaued peak overpressure synonymous with a normal shock wave pressure profile. It was also observed that the shorter the straight driver profiles the shorter the duration of the plateaued peak overpressure. At $3.00m$ from the diaphragm it was noted that for the $140mm$, $90mm$ and $65mm$ long drivers the plateaued peak overpressures disappeared entirely. It was found that shortening the straight driver section caused the rate of peak overpressure decay and velocity decay with distance to increase. It was determined that the minimum expanded value of the generated blast waves, regardless of the length of the straight driver section, plateaued to the same value however the shorter the length of the straight driver the shorter the duration of the expansion phase. After comparing the blast pressure profiles generated by the straight driver profiles to the Friedlander profiles it was deduced that none of the generated waves had realistic blast profiles and unlike the linearly diverging profiles, lowering the driver pressure and shortening the driver resulted in the best pressure profile.

8.3 Polynomial Section

Based on the results and analysis performed in the subsection 4.1.3 and subsection 4.1.4 as well as the research carried out by Whalley (2016), it was deduced that a driver section required a few key features in order to generate a blast wave with a realistic Friedlander

pressure profile namely, the driver section must end in a sharp corner in order to enable expansion focusing to occur, the walls of the driver section must be divergent to cause the expansion waves to reflect downstream almost immediately after the diaphragm bursts as well to drive the expansion focusing, the walls of the driver section must transition smoothly, that is without a corner, into the expansion section walls and the walls of the driver section must be curved in order to induce smooth and continuous expansion wave reflection and focusing. After some tests were carried out on a few iterations of driver section shapes, three shapes were settled on, namely a concave driver, a linear driver and a convex driver.

The next stage of the design development process of the blast tube driver section was assessing what effect the location of the diaphragm had on the formation of the blast wave pressure profile. Moving the location of the diaphragm from the point where the driver section and expansion sections met, to further upstream in the driver section, led to the appearance of the transition section, a section of the expansion section having diverging walls. It was observed from the CFD simulations that the effects of altering the location of the diaphragm was much the same for the concave, linear and convex profiles. Shifting the location of the diaphragm upstream was observed to have a similar effect to increasing the angle of divergence of the linearly diverging drivers sections, that is to say, it reduced the peak overpressure of the blast wave, it reduced the duration of the both the blast wave overpressure and expansion phases, it causes the peak overpressure to sharpen, it causes the pressure decay trailing the shock front to be smoother and more rapid and it increases the rate at which the velocity of the shock front decays with distance. It was observed that the difference between the expansion sections of the measured pressures and the corresponding Friedlander expansion sections increased with decreasing percentage of driver length diaphragm placement. This was deemed to be in all likelihood due to the inability of the Friedlander equation to account for the the large secondary shocks induced by the shortened driver sections. It was also deduced that for the diaphragm locations simulated, the further upstream the diaphragm was located, the better the pressure decay behind the shock front matched the Modified Friedlander pressure profile. However, after some iterative analysis, it was determined that the best overall blast profile was generated by a driver section having the diaphragm located at 33% of the combined driver section and transition section length.

Once the best relative location of the diaphragm was determined, the effects of increasing both the length of the driver section and the transition sections, while keeping the relative diaphragm location fixed, on the generation of the blast waves were assessed. This assessment was performed by simulating driver and transition sections having combined lengths of 50%, 75%, 100%, 125%, 150% of the $500mm$ length of the driver tested in subsection 4.1.6 and with the diaphragm located at 33% of this length. It was determined that the flow characteristics induced by varying the driver and transition lengths was much the same for the concave, linear

and convex driver sections. It was determined that decreasing the length of the driver and transition sections had the tendency to steepen the gradient of the pressure decay trailing the shock front as well as to reduce the duration of both the overpressure and expansion phases of the blast wave. It was also observed to quicken the rate at which the velocity of the blast wave decayed as the wave propagated down the tube, to lower the peak overpressure of the blast wave, to increase the minimum expansion pressure and to reduce the magnitude of the secondary shock wave. If one accounts for the increased peak overpressures and reduced minimum expansion pressures, it was deduced that the five different driver and transition length produced blast waves having almost identical pressure decays and overall shapes. It was ascertained that all five driver and transition section lengths generated realistic blast waves which was inferred from the almost perfect alignment of the generated pressure profiles with the corresponding Modified Friedlander profile. From this it was deduced that as long the diaphragm location of approximately 33% as well as the overall shape of the profile is maintained, various blast wave configurations can be generated by a similarly shaped driver profile by increasing the length of both the driver and transition section proportionally. It was thus determined that varying the driver and transition sections lengths, along side varying the driver pressure, are the best methods for obtaining the desired blast wave pressure profile.

Upon settling on a driver and transition length having a combined length of 500mm and diaphragm located at 33% for carry out the experimentation and validation of the blast tube design, it was also decided to assess what effect the length of the expansion section would have on the development of the blast wave. The affects of expansion section length were assessed by simulating a blast tube having a $5m$ long open ended expansion section. It was also decided that an assessment be carried out to ascertain if there was any difference between the blast waves generated by the concave, linear and convex driver. It was noted that the convex driver produced the blast wave with the highest peak overpressure and longest overpressure and expansion phases while the concave driver produced waves with the lowest peak overpressures and shortest overpressure and expansion phases. Accounting for the different peak overpressures, minimum expansion pressures and blast durations it was observed that all three driver profiles produce waves with almost identical pressure decay profiles. It was found that effects of increasing the driver pressure of the concave, linear and convex drivers on the pressure profile was to increase the peak overpressure, blast duration, expansion phase duration, secondary shock strength and reduce the minimum expansion pressure. It was also observed that regardless of driver pressure the blast waves generated had almost identical decay profiles. It was seen that all three drivers produced waves which from $1.00m$ downstream of the diaphragm perfectly matched the Modified Friedlander profile. This implies that along with driver pressure and driver shaping, altering the length of the driven section is another property of the blast tube that can be modified in order to produce the desired blast wave pressure profile and impulse.

8.4 Blast Tube Validation

There were two main objectives of the design of the blast tube, namely to design a blast tube that could generate blast waves having realistic blast wave pressure decay profiles and blast waves of good visual quality so as to allow visual experimentation to be performed with the blast tube. Once the blast tube design had been completed and the tube fabricated and assembled a few tests of the tube were performed and pressure data from four transducers was collected and axisymmetric schlieren photographs were taken. Three key factors that were found to effect the quality of the blast tube validation were: firstly the test section having a closed end resulting in a reflected blast wave travelling upstream before the blast wave had time to fully develop, secondly the pressure differential which arose between the driver section and the pressure vessel which caused the direct-loaded poppet valves to open letting in high pressure air into the driver section which disrupted the expansion focusing process and in turn the blast wave formation and lastly the formation of diffracted and transverse waves trailing the shock front caused by notches and steps in the blast tube where the different sections of the blast tube were joined as well as where the test piece was connected to the test section. When these three factors were accounted for it was deduced that the blast tube did in fact produce realistic blast waves as the pressure profiles produced by the transducers for all the blast tube configurations were found to correspond almost perfectly with the Friedlander and Modified Friedlander pressure profiles. Having verified that the blast tube did in fact produce realistic blast waves, it was ascertained through the schlieren images that were taken that all the blast tube configurations produced blast waves of high visual quality as the blast wave shock fronts were flat and perpendicular to the direction of travel.

8.5 Blast Wave Diffraction

The diffraction of blast waves across a 90° convex corner was studied over a range of incident blast wave Mach numbers ($1.2 < M_s < 1.4$). It was observed that the diffraction of the blast wave is characterised by the diffracted blast wave travelling down the side of the test piece while a sound wave travels back upstream. It was found that very high density gradients arose in the region of the flow encapsulated by the diffracted blast wave and reflected sound wave. After some time it was observed that a vortex forms at the corner of the test piece. As time progressed further it was found that vortex grew in size and the straight section of the incident blast wave reduced in length. Due to the range of Mach numbers at which the testing was carried out, it was seen that no contact surface was generated as the entropy change induced by these waves was not high enough to do so. It was observed that increasing the Mach number of the incident blast wave resulted in a larger vortex being generated and

a slightly different flow patterns regarding the reflected sound wave. Due to the different blast tube configurations producing similar blast waves, it was seen that the there was no discernible difference in the characteristics and nature of the blast wave diffraction around the 90° between the blast waves generated by the concave, linear and convex driver and transition shapes. When comparing the blast wave diffraction to normal shock diffraction it was noted that the only discernible difference between the two diffractions was the more circular nature of the normal shock induced reflected sound wave.

8.6 Blast Wave Reflection

The reflection of blast waves impinging 15°, 30° and 45° wedges were examined over a range of incident blast wave Mach numbers ($1.2 < M_s < 1.4$). It was observed that the reflection induced by the blast wave impacting the 15° and 30° wedges was DiMR, inferred from the Mach stem increasing in length with time which implied the triple point moves away from the edge surface, while the reflection caused by the blast wave contacting the 45° wedge was observed to be regular oblique reflection, deduced by the lack of the formation of a Mach stem. It was observed for all three blast reflections that a high density gradient was induced behind the reflected blast wave. For both the 15° and 30° reflections a high density gradient behind the Mach stem was also observed. It was noticed in both the 15° and 30° wedge reflection cases that increasing the Mach number of the incident blast wave resulted in a comparably longer Mach stem, a higher density gradient trailing the Mach stem, a stronger reflected blast waves and the formation of a prominent slipstream. The key difference that was found to exist between the blast wave reflection induced by the 15° wedge and the 30° wedge was the the length of the Mach stem with the 30° reflection generating a much short Mach stem than the comparable 15° reflection. It was found that the difference that increased incident blast wave Mach number had on the 45° reflection was to reduce the length of the straight section of the reflected wave near the point of reflection. For all three reflection cases no discernible difference in the reflection characteristics and features were observed between the blast waves generated by the concave, linear and convex driver profiles. From the comparison between the blast wave reflection and normal shock wave reflection it was deduced that the only difference that arose between the two wave types was the normal shock wave oblique reflection induced a longer straight section in the reflected wave by the point of reflection than the comparative regular oblique blast wave reflection.

Chapter 9 Recommendations

The current work involved analysing an assortment of numerical and experimental data. Due to the design and validation of a non-explosively driver blast tube carried out for this work being very novel, it opens the door for further research and development to be carried out. Recommendations for future work are given below:

- One of the main flaws of the current prototype blast tube is the compressed gas driver filling mechanism in that the current mechanism does not allow for the minutiae and finical control and adjustment of the pressure of the air going into the driver section and the filling mechanism also allows compressed air to flow into the driver section during testing. Both of these flaws invariable reduce the performance of the blast tube as well as the quality of the blast waves the tube can generate. It is therefore recommended that any further developments of the blast tube involve looking at replacing the the current direct-loaded poppet valve filling mechanism with one that will allow for more control and that will prevent air entering the driver section during testing.

- An issue that arose during testing of the blast tube was the realisation that the current aspect ratio of the internal dimensions of the blast tube were not optimised for the diaphragm burst. This resulted in the diaphragms not petal-ling fully which in turn negatively effected the blast wave formation. It is therefore recommended that any further development of the blast should involve an analysis of the internal dimension of the blast tube in order to ascertain what internal dimensions of the blast tube will give the best aspect ratio to enable the diaphragm to petal properly upon bursting.

- During the validation process of the blast tube it was realised that a problem with the current design is the closed end nature of the downstream end of the test section. The problem that arises is the incident blast wave reflects back upstream off the end of the test section before the blast wave has had sufficient time to fully develop. Is therefore recommended that the next iteration of the blast tube places the test section in the middle of the driven section or replaces the closed end of the test section with a diffuser so as to allow for the blast wave to fully develop.

- During the validation of the visual quality of the wave it was noticed that there were numerous transverse and diffracted waves trailing the shock front. It was deduced that this was caused by the notches and steps arising at the numerous joints along the length of the blast tube. It is therefore recommended that if further work is carried out on the blast tube design, every effort should be made to reduce the number of sections making up the blast tube which will in turn reduce the number of joints and to ensure that internal surface of the blast tube is as smooth as possible.

- In this work other driver and transition sections were posited as possible solutions to generating blast waves non-explosively than the configurations fabricated, assembled and tested. It is therefore recommend that the other blast tube driver section and transition section configurations be experimentally tested and validated.

- During the current work, only a small range of driver pressures and incident blast wave Mach numbers were simulated and tested. It is recommended that an attempt be made to verify whether or not the blast tube can be used to simulate blast waves generated by larger explosions up to and including nuclear explosions. This would in all likelihood require testing the tube with driver pressures upwards of $100bar$.

- It is recommended that a more thorough comparison between normal shock wave and blast wave diffraction and reflection be carried out. Since the current comparison was performed using images from different test rigs and with a relatively small test section a further recommendation is that any further normal shock wave and blast wave flow comparisons should be carried out using the same test rig and with a larger test section that allows for longer durations for the reflected shock to develop, that is in the thousands of microseconds instead of in the hundreds of microseconds.

- In this work the flow characteristics arising when the the blast wave impinged wedges and corners were analysed. To ensure the real world practicality of the blast tube it is recommend that models of real word objects such as tanks and armoured vehicles be tested and the loads on these models measured and compared to the loads said vehicles would experience when impacted by an explosively generated blast wave.

Bibliography

Anderson, J. D. (1990). *Modern Compressible FLow with Historical Perspective*. 2nd. Singapore: McGraw-Hill Publishing.

Baker, W. E. (1973). *Blast Waves*. 1st. Austin: University of Texas Press.

Ben-Dor, G. (2007). *Shock Wave Reflection Phenomena*. New York: Springer.

Ben-Dor, G., O. Igra and T. Elperin (2001a). *Handbook of Shockwaves, Volume 1*. 1st. London: Academic Press.

Ben-Dor, G., O. Igra and T. Elperin (2001b). *Handbook of Shockwaves, Volume 1*. London: Academic Press.

Brode, H. L. (1959). 'Blast Wave from a Spherical Charge'. In: *Physics of Fluids* 2.2, pp. 217–229.

Courant, R. and K. O. Friedrichs (1948). *Supersonic Flow and Shock Waves*. 1st. New York: Interscience Publishers Inc.

Filler, W. S. (1960a). *Design Characteristics of a Conical Shock Tube for the Simulation of Very Large Charge Blasts*. Tech. rep. White Oak.

Friedlander, F. G. (1946). 'The Diffraction of Sound Pulses. I. Diffraction by a Semi-Infinite Plane'. In: *Proceedings of The Royal Society A: Mathematical, Physical and Engineering Sciences* 186.1006, pp. 322–344.

Henderson, L. F. and A. Lozzi (1975). 'Experiments on the transition of Mach reflexion'. In: *Journal of Fluid Mechanics* 68, pp. 139–155.

Hornung, H. G., H. Oertel Jr and Sandeman (1979). 'Transtion to Mach reflection of shock waves in steady and pseudo-steady flows with and without relaxtion'. In: *Journal of Fluid Mechanics*, pp. 541–560.

Igra, O., J. Falcovitz and W. Heilig (2003). 'Blast Wave Reflection from Wedges'. In: *ASME* 125, pp. 510–519.

Kinney, G. F. (1962). *Explosive Shocks in Air*. 1st. New York: The Macmillan Company.

Needham, C. E. (2010). *Blast Waves*. 1st. Heidelberg: Springer.

Ritzel, D. V. et al. (2015). *Experimental Blast Simulation for Injury*. Tech. rep. Brussels.

Skews, B. W. (1967b). 'The perturbed region behind a diffracting shock wave'. In: *Journal of Fluid Mechanics*, pp. 705–719.

Skews, B. W. (1966). 'Shock Wave Diffraction'. PhD thesis. University of the Witwatersrand.

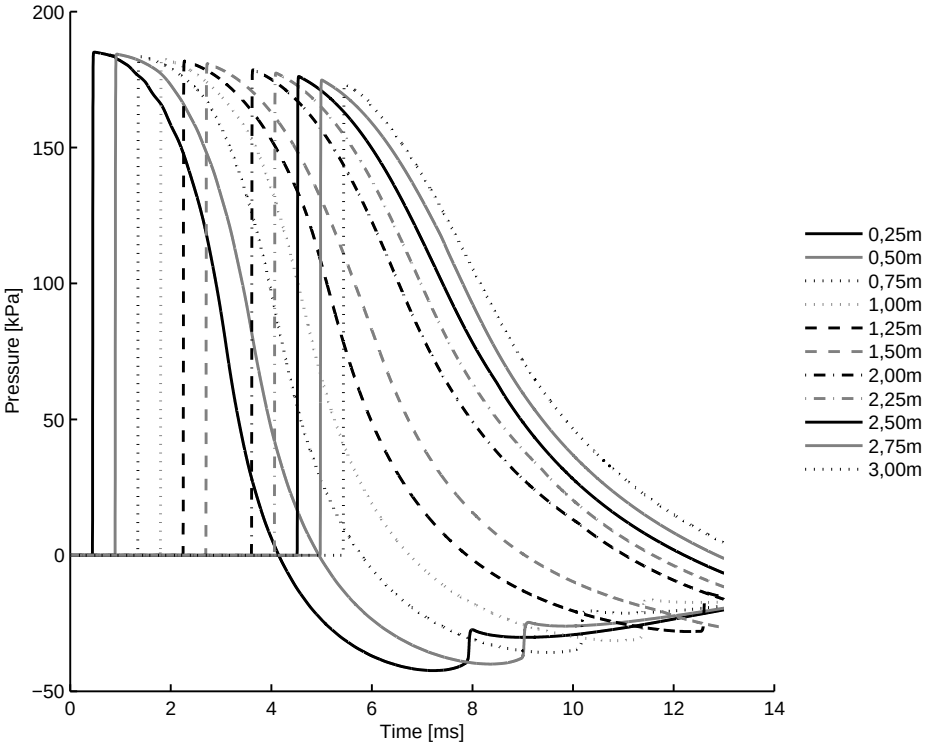
Whalley, M. S. (2016). *Focusing of Expansion Waves*. Tech. rep. Johannesburg.

Whitham, G. B. (1958). 'On the propagation of shock waves through regions of non-uniform area flow'. In: *Journal of Fluid Mechancis*, p. 337.

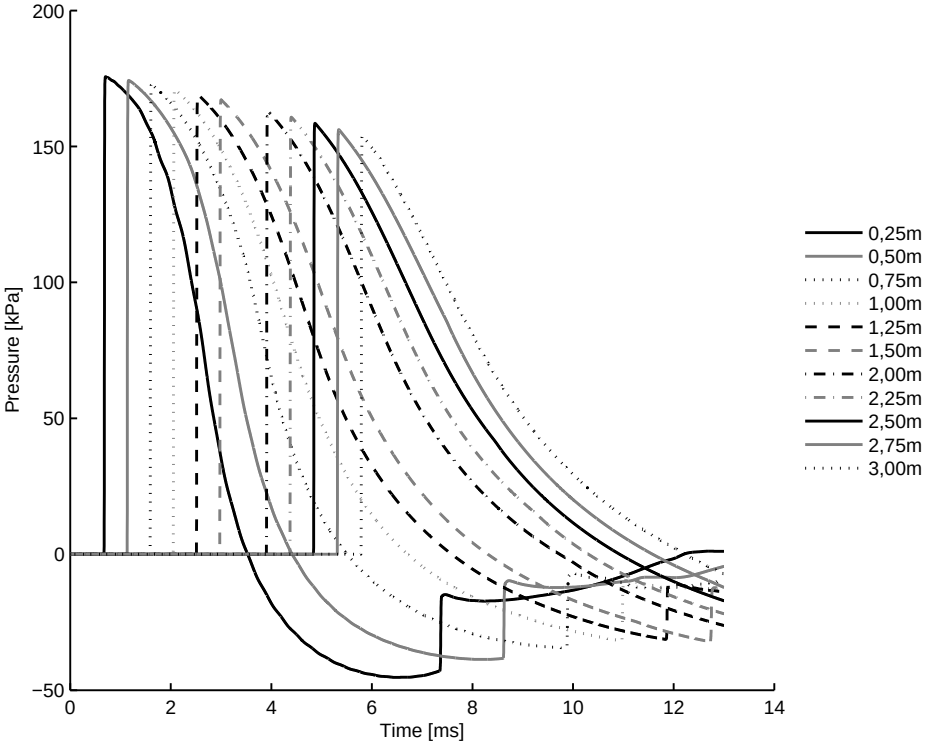
Wright, J. K. (1961). *Shock Tubes*. 1st. London: Methuen & Co.

Appendix A Varying Diaphragm Location CFD Data

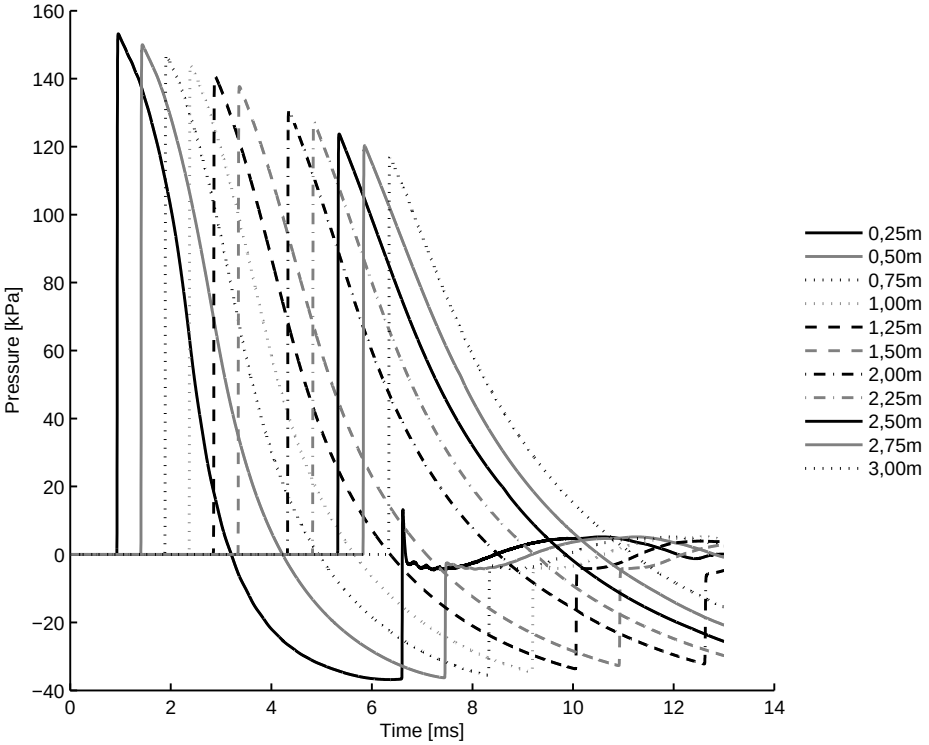
A.1 Linear Driver Section CFD Data



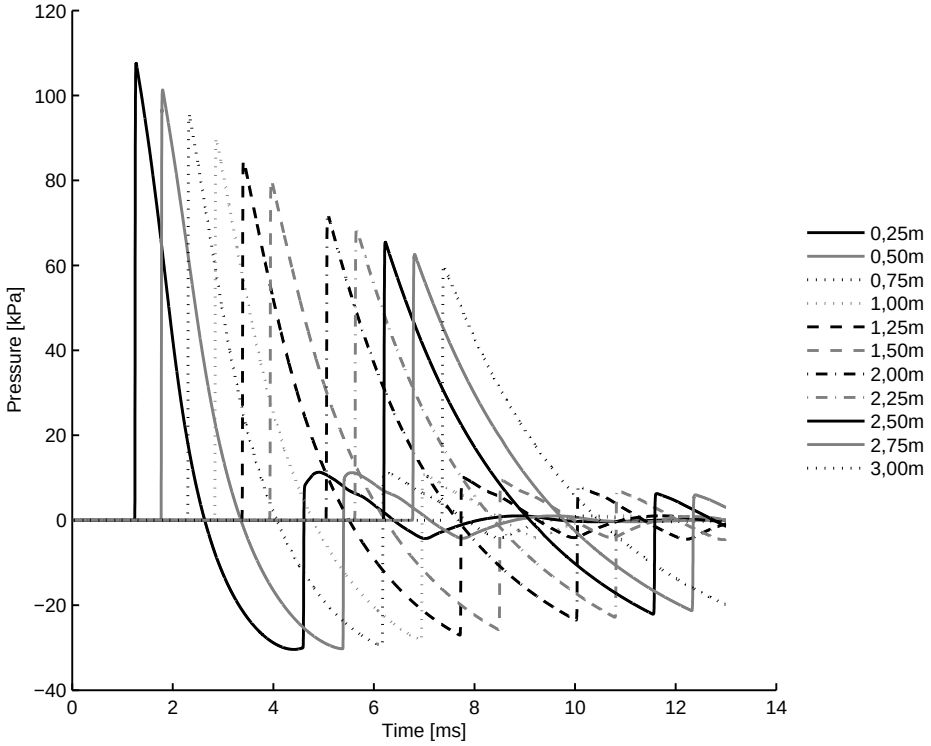
A.1 (a): 100% of Linear Driver Length 10*bar*



A.1 (b): 75% of Linear Driver Length 10*bar*

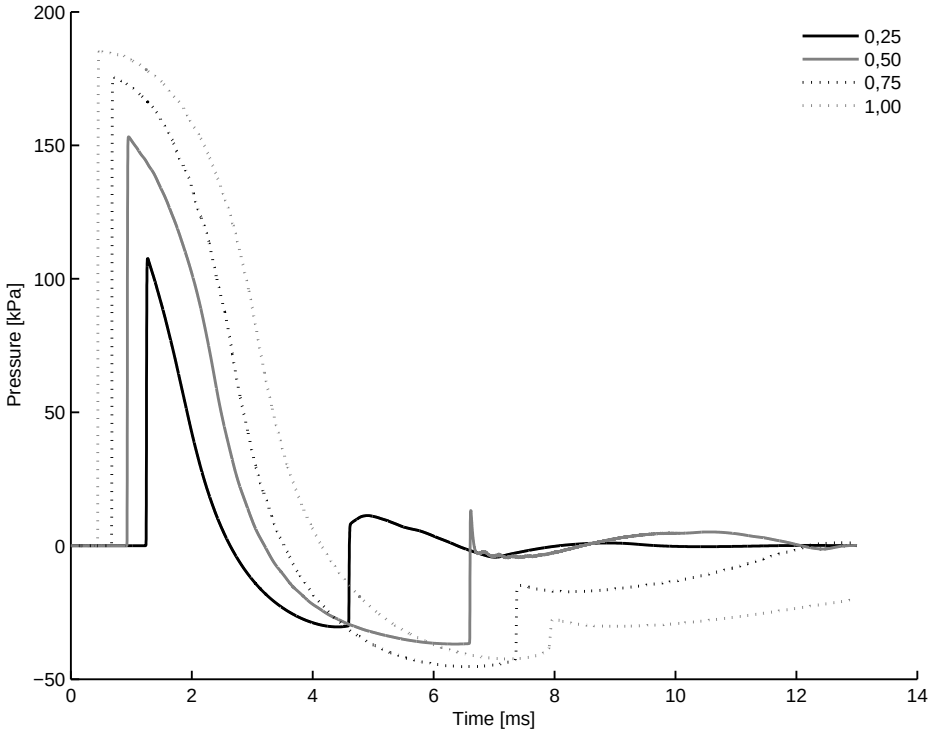


A.1 (c): 50% of Linear Driver Length 10*bar*

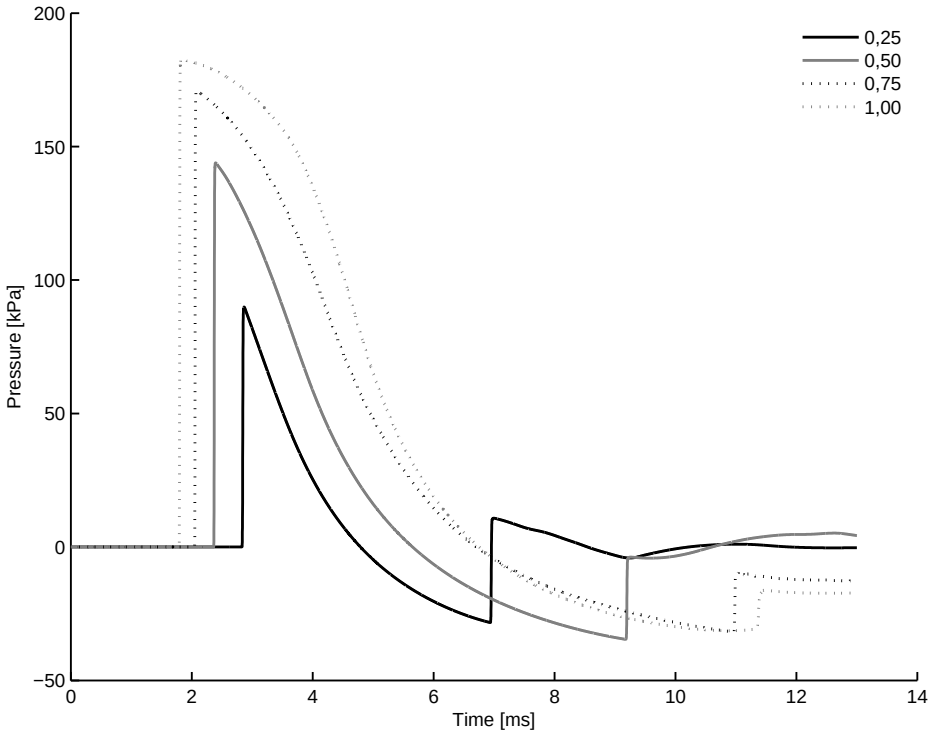


A.1 (d): 25% of Linear Driver Length 10*bar*

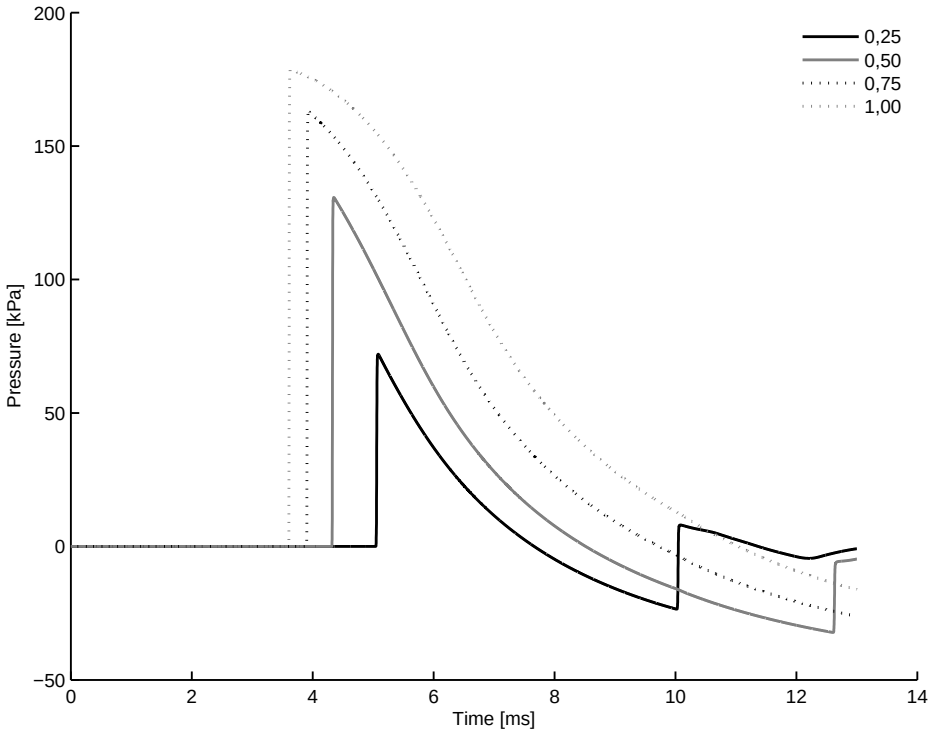
Figure A.1: The Development of the Blast Pressure Profile for Varying Diaphragm Locations in the Linear Driver Section



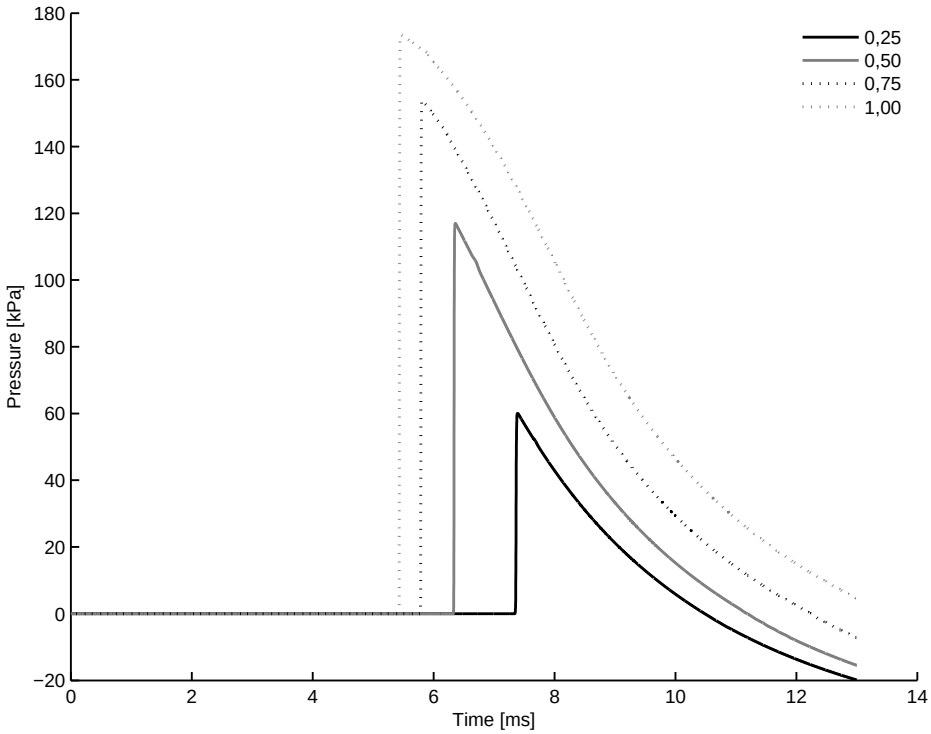
A.2 (a): 0.25*m* 10*bar*



A.2 (b): $1.00m$ $10bar$

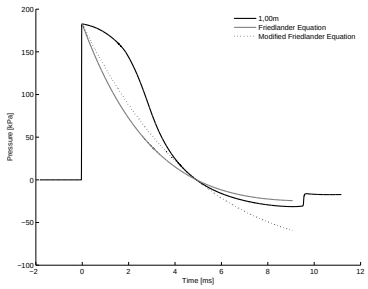


A.2 (c): $2.00m$ $10bar$

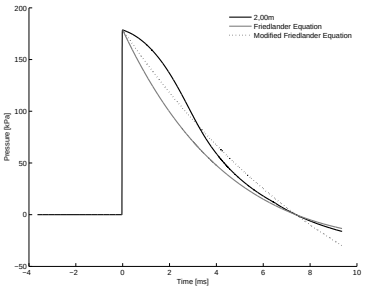


A.2 (d): 3.00m 10bar

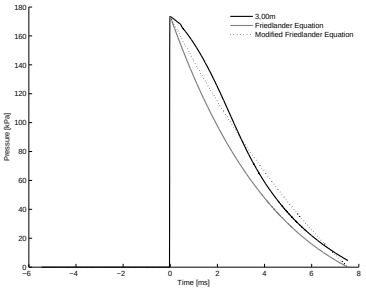
Figure A.2: The Effect of Varying Diaphragm Locations in the Linear Driver Section on the Pressure Profile



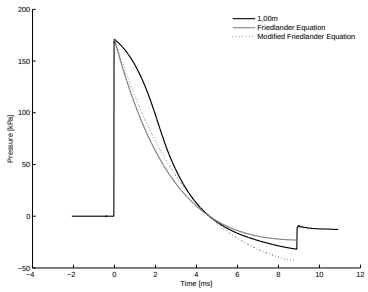
A.3 (a): 100% of Linear Driver Length 10bar 1.00m



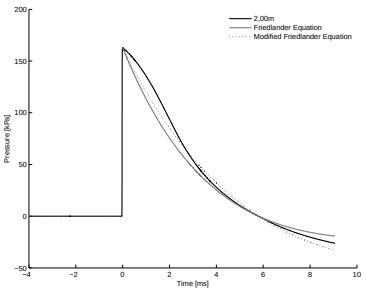
A.3 (b): 100% of Linear Driver Length 10bar 2.00m



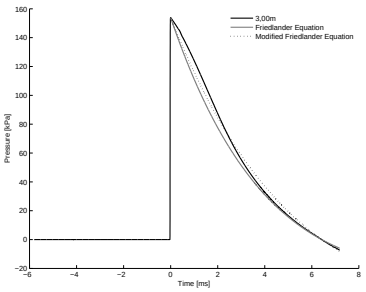
A.3 (c): 100% of Linear Driver Length 10bar 3.00m



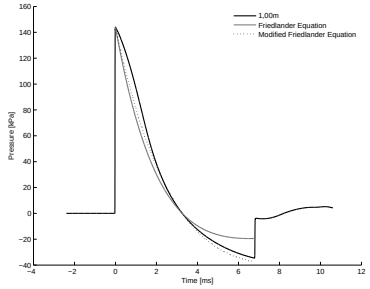
A.3 (d): 75% of Linear Driver Length 10bar 1.00m



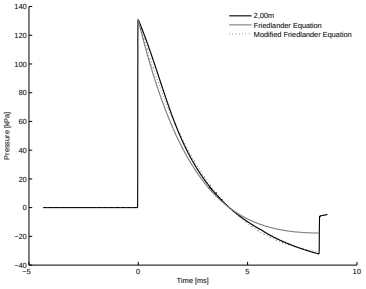
A.3 (e): 75% of Linear Driver Length 10bar 2.00m



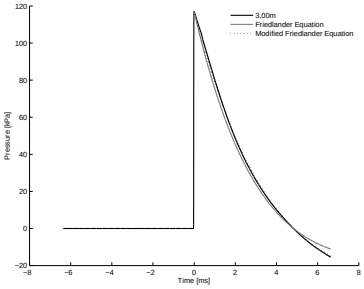
A.3 (f): 75% of Linear Driver Length 10bar 3.00m



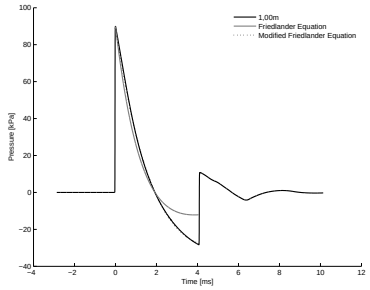
A.3 (g): 50% of Linear Driver Length 10bar 1.00m



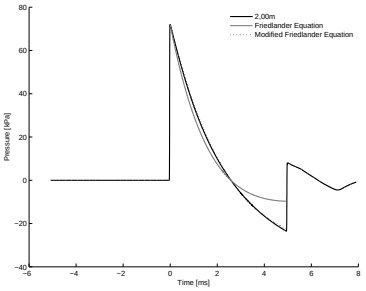
A.3 (h): 50% of Linear Driver Length 10bar 2.00m



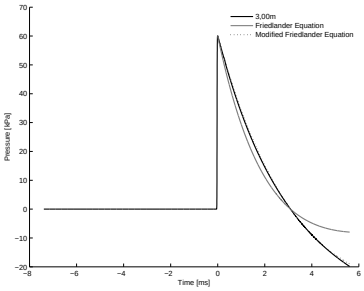
A.3 (i): 50% of Linear Driver Length 10bar 3.00m



A.3 (j): 25% of Linear Driver Length 10bar 1.00m

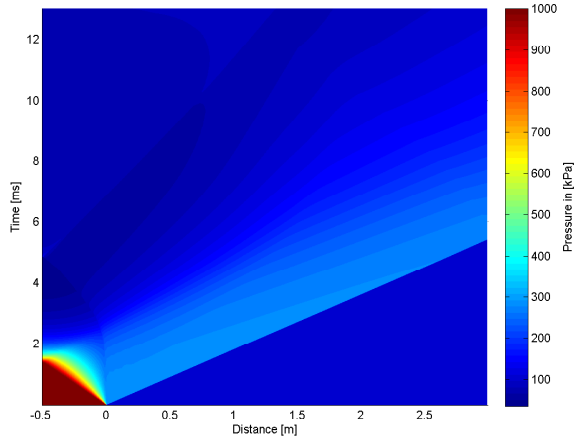


A.3 (k): 25% of Linear Driver Length 10bar 2.00m

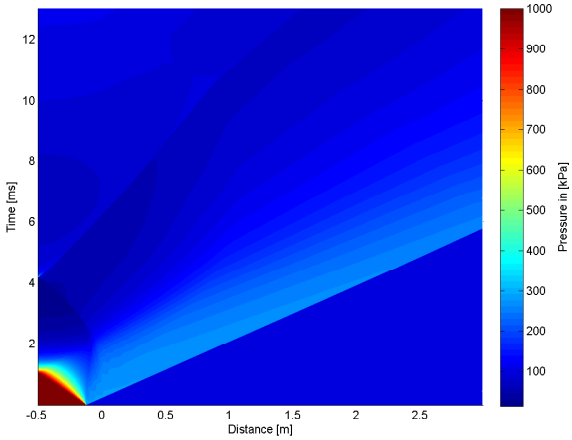


A.3 (l): 25% of Linear Driver Length 10bar 3.00m

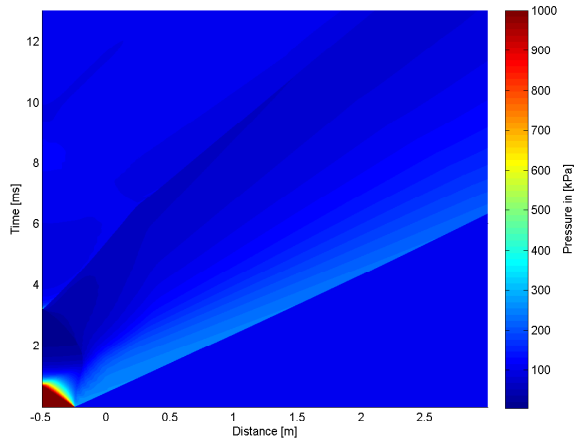
Figure A.3: Comparing the Effect of Varying Diaphragm Location in the Linear Driver Section on Friedlander Pressure Profile



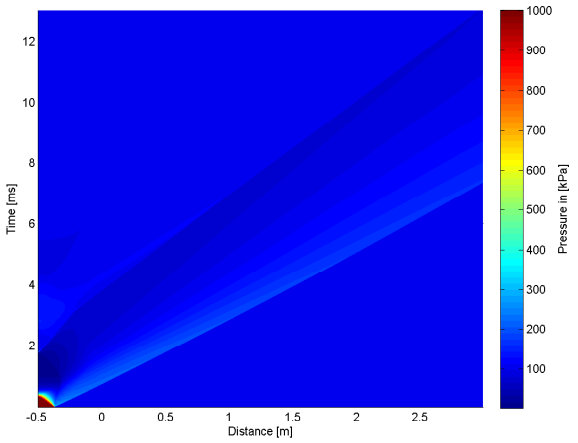
A.4 (a): 100% of Linear Driver Length 10bar



A.4 (b): 75% of Linear Driver Length 10bar

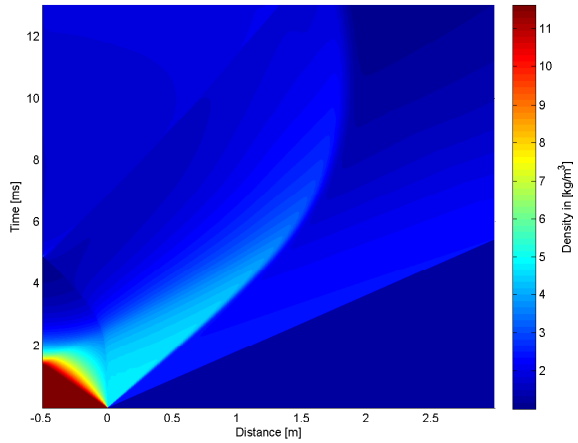


A.4 (c): 50% of Linear Driver Length 10*bar*

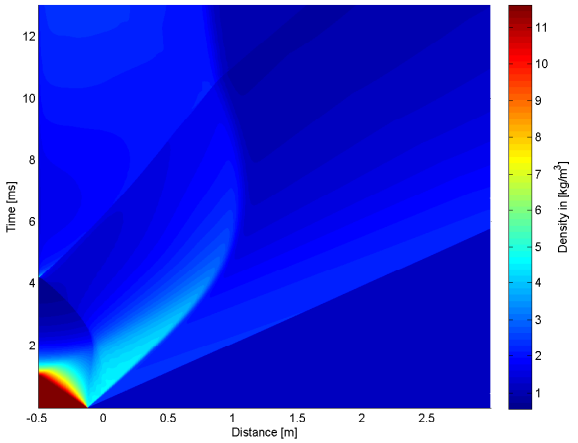


A.4 (d): 25% of Linear Driver Length 10*bar*

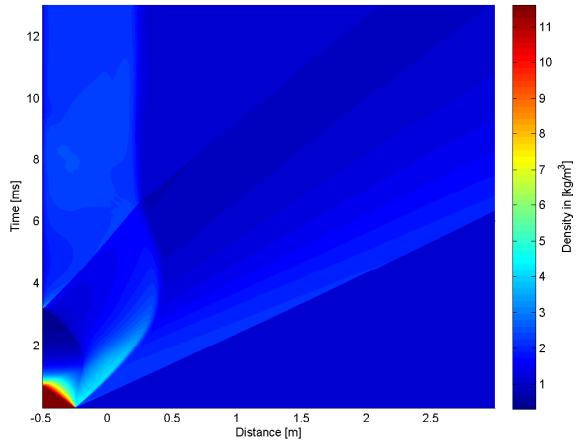
Figure A.4: X-T Diagram for Varying Diaphragm Locations in Linear Driver Section (Pressure)



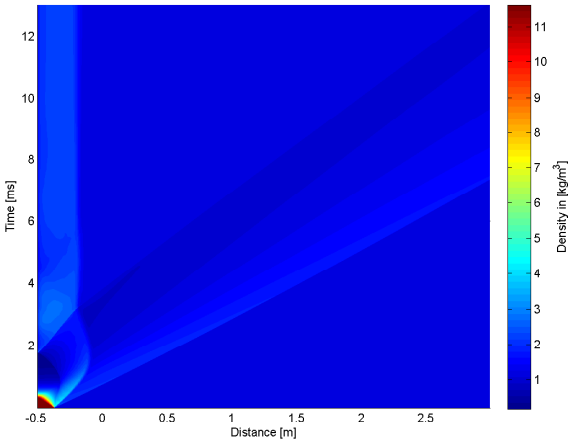
A.5 (a): 100% of Linear Driver Length 10*bar*



A.5 (b): 75% of Linear Driver Length 10*bar*

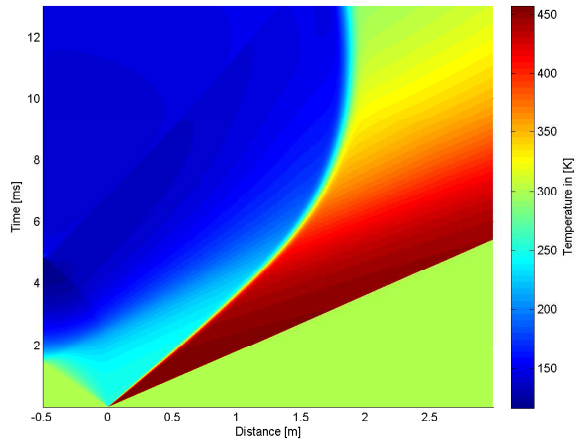


A.5 (c): 50% of Linear Driver Length 10*bar*

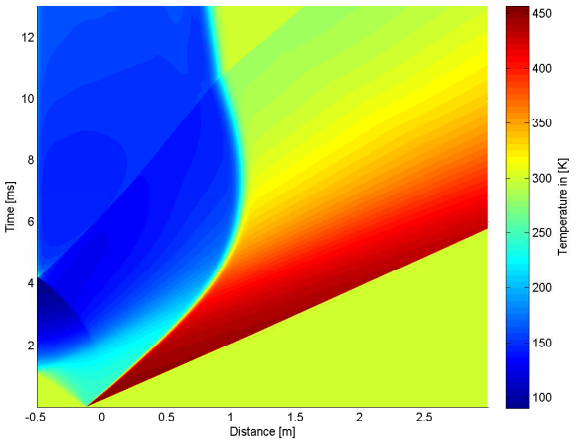


A.5 (d): 25% of Linear Driver Length 10*bar*

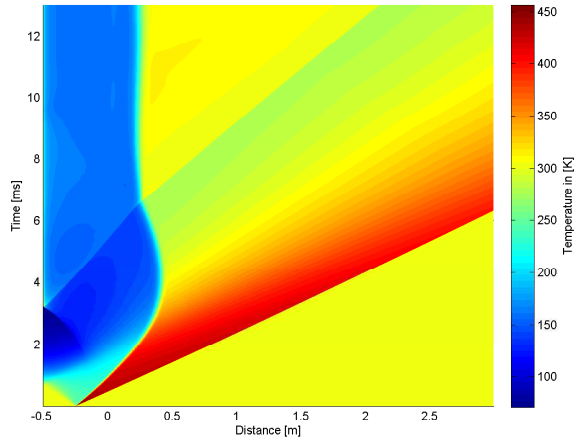
Figure A.5: X-T Diagram for Varying Diaphragm Locations in the Linear Driver Section (Density)



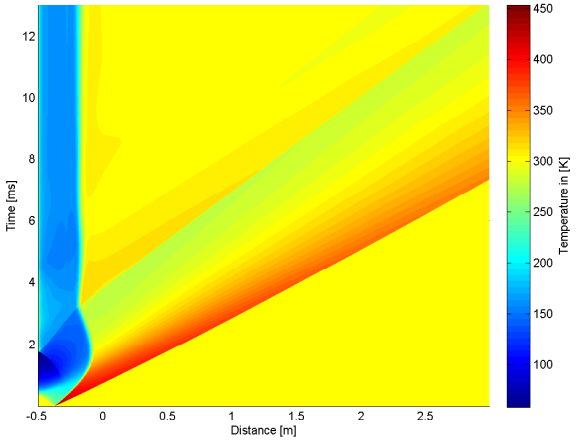
A.6 (a): 100% of Linear Driver Length 10*bar*



A.6 (b): 75% of Linear Driver Length 10*bar*

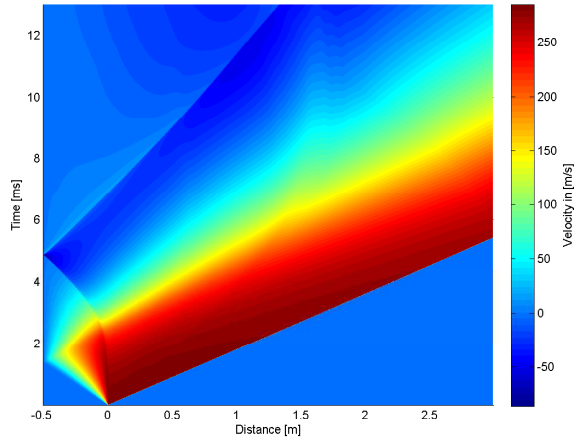


A.6 (c): 50% of Linear Driver Length 10*bar*

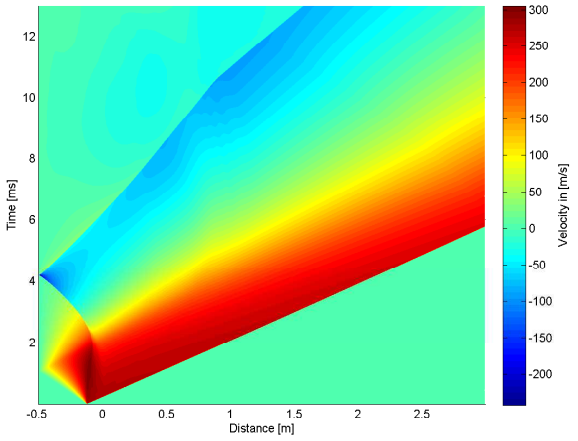


A.6 (d): 25% of Linear Driver Length 10*bar*

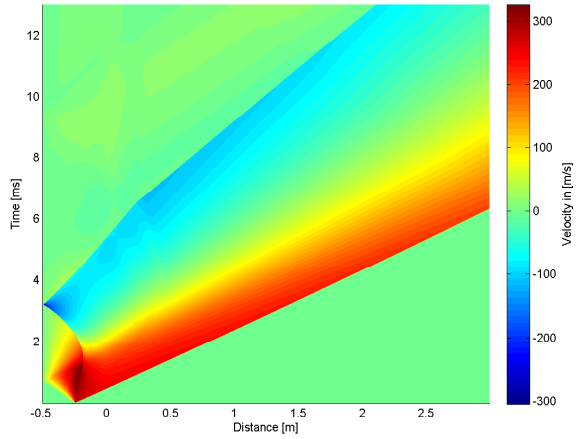
Figure A.6: X-T Diagram for Varying Diaphragm Locations in the Linear Driver Section (Temperature)



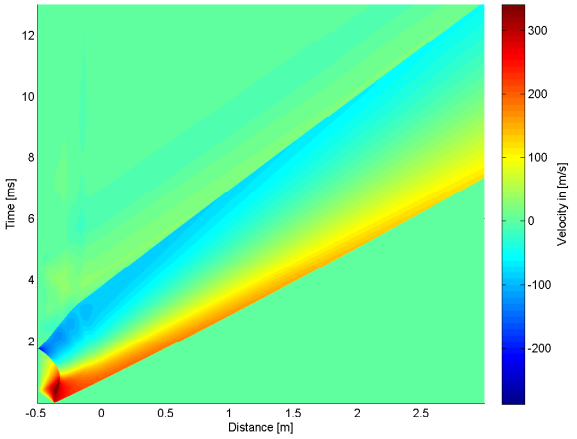
A.7 (a): 100% of Linear Driver Length 10*bar*



A.7 (b): 75% of Linear Driver Length 10*bar*



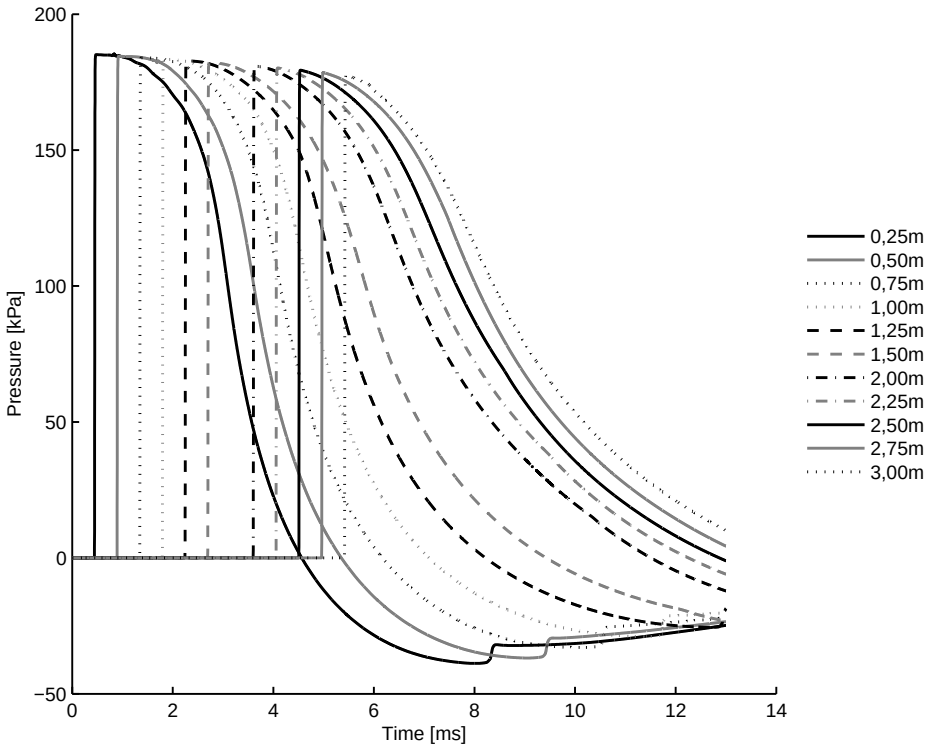
A.7 (c): 50% of Linear Driver Length 10*bar*



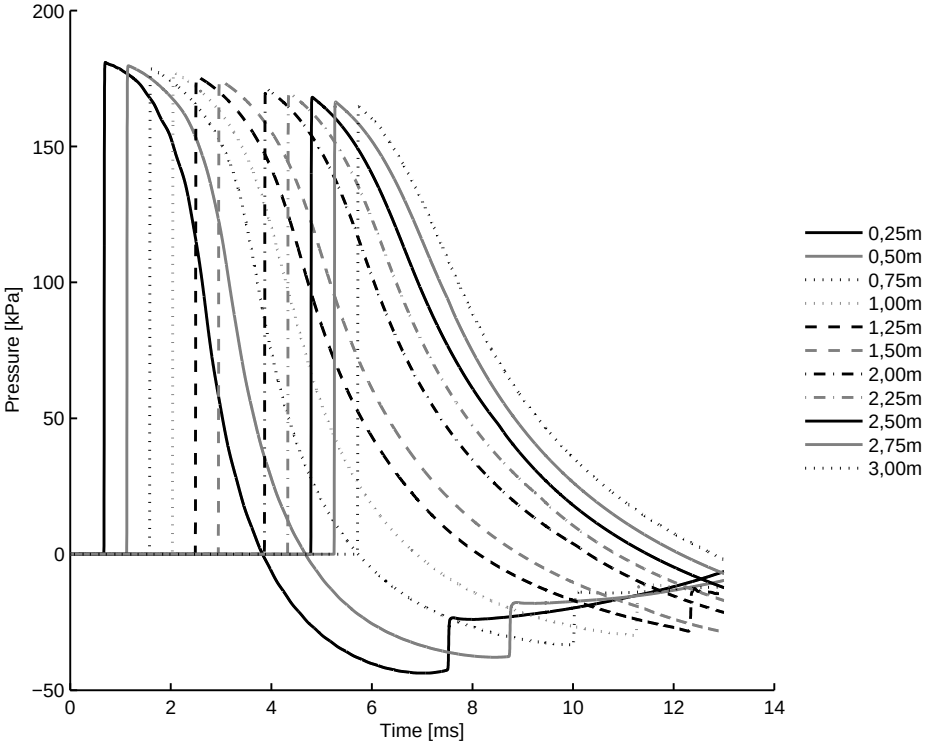
A.7 (d): 25% of Linear Driver Length 10*bar*

Figure A.7: X-T Diagram for Varying Diaphragm Locations in the Linear Driver Section (Velocity)

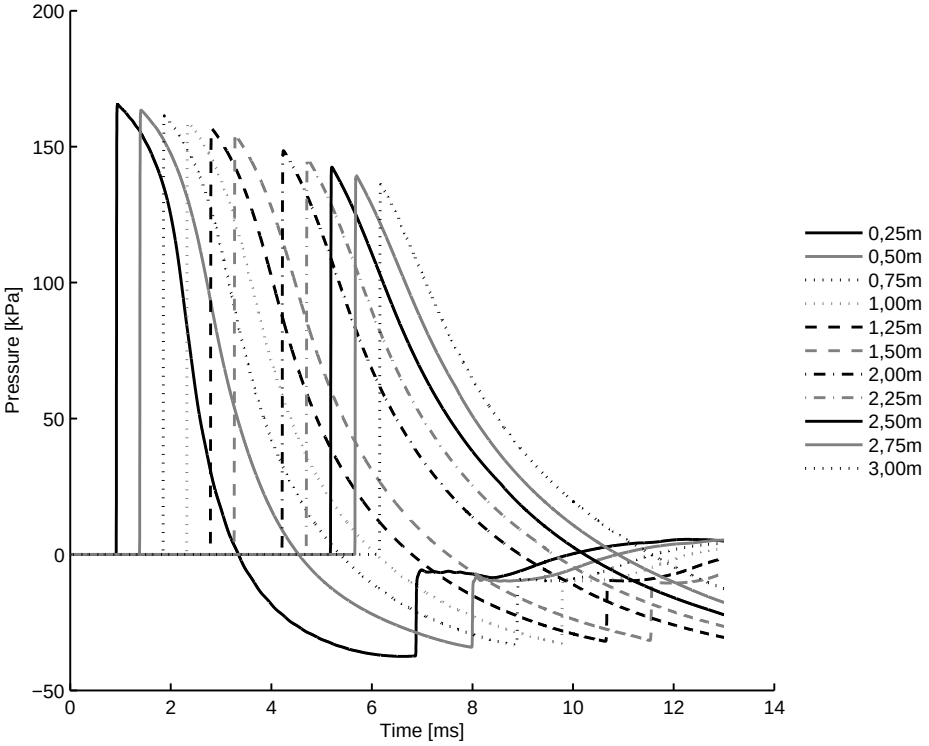
A.2 Convex Driver Section CFD Data



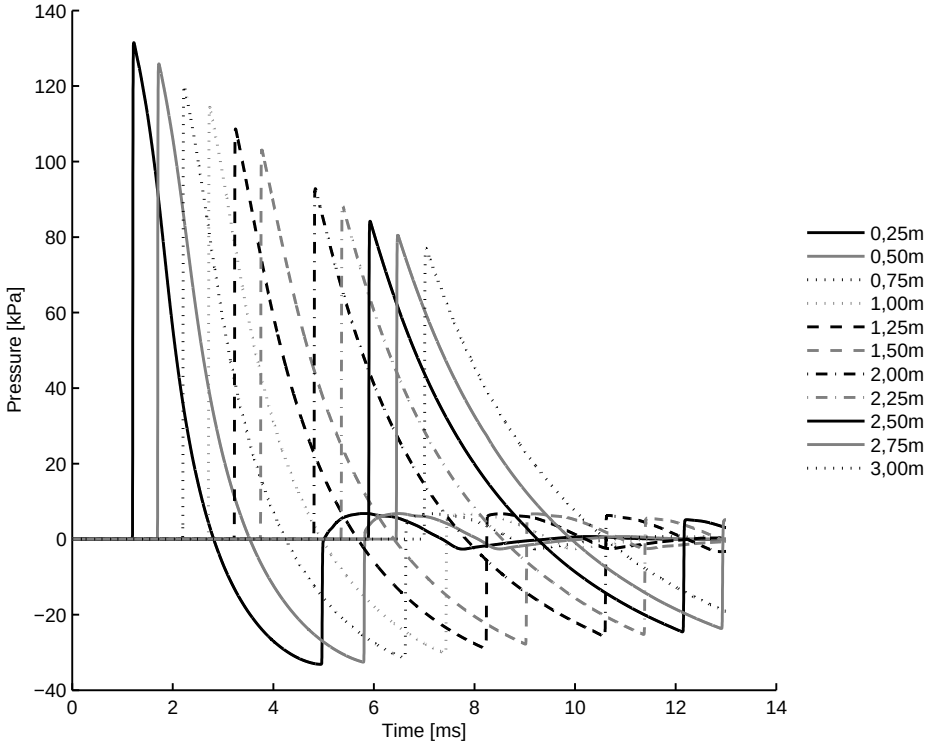
A.8 (a): 100% of Convex Driver Length 10*bar*



A.8 (b): 75% of Convex Driver Length 10*bar*

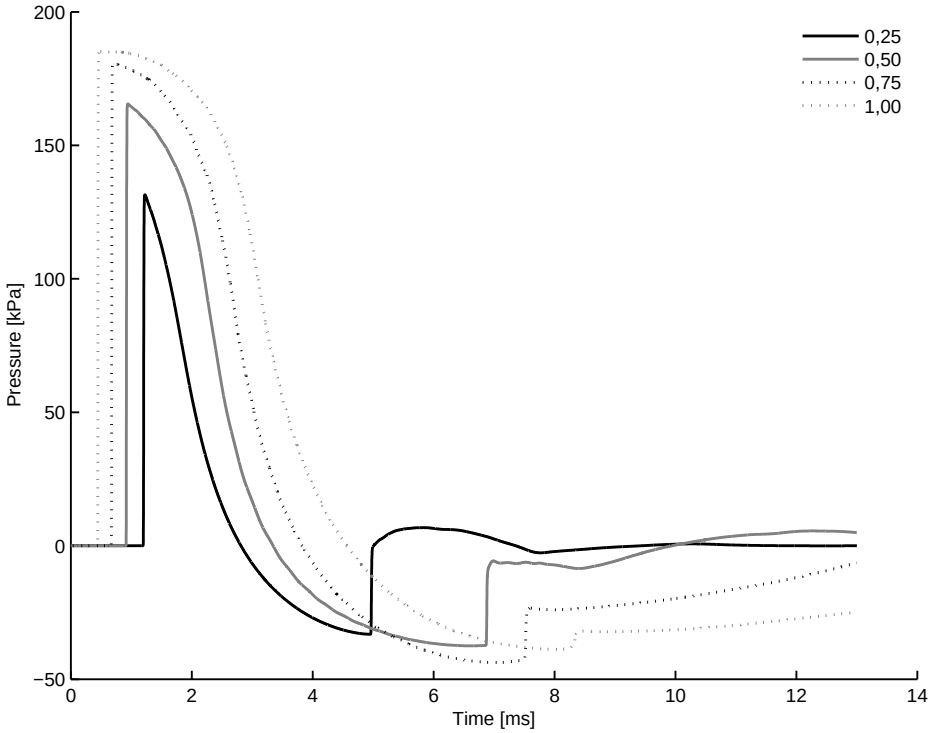


A.8 (c): 50% of Convex Driver Length 10*bar*

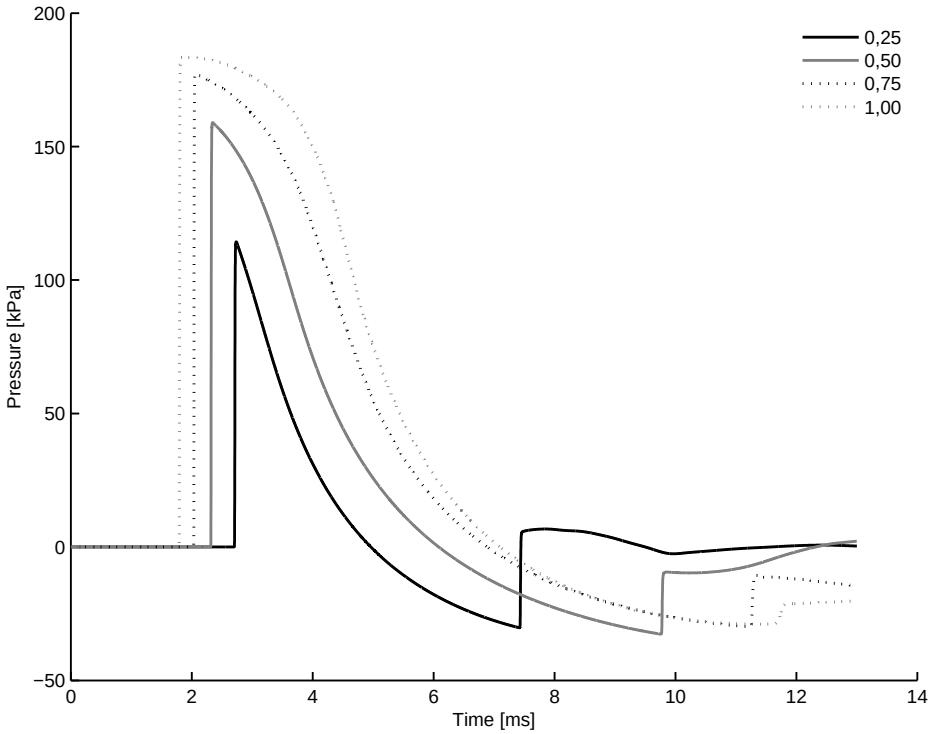


A.8 (d): 25% of Convex Driver Length 10*bar*

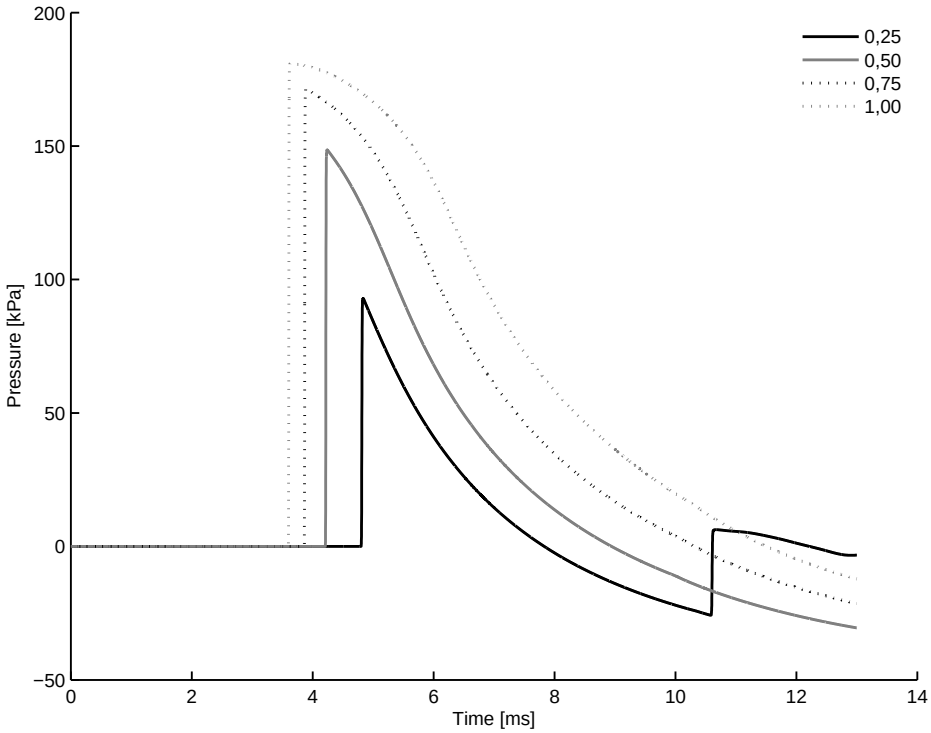
Figure A.8: The Development of the Blast Pressure Profile for Varying Diaphragm Locations in the Convex Driver Section



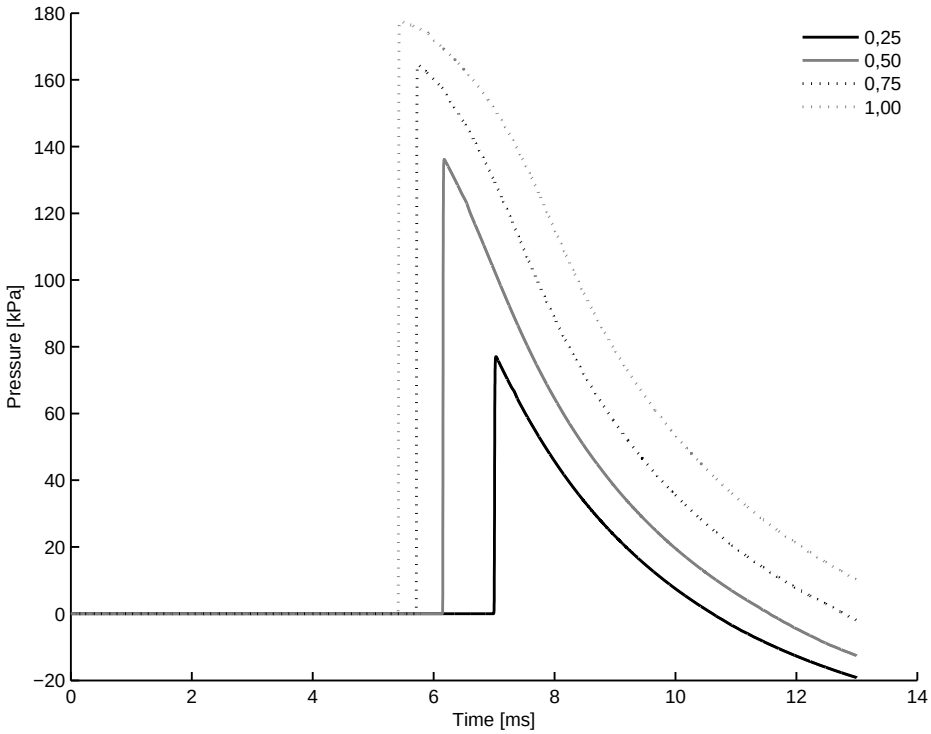
A.9 (a): 0.25m 10*bar*



A.9 (b): $1.00m$ $10bar$

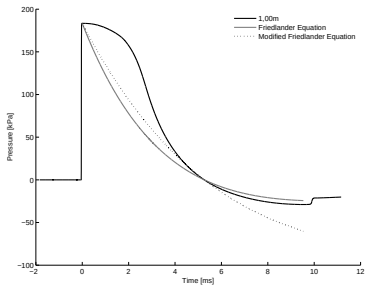


A.9 (c): $2.00m$ $10bar$

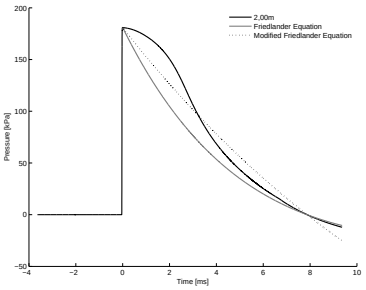


A.9 (d): 3.00m 10bar

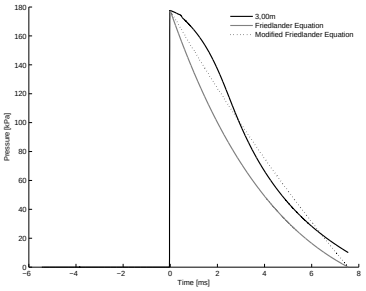
Figure A.9: The Effect of Varying Diaphragm Locations in the Convex Driver Section on the Pressure Profile



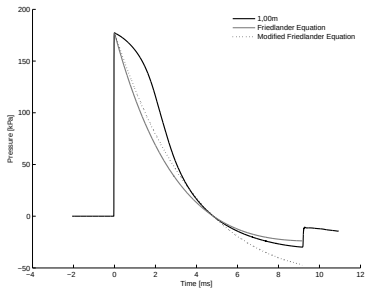
A.10 (a): 100% of Convex Driver Length 10bar 1.00m



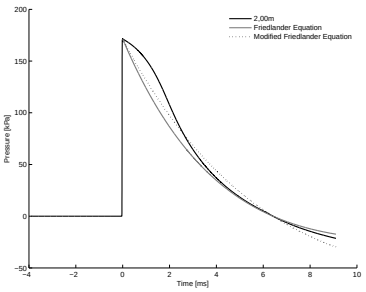
A.10 (b): 100% of Convex Driver Length 10bar 2.00m



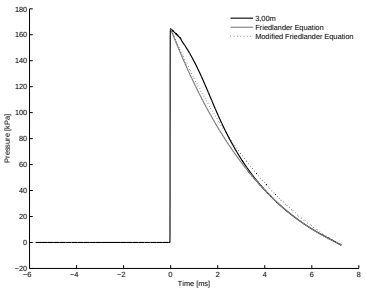
A.10 (c): 100% of Convex Driver Length 10bar 3.00m



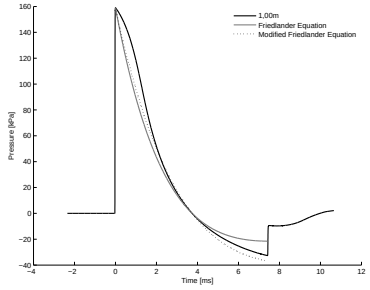
A.10 (d): 75% of Convex Driver Length 10bar 1.00m



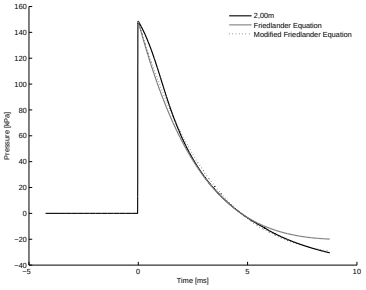
A.10 (e): 75% of Convex Driver Length 10bar 2.00m



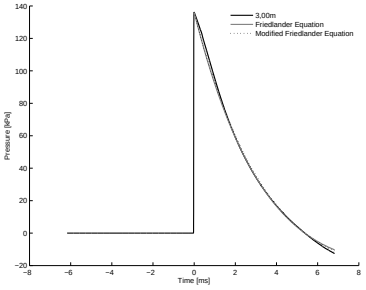
A.10 (f): 75% of Convex Driver Length 10bar 3.00m



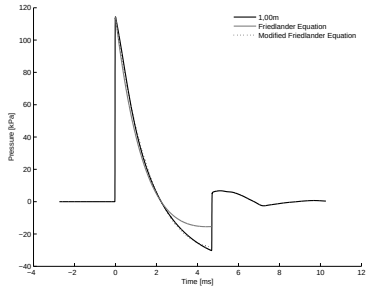
A.10 (g): 50% of Convex Driver Length 10bar 1.00m



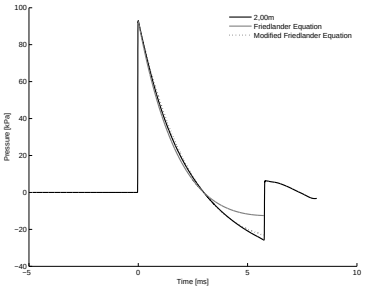
A.10 (h): 50% of Convex Driver Length 10bar 2.00m



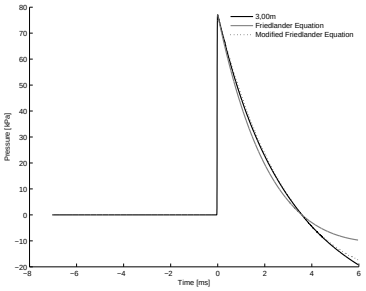
A.10 (i): 50% of Convex Driver Length 10bar 3.00m



A.10 (j): 25% of Convex Driver Length 10bar 1.00m

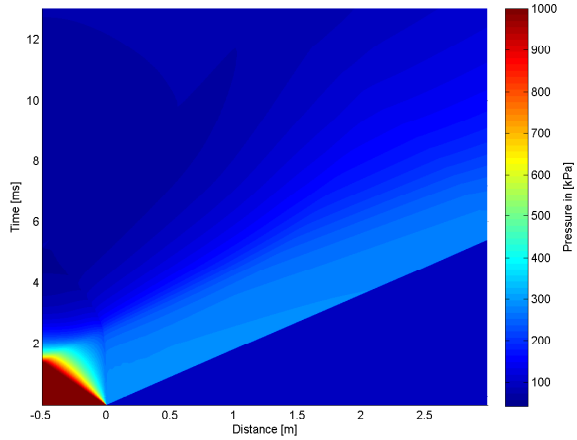


A.10 (k): 25% of Convex Driver Length 10bar 2.00m

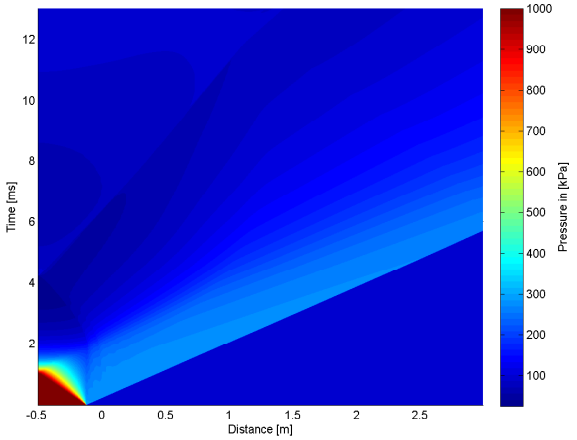


A.10 (l): 25% of Convex Driver Length 10bar 3.00m

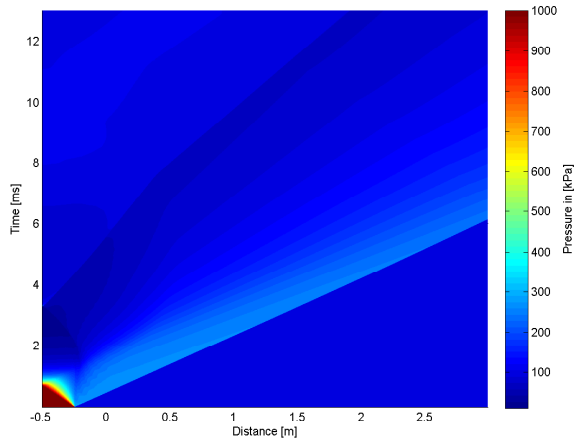
Figure A.10: Comparing the Effect of Varying Diaphragm Location in the Convex Driver Section on Friedlander Pressure Profile



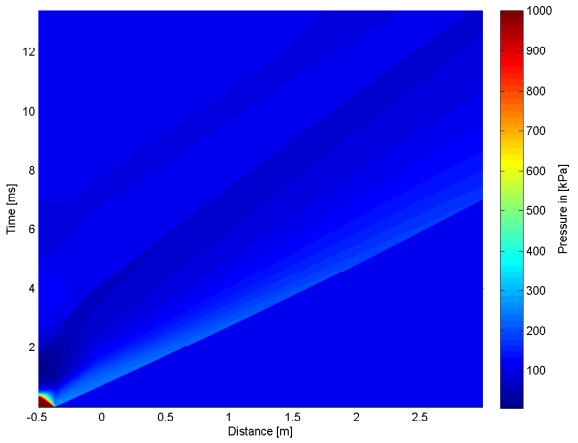
A.11 (a): 100% of Convex Driver Length 10bar



A.11 (b): 75% of Convex Driver Length 10bar

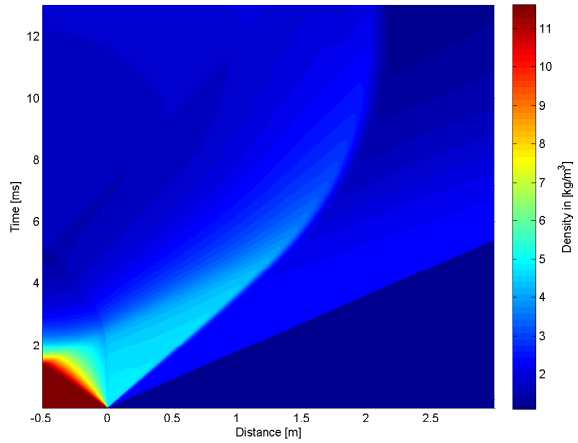


A.11 (c): 50% of Convex Driver Length 10*bar*

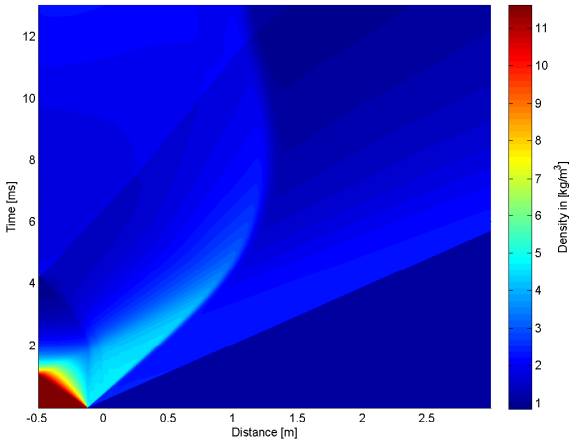


A.11 (d): 25% of Convex Driver Length 10*bar*

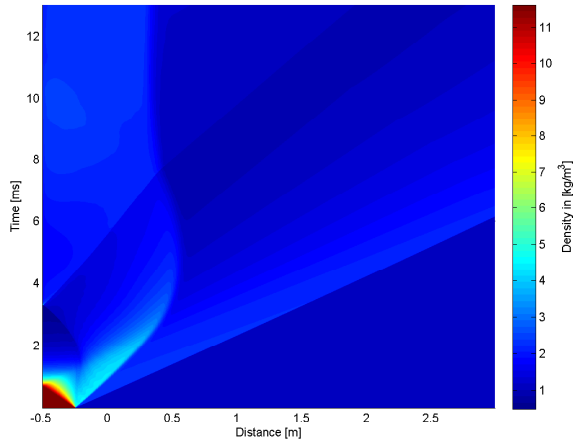
Figure A.11: X-T Diagram for Varying Diaphragm Locations in the Convex Driver Section (Pressure)



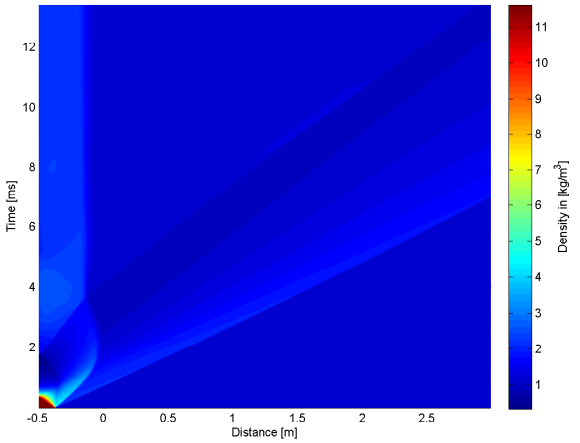
A.12 (a): 100% of Convex Driver Length 10*bar*



A.12 (b): 75% of Convex Driver Length 10*bar*

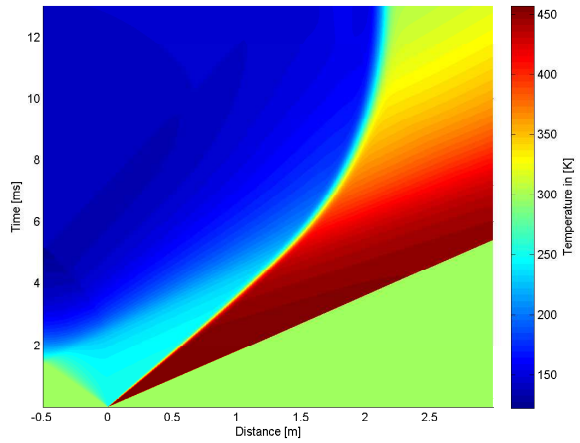


A.12 (c): 50% of Convex Driver Length 10*bar*

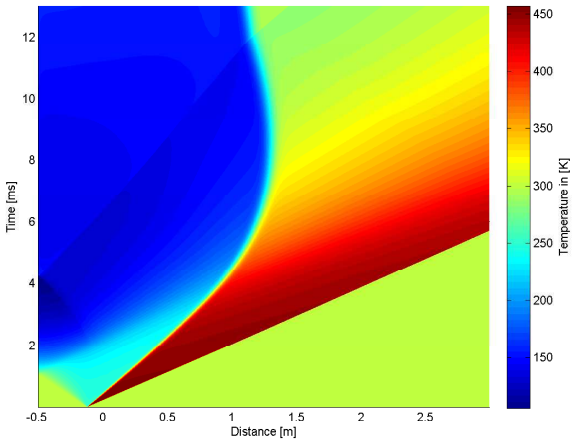


A.12 (d): 25% of Convex Driver Length 10*bar*

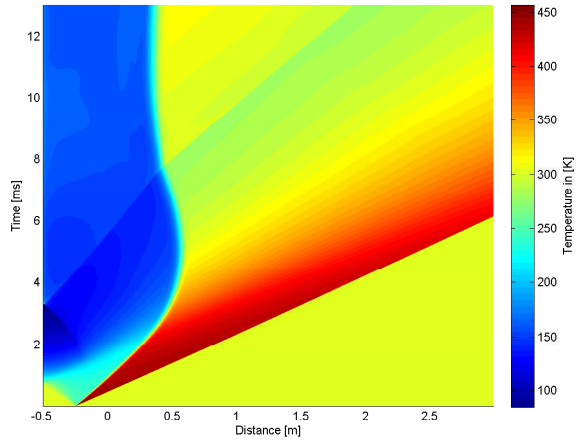
Figure A.12: X-T Diagram for Varying Diaphragm Locations in the Convex Driver Section (Density)



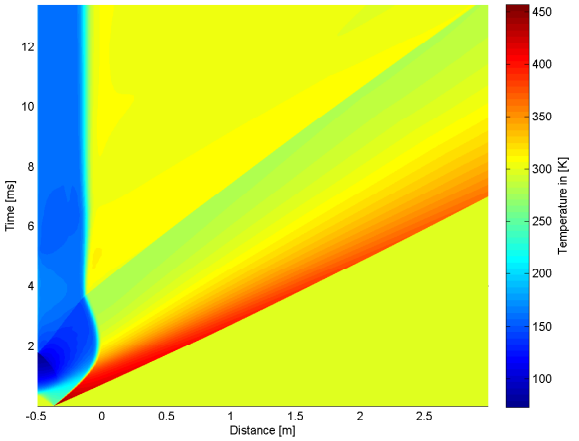
A.13 (a): 100% of Convex Driver Length 10*bar*



A.13 (b): 75% of Convex Driver Length 10*bar*

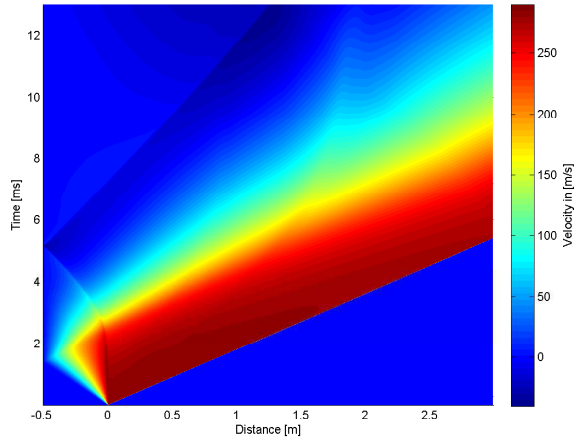


A.13 (c): 50% of Convex Driver Length 10*bar*

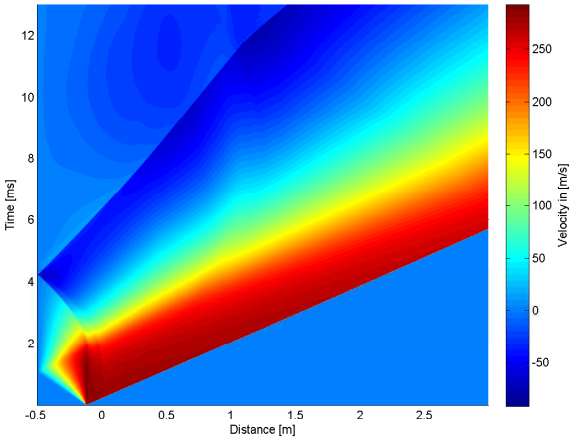


A.13 (d): 25% of Convex Driver Length 10*bar*

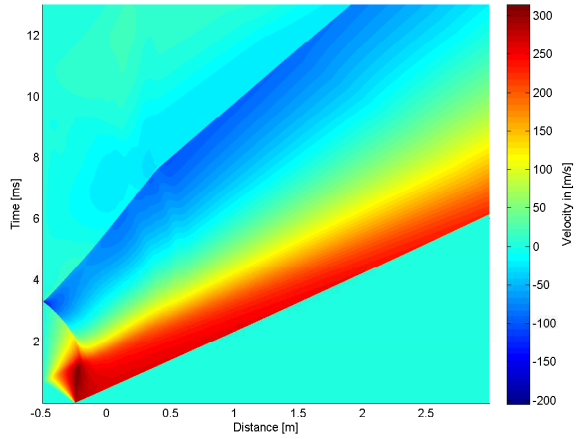
Figure A.13: X-T Diagram for Varying Diaphragm Locations in the Convex Driver Section (Temperature)



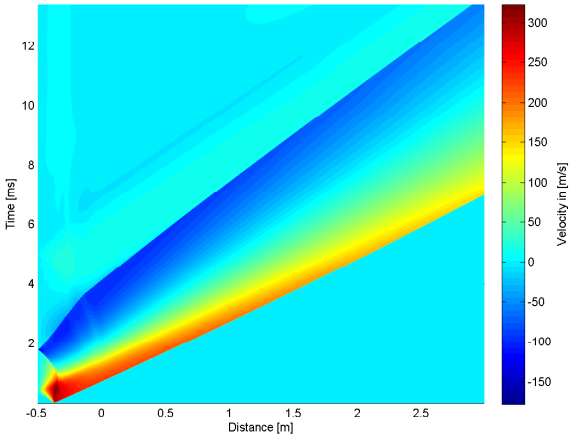
A.14 (a): 100% of Convex Driver Length 10*bar*



A.14 (b): 75% of Convex Driver Length 10*bar*



A.14 (c): 50% of Convex Driver Length 10*bar*

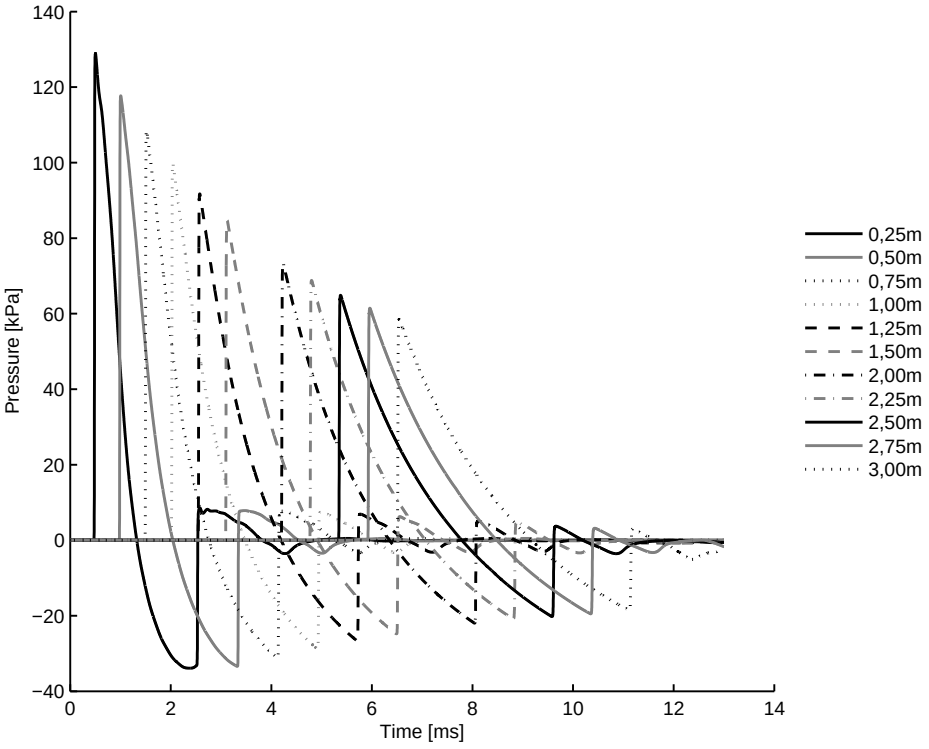


A.14 (d): 25% of Convex Driver Length 10*bar*

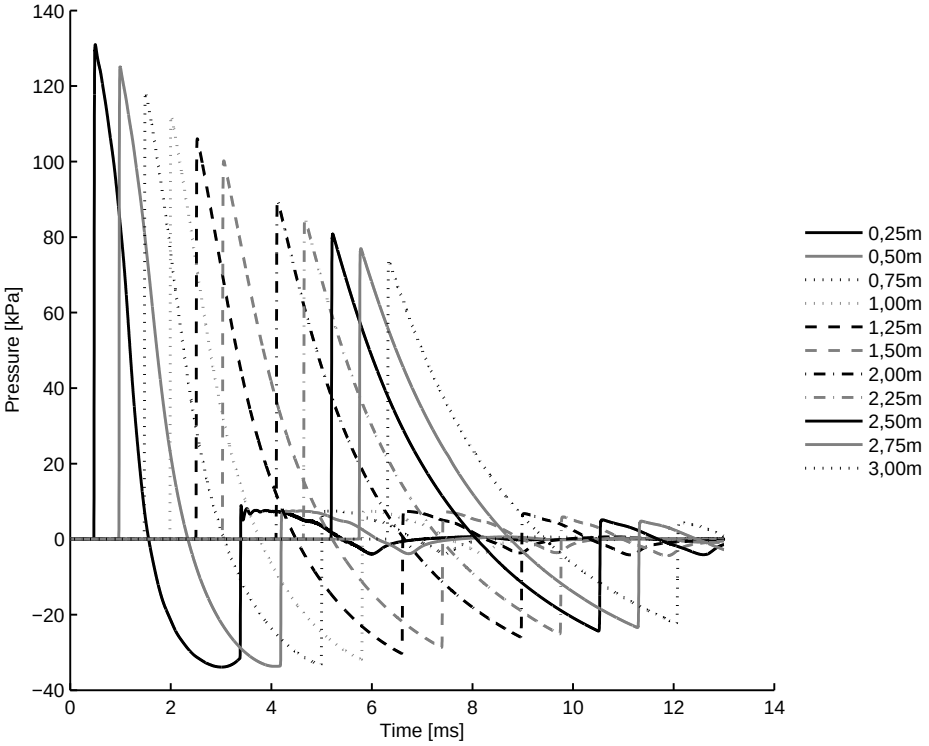
Figure A.14: X-T Diagram for Varying Diaphragm Locations in the Convex Driver Section (Velocity)

Appendix B Varying Driver Section and Transition Section Lengths CFD Data

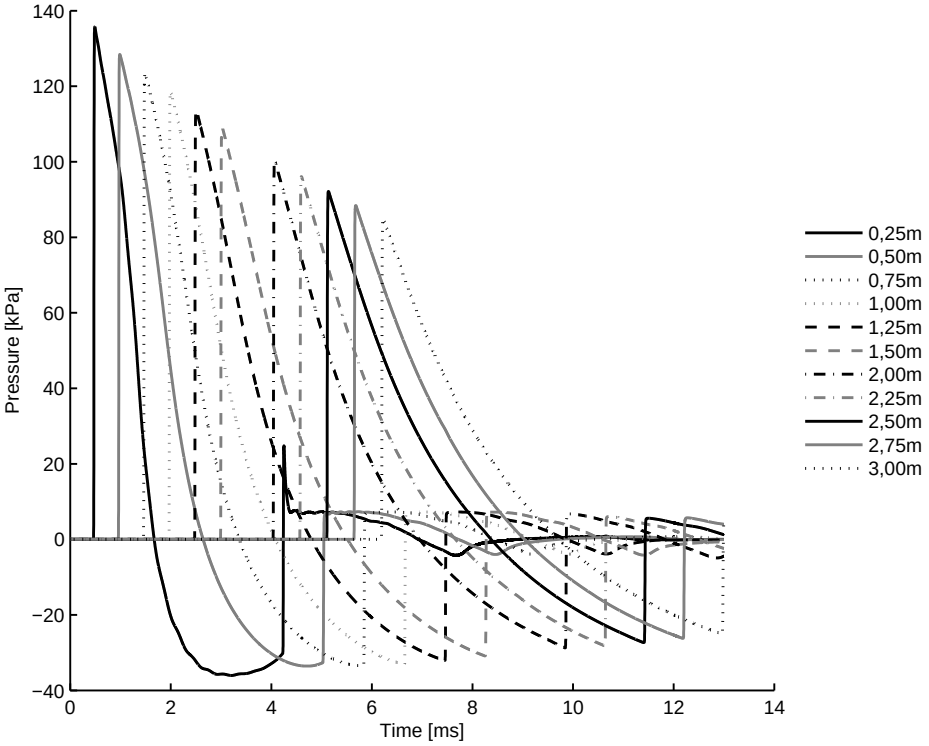
B.1 Varying Linear Driver Section Length CFD Data



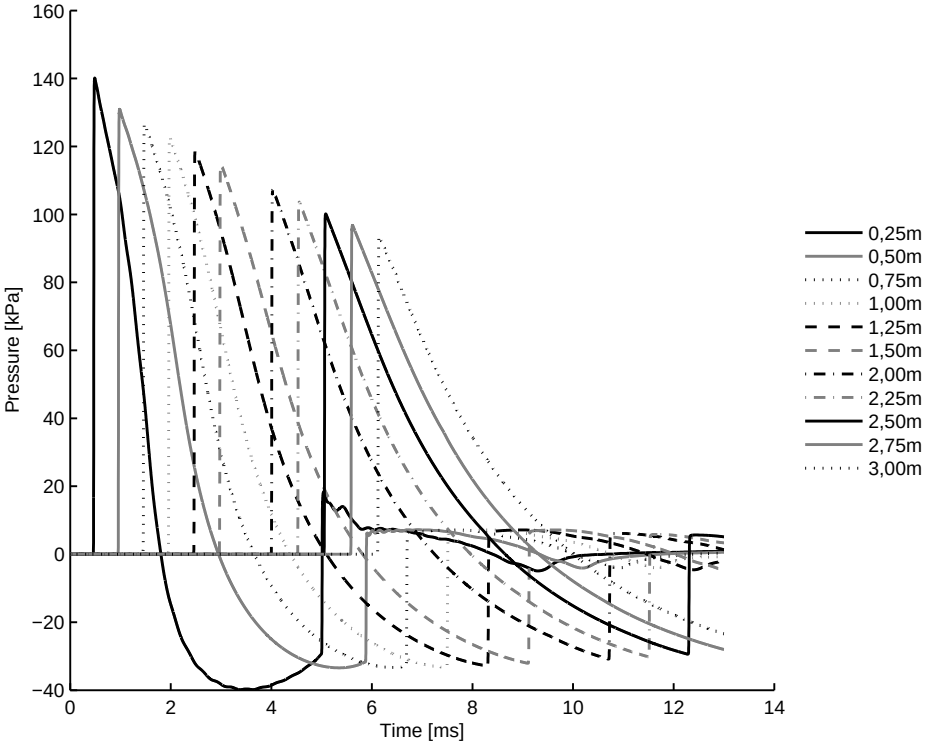
B.1 (a): 50% of Linear Driver and Transition Length 10*bar*



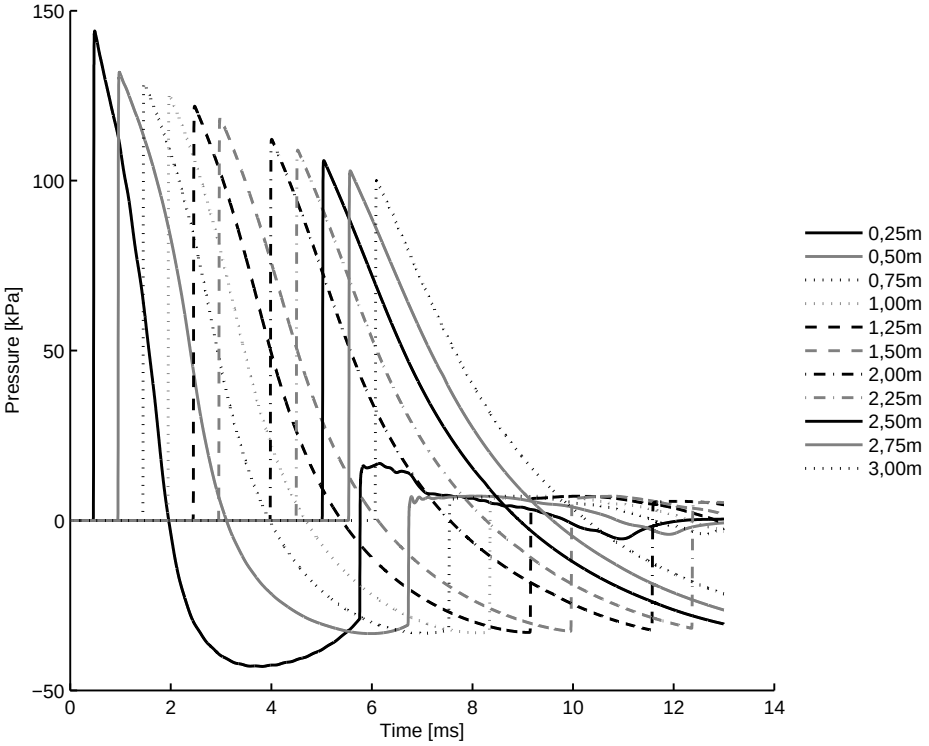
B.1 (b): 75% of Linear Driver and Transition Length 10*bar*



B.1 (c): 100% of Linear Driver and Transition Length 10*bar*

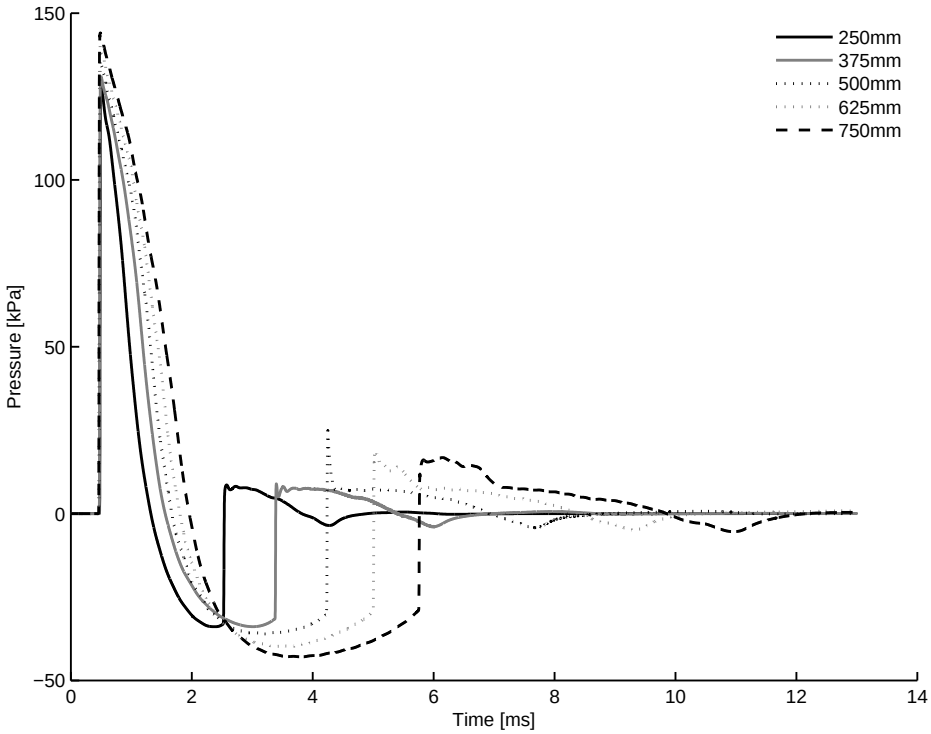


B.1 (d): 125% of Linear Driver and Transition Length 10*bar*

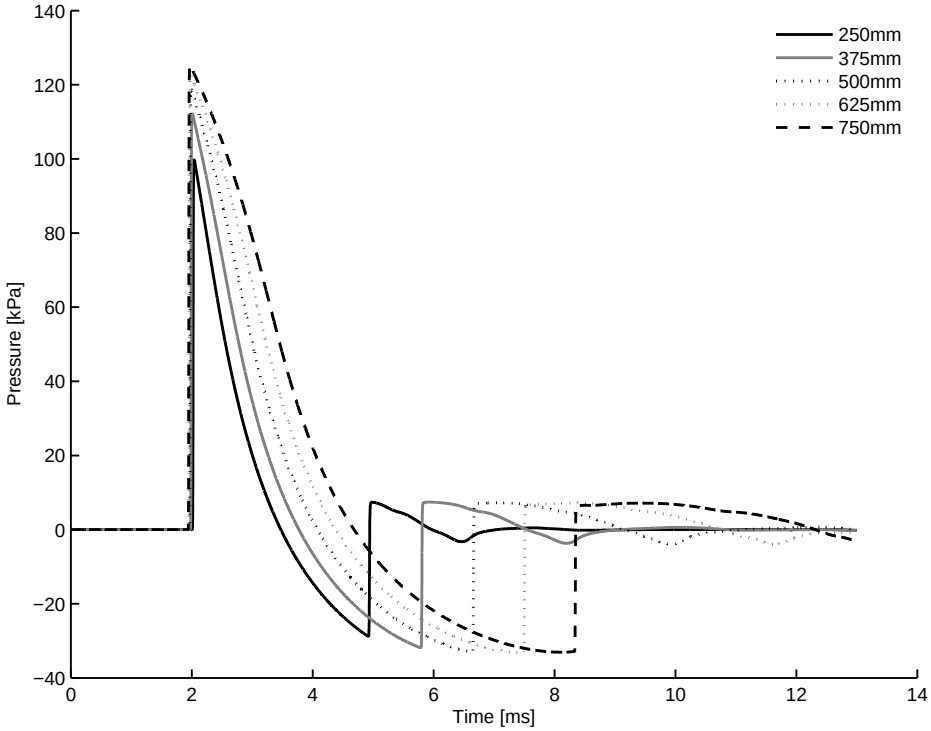


B.1 (e): 150% of Linear Driver and Transition Length 10*bar*

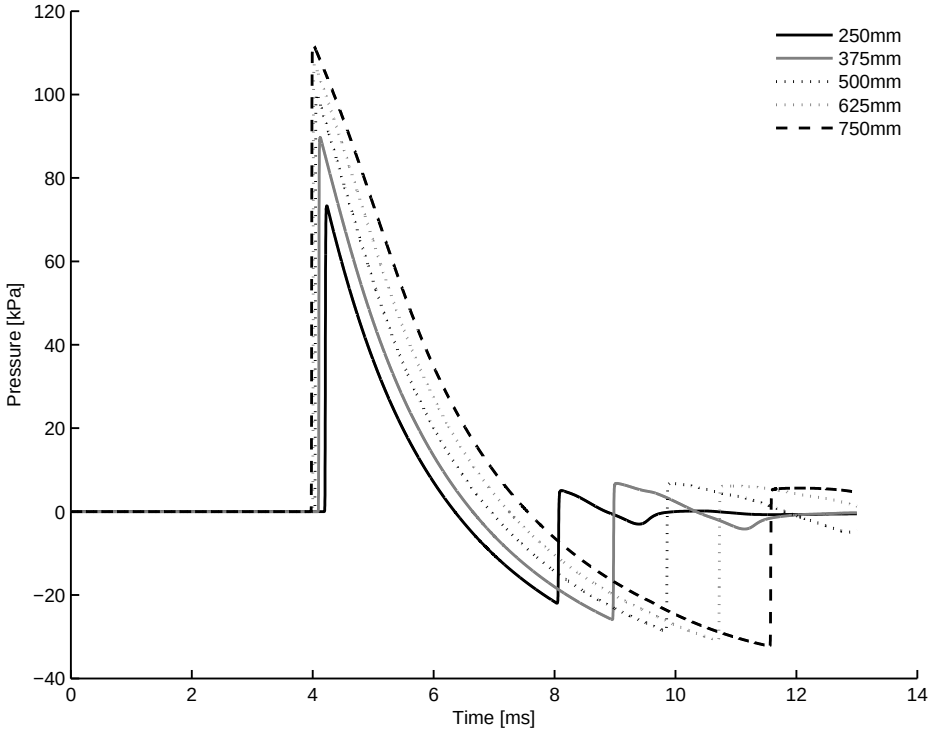
Figure B.1: The Development of the Blast Pressure Profile for Increasing Linear Driver and Transition Length



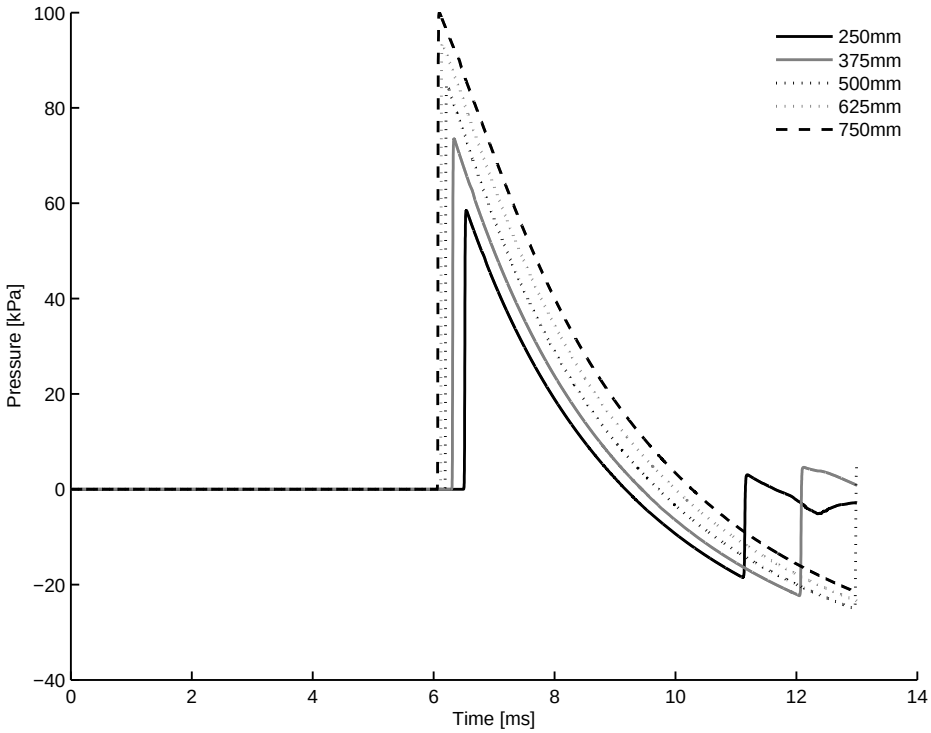
B.2 (a): $0.25m$ $10bar$



B.2 (b): $1.00m$ $10bar$

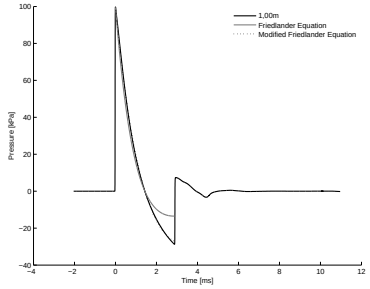


B.2 (c): $2.00m$ $10bar$

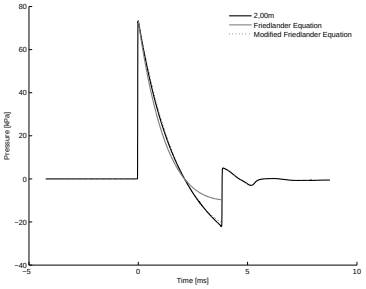


B.2 (d): $3.00m$ $10bar$

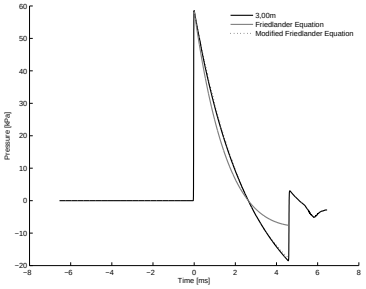
Figure B.2: The Effect of Increasing the Linear Driver and Transition Section Length on the Pressure Profile



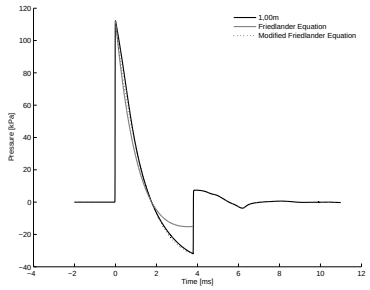
B.3 (a): 50% of Linear Driver and Transition Length 10bar 1.00m



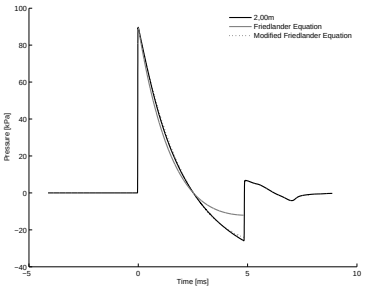
B.3 (b): 50% of Linear Driver and Transition Length 10bar 2.00m



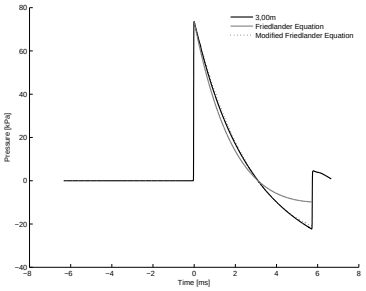
B.3 (c): 50% of Linear Driver and Transition Length 10bar 3.00m



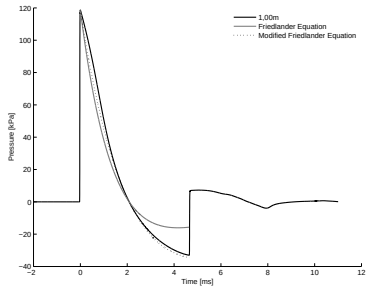
B.3 (d): 75% of Linear Driver and Transition Length 10bar 1.00m



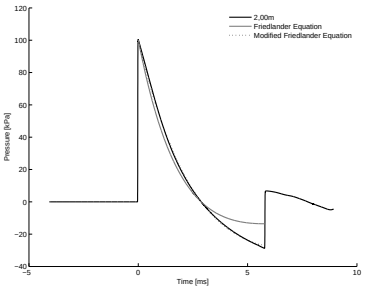
B.3 (e): 75% of Linear Driver and Transition Length 10bar 2.00m



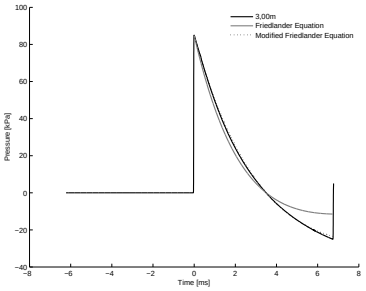
B.3 (f): 75% of Linear Driver and Transition Length 10bar 3.00m



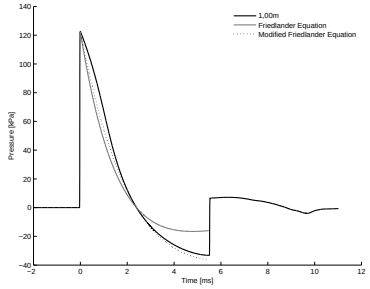
B.3 (g): 100% of Linear Driver and Transition Length 10bar 1.00m



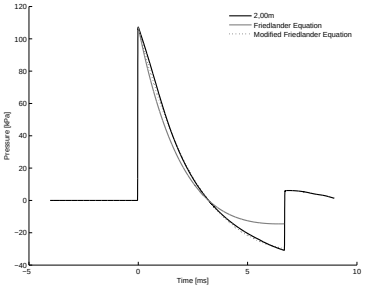
B.3 (h): 100% of Linear Driver and Transition Length 10bar 2.00m



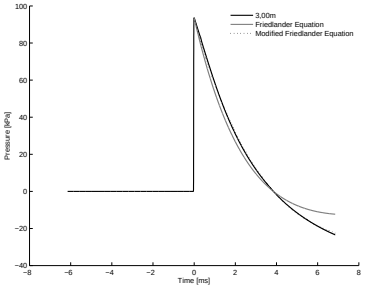
B.3 (i): 100% of Linear Driver and Transition Length 10bar 3.00m



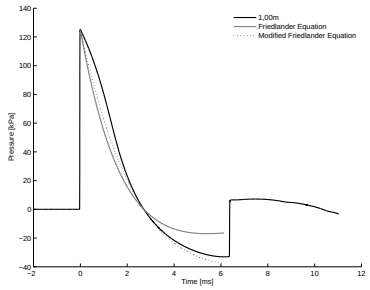
B.3 (j): 125% of Linear Driver and Transition Length 10*bar* 1.00*m*



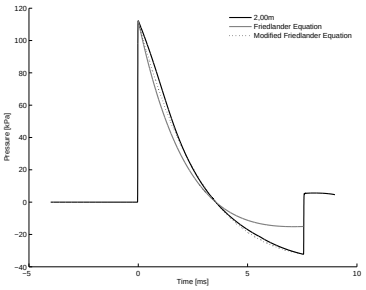
B.3 (k): 125% of Linear Driver and Transition Length 10*bar* 2.00*m*



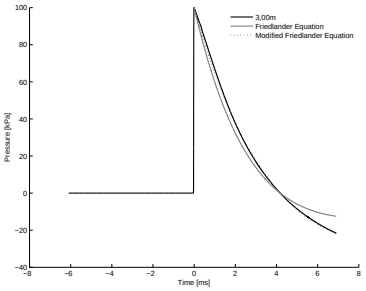
B.3 (l): 125% of Linear Driver and Transition Length 10*bar* 3.00*m*



B.3 (m): 150% of Linear Driver and Transition Length 10*bar* 1.00*m*

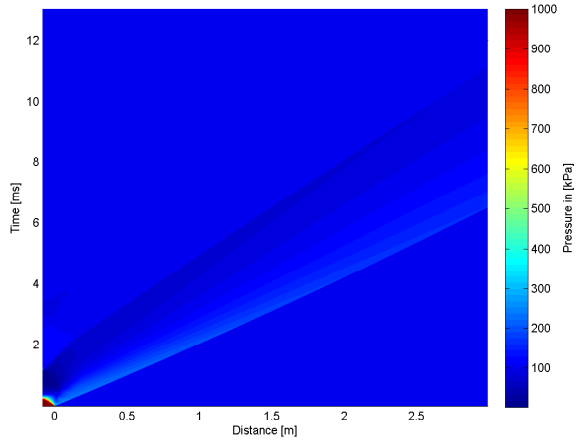


B.3 (n): 150% of Linear Driver and Transition Length 10*bar* 2.00*m*

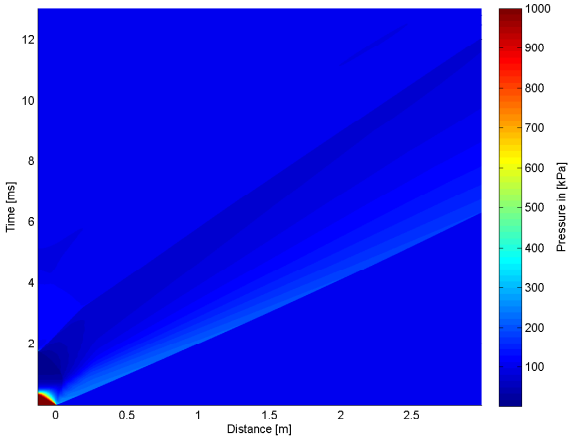


B.3 (o): 150% of Linear Driver and Transition Length 10*bar* 3.00*m*

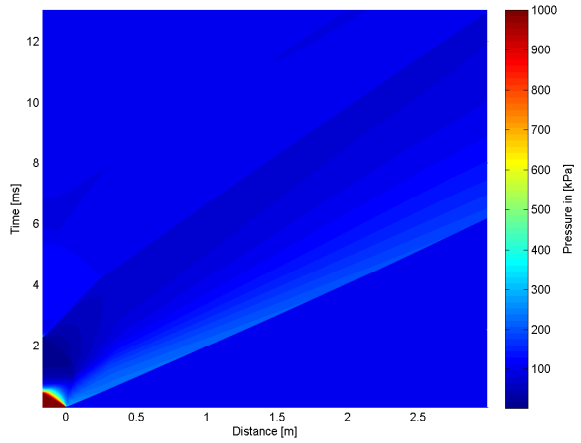
Figure B.3: Comparing the Effect of Varying the Linear Driver and Transition Section Length on the Friedlander Pressure Profile



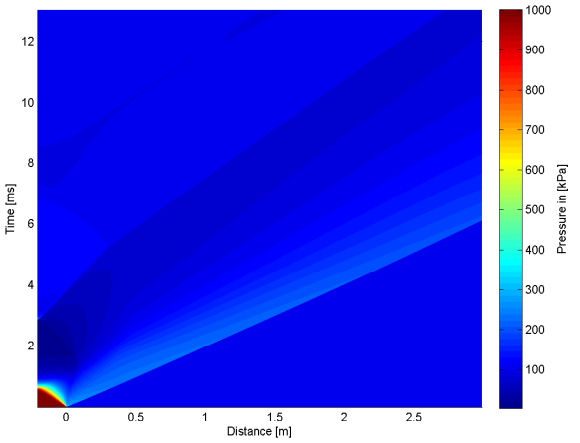
B.4 (a): 50% of Linear Driver and Transition Length 10*bar*



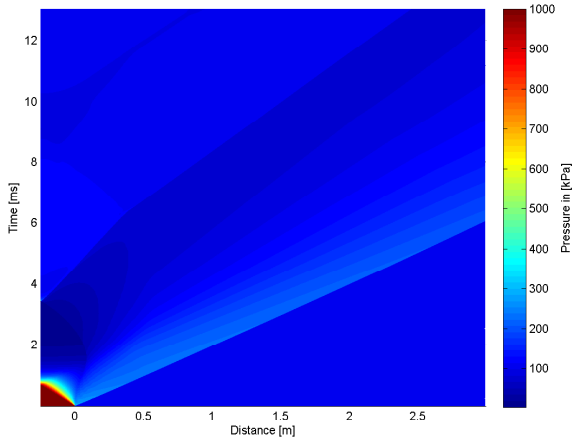
B.4 (b): 75% of Linear Driver and Transition Length 10*bar*



B.4 (c): 100% of Linear Driver and Transition Length 10*bar*

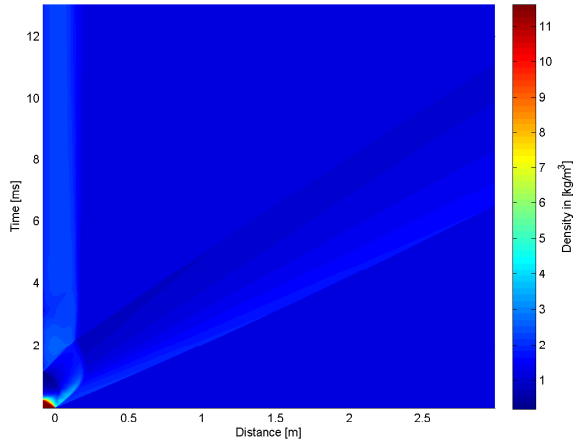


B.4 (d): 125% of Linear Driver and Transition Length 10*bar*

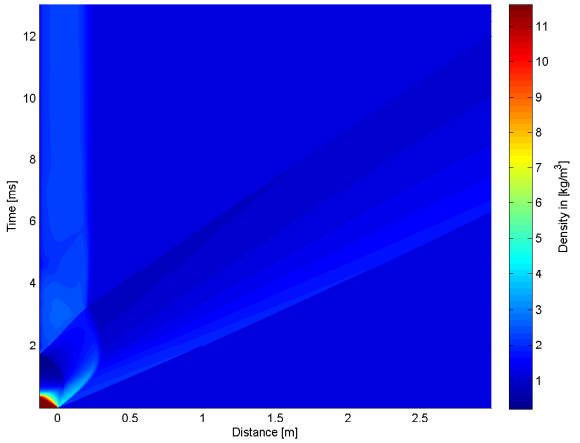


B.4 (e): 150% of Linear Driver and Transition Length 10*bar*

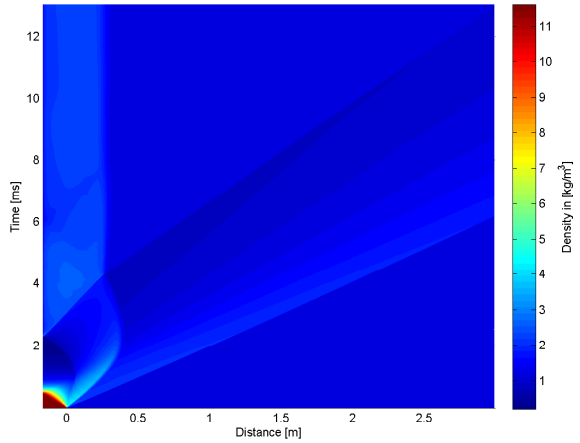
Figure B.4: X-T Diagram for Varying the Linear Driver and Transition Section Length (Pressure)



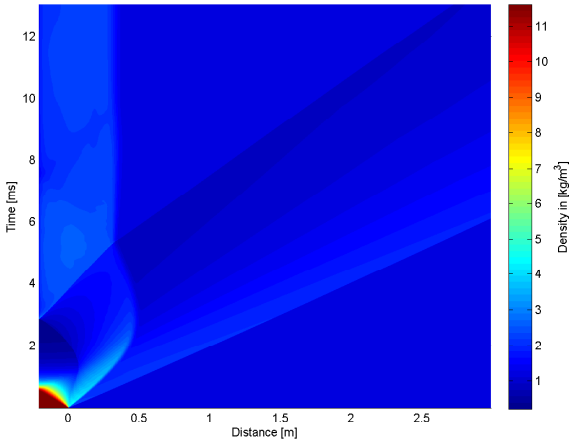
B.5 (a): 50% of Linear Driver and Transition Length 10*bar*



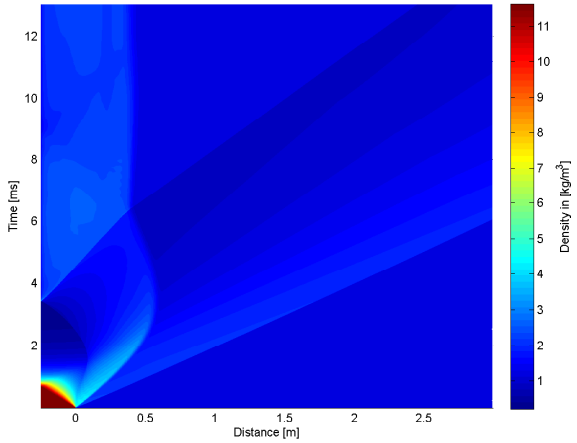
B.5 (b): 75% of Linear Driver and Transition Length 10*bar*



B.5 (c): 100% of Linear Driver and Transition Length 10*bar*

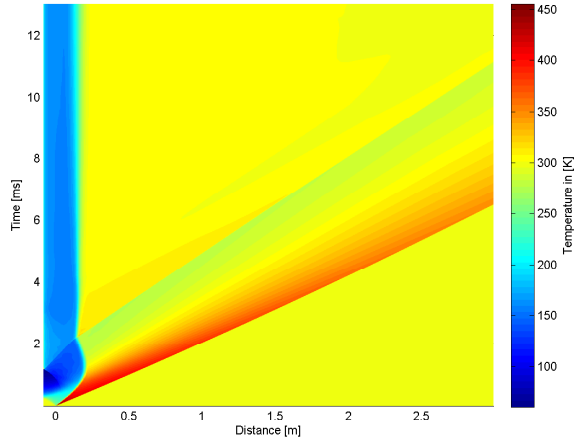


B.5 (d): 125% of Linear Driver and Transition Length 10*bar*

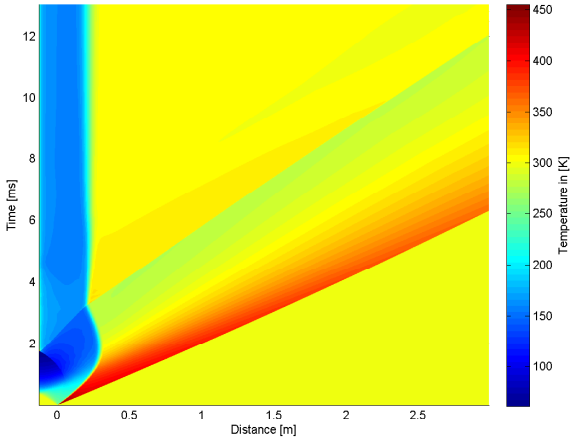


B.5 (e): 150% of Linear Driver and Transition Length 10*bar*

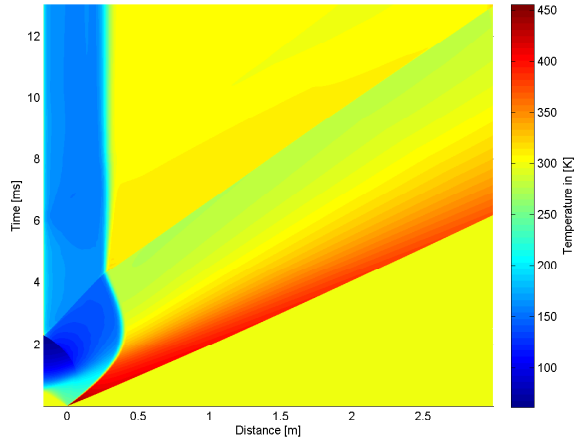
Figure B.5: X-T Diagram for Varying the Linear Driver and Transition Section Length (Density)



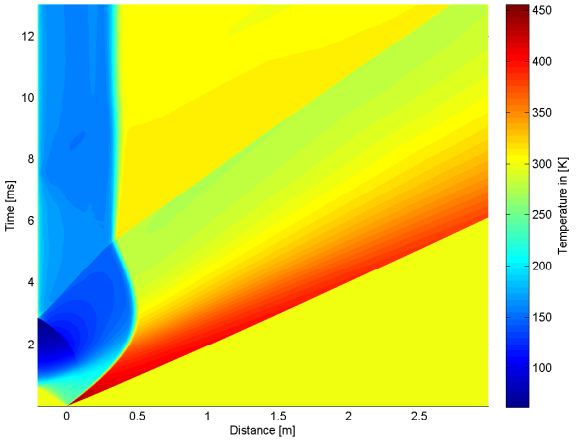
B.6 (a): 50% of Linear Driver and Transition Length 10*bar*



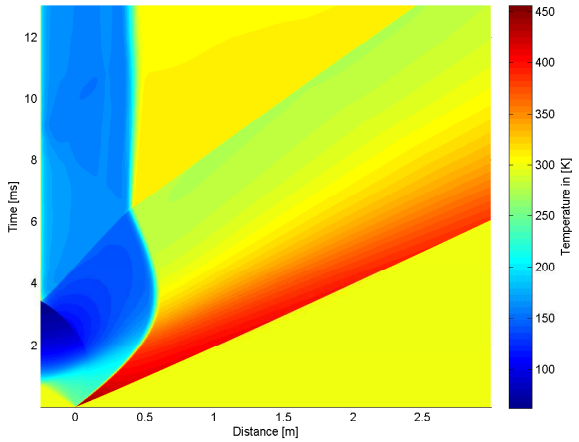
B.6 (b): 75% of Linear Driver and Transition Length 10*bar*



B.6 (c): 100% of Linear Driver and Transition Length 10*bar*

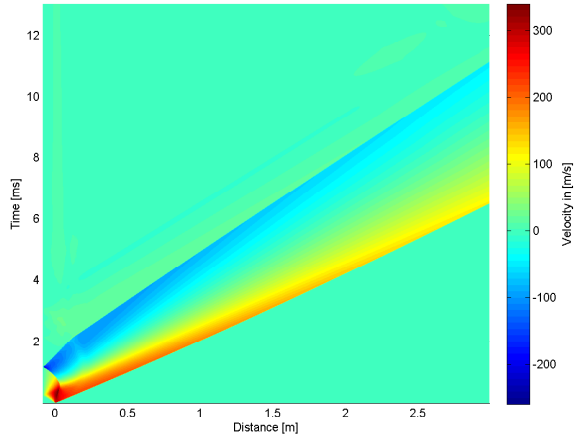


B.6 (d): 125% of Linear Driver and Transition Length 10*bar*

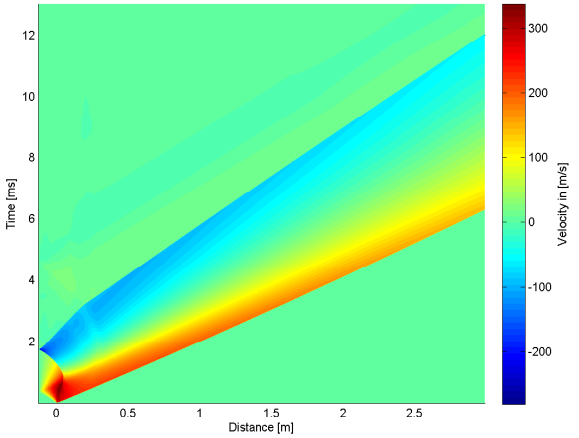


B.6 (e): 150% of Linear Driver and Transition Length 10*bar*

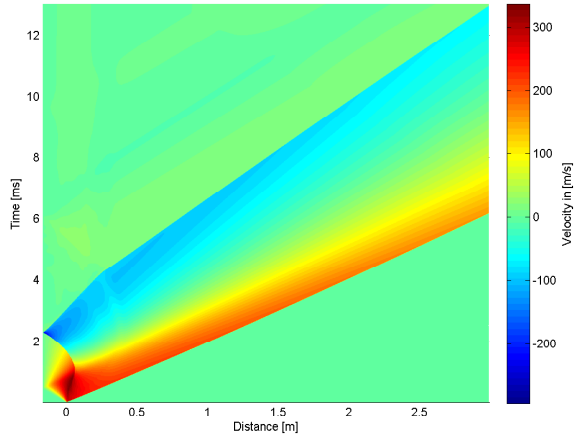
Figure B.6: X-T Diagram for Varying the Linear Driver and Transition Section Length (Temperature)



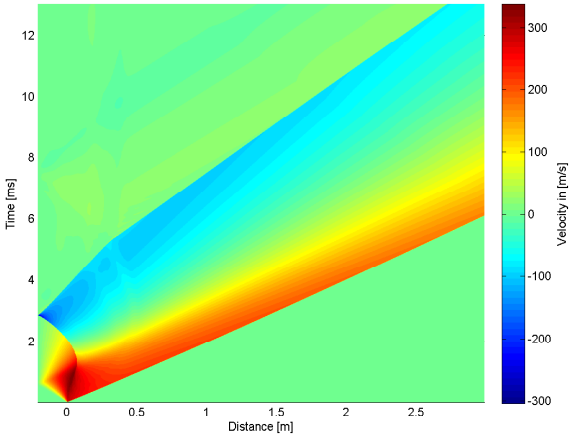
B.7 (a): 50% of Linear Driver and Transition Length 10*bar*



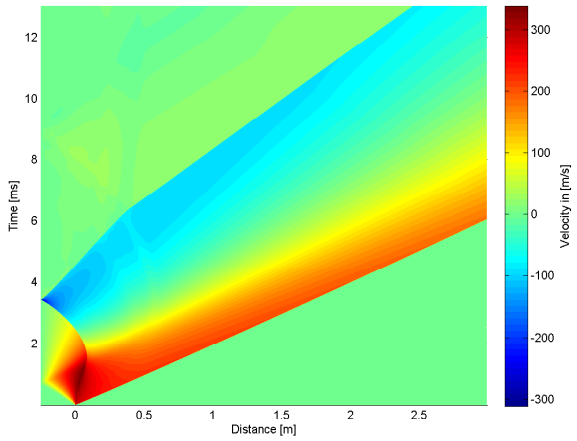
B.7 (b): 75% of Linear Driver and Transition Length 10*bar*



B.7 (c): 100% of Linear Driver and Transition Length 10*bar*



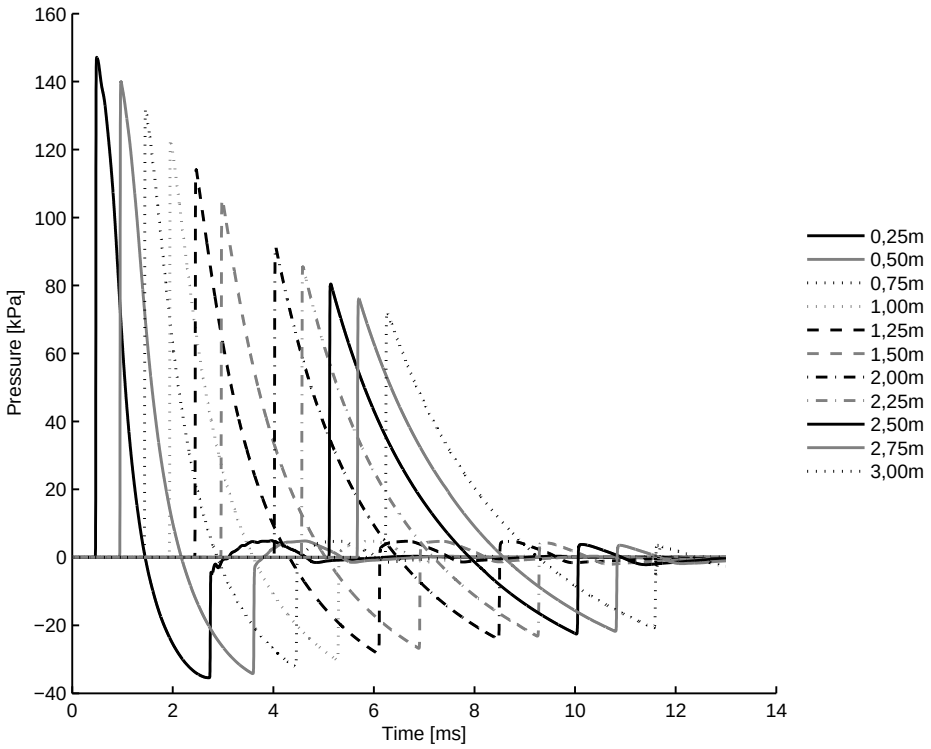
B.7 (d): 125% of Linear Driver and Transition Length 10*bar*



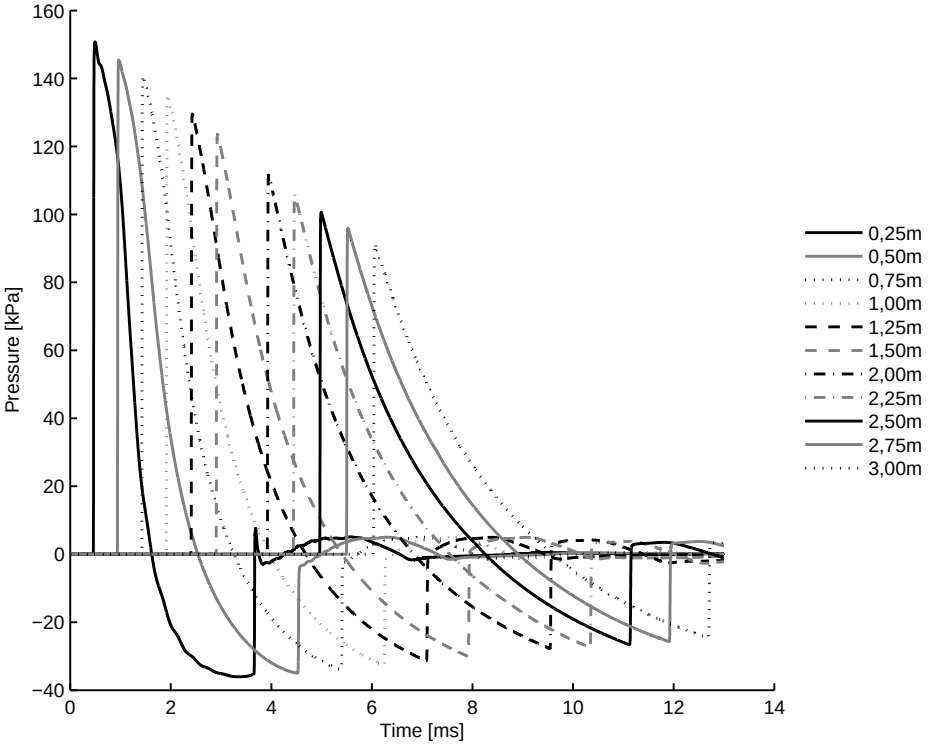
B.7 (e): 150% of Linear Driver and Transition Length 10*bar*

Figure B.7: X-T Diagram for Varying the Linear Driver and Transition Section Length (Velocity)

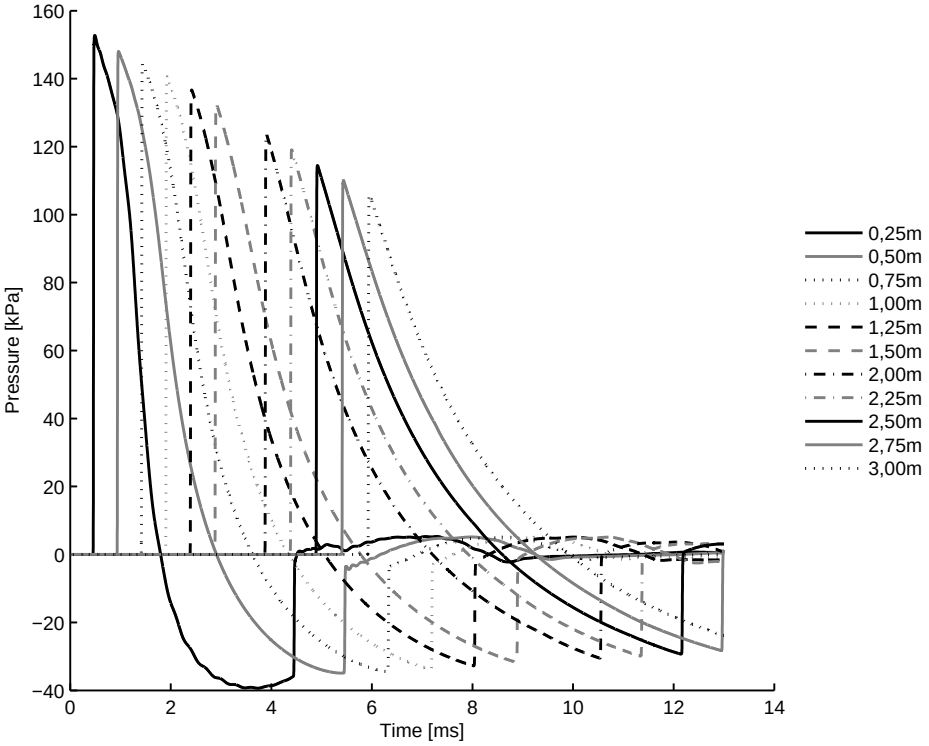
B.2 Varying Convex Driver Section Length CFD Data



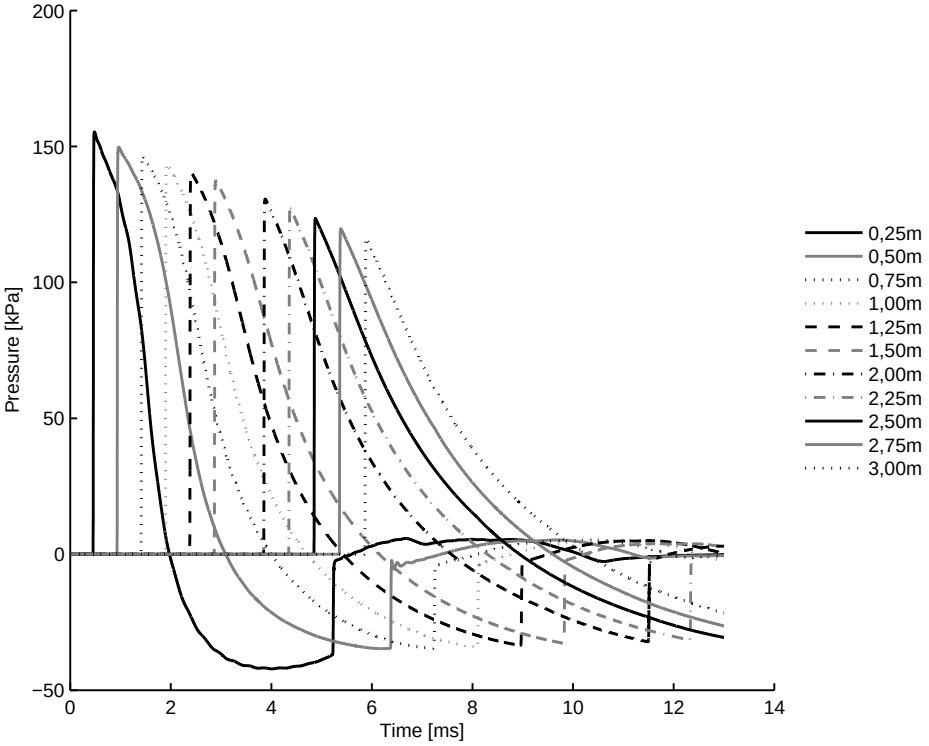
B.8 (a): 50% of Convex Driver and Transition Length 10*bar*



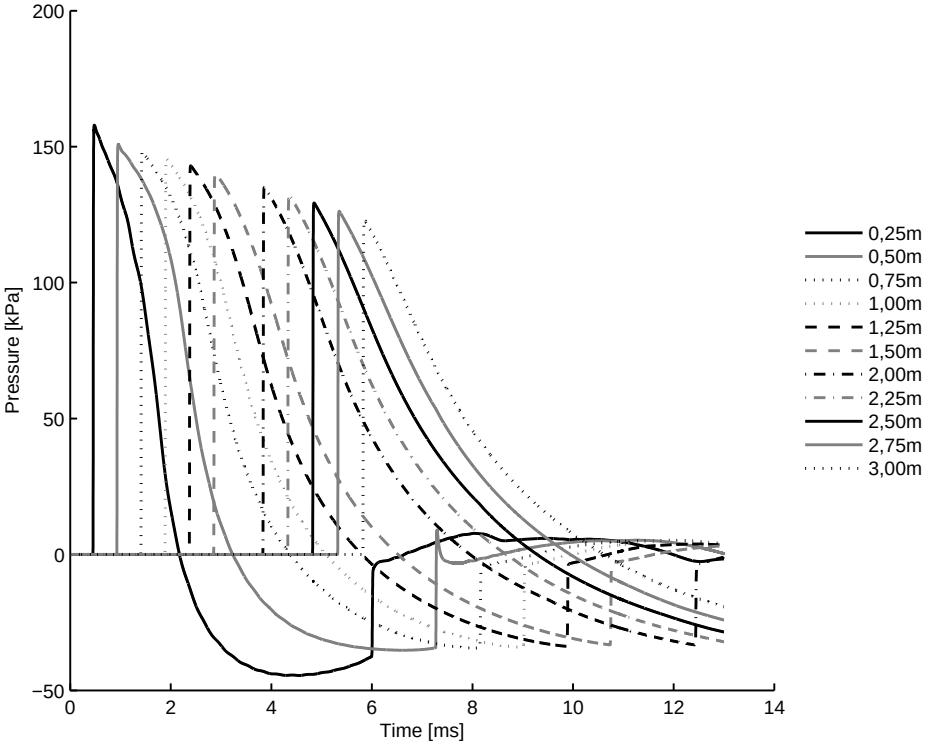
B.8 (b): 75% of Convex Driver and Transition Length 10*bar*



B.8 (c): 100% of Convex Driver and Transition Length 10*bar*

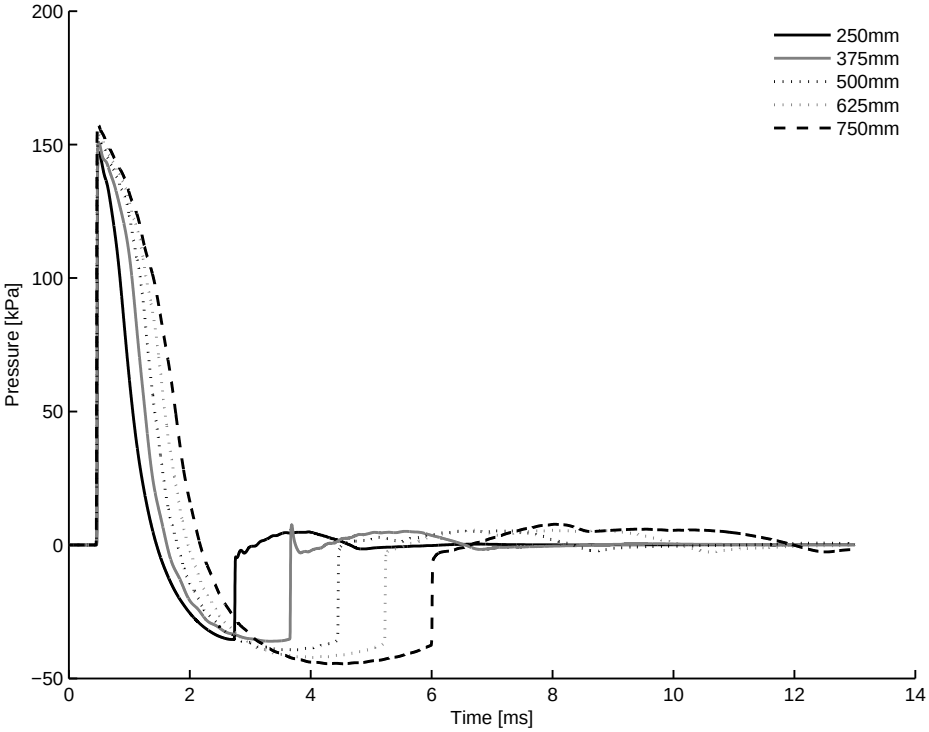


B.8 (d): 125% of Convex Driver and Transition Length 10*bar*

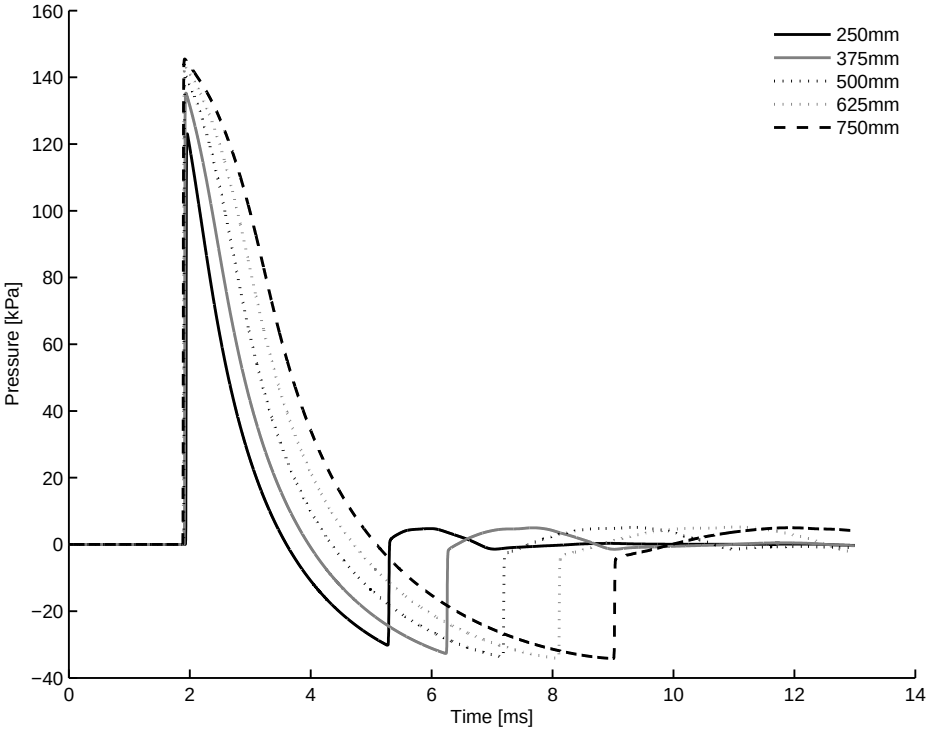


B.8 (e): 150% of Convex Driver and Transition Length 10*bar*

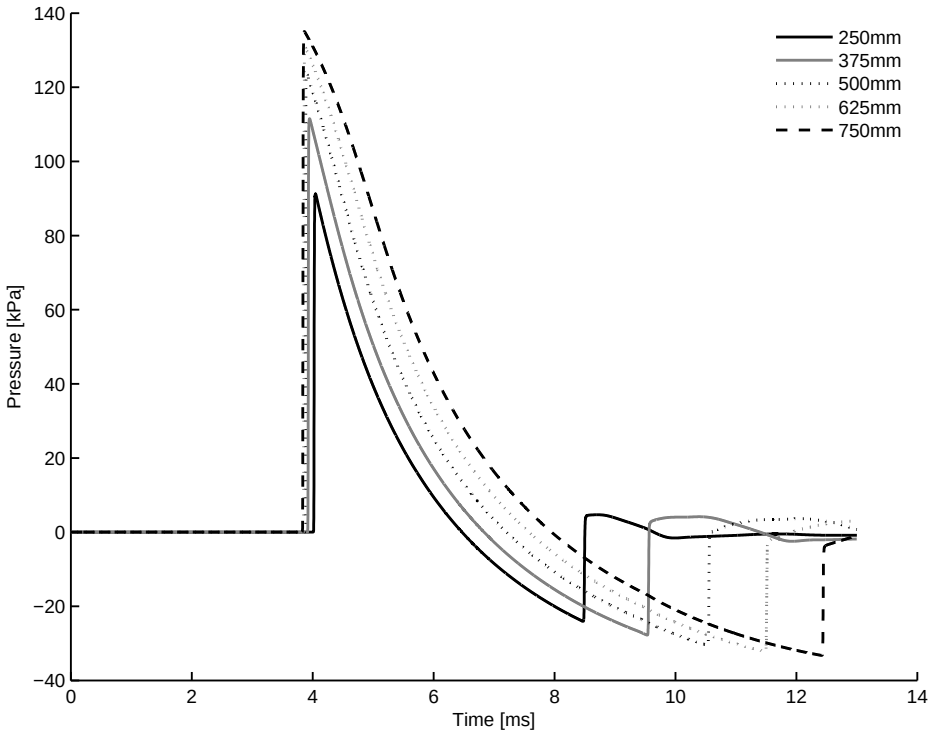
Figure B.8: The Development of the Blast Pressure Profile for Increasing Convex Driver and Transition Length



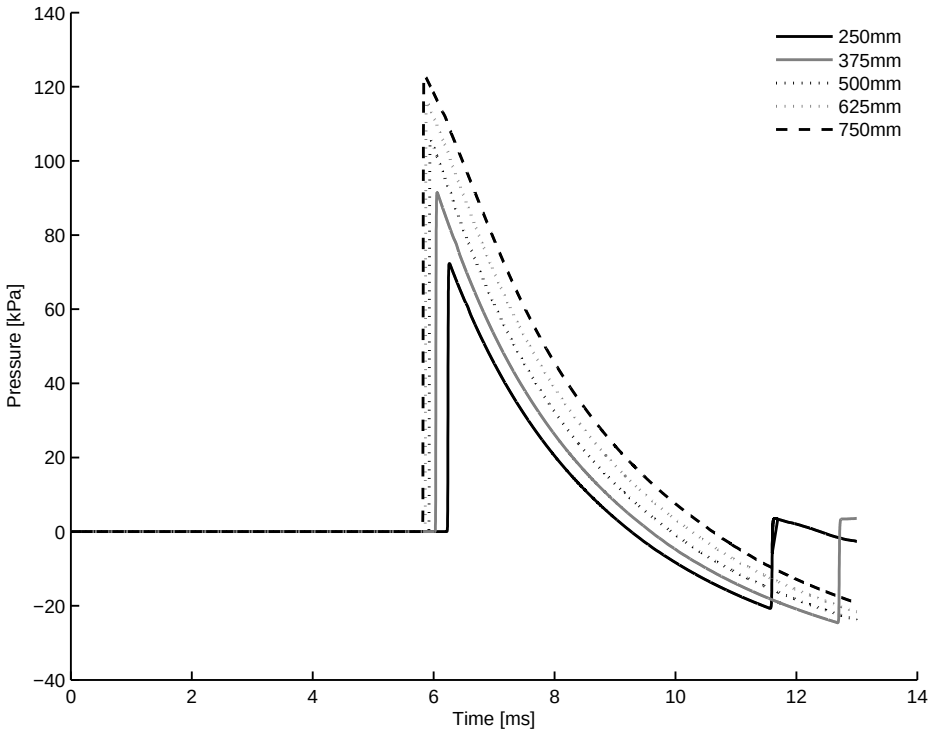
B.9 (a): $0.25m$ $10bar$



B.9 (b): $1.00m$ $10bar$

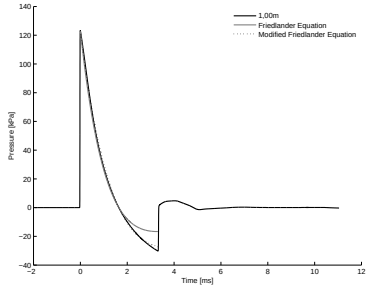


B.9 (c): 2.00m 10bar

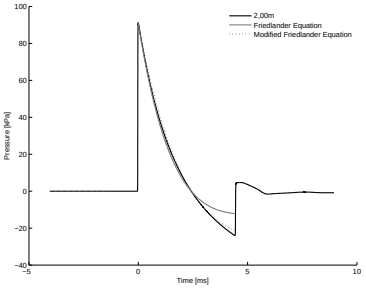


B.9 (d): 3.00m 10bar

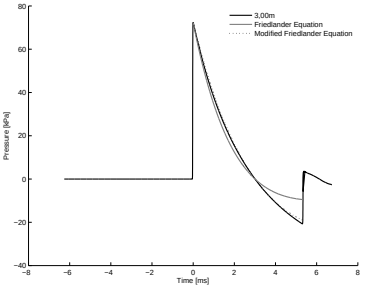
Figure B.9: The Effect of Increasing the Convex Driver and Transition Section Length on the Pressure Profile



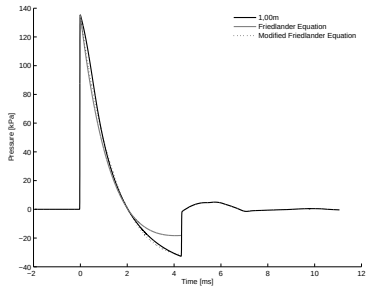
B.10 (a): 50% of Convex Driver and Transition Length 10bar 1.00m



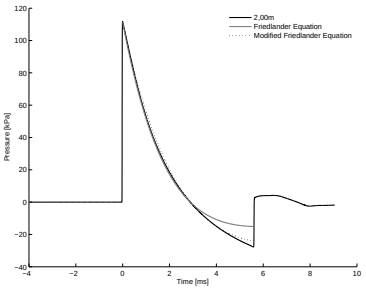
B.10 (b): 50% of Convex Driver and Transition Length 10bar 2.00m



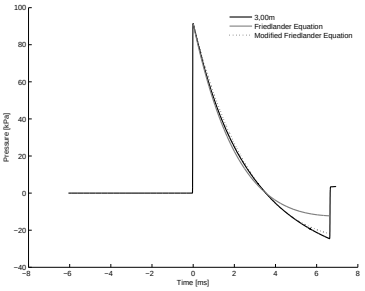
B.10 (c): 50% of Convex Driver and Transition Length 10bar 3.00m



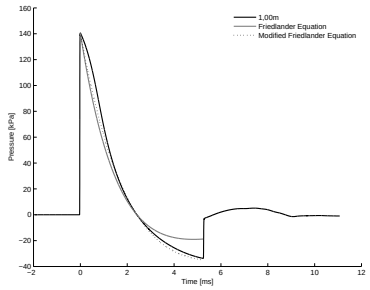
B.10 (d): 75% of Convex Driver and Transition Length 10bar 1.00m



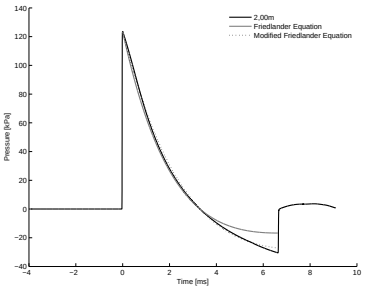
B.10 (e): 75% of Convex Driver and Transition Length 10bar 2.00m



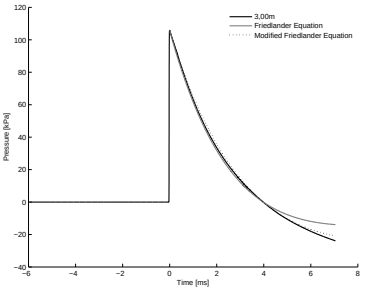
B.10 (f): 75% of Convex Driver and Transition Length 10bar 3.00m



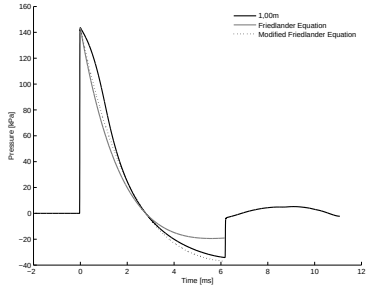
B.10 (g): 100% of Convex Driver and Transition Length 10bar 1.00m



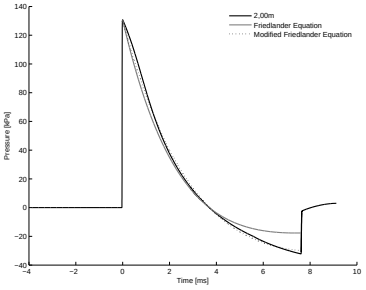
B.10 (h): 100% of Convex Driver and Transition Length 10bar 2.00m



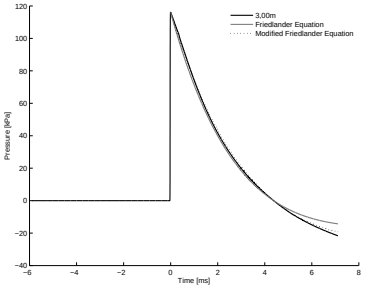
B.10 (i): 100% of Convex Driver and Transition Length 10bar 3.00m



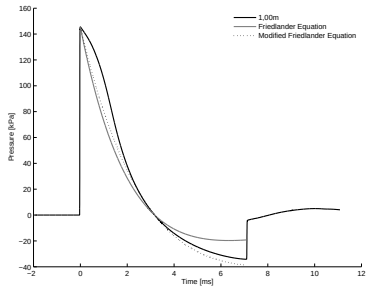
B.10 (j): 125% of Convex Driver and Transition Length 10*bar* 1.00*m*



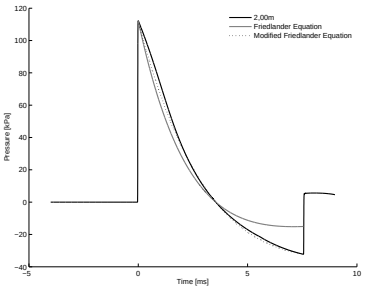
B.10 (k): 125% of Convex Driver and Transition Length 10*bar* 2.00*m*



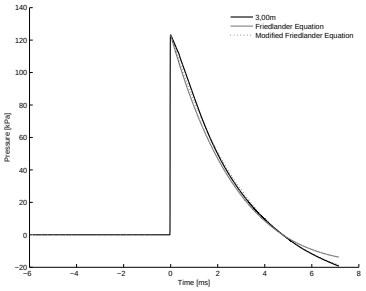
B.10 (l): 125% of Convex Driver and Transition Length 10*bar* 3.00*m*



B.10 (m): 150% of Convex Driver and Transition Length 10*bar* 1.00*m*

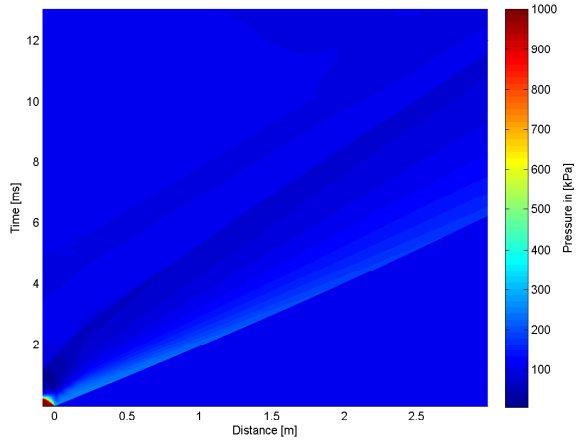


B.10 (n): 150% of Convex Driver and Transition Length 10*bar* 2.00*m*

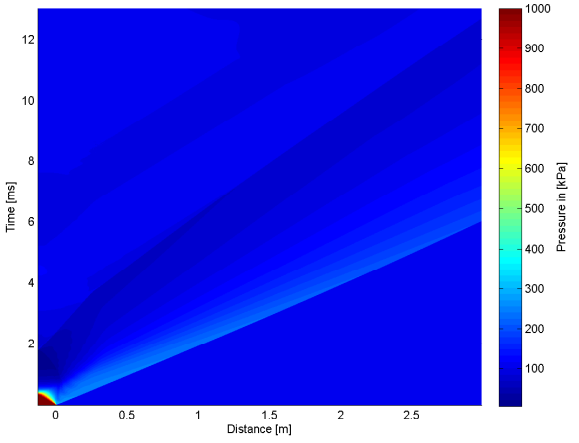


B.10 (o): 150% of Convex Driver and Transition Length 10*bar* 3.00*m*

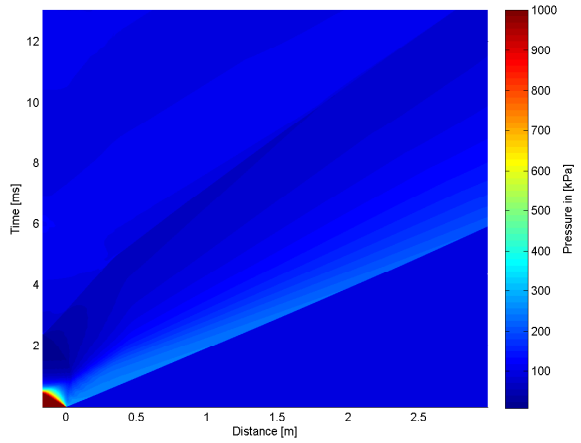
Figure B.10: Comparing the Effect of Varying the Convex Driver and Transition Section Length on the Friedlander Pressure Profile



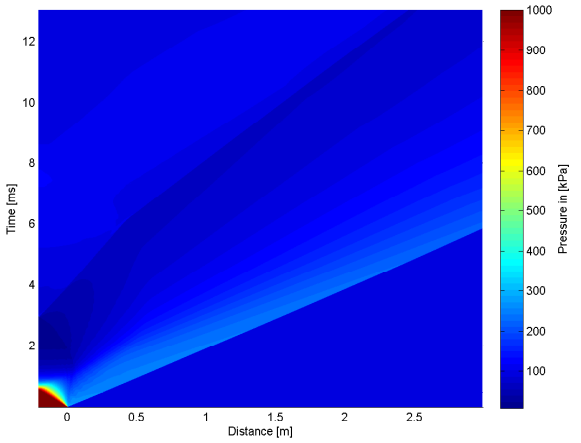
B.11 (a): 50% of Convex Driver and Transition Length 10*bar*



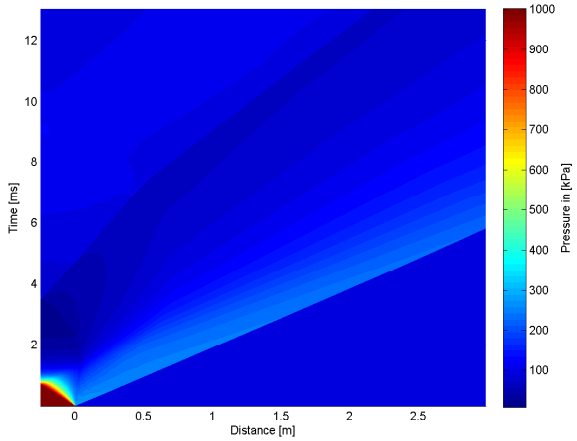
B.11 (b): 75% of Convex Driver and Transition Length 10*bar*



B.11 (c): 100% of Convex Driver and Transition Length 10*bar*

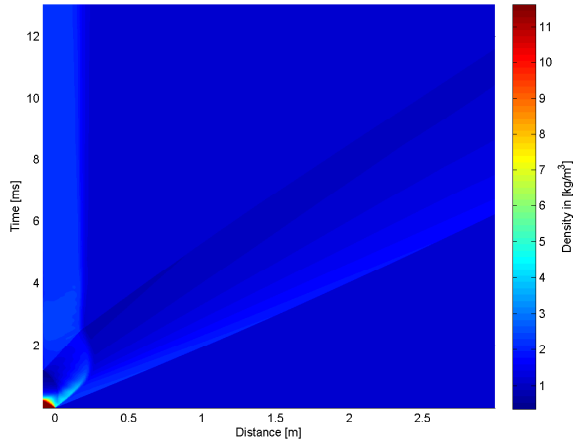


B.11 (d): 125% of Convex Driver and Transition Length 10*bar*

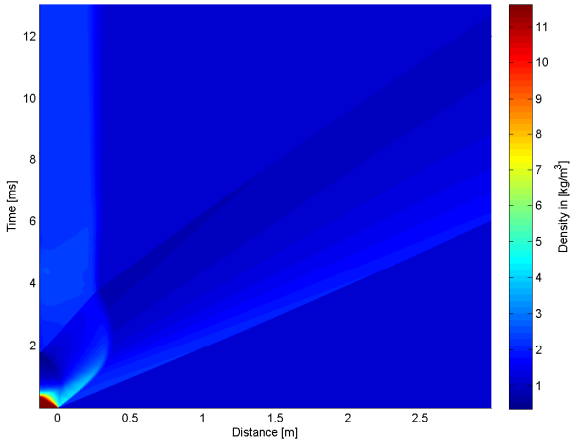


B.11 (e): 150% of Concave Driver and Transition Length 10*bar*

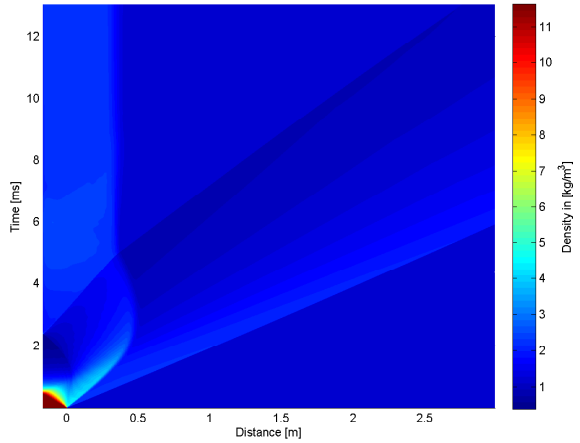
Figure B.11: X-T Diagram for Varying the Convex Driver and Transition Section Length (Pressure)



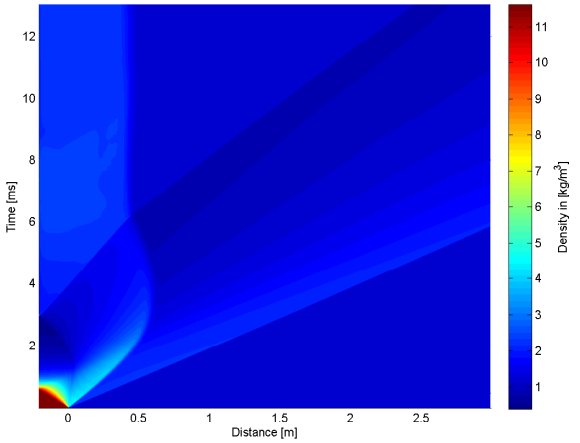
B.12 (a): 50% of Convex Driver and Transition Length 10*bar*



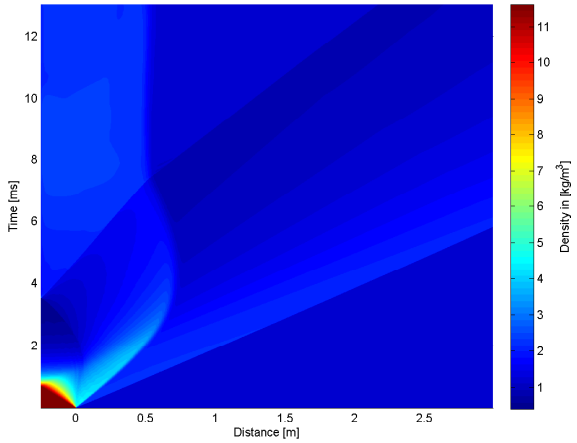
B.12 (b): 75% of Convex Driver and Transition Length 10*bar*



B.12 (c): 100% of Convex Driver and Transition Length 10*bar*

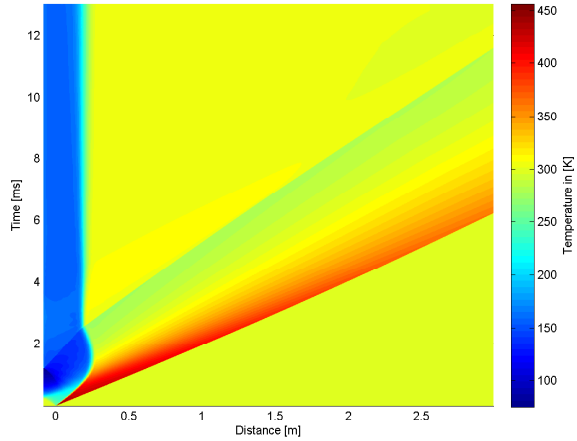


B.12 (d): 125% of Convex Driver and Transition Length 10*bar*

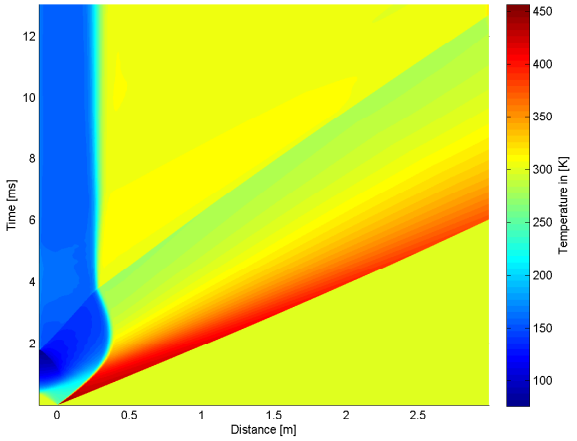


B.12 (e): 150% of Convex Driver and Transition Length 10*bar*

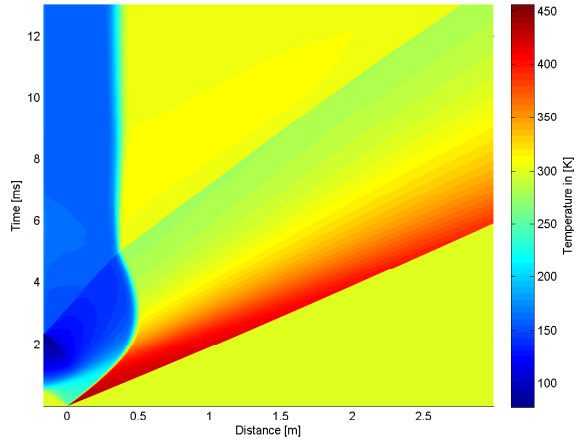
Figure B.12: X-T Diagram for Varying the Convex Driver and Transition Section Length (Density)



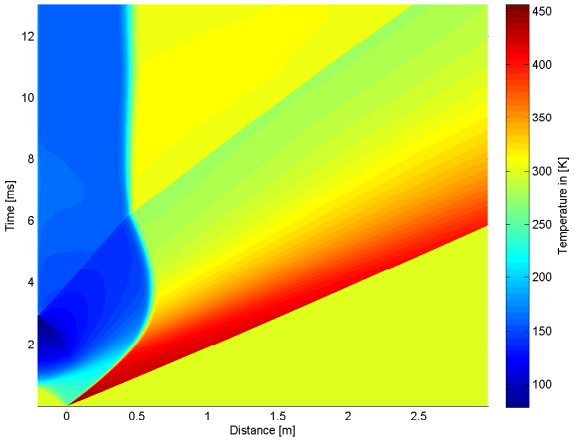
B.13 (a): 50% of Convex Driver and Transition Length 10*bar*



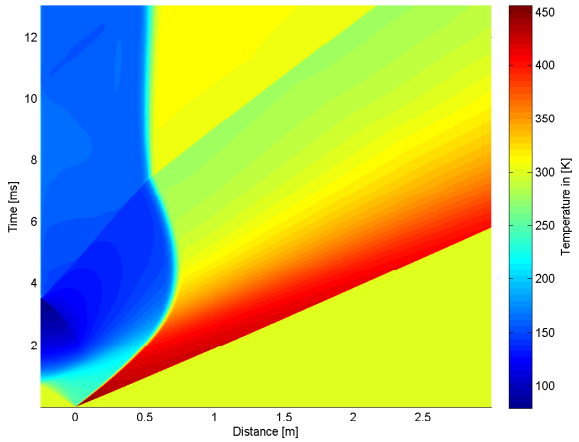
B.13 (b): 75% of Convex Driver and Transition Length 10*bar*



B.13 (c): 100% of Convex Driver and Transition Length 10*bar*

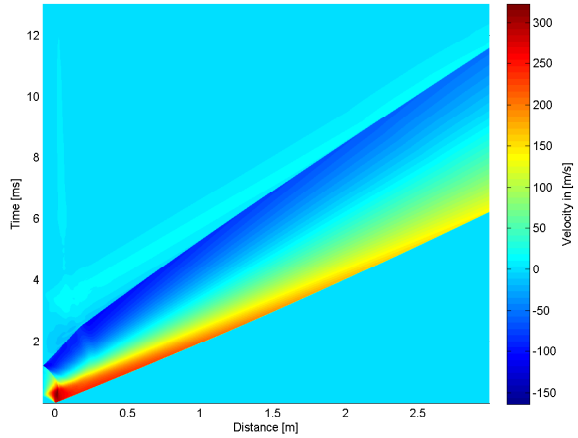


B.13 (d): 125% of Convex Driver and Transition Length 10*bar*

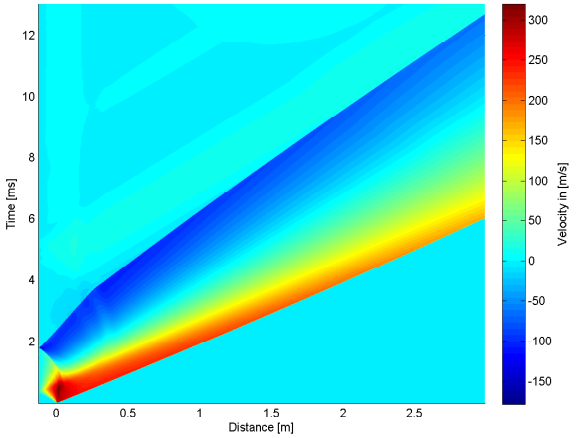


B.13 (e): 150% of Concave Driver and Transition Length 10*bar*

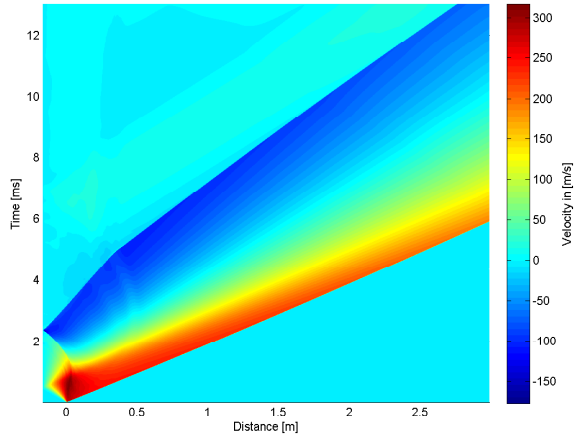
Figure B.13: X-T Diagram for Varying the Convex Driver and Transition Section Length (Temperature)



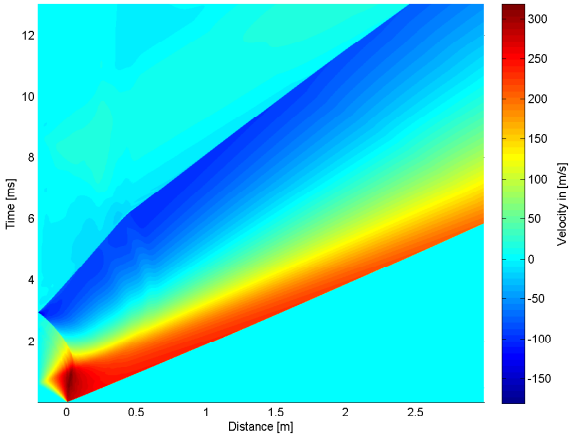
B.14 (a): 50% of Convex Driver and Transition Length 10*bar*



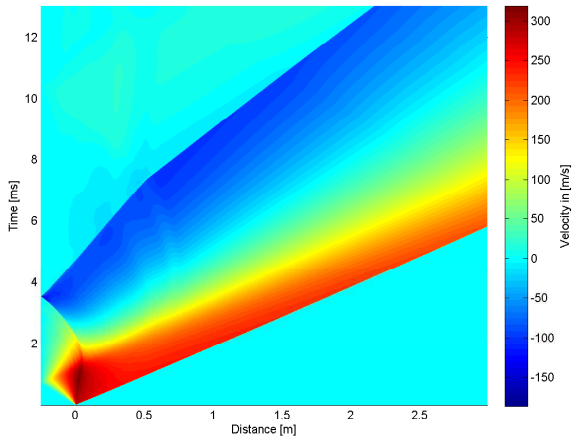
B.14 (b): 75% of Convex Driver and Transition Length 10*bar*



B.14 (c): 100% of Concave Driver and Transition Length 10*bar*



B.14 (d): 125% of Convex Driver and Transition Length 10*bar*



B.14 (e): 150% of Convex Driver and Transition Length 10*bar*

Figure B.14: X-T Diagram for Varying the Convex Driver and Transition Section Length (Velocity)

Appendix C Digital Appendix

The digital appendix submitted in conjunction with this research consists of the following sections:

C.1 Blast Tube Research and Design CFD Simulations

C.2 High Speed Experimental Images

C.3 Engineering Drawings of Blast Tube Driver Section

C.4 Engineering Drawings of Blast Tube Transition Section

C.5 Data Processing MATLAB Codes